University of Southampton

Faculty of Engineering and Physical Sciences

School of Engineering

Soil Parameters for Modelling Critical Velocity Effects of Railways

by

Alice Duley

Thesis for the degree of Engineering Doctorate (EngD)

December 2018

University of Southampton

Abstract

Faculty of Engineering and Physical Sciences

School of Engineering

Thesis for the degree of Engineering Doctorate

Soil Parameters for Modelling Critical Velocity Effects of Railways

by

Alice Jane Frances Duley

In many countries high speed rail is playing a growing role in improving the capacity, availability and carbon cost of national infrastructure. Higher speeds require straighter railway alignments, which often means crossing areas of soft ground that have historically been avoided. Due to their low ground-borne surface wave speeds, there is a greater likelihood in such areas of the train passage resulting in critical velocity effects – a phenomenon in which excessive ground and track movement and vibration occurs. This can cause extensive damage, and may result in a forced reduction of train speeds.

The aim of this research is to assess methods of determining appropriate soil parameters for use in simple elasticity-based models for the prediction of critical velocity effects on railways. After a review of existing knowledge, the research consists of field measurements, laboratory experiments and modelling.

This research focuses around two case study sites on the UK rail network. Soil samples were extracted from each site, and tested in resonant column and triaxial equipment, to investigate their strain-dependent stiffness and damping. This involved testing on soil types for which there is little published data, including highly organic silts. The results are compared with measurements taken in situ, including seismic analysis and heavy probe tests.

A linear elastic model, MOTIV, of train-induced vibration is used to investigate the key soil and model parameters required for critical velocity analysis, as well as to assess the importance of the non-linearity of soil stiffness and damping with strain. It is clear that the use of strain-degraded soil parameters, for example through the use of an equivalent linear model, is essential. Recommendations are made for the best methods to obtain the relevant data, from which reliable critical velocity predictions can be made using linear soil models.

Table of Contents

Table of Contents ..... **i**

List of Tables ..... **vii**

List of Figures ..... **ix**

List of Accompanying Materials ..... **xxi**

Research Thesis: Declaration of Authorship ..... **xxiii**

Acknowledgements ..... **xxv**

List of Symbols and Abbreviations ..... **xxvii**

Chapter 1 Introduction **33**

1.1 Background 33

1.2 Research Aims and Methodology 36

1.2.1 Aims and objectives 36

1.2.2 Methodology 37

1.3 Thesis overview 37

1.4 Original contributions of thesis 38

Chapter 2 Background **41**

2.1 Critical velocity effects – Causes, measurements and modelling 41

2.1.1 An introduction to critical velocity effects 41

2.1.2 Rayleigh waves and other causes 42

2.1.3 Modelling critical velocity effects 45

2.2 Measuring dynamic properties of soils 55

2.2.1 Soil stiffness and damping 55

2.2.2 Site and laboratory equipment overview 57

2.2.3 Anisotropy considerations 59

Chapter 3 Modelling Background **61**

3.1 MOTIV model theory and past work 61

3.1.1 Background and theory 61

3.2 Parametric study 63

3.2.1 Basic model parameters 63
3.2.2 Geometries 67
3.2.3 Model dimensions 75
3.2.4 Track and vehicle parameters 77
3.2.5 Ground parameters 78
3.2.6 Impact of saturation levels 81
3.2.7 Parametric study conclusion 84
3.3 More detailed modelling 85
3.3.1 Impact of more detailed model geometry 86
3.3.2 Impact of thickness of stiffer surface layer 89
3.3.3 Impact of thickness of lower softer layer 91
3.3.4 Impact of stiffness ratios of soil layers 93
3.3.5 Assumptions and compromises 95
Chapter 4 Site and Experimental Methods 97
4.1 In situ site measurements 97
4.1.1 Penetration tests 97
4.1.2 Seismic measurements 97
4.2 Site sampling 98
4.2.1 Sampling techniques and considerations 98
4.3 The resonant column 103
4.3.1 Overview and adaptations 103
4.3.2 Theoretical considerations for the resonant column 108
4.3.3 Shear moduli and strain measurement 112
4.3.4 Resonant column calibration 114
4.3.5 Resonant column test procedure 118
4.3.6 Assumptions 120
4.4 The triaxial machine 121
4.4.1 Overview and adaptations 121
4.4.2 Derivation of parameters 123
4.4.3 Triaxial calibration 125

4.4.4 Triaxial test procedure 125

4.5 Bender elements 126

4.5.1 Theory and past use 126

4.5.2 General test procedure 129

4.6 Additional laboratory techniques 130

4.6.1 Transport, storage and logging of window samples from field work 130

4.6.2 Additional index testing 130

4.7 Sample preparation 131

Chapter 5 Gravel Hole Case Study Site 133

5.1 Site background and stratigraphy 133

5.2 Site measurements and sampling 136

5.2.1 Track and ground movement 136

5.2.2 Seismic testing 138

5.2.3 In situ sampling 139

5.3 Laboratory testing regime for site samples 145

5.3.1 Sample selection 145

5.3.2 Testing stresses and procedure 149

5.4 Laboratory test results 152

5.4.1 General index and organic content testing results 152

5.4.2 Resonant column / bender element results 153

5.4.3 Triaxial / bender element results 163

5.4.4 Comparison of results from both methods 176

5.5 Modelling with laboratory parameters 181

5.5.1 Parameter selection and incorporation of strain 181

5.5.2 Results – non-degraded and degraded parameters 186

5.6 Discussion of site testing and modelling 191

Chapter 6 Fishbourne Case Study Site 195

6.1 Site background and stratigraphy 195

6.2 Site measurements and sampling 197

6.2.1 Track and ground movement 197
6.2.2 Seismic testing 197
6.2.3 In situ sampling 200
6.3 Initial modelling 205
6.3.1 Modelling with basic site investigation parameters 205
6.4 Laboratory testing regime for site samples 208
6.4.1 Sample selection 208
6.4.2 Testing stresses 209
6.5 Laboratory test results 210
6.5.1 General index testing 210
6.5.2 Resonant column results 211
6.5.3 Triaxial / bender element results 213
6.5.4 Comparison of results from both methods 217
6.6 Modelling with laboratory parameters 219
6.6.1 Parameter selection and incorporation of strain 219
6.6.2 Results – non-degraded parameters 222
6.6.3 Results - degraded parameters 223
6.7 Discussion of site testing and modelling 226

Chapter 7 Discussion – Case Study Results 229

7.1 Key parameters and modelling factors 229
7.2 The impact of parameter source 229
7.2.1 Density 229
7.2.2 Stratigraphy 230
7.2.3 Strength parameters 230
7.3 The importance of model geometry 231
7.4 The importance of strain degradation 232

Chapter 8 Conclusions and recommendations 235

8.1 Conclusions 235
8.2 Recommendations for future work 239

Appendix A Gravel Hole Borehole Results 243

Appendix B Fishbourne Borehole Results 251

Bibliography 255

List of Tables

Table 2.1: Maximum train speeds for un-modified trains.....42

Table 3.1: Default track and vehicle input parameters for MOTIV. 64

Table 3.2: Initial Gravel Hole modelling ground paramters. 67

Table 3.3: Beta and Gamma max values. 76

Table 3.4: Refined ground parameters.....79

Table 3.5: Peat parameters for various levels of saturation 82

Table 3.6: Soil parameters for MOTIV model T3.9 - multiple layers above a stiffer halfspace. 87

Table 3.7: Ground parameters for models T4.4 and T4.5. 89

Table 5.1: Summary of Network Rail Gravel Hole borehole measurements, after Aspin Foundations Ltd (2013).....134

Table 5.2: Gravel Hole wavespeed measurements (Rushworth, 2014). 138

Table 5.3: Gravel Hole lab sample initial parameters. 146

Table 5.4: Calculated in situ stresses and target testing stresses for Gravel Hole samples. 151

Table 5.5: Organic content results for Gravel Hole. 153

Table 5.6: G_O values for all Gravel Hole Samples, from both resonant column and bender element techniques. 160

Table 5.7: Compressional and shear wave speeds measured in the RC using bender elements. 160

Table 5.8: Peak undrained strengths - triaxial tests 175

Table 5.9: Gravel Hole post-laboratory modelling parameters 183

Table 5.10: Input and output strains for Gravel Hole models. 190

List of Tables

Table 6.1: Fishbourne ground properties from MASW and MOTIV analysis (Wiseman, 2015)..... 198

Table 6.2: Estimated of ground strength and Young's modulus parameters based on the wavespeed measurements and modelling predictions of Wiseman (2015) for the Fishbourne site. 198

Table 6.3: Fishbourne (FB1) initial modelling parameters..... 206

Table 6.4: Fishbourne lab sample details. 209

Table 6.5: Calculated in situ stresses and target testing stresses for samples FB2G and FB2H. 210

Table 6.6: Compressional and shear wave speeds measured in the RC using bender elements. 213

Table 6.7: Details of probe tests for FB2G 214

Table 6.8: Fishbourne post-laboratory test modelling parameters. 221

Table 6.9: Input and output strains for Fishbourne models. 225

Table 8.1: Full Gravel Hole borehole results – GHS1 243

Table 8.2: Full Gravel Hole borehole results – GHS2 246

Table 8.3: Gravel Hole sample register 249

Table 8.4: Full Fishbourne borehole results - FBS1..... 251

Table 8.5: Full Fishbourne borehole results – FBS2 252

Table 8.6: Fishbourne sample register..... 254

List of Figures

Figure 1.1**:** Track displacement with increasing speed for Ledsgård, Sweden. After Kaynia *et al.* (2000).....33

Figure 2.1: Track displacements, normalised by static displacements, for Ledsgård (Sweden), Utrecht (Netherlands and Stilton Fen (UK) critical velocity sites. 42

Figure 2.2: Relationship between Poisson's ratio, P-wave, S-wave and Rayleigh wavespeeds, in a linear elastic homogeneous halfspace (Richart, 1962). 43

Figure 2.3 : Train geometry and loads in comparison to measured and simulated vertical displacement response: ▬ measured; — simulated. Ledsgård, Sweden. (b) is a southbound train, (c) and (d) northbound (Madshus and Kaynia, 2000).....47

Figure 2.4: Stress-strain loop, showing hysteretic damping loop and linearity of response at low strain levels. Modified from Houbrechts *et al.* (2011).....49

Figure 2.5: Shear modulus degradation curves from triaxial tests on samples taken from the Ledsgård critical velocity site. Figure b is the shear modulus reduction curve with strain and figure c the damping (%) reduction curve with strain (Madshus and Kaynia, 2000) 50

Figure 2.6: Simulated stress path of a point in the soft soil layer at the Ledsgård critical velocity site, with train passage of 70 km/h (a) and 204 km/h (b). dp is the mean stress increment, whilst dq is the shear stress increment (Alves Costa *et al.*, 2010).....52

Figure 2.7: Maximum ground displacement vs. train speed. Redrawn from Powrie *et al.* (2008).....54

Figure 2.8: Secant shear-stiffness versus shear-strain data for a variety of soil types (Vardanega and Bolton, 2013).....56

Figure 2.9: Typical damping ratio increase with shear strain, in relation to soil plasticity (Vucetic and Dobry, 1991). OCR 1-8 defines the over-consolidation ratio range for which this damping-strain relationship is considered valid.....56

Figure 2.10: Typical shear modulus behaviour with strain.....57

Figure 2.11: Common in-situ and laboratory tests. Modified from Schneider et al. (1999).58

List of Figures

Figure 2.12: Strain deformation range for a variety of dynamic lab tests (Houbrechts et al., 2011)..... 59

Figure 3.1: Schematics of MOTIV model for bogied vehicle (Sheng *et al.*, 2003). 61

Figure 3.2: Schematics of MOTIV model for track-ground system (Sheng *et al.*, 2003). .. 62

Figure 3.3: Gravel Hole boreholes cross section (After Aspin Foundations Ltd (2013)). .. 63

Figure 3.4: Cross-section schematic of track and sub-system components. 65

Figure 3.5: Schematic of train vehicle dimensions. 65

Figure 3.6: MOTIV parametric study ground geometry types. 66

Figure 3.7: Rail displacement vs. load speed curves for a single point load and a single vehicle moving across a peat halfspace. Geophone measurement results for site also presented. 68

Figure 3.8: Displacement vs. load speed curves for a single point load and a single vehicle moving across a 2 m peat layer over a rigid foundation. Geophone measurement results for site also presented. 69

Figure 3.9: Displacement vs. load speed curves for a single point load moving across a peat layer over a rigid foundation, for various depths of peat. Geophone measurement results for site also presented. 70

Figure 3.10: 1/3 octave band pass-by response power spectrum of the rail for a full train (4 vehicles) running over a 2 m peat layer over rigid foundation at 20 ms^{-1}. 71

Figure 3.11: 1/3 octave band pass-by response power spectrum of the rail for a full train (4 vehicles) running over a 2 m peat layer over rigid foundation at 50 ms^{-1}. Geophone site measurements also presented. 72

Figure 3.12: 1/3 octave band pass-by response power spectrum of the rail for a full train (4 vehicles) running over a 2 m peat layer over rigid foundation at 90 ms^{-1}. 72

Figure 3.13: Displacement vs. load speed curves for a single point load and a single vehicle moving across a 2 m thick peat layer over a halfspace of stiffer material. Geophone measurement results for site also presented. 73

Figure 3.14: 1/3 octave band pass-by response power spectrum of the rail for a full train (4 vehicles) running over a 2 m peat layer over a halfspace of stiffer material at 50 ms-1. Geophone site measurements also presented.....74

Figure 3.15: Displacement vs. load speed curves for the second bogie of a single vehicle moving across all three ground types. Ground type 1 is a peat halfspace. Ground type 2 is a 2 m peat layer over a rigid foundation. Ground type 3 is a 2 m peat layer over a halfspace of stiffer material. Geophone measurement results for site also presented. 75

Figure 3.16: Rail displacement vs. wavenumber relationship, peat halfspace with a single moving load. 77

Figure 3.17: Displacement vs. load speed curves for the second bogie of a single vehicle running across ground type 3, using initial estimates and refined parameters. Geophone measurements results for site also presented. 80

Figure 3.18: 3D plot of ground surface displacement, for a single vehicle travelling at 67 ms^{-1} across a 2 m peat layer (refined peat parameters) above a stiffer half-space.80

Figure 3.19: Full train pass-by vibration response for 4 vehicles running at 53 ms^{-1} across ground type 3, using refined peat parameters. Site measurements also presented.....81

Figure 3.20: Displacements vs. load speed for a single vehicle running across a 2 m peat layer above a stiffer halfspace, using parameters given in Table 4. Geophone measurements are also shown.....83

Figure 3.21: Track receptances for different soil conditions, and wheelset receptance 84

Figure 3.22: Ground geometry for MOTIV model T3.9. 86

Figure 3.23: MOTIV model T3.9 - 0.4 m ballast-type gravel, over 0.3 m sand, over 2 m peat over a stiffer halfspace of sands, gravels and clays and MOTIV model T3.10 – 2 m peat over a stiffer halfspace of sands, gravels and clays, for a single vehicle. 88

Figure 3.24: Model T4.4 geometry, with upper sand and gravel layer of varying thickness.89

Figure 3.25: Displacement versus speed curves for a sand and gravel layer of varying thickness, over 2 m of peat over a sand and gravel halfspace.....90

List of Figures

Figure 3.26: Summary of impact of varying thickness (X) of surface layer (sands and gravels), over 2 m of peat over a sand and gravel halfspace..... 90

Figure 3.27: Model T4.5 geometry. 91

Figure 3.28: Displacement versus speed curves for a peat layer of varying thickness, between 1.5 m of sand and gravel and a sand and gravel halfspace. 92

Figure 3.29: Summary of impact of varying thickness (X) of soft peat layer, between 1.5 m of sand and gravel and a sand and gravel halfspace. 92

Figure 3.30: Model T4.6 geometry. 93

Figure 3.31: Displacement versus speed curves for 1.5 m of sand and gravel over 2 m of peat and a sand and gravel halfspace, for varied values of Young's modulus (E, MPa) and shear wave velocity (S, ms^{-1}) of the 1.5 m layer. 94

Figure 3.32: Summary of impact of varying ratio of stiffness between the upper stiffer layer, and the softer organic peat layer, for a model of 1.5 m of sand and gravel over 2 m of peat and a sand and gravel halfspace. 94

Figure 4.1: Windowless sampling rig in use AECOM Ltd. (2016)..... 102

Figure 4.2: Example frequency response curve for a Gravel Hole sample in the RC. 103

Figure 4.3: SRC – Typical fixed-free apparatus (Priest et al., 2005) – Modified from Stokoe et al. (1999). 104

Figure 4.4: Model of RC as a single degree of freedom, fixed-free configuration, with excitation modes shown. 104

Figure 4.5: Coil and magnet configuration for torsional and flexural excitation. Modified from Cascante *et al.* (1998). 105

Figure 4.6: Resonant column apparatus schematic, with bender elements installed. ... 106

Figure 4.7: The modified RC, showing modification brackets in red. Image A: top view of driveplate without top plate. B: top plate including mount for LVDT. C: Side view of drivehead bolted to support frame. D: Side view of magnet inside coil, embedded in acrylic. E: Left to right – pressure cell, base platen, support cell and drivehead. F: Inside view of top plated with embedded BE. 107

Figure 4.8: Typical free vibration decay plot showing sampling points in detail for a Gravel Hole sample. 109

Figure 4.9: Typical free vibration decay plot showing peak accelerometer output per cycle for a Gravel Hole sample. 110

Figure 4.10: Half-power bandwidth method for damping 110

Figure 4.11: Results of Stokoe RC testing on dense Leighton Buzzard sand (Clayton, 2011).112

Figure 4.12: Idealisation of wave propagation in a solid elastic cylinder (Otter, 2011). ..114

Figure 4.13: Standard aluminium calibration bars. 116

Figure 4.14: Single degree of freedom calibration for RC 117

Figure 4.15: Single degree of freedom calibration for RC I_O using regression analysis. 117

Figure 4.16: RC sample assembly - radial drain followed by latex membrane, greased foil strips and a second latex membrane.....119

Figure 4.17: Typical triaxial machine setup (Rees, 2016) 121

Figure 4.18: LVDT and bender elements (blue) set up on triaxial specimen.....122

Figure 4.19: Typical BE set-up within a triaxial cell (Camacho-Tauta *et al.*, 2012).....126

Figure 4.20: An example of start-to-start (time of first arrival) ,peak-to-peak and cross-correlation measurement methods for BE signals (Kumar and Madhusudhan, 2010).....128

Figure 5.1: Gravel Hole boreholes cross-section (After Aspin Foundations Ltd (2013)). 134

Figure 5.2: Summarised borehole results at various distances surrounding Gravel Hole (British Geological Society, 2016). Includes location map of boreholes relative to site (red dot). 135

Figure 5.3: Gravel Hole local contouring, red dot indicates site (Ordnance Survey, 2016).136

Figure 5.4: Gravel Hole site with geophones installed. 137

Figure 5.5: Geophone trace showing vertical displacement of a sleeper when passed by a 9-car Class 390 (Pendolino) at 195 km/h (54 m/s). 137

Figure 5.6: Averaged measured displacements and speed for all geophones at Gravel Hole, pre-remediation. Train type and range of displacement per train also shown.138

Figure 5.7: Sampling at Gravel Hole. 139

Figure 5.8: Summary of Gravel Hole window sampling results. Note sample iDs in blue ovals are further discussed in section 5.3.1. 141

Figure 5.9: Estimate undrained shear strengths from drop cone tests for Gravel Hole borehole samples. 142

Figure 5.10: SHDP results for Gravel Hole, converted to N_{300}, overlaid with relative densities for non-cohesive soils (Terzaghi and Peck, 1948; USACE., 1994)..... 143

Figure 5.11: Gravel Hole borehole density and gravimetric moisture content variation with depth. 144

Figure 5.12: Selection of Gravel Hole samples for testing. Top row from left: GH1D pre-test, GH1D post-test, GH2K pre-test. Bottom row from left: GH1P pre-test, GH2D pre-trim, GH2C pre-test. 147

Figure 5.13: Gravel Hole samples cross-sections. 148

Figure 5.14: Idealised pressure distribution beneath the sleeper. Figure from Abadi (2015), after AREMA (2003)..... 150

Figure 5.15: Gravel Hole sample GH1O/P plasticity classification chart. Modified from BS5930 (British Standards Institute, 2015). 152

Figure 5.16: Height change with vertical effective stress during consolidation for all Gravel Hole RC samples, normalised by initial sample height..... 154

Figure 5.17: Shear modulus degradation with strain for sample GH1O during torsional excitation in the RC, at a range of vertical effective stresses. Strain limit not met for 150 kPa and 250 kPa due to lack of power..... 156

Figure 5.18: Shear modulus degradation with strain for sample GH1D during torsional excitation in the RC, at a range of vertical effective stresses. Strain limits not met. 157

Figure 5.19: Shear modulus degradation with strain for sample GH2K during torsional excitation in the RC, at a range of vertical effective stresses. Strain limit met for all but 75 kPa and 125 kPa. 157

Figure 5.20: Shear modulus degradation with strain for sample GH2C during torsional excitation in the RC, at a range of vertical effective stresses. Strain limit met for 75 kPa. 158

Figure 5.21: Normalised shear modulus degradation with strain for all Gravel Hole samples in the RC, for a range of vertical effective stresses, normalised by small strain shear modulus at the start of each test. 158

Figure 5.22: Comparison of shear modulus derived from both torsional excitation and BE in the RC, for all Gravel Hole samples for a range of vertical effective stresses.159

Figure 5.23: Relationship between damping and strain for sample GH1O, during torsional excitation in the RC, for a range of vertical effective stresses. 161

Figure 5.24: Relationship between damping and strain for sample GH1D, during torsional excitation in the RC, for a range of vertical effective stresses. 162

Figure 5.25: Relationship between damping and strain for sample GH2K, during torsional excitation in the RC, for a range of vertical effective stresses. 162

Figure 5.26: Relationship between damping and strain for sample GH2C during torsional excitation in the RC, for a range of vertical effective stresses. 163

Figure 5.27: Example of K_O consolidation and stress probe paths for sample GH2J in the triaxial machine. 165

Figure 5.28: Example stress strain data for a constant p' probe (42 kPa) on sample GH2D.165

Figure 5.29: Example stress strain data for a constant p' probe (42 kPa) on sample GH2D, showing variance in global and axial strain levels. 166

Figure 5.30: Example stress-strain curve for a drained constant q probe (42kPa) on sample GH2D. 166

Figure 5.31: Resulting distortional strain for sample GH2D during increasing q, constant p' probes, at a range of mean effective stresses. 167

Figure 5.32: Example of stress-strain curve fitting to enable derivation of shear modulus, for sample GH2D during a constant p', increasing q probe at p'=48 kPa. Error bars for deviator stress and distortional strain measurement also shown (+/- 0.25 kPa q ; +/- 0.005% strain). 167

Figure 5.33: Relationship between shear modulus and strain for similar samples GH1O (RC) and GH1P (Triaxial) tested at a range of mean effective stresses. 169

Figure 5.34: Summary comparison of G_O for similar samples GH1O (RC and RC BE) and GH1P (Triaxial) tested at a range of mean effective stresses. 169

Figure 5.35: Shear modulus degradation with strain for sample GH2J from constant p', increasing q triaxial probes, at a range of mean effective stresses. 171

Figure 5.36: Shear modulus degradation with strain for sample GH2D from constant p', increasing q triaxial probes, at a range of mean effective stresses. 171

Figure 5.37: Comparison of relationship between very small strain shear modulus and vertical effective stress, for samples tested in the RC, RC BE and triaxial machines. Samples GH2K and 2H2J are considered similar, as are GH2C and GH2D. 172

Figure 5.38: Example application of a linear trendline to axial and radial strain data, to allow estimation of Poisson's ratio from constant σ'_h, increasing σ'_v triaxial probes for sample GH1P. 173

Figure 5.39: Relationship between Poisson's ratio and mean effective stress for sample GH1P tested with constant σ'_h, increasing σ'_v triaxial probes..... 173

Figure 5.40: Relationship between Poisson's ratio and axial strain, for sample GH2J tested with constant p', increasing q triaxial probes. 174

Figure 5.41: Relationship between Poisson's ratio and axial strain, for sample GH2D tested with constant p', increasing q triaxial probes. 174

Figure 5.42: Peak undrained strength calculation from large shear test - GH1P. Peak strength is equal to half the peak stress. 175

Figure 5.43: Comparison of the small strain shear moduli parameters G*, derived from undrained triaxial tests, and G_{hv}, derived from bender element tests, presented for a range of test pressures. 176

Figure 5.44: Normalised shear modulus degradation with strain for similar Gravel Hole sample pairs GH2K + GH2J and GH2C + GH2D, in the RC and triaxial machines. Results shown are for a range of mean effective stresses. 177

Figure 5.45: Normalised shear modulus degradation with strain for similar Gravel Hole sample pairs GH1P+ GH1O and sample GH1D, in the RC and triaxial machines. Results shown are for a range of mean effective stresses 177

Figure 5.46: Normalised shear modulus degradation with strain for GH1O/P clay samples, shown for a range of effective stresses. Also shown are typical normalised shear modulus with strain relationships for various clay plasticity indexes, after Zen *et al.* (1978). GH1O/P PI is 10.9%. 178

Figure 5.47: Normalised shear modulus degradation with strain for Gravel Hole silt samples, for a range of effective stresses. Also shown are typical normalised shear modulus with strain relationships for various offshore silty clay samples, from Sun *et al.* (1988), summarising data from Idriss *et al.* (1976); Anderson (1980); Stokoe *et al.* (1980).....179

Figure 5.48: Shear modulus degradation of samples GH2K, GH2C and GH1D compared to those for a variety of materials. Modified from Kallioglou *et al.* (2008). 180

Figure 5.49: Measured damping for Gravel Hole RC samples, compared to typical clay damping ratios modified from Sun *et al.* (1988) and Seed and Idriss (1970).181

Figure 5.50: Gravel Hole modelling geometry based on site boreholes. 182

Figure 5.51: Typical G/ G_O versus strain relationship for sands (Seed and Idriss, 1970) and gravels (Seed *et al.*, 1986) as summarised in Rollins *et al.* (1998).....185

Figure 5.52: Damping variation with strain from a range of investigations, as summarised in Rollins *et al.* (1998). 186

Figure 5.53: Vertical strain variation with load speed and depth, for model ND1, with layer boundaries marked.....186

Figure 5.54: Total peak sleeper displacements with load speed for Gravel Hole models ND1, B1, B2 and B3, with site measurements for reference.....187

Figure 5.55: Output strain versus assumed (input) strains for Gravel Hole models. 188

Figure 5.56: Total peak sleeper displacements with load speed for Gravel Hole models B4, B5, B6, and B7, with site measurements for reference. 189

Figure 5.57: Vertical strain variation with load speed and depth, for model B6, with layer boundaries marked. 189

Figure 5.58: Vertical strain variation with load speed and depth, for model B5, with layer boundaries marked. 190

Figure 6.1: Summarised borehole results at various distances surrounding Fishbourne (British Geological Society, 2016). Includes location map of boreholes relevant to site (site shown by red dot). 196

Figure 6.2: Fishbourne local contouring, red dot indicates site (Ordnance Survey, 2016).197

Figure 6.3: Soil dispersion plot for Fishbourne based on site seismic measurements. Scale for amplitude of Z-axis response shown. After Wiseman (2015). 199

Figure 6.4: Soil dispersion plot from Fishbourne seismic measurements, normalised by the maximum amplitude in each frequency. Scale for comparative amplitude of Z-axis response shown. After Wiseman (2015) 200

Figure 6.5: Fishbourne site sampling location. Rail track behind hedge along yellow line.201

Figure 6.6: Summary of Fishbourne boreholes 202

Figure 6.7: Estimate undrained shear strengths from drop cone test for Fishbourne borehole samples. 203

Figure 6.8: SHDP results for Fishbourne, with overlaid estimated relationship between SHDP and clay strength classification, taken from Huntley (1990) 204

Figure 6.9: Fishbourne borehole density variation with depth 205

Figure 6.10: Fishbourne model FB1 (desk-study) geometry 206

Figure 6.11: MOTIV displacement results for Fishbourne model FB1 - desk study parameters. 207

Figure 6.12: Dispersion plot for Fishbourne model FB1 - desk study parameters. 207

Figure 6.13: Fishbourne boreholes - selection of dried density samples, displaying variation in soil colouring and type. 208

Figure 6.14: Fishbourne bore 2, sections 1-2 m (left) and 3-4 m (right) 208

Figure 6.15: Fishbourne samples 2G (left) and 2H (right) before trimming (top) and after trimming (bottom). 209

Figure 6.16: Fishbourne sample 2G/2H plasticity classification chart. Chart modified from BS5930 (British Standards Institute, 2015). 210

Figure 6.17: Shear modulus degradation with strain for sample FB2H during torsional excitation in the RC, at a range of mean effective stresses. Strain limits not met. 211

Figure 6.18: Relationship between damping and strain for sample FB2H, during torsional excitation in the RC, for a range of mean effective stresses. 212

Figure 6.19: Measured damping for FB2H compared to typical clay damping ratios modified from Sun *et al.* (1988). 212

Figure 6.20: Shear modulus degradation with strain for sample FB2G from constant p', increasing q triaxial probes, at a range of mean effective stresses. 214

Figure 6.21: Relationship between Poisson's ratio and axial strain, for sample FB2G tested with constant p', increasing q triaxial probes. 215

Figure 6.22: Large undrained triaxial shear result for FB2G, at a confining pressure of 146 kPa. 216

Figure 6.23: Comparison of the small strain shear moduli parameters G*, derived from undrained triaxial tests, and G_{hv}, derived from bender element tests, for a range of test pressures. 217

Figure 6.24: Comparison of relationship between very small strain shear modulus and vertical effective stress, for similar samples FB2G and FB2H tested in the RC, RC BE and triaxial machines. 218

Figure 6.25: Normalised shear modulus degradation with strain for similar Fishbourne samples FB2H and FB2G in the RC and triaxial machines. Results shown are for a range of vertical effective stresses. Also shown are typical normalised shear modulus with distortional strain relationship for various clay plasticity indexes, after Zen *et al.* (1978). 219

List of Figures

Figure 6.26: Model geometry for Fishbourne models FB2,FB3 and FB4..... 220

Figure 6.27: Relationship between load speed and sleeper displacement, 4 vehicle model– Fishbourne model FB2 (Lab-based parameters, non-degraded). 223

Figure 6.28: Dispersion plot for Fishbourne model FB2- Non-degraded lab based parameters. 223

Figure 6.29: Total peak sleeper displacements with load speed for all Fishbourne lab-based models. 225

Figure 6.30: Input versus peak output strains for Fishbourne models. 226

List of Accompanying Materials

Appendix A:	Full Gravel Hole borehole sampling results and sample register
Appendix B	Full Fishbourne borehole sampling results and sample register

Research Thesis: Declaration of Authorship

Print name:	Alice Jane Frances Duley

Title of thesis:	Soil Parameters for Modelling Critical Velocity Effects of Railways

I declare that this thesis and the work presented in it are my own and has been generated by me as the result of my own original research.

I confirm that:

1. This work was done wholly or mainly while in candidature for a research degree at this University;
2. Where any part of this thesis has previously been submitted for a degree or any other qualification at this University or any other institution, this has been clearly stated;
3. Where I have consulted the published work of others, this is always clearly attributed;
4. Where I have quoted from the work of others, the source is always given. With the exception of such quotations, this thesis is entirely my own work;
5. I have acknowledged all main sources of help;
6. Where the thesis is based on work done by myself jointly with others, I have made clear exactly what was done by others and what I have contributed myself;
7. Parts of this work have been published as:

Duley, A., Powrie, W., Thompson, D & Le Pen, L. (2016). Understanding critical velocity effects on high speed railways. Proceedings of the 1st International Meeting of Young Transportation Geotechnics Engineers of the ISSMGE, Guimaraes, Portugal

Duley, A., Le Pen, L., Thompson, D.J., Powrie, W., Watson, G,V,R.,Musgrave,P., & Cornish, A. (2015). Critical train speeds and associated track movements: a case study. Proceedings of the XVI ECSMGE Geotechnical Engineering for Infrastructure and Development, ICE Publishing, pp 253-258, Edinburgh, UK

Duley, A., Le Pen, L., Thompson, D.J., Powrie, W., Watson, G,V,R.,Musgrave,P., & Cornish, A. (2014). Modelling and measurements of critical train speed effects and associated track movements. Proceedings of the International Conference on High Speed Rail, Birmingham, UK.

Signature:		Date:	

Acknowledgements

Firstly I wish to sincerely thank my supervisors Professor David Thompson, Professor William Powrie and Dr Louis Le Pen for providing this opportunity, their knowledge, guidance and advice.

I am indebted to both Dr. Madhusudhan and Harvey Skinner for their assistance with mastering the laboratory testing, as well as the other researchers within the geotechnics laboratory and the wider department, for the continued moral support during the trials and tribulations of lab testing.

I am grateful to my colleagues within the Dynamics research group, for their assistance with site measurements and modelling, particularly Dr. Ntotsios.

Thanks go to the Engineering and Physical Sciences Research Council, and HS2 Ltd., for the funding which made this research possible. Additional thanks are required to Dr Matthew Brough of AECOM Ltd. and various colleagues at Network Rail for enabling us to close a railway to allow site sampling to take place.

Finally, I would like to thank my family and friends, for the endless pep talks, distractions and motivational speeches. Most importantly, I thank my wife Natalie, for always believing in me even if I sometimes didn't believe in myself and for being so sure that there was light at the end of the tunnel.

List of Symbols and Abbreviations

b	Sleeper width
c	Phase velocity
c_g	Group velocity
d	Diameter of the sample
d_i	Diameter of the component
f	Resonant frequency in Hz
f_r , $f_1$and f_2	Frequencies at $A_{max}/\sqrt{2}$ Above and below the resonant frequency
g	Gravitational constant
h	Height of the water table below the ground
i	Average cone penetration in mm for the sample
k	A torsional spring of stiffness
k	Wavenumber
k_1	Primary suspension stiffness (and damping) per axle
k_2	Secondary suspension stiffness per bogie
L	Sleeper length
m	Mass of the cone in grams
m_i	Mass of an added mass
p’	Mean effective stress
q	Deviator stress
r	Specimen radius
t_0	Time
t_1	Thickness of ground layer 1
w_r	Resonant frequency
x	The distance to the accelerometer from the central axis of the sample
γ	Shear strain
y	The displacement of vibration amplitude
z	Depth of the soil sample
Acc	Acceleration amplitude
A_{max}	The frequency response function amplitude at the resonant frequency
A_1	Amplitude of vibration for first cycle after the power is cut
A_{1+n}	Amplitude of cycle 1+n of free vibration
C_U	Undrained shear strength
C_u	Peak undrained strength

C_{ufc}	Undrained shear strength of the undisturbed specimen in its tested state
D	Damping ratio
D_E	Effective damper rate
E	Young's modulus
F_h	Horizontal modulus
F_{max}	Maximum railseat load per rail
G	Shear modulus
G*	Undrained shear modulus parameter (Graham and Houlsby, 1983)
G'	Shear modulus parameter (Atkinson *et al.*, 1990)
G_{hv}	Vertical shear modulus
G_0	Maximum Shear modulus value
G_O	Small strain shear modulus
I	Mass polar moment (MPM) of inertia
I_{am}	Additional masses
I_i	MPM of a cylindrical component
I_P	Plasticity index
I_x	MPM of the drive-system including calibration bar top plate
I_0	MPM of the drive-system (of inertia)
J_C	Moments of inertia
J'_{pq}	Coupling modulus parameter (Hird and Pierpoint, 1994)
J_B	Moments of inertia
K	The ratio between Rayleigh and S wave speeds
K'	Bulk modulus parameter (Atkinson *et al.*, 1990)
K_O	In situ earth pressure coefficient
L	Specimen length
L_x	Length in the direction of the track
L_y	Length perpendicular to the track
M_C	Mass of a vehicle body
M_W	Mass of the wheel set
M_B	Mass of the bogie
P	Dilation (compressional) wave
$P_n(t)$	Vertical wheel-rail forces for n forces
Rr	Effective shear strain factor
S	Shear wave speed
T	Torque

T	Total duration of the time record of the test
V_{hh}	Poisson's ration (horizontal to horizontal)
V_P	P-wave velocity
V_R	Rayleigh velocity
V_{RMS}	Root mean squared voltage
V_S	Shear wave speed
V_{vh}	Poisson's ration (vertical to horizontal)
V'_{hh}	Poisson's ratio for horizontal stress on horizontal strain
V'_{vh}	Poisson's ratio for vertical stress on horizontal strain
X	Thickness of the sands and gravels
$X(t)$	Receiver signal
X_{VC}	A limiting factor to apply to the site critical velocity
$Y(t)$	Source signal
α	Angular acceleration
β	Wavenumber domain (along the track)
β_{max}	Maximum wavenumber along the track
γ	Wavenumber domain (normal to the track)
γ_c	Torsional strain
γ_{eff}	'Effective' shear strain amplitude
γ_t^e	Linear elastic threshold shear strain
γ_{max}	Maximum shear strain
γ_{max}	Maximum wavenumber normal to the track
γ_t^v	Volumetric threshold shear strain
γ_w	Unit weight of water
δ	Logarithmic decrement
δβ	Wavenumber step in the β direction
δγ	Wavenumber step in the γ direction
E_h	Horizontal Young's modulus
E_v	Vertical Young's modulus
ε_a	Axial strain
ε_h	Horizontal direct strain
ε_r	Radial strain
ε_p	Volumetric strain
ε_q	Distortional strain
ε_q	Distortional strain (triaxial shear strain)

ε_{xx}	Horizontal direct strain
ε_v	Vertical direct strain
ε_{yy}	Horizontal direct strain
ε_{zz}	Vertical direct strain
Θ	The angle of cross-section torsion of the rod
θ	Angle of rotation
λ	Lamé constant
λ	Wavelength of vibration
μ	Pore water pressure
μ	Lamé constant
ν	Poisson's ratio
ν_{vh}	Poisson's ration (horizontal to vertical)
ρ	Material (specimen) density
ρ_1	Density of soil layer 1
σ_{max}	Maximum pressure between the sleeper
σ_{vg}	Vertical stress due to the ground
σ_{vr}	Rail mass
σ_{vs}	Sleeper mass
σ_{vtl}	Vertical stress due to train loading
σ_h'	Horizontal effective stress
σ'_{vg}	Vertical effective stress
σ_v'	Vertical effective stress
σ'_{xx}	Effective horizontal stress
σ'_{yy}	Effective horizontal stress
σ'_{zz}	Effective vertical stress
τ	Time shift
τ_{xy}	Shear stress in horizontal plane
τ_{yz}	Shear stress in vertical plane
τ_{zx}	Shear stress in vertical plane
ω	Circular frequency
ω_d	Damped natural frequency
ω_L	Liquid limit
ω_n	The natural circular frequency of vibration of the system
ω_n	Natural circular frequency of the calibration bar
ω_P	Plastic limit

BE	Bender element
BE	Boundary elements
BGL	Below ground level
BGS	British Geological Society
CPT	Cone penetration tests
CU	Consolidated undrained
DPT	Differential pressure transducer
EMF	Electro-motive force
FE	Finite elements
FEM	Finite element model
FWD	Falling Weight Deflectometer
IEM	Infinite element model
LVDT	Linear variable differential transformer
MASW	Multichannel Analysis of Surface Waves
MPM	Mass polar moment
RC	Resonant Column
RFM	Remote feedback module
SASW	Seismic Analysis of Surface Waves
SHDP	Super Heavy Dynamic Probe
SPT	Standard penetration tests
SRC	Stokoe Resonant Column
TGV	2.5D semi-analytical model, now called MOTIV
WS	Windowless Sampling

Chapter 1 Introduction

1.1 Background

Rail networks around the world are changing, due to ever increasing demand and customer expectations. In many countries high speed rail is playing a growing role in improving the capacity, availability and carbon cost of national infrastructure. The proposed High Speed 2 route in the UK has an intended running speed of 360 km/h (225 mph) (HS2 Ltd., 2012), almost twice that of the UK East Coast Main Line, which is considered a 'fast' standard railway (Network Rail Ltd., 2010). Higher speeds require straighter railway alignments, which often means crossing ground that has historically been avoided. The soils in typical boggy or marshland areas consist of peat, organic clays and soft marine clays with shear wave velocities as low as 30 ms^{-1}. In such areas there is a much greater likelihood of the train speed approaching or exceeding the speed of ground-borne surface waves, known as Rayleigh waves, potentially resulting in phenomena termed critical velocity effects (Madshus and Kaynia, 2000).

One of the most well documented and highly cited occurrences is that in Ledsgård in Sweden, where soft organic clays caused the onset of critical velocity effects at approximately 150 km/h (42 ms^{-1}). Figure 1.1 shows the track displacements, which increase rapidly as the train approaches the critical velocity.

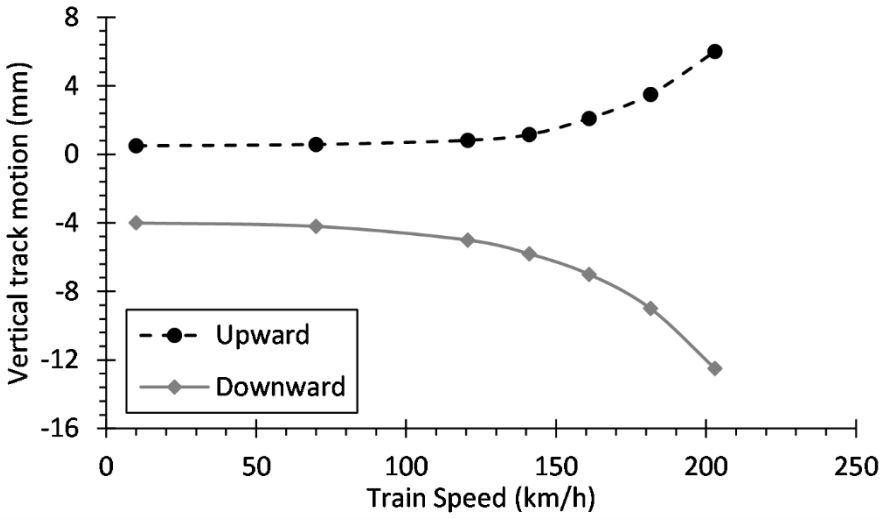

Figure 1.1: Track displacement with increasing speed for Ledsgård, Sweden. After Kaynia *et al.* (2000).

These effects typically involve excessive ground-borne vibration and large vertical track movements, potentially resulting in structural track damage, reduced track life, increased maintenance costs, and possibly the imposition of lower running speeds on the affected section of track. Other consequences include foundation or embankment degradation, the potential disruption of power supply lines and decreased ride comfort. Critical velocity effects have been observed in many countries including France, Germany, Great Britain, Holland, Sweden and Switzerland, especially in locations where the running speed on the existing classic rail network has been raised (Kaynia *et al.*, 2000).

Various mitigation measures have been implemented on classic railway lines, with varying levels of success and often at great expense. The aim of potential solutions is generally to strengthen and / or stiffen the ground beneath the railway, and the embankment if applicable. Ground strengthening techniques include dry deep-mixing methods (typically mixing dry lime-cement binder with the soft soil to create piles), or the installation of a stiff, piled concrete deck or a stiffening beam in the ground or the embankment itself (Holm *et al.*, 2002). It is preferable for critical velocity effects to be considered at the design stage of new railway track, but lack of experience and knowledge may result in expensive and possibly over-conservative strengthened track designs.

The potential impact of critical velocity effects was first raised by de Nie (1948) after making experimental observations of large track deflections on soft soil. Theoretical work in this area was then developed by several authors, including Kenney (1954) and Fryba (1972). Cole and Huth (1958) presented a solution for a moving load exciting a homogeneous elastic half-space, for speeds below, at and above the Rayleigh wavespeed of the ground. Krylov (1994,1995), predicted a large increase in ground movement at speeds above the Rayleigh wave speed. Subsequently several authors (e.g. Krylov, 1998; Sheng *et al.*, 1999; Auersch, 2005) incorporated the effect of layered ground into their predictions.

Models of railway vibration are mostly based on the assumption that soils can be modelled as a layered elastic halfspace, with each layer behaving in a linear elastic isotropic manner and with material properties which do not vary horizontally. As the vibrations induced by railways in the free field typically have low amplitudes, small strain behaviour is normally assumed to occur, valid for shear strains smaller than about 10^{-3} %. However, if this small strain limit is exceeded, the shear modulus of the soil begins to degrade with increasing strain levels, and so the soil acts in a non-linear manner (Houbrechts *et al.*, 2011). This can lead to critical velocity effects, as well as the accumulation pf permanent displacements, a longer-term phenomenon not considered in critical velocity modelling. Although the use of small-strain parameters and modelling is widely accepted

and has been well researched for many rail sites, it is not yet fully understood under what conditions it is necessary to model the soil beneath the track with non-linear elastic parameters. Moreover, data on these parameters, such as strain-dependent shear modulus and damping, is limited. It is important to understand the strain levels occurring beneath the train, and hence whether or not it is necessary to incorporate non-linear stiffness into the models.

Many authors have used linear elastic soil models, although some have included more complex non-linear elastic effects. A 2.5 dimensional (2.5D) approach has been used by various authors to give increased model efficiency. By assuming the ground and track structure to be homogeneous in the track direction, this approach uses a sequence of identical 2D models for different wavenumbers in the third dimension from which the 3D response can be reconstructed. Madshus and Kaynia (2000), Karlström and Boström (2006) and Alves Costa *et al.* (2010) used equivalent linear models to represent the non-linear soil properties in an approximate way. Equivalent linear models approximate real hysteretic behaviour by introducing a reduced secant shear modulus and an increased hysteretic damping, to represent parameter degradation with strain. Some authors, such as Shih *et al.* (2016) and Woodward *et al.* (2015) are working on more complex models, which incorporate non-linearity of the relationship between soil stiffness, damping and strain. In principle, these offer greater accuracy and flexibility, but they come at a cost of far higher computational intensity and require a more complex set of input parameters.

Although the Rayleigh wave speed of the ground is a good indicator of the likelihood of critical velocity problems, in practice it is not simple to measure it. Moreover, for an inhomogeneous ground there is no longer a unique value of Rayleigh wave speed: surface waves have a frequency-dependent wave speed. To determine this it is important to characterise the soil stiffness as a function of depth and this can be expressed in terms of the shear wave speed. Hence the shear wave speed is often the parameter of interest in any investigation. Additional parameters required for modelling are the compressional wave speed (or the Poisson's ratio), the density and the depths of the ground layers. Most of these parameters can be found through laboratory testing on site samples. It is also possible to measure them at a lower cost but also a lower accuracy using in-situ seismic tests. Results from basic desk studies, such as borehole logs and relevant literature, can be obtained more cheaply and can provide approximations for these values, but will lead to greater uncertainty in the results of modelling.

Due to a lack of available data on critical velocity sites, the majority of recent publications are based around Ledsgård in Sweden (Madshus and Kaynia, 2000; Karlström and Boström, 2006; Alves Costa *et al.*, 2010; Shih *et al.*, 2017). More research is needed which directly compares model results with specific site data and mitigation measure performance, hence the investigation

of additional case study sites is required to gain an improved understanding of the dependence of critical velocity effects on the ground characteristics.

1.2 Research Aims and Methodology

1.2.1 Aims and objectives

The aim of this research is to assess methods of determining appropriate soil parameters for use in simple elasticity-based models for the prediction of critical velocity effects. This will allow improvements in the simulation of track performance in pre and post-remediated states, as well as in the design of any required remediation.

The aim will be achieved through fulfilment of the following objectives:

- Investigating the strain-dependent soil stiffness and damping of typical soil samples from example sites at which critical velocity effects may be expected, in particular organic, silt and clay soils.
- Comparing different methods of obtaining these parameters for the various soil samples. This will include laboratory measurements using resonant column, bender elements, and triaxial tests and existing field measurements using SASW.
- Using suitable modelling to determine the impact of assumed soil stiffness on critical velocity assessment of example sites, and whether it is important to allow for the non-linear behaviour of soils. This will be based on linear elastic models, if necessary using equivalent parameters to allow for stiffness degradation.
- Determining the key soil and model parameters required when using 2.5D linear elastic models to predict track deflections on difficult sites.
- Comparing model predictions with field measurements of track deflections where available.
- Producing recommendations for the information required to obtain reliable critical velocity predictions using linear soil models and the best methods for obtaining this information.

1.2.2 Methodology

The work described in this thesis focuses around two sites on the UK classic rail network, from which soil samples have been taken and tested in the laboratory. At Gravel Hole, north of Preston on the West Coast Main Line, the track experienced large displacements after train speeds were raised from 160 km/h to 200 km/h. Boreholes show the site to be underlain by a horizon of peat, over stiffer sands and gravels. The second site, at Fishbourne, Sussex, does not currently experience critical velocity problems due to lower train speeds, but owing to its location over soft clay this could change if line speeds were increased.

Geophones have been used at Gravel Hole to monitor track movement during train passage. MASW (Multi-Channel Analysis of Surface Waves) seismic measurements are also available as an additional indicator of site soil properties at both sites (Rushworth, 2014; Wiseman, 2015).

A 2.5D semi-analytical linear elastic model was available for use in this project. Additionally Resonant Column (RC), Bender Element (BE) and Triaxial equipment was available in the geotechnical laboratory.

1.3 Thesis overview

Following this introduction, the thesis is organised into seven further chapters. The two main areas of the research, geotechnical testing and critical velocity modelling, are incorporated throughout the chapters.

Chapter 2 describes the background to the research. It contains a review of the causes of critical velocity effects, and recorded occurrences, as well as a summary of existing modelling. The key parameters and issues involved with modelling are discussed, as are methods for obtaining such parameters. This includes site and laboratory measurements.

Chapter 3 gives more information on the modelling technique used in this research. The history and limitations of the model are set out, followed by a parametric study to assess the key factors involved in critical velocity modelling.

Chapter 4 details the methodology for both site measurements and experimental techniques. This includes in-situ probe testing, windowless sampling and seismic wave speed measurements. The experimental methodology describes the theory, calibration and test procedures for the resonant column, the triaxial machine and bender elements. General indexing, organic content measurement and sample preparation techniques are also described.

Chapter 5 presents the results for the first case study site, Gravel Hole. This includes the site background plus site measurements and sampling results. Results from advanced laboratory testing are presented and analysed, followed by modelling which utilises the laboratory results. An investigation is made into the impact of strain degradation on model output, with model output compared to measured track displacements.

Chapter 6 presents the results for the second case study site, Fishbourne. The content follows a similar outline to that of the preceding chapter, although model output is compared to seismic dispersion curves rather than track displacements. The impact of a potential future increase in line speed on the site is discussed.

Chapter 7 synthesises common points from the two case study chapters, and discusses any differences. A summary is made of the key parameters involved in critical velocity modelling, as well as the impact of the parameter sourcing method on accuracy. The impacts of various aspects of model geometry are discussed. Finally the importance of the inclusion of strain degradation when selecting modelling parameters is considered.

Chapter 8 presents conclusions based upon the completed laboratory and modelling work, discusses their relevance for future work and gives recommendations for further research.

1.4 Original contributions of thesis

The proposed list of original contributions of the thesis is as follows:

1) *Categorisation of the soil and ground parameters of a new critical velocity case study site*

An extensive site investigation has taken place, including the drilling of new boreholes and the completion of dynamic probe tests .After full index testing of 20 metres of borehole sampling, a large data set of soil stratigraphy, density and other general index measurements has been produced. Testing of 10 samples in advanced laboratory equipment has been completed, providing data for stiffness and damping variation with strain from both the resonant column and triaxial machine. In combination with pre-existing seismic measurements and track displacement measurements, this data provides all the information required for the use of this site as a new critical velocity case study.

2) *Advanced laboratory testing of soils for which limited published data is available*

Extensive testing on highly organic silts has taken place, a soil material for which little data is published. The stiffness degradation curves, and measurements of increase in damping with strain, for a range of effective stresses, provide a useful data set for reference in future work.

Testing also took place on a set of clays; although this is a more frequently tested material it does provide an additional data set for comparison with previously published data.

3) *Comparison of results from a variety of advanced laboratory test techniques*

Through the use of similar sample pairs, results from resonant column, bender element and triaxial testing have been compared. Whilst good agreement is found between tests which used isotropic consolidation, values for samples consolidated using in situ (K_O) methods differ. The difference in measured shear modulus appears to be due to the consolidation methods, an area in which there is little published data.

4) Incorporation of soil non-linearity through equivalent linear modelling

Modelling of a case study site, using a linear elastic model, has been used to show the importance of considering soil non-linearity when investigating critical velocity effects. An equivalent linear modelling approach has been applied, using the data measured from the case study site. The value of an appropriate factor for calculating the 'effective' shear strain is discussed.

5) *Recommendations of key soil and model parameters for use in linear-elastic models, and the best methods for obtaining such data*

Through a parametric study using a linear elastic model, key soil and model parameters have been discussed. Comparison of in-situ site measurements to various forms of laboratory measurements has been used to investigate the most effective methods for sourcing data. In combination with the above contributions, recommendations are made as to the sourcing and selection of soil parameters, the sourcing and selection of model geometry, and a variety of other modelling factors.

Chapter 2 Background

2.1 Critical velocity effects – Causes, measurements and modelling

2.1.1 An introduction to critical velocity effects

Recorded Occurrences

As already discussed, critical velocity effects occur when the train speed approaches the characteristic wave speed of the track system, resulting in a large increase in track motion. The critical velocity is dependent on the Rayleigh wave velocity of the underlying ground/embankment and the natural flexural wave velocity of the rail. Rayleigh waves are the result of the interaction at the free surface between 'P'-waves (dilatational waves where the soil particles move parallel to the wave propagation direction) and 'S'- waves (shear waves where the soil particles move perpendicular to the wave propagation direction). The P wave is fastest, however it attenuates rapidly with distances from the excitation point. The Rayleigh wave is the slowest, and can propagate over large distances across the ground surface.

Typical Rayleigh velocities in very soft ground may be as low as 30 ms^{-1} (Madshus and Kaynia, 2000). In comparison, the alignment design speed for High Speed 2 is 100 ms^{-1} (HS2 Ltd., 2012) and is likely to cross several areas of low stiffness ground. The most well-known, and well-researched, critical velocity site is that of Ledsgård in Sweden. The Swedish State Railways carried out extensive site measurements, which were followed by laboratory testing of soil samples, after excessive rail, embankment and ground movements were monitored during train passage. Peak track movement reached 15 mm to 20 mm, see Figure 1.1, exceeding safety limits (Kaynia *et al.*, 2000; Madshus and Kaynia, 2000).

Similar areas of low stiffness / soft ground have already been monitored in the UK. Rail deflection measurements at Stilton Fen, a nature reserve just south of Peterborough, UK, found movements for a train speed of 51 ms^{-1} (185 kmh^{-1}) were 12 mm, almost double the rail response at lower speeds (Hunt, 1994). Elsewhere in the UK extensive use of expensive piled slab was required on the Channel Tunnel Rail Link across the Rainham marshes (Dyson and Kirk, 2006). Measurements of track movement at Stilton Fen are presented in Figure 2.1, normalised by the static track displacement, in comparison with two other critical velocity sites. A strong trend of significant increase in displacement with speed is shown.

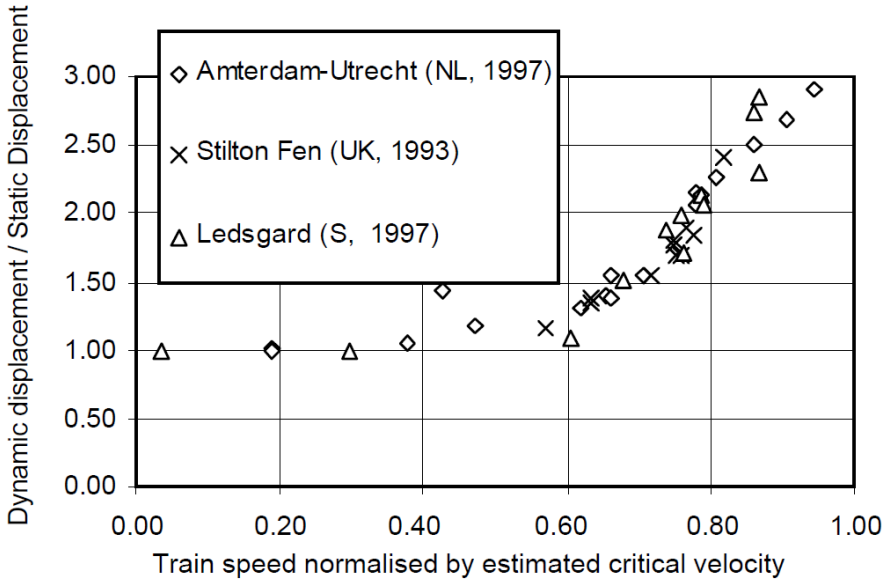

Figure 2.1: Track displacements, normalised by static displacements, for Ledsgård (Sweden), Utrecht (Netherlands and Stilton Fen (UK) critical velocity sites.

Maximum train speeds have increased rapidly over the past century, with the records for a selection of un-modified trains presented in Table 2.1. Although these are maximum train speeds, as these values increase the general operational speeds of lines also increase. Over time this will lead to an increasing number of sites which had no problems at lower speeds to start to suffer from critical velocity effects.

Table 2.1: Maximum train speeds for un-modified trains.

Speed (km/h)	Speed (ms^{-1})	Year	Country	Train Type
210	58	1903	Germany	AGE
215	60	1939	Germany	DRG SVT 137
243	68	1954	France	Alsthom CC 7121
380	106	1981	France	TGV
407	113	1988	Germany	ICE-V
486	135	2010	China	CRH380

2.1.2 Rayleigh waves and other causes

Viktorov (1967) showed that for real media (i.e. those with a Poisson's ratio of between 0 and 0.5) only one real and acceptable solution for Rayleigh surface wave propagation in a linear elastic

homogeneous medium exists, with the ratio between Rayleigh and shear wave speeds (K) being given approximately by:

$$K = \frac{V_R}{V_S} \cong \frac{0.87+1.12\nu}{1+\nu} \qquad \text{Equation 2-1}$$

Where V_R is the Rayleigh velocity, V_S is the shear wave velocity and ν is the Poisson's ratio of the medium. Work by Richart (1962) also produced a similar relationship between shear and Rayleigh wave velocities (see Figure 2.2), which equates to:

$$0.87 < K < 0.96 \qquad \text{Equation 2-2}$$

In a homogeneous halfspace the speed of Rayleigh waves does not depend on frequency and they are therefore non-dispersive. However in a layered halfspace dispersive waves occur due to the variation of soil properties with depth. At high frequencies soil motion is mainly influenced by, and is localised within, the top soil layer near the surface. At low frequencies the Rayleigh waves reach far deeper into the soil (Houbrechts *et al.*, 2011).

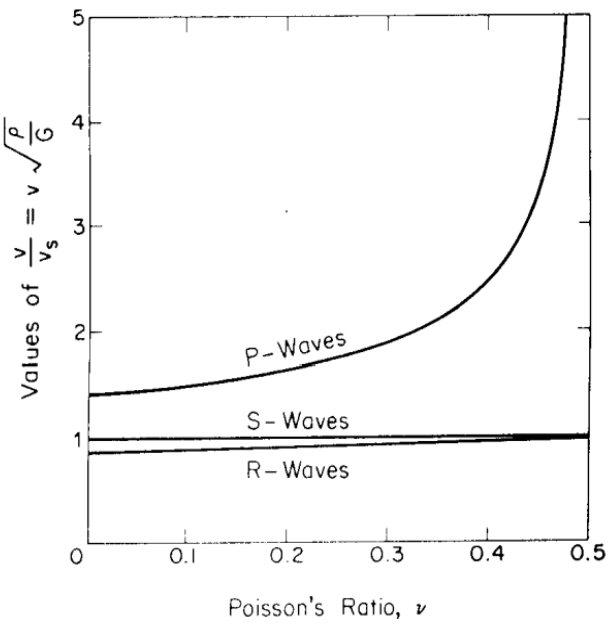

Figure 2.2: Relationship between Poisson's ratio, P-wave, S-wave and Rayleigh wavespeeds, in a linear elastic homogeneous halfspace (Richart, 1962).

The relationship between common soil parameters, such as Young's modulus and the Poisson's ratio, and wave speeds can be obtained from Navier's equations of motion for an elastic , isotropic solid. Such equations can be used to infer soil modelling parameters from site measured wave speeds or to infer wave speeds from parameters measured in a laboratory. The Lamé constants λ and μ are related to the Young's modulus E and Poisson's ratio ν by:

$$\lambda = \frac{E\nu}{(1+\nu)(1-2\nu)}$$ Equation 2-3

$$\mu = \frac{E}{2(1+\nu)}$$ Equation 2-4

The compressional wave speed V_P and shear wave speed V_S are given by:

$$V_P = \sqrt{\frac{\lambda+2\mu}{\rho}}$$ Equation 2-5

$$V_S = \sqrt{\frac{\mu}{\rho}}$$ Equation 2-6

where ρ is the material density.

Due to the close relationship between Rayleigh wave and shear wave speeds, being able to accurately determine the S-wave speed of the ground layers is essential for identifying potential problem areas and for modelling critical velocity effects. The scope of site investigations needed to gain this information, as well as for other ground parameters such as ground geometry and damping, can be fairly intensive. For example, Madshus and Kaynia (2000) used penetration testing to classify soil layering and soil types, several seismic spectral analysis methods for in-situ determination of ground wave velocities and dynamic triaxial tests to establish mass density and stiffnesses.

Aside from low ground wavespeeds, the physical excitation of the ground by rail traffic must also be understood. It falls into two main categories – dynamic and quasi-static. Dynamic excitation, which dominates at higher frequencies, results from train-track interactions due to wheel and track unevenness as well as spatial variation in track support stiffness and impacts due to features such as rail joints and wheel flat-spots. Quasi-static excitation is that resulting from the passage of axle loads, so its pattern and amplitude do not change with train speed; this dominates the ground response at lower frequencies. As speed increases the area of the frequency spectrum over which quasi-static forces dominate increases. For this reason, on high speed railways the traditional method of reducing vibration by reducing track 'roughness' through track maintenance will not be effective, hence the need for mitigation measures which stiffen the ground (Jones, 2009).

2.1.3 Modelling critical velocity effects

Existing models can be split into two categories: analytical – expressed in terms of ground wavenumbers, and numerical – which uses finite elements (FE) and/or boundary elements (BE). FE/BE models offer greater modelling flexibility. The wavenumber (k) represent the spatial frequency of a wave, with k being the phase change per unit distance, equal to $2\pi/\lambda$, where λ is the wavelength of vibration. Semi-analytical models, although less adaptable, are more computationally efficient. In such numerical models finite elements are used to represent the track structure, and boundary elements may be used to represent the ground of infinite extent. These boundary elements are essential to a model's realism, by efficiently allowing waves to travel through model boundaries, not artificially reflecting back off them. FE analysis with infinite elements may also be used to achieve this but such FE models become very large. Predictive FE/BE models which are either two-dimensional (2D) or three-dimensional (3D) have been produced in the past. 3D models are the most flexible and effective, but are very complex and computationally intensive, while 2D models cannot account for wave propagation in the track direction.

To reach a balance between model efficiency and flexibility much focus has been placed on 2.5D models, in which the ground and track structure is assumed to be homogeneous in the track direction to increase computational efficiency (Sheng *et al.*, 2006). Essentially a sequence of 2D models represents the track, with the model solved for a range of wavenumbers in the direction of train travel, with the maximum wavenumber selected relating to the maximum length of track considered . A lower total number of degrees of freedom reduces the computational intensity – a consequence of element discretisation only occurring over the cross-section of the model. This does have the disadvantage of being unable to represent periodic rail support along the length of the track, which is a source of high-frequency vibrations (Sheng *et al.*, 2006). A Fourier transform is then used to recover the three-dimensional field.

As interest in modelling high-speed trains has increased, many models have focused on quasi-static loads due to their dominance over high-speed vibrations. Lai et al. (2000) show that exclusion of responses to dynamic wheel-rail loads may underestimate the actual response compared with site measurements. For a more accurate model which can be compared more directly with site measurements it is necessary to include both quasi-static and dynamic excitation mechanisms, as produced by Sheng *et al.* (2003). This 2.5D semi-analytical model, called TGV (now MOTIV), was applied to Ledsgård, (a site on the West Coast Line in Sweden) where excessive ground vibrations were encountered when X2000 trains operated at 200 km/h. This site is a well-

cited example of critical velocity effects (Kaynia *et al.*, 2000; Paolucci *et al.*, 2003; Takemiya, 2003; Karlström and Boström, 2006; Alves Costa *et al.*, 2010; Shih *et al.*, 2017).

The TGV model used an Euler-Bernoulli beam on top of a layered visco-elastic halfspace. The predicted response was shown to be very accurate at reproducing the total vibration, especially the dominance of the quasi-static loads in the frequency range at which the train speed excites the first mode of the ground (3-8 Hz). For higher frequencies however, the dynamically induced vibration appeared to be under-estimated. This was partly attributed to a lack of knowledge of the vertical profile of the track; instead an idealised profile was used. This is typical of the common lack of sufficient site data and measurements to enable comprehensive comparisons between site measurements and model results. Karlström and Boström (2006) also introduced a model similar to that of Sheng *et al.* (2003) for the Ledsgård site, and found that varying the depth of second ground layer by just 15% made a large difference to the predicted results. This again shows the importance of a detailed site investigation.

Madshus and Kaynia (2000) and Kaynia *et al.* (2000) also carried out modelling work based on the Ledsgård site, using Vibtrain, a model which uses a finite element viscoelastic beam on a layered half-space. They found that well below the critical speed the displacements were in phase with the train loads, shown by the direct relation between the position of the axles and the displacements peaks in Figure 2.3a,b. When trains travelled above the critical speed the displacements became non-symmetric and out of phase with the axles, resulting in a tail of oscillations behind the train (Figure 2.3c,d). The Vibtrain model reproduced these results well.

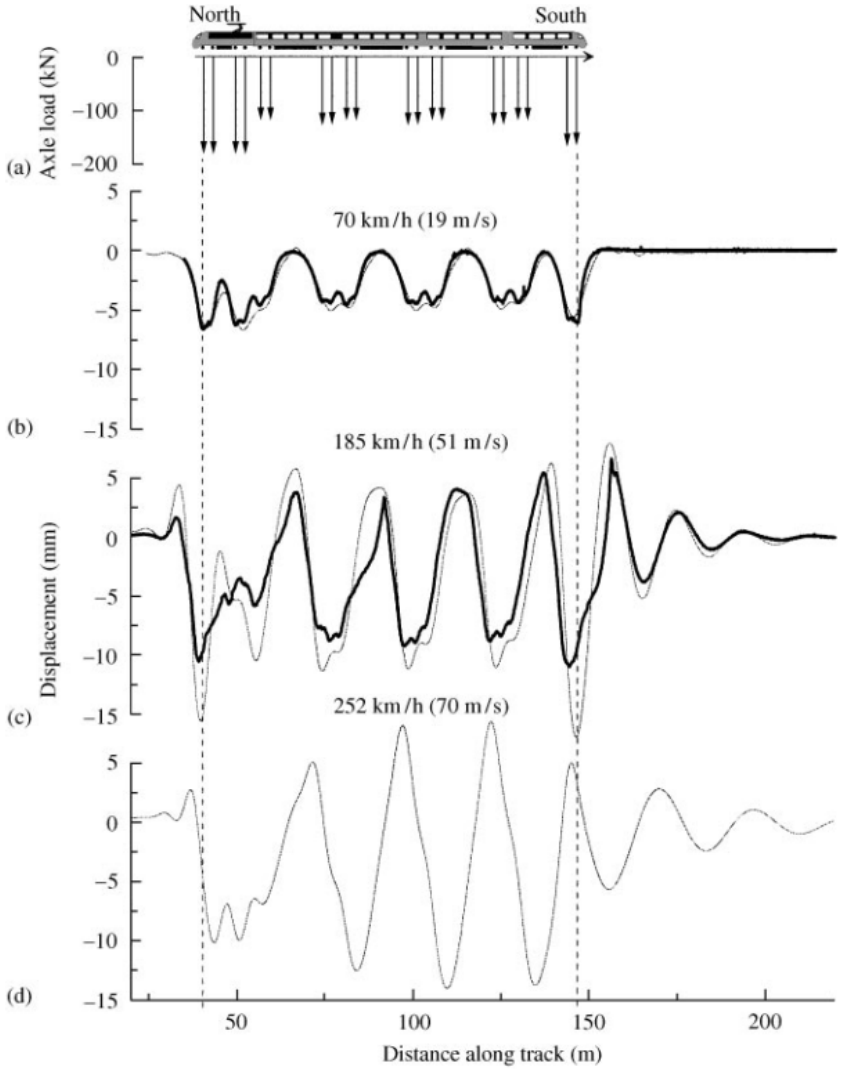

Figure 2.3 : Train geometry and loads in comparison to measured and simulated vertical displacement response: ▬ measured; — simulated. Ledsgård, Sweden. (b) is a southbound train, (c) and (d) northbound (Madshus and Kaynia, 2000).

Kaynia *et al.* (2000) also used Vibtrain to investigate the potential effectiveness of using either a concrete slab underneath the embankment or a concrete box inside the embankment to mitigate critical velocity effects through stiffening the ground. A reduction in peak deformations of up to 60% was predicted for high-speed trains, although at that time no mitigation had been carried out on the Ledsgård site to allow model calibration. The validation of models which can predict mitigation measure effectiveness is a key area for future work.

Yang *et al.* (2009) point out the significant effect that a train accelerating or braking has on the soil stresses and displacements, making the soil more likely to fail, although they did not investigate above-critical speeds. This can result in ground displacement problems at lower speeds, in areas of frequent braking/acceleration.

To allow comparison between model results and reality, accurate monitoring of critical velocity sites is needed. All theoretical models require selection of parameters to represent the ground at the site, with key values being the ground geometry, wave speeds and damping. This often requires intensive site investigation.

Auersch (2008) concluded that to produce useful results great care must be taken in selecting soil stiffness and damping parameters, and particularly defining the stiffness's of different layers. These parameters can be talked about in terms of the soil stiffness ratio – the ratio between the highest and lowest stiffness soils in the model. In their modelling study of a near-critical site in Germany a soil stiffness ratio of 100 (i.e. the stiffness of the stiffest soil was 100 times that of the softest soil) yielded displacements up to 35 times higher in the soft soil than the stiff soil.

Although it is assumed in many models, it is not usually sufficient to represent the ground as a homogeneous half-space, or a single soil layer over a stiffer homogeneous half-space. The layering and characteristics of the site geology will greatly affect wave propagation. The overall critical response velocity becomes more complex to predict, as it is a combination of the wave speeds in the various layers. Sheng *et al.* (2004b) found that, as well as stiffening the track, decreasing the track mass can also increase the overall critical response speed of the track-ground system so that it is higher than the Rayleigh wave speed in the upper layer.

Regardless of the model type, it is clear from the literature that a model must be able to represent the soil layers in the ground, and the corresponding variations in strength and other soil parameters. It is clear that, to model a site well, data on the underlying stratigraphy is essential.

Influential Parameters

As part of the RIVAS project, Houbrechts et al. (2011) recommend that for small-strain behaviour five parameters are determined for each soil layer: the shear and compressional wave speeds, the mass density and the material damping ratios, up to a depth of 20 to 30 m below the track. Connolly et al. (2014a) elected, for a simple scoping model, to use solely Young's modulus to describe the soil, as the predicted ground movement appears most sensitive to Young's modulus and shear wave speed. However, for more detailed critical velocity modelling it is important to have a much larger parameter set.

Non-Linearity Considerations

Models of railway vibration are often based on the assumption that soils can be modelled as a layered elastic halfspace, with each layer behaving in a linear elastic isotropic manner and with material properties which do not vary horizontally. As the vibrations induced by railways in the

free field typically have low amplitudes, small strain behaviour is normally assumed to occur, presuming shear strains are smaller than 10^{-3} %. According to Houbrechts *et al.* (2011) it is usually only in the ballast, subballast and upper embankment of the track where strains above this level occur, this report however was not focussed on high-speed trains .

Under cyclic loading the soil stress—strain path follows a hysteresis loop, which follows a different path during unloading and loading phases, as seen in Figure 2.4. This loop represents the dissipation of energy in the soil, mainly through friction between solid particles in the soil skeleton and also relative motion between the skeleton and pore fluid. The small strain shear modulus is represented by the slope of the tangent at zero strain to the soil stress-strain curve. At small strains (up to around 10^{-3} % in most soils) it can be seen that the soil material presents an almost linear response, therefore the damping from the hysteresis effect is so low as to be negligible. This strain level equates to a damping ratio of between approximately 1 % to 5.5% for normally and over-consolidated soils, with the damping ratio decreasing as the plasticity index of the soil increases (Vucetic and Dobry, 1991).

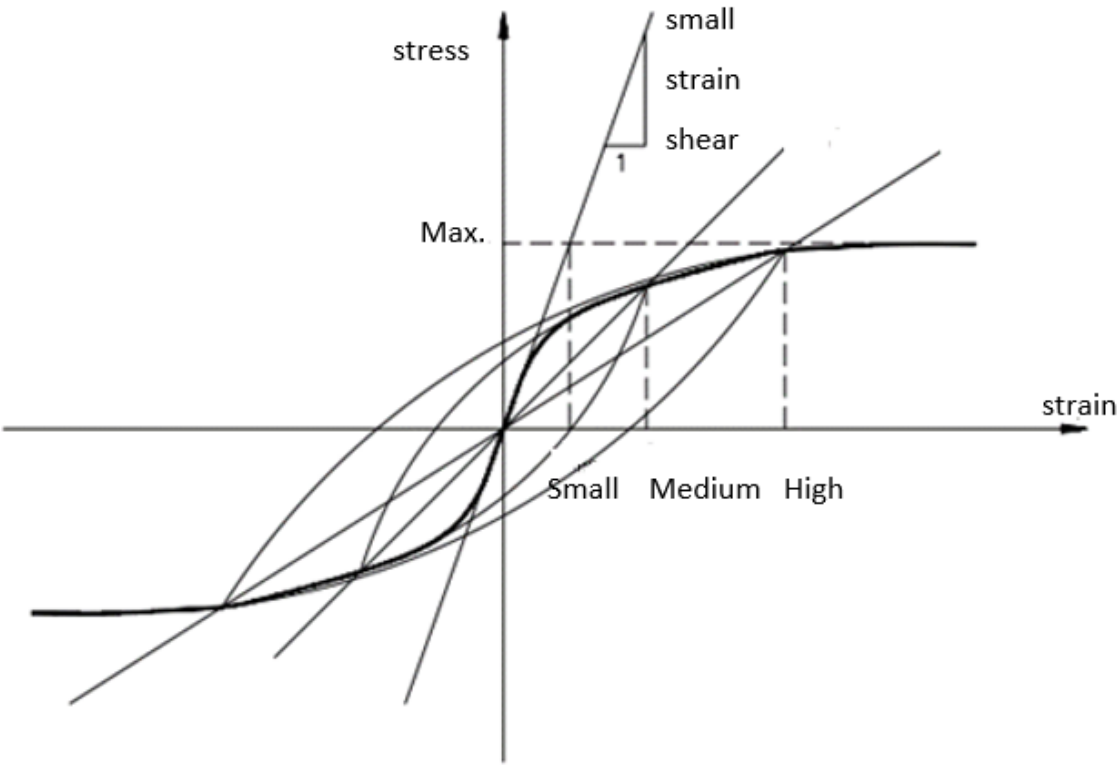

Figure 2.4: Stress-strain loop, showing hysteretic damping loop and linearity of response at low strain levels. Modified from Houbrechts *et al.* (2011).

Above a small strain limit of around 10^{-3} %, the shear modulus begins to degrade with increasing strain level, shown by the decreasing slope of the tangents and therefore shear moduli for medium and high strains in Figure 2.4, and for samples tested in a triaxial machine, taken from the Ledsgård critical velocity site Figure 2.5. This degradation also causes the size of the hysteresis

loop to increase, which in turn leads to the material damping becoming strain dependant. The next strain threshold is the point at which soils begin to behave plastically, that is residual strains remain upon stress release. This tends to occur at a strain of approximately 10^{-2} % in most soils (Ishihara, 1996).

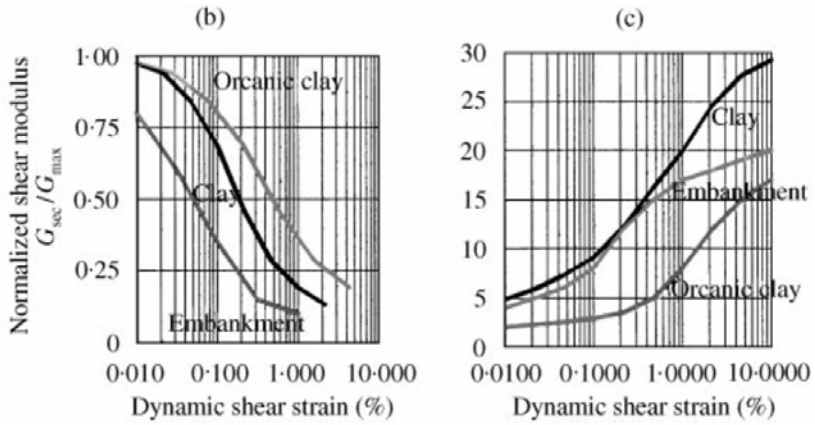

Figure 2.5: Shear modulus degradation curves from triaxial tests on samples taken from the Ledsgård critical velocity site. Figure b is the shear modulus reduction curve with strain and figure c the damping (%) reduction curve with strain (Madshus and Kaynia, 2000)

Although the use of small-strain parameters in modelling is widely accepted and has been well researched for many rail sites, it is not yet fully understood whether or not it is necessary to model the soil beneath the track at critical velocity effect sites with non-linear parameters, moreover data on these parameters, such as strain-dependent shear modulus and damping, is limited. It is important to understand the strain levels occurring beneath the train, and hence whether or not it is necessary to incorporate non-linear stiffness into the models.

Kaynia *et al.* (2000) also found that, on the Ledsgård site at least, the dynamic strains from high-speed train passage were so high that materials behaved non-linearly. For this reason an equivalent linear approach was used to model the site– where real hysteretic behaviour is approximated by introducing a reduced secant shear modulus and an increased hysteretic damping. Maximum cyclic strains for the site were reported as 1 % in the embankment, 0.8 % in the organic clay and 0.2 % in the upper marine clay (Madshus and Kaynia, 2001).

Modulus reduction and damping increase as a function of strain were found from dynamic triaxial tests, carried out over a shear strain range 0.2 % to 2 % (Figure 2.5). From this non-linear stress strain response, best equivalent linear parameters were determined that represent the decrease in stiffness and increase in energy dissipation (damping) which occurred as strain levels increased beyond small strain. Under cyclic loading the soil behaviour can be represented by multiple hysteresis loops, like that shown in Figure 2.4, which change with strain level. An approximation

of these loops is used in the equivalent linear approach, based on the width (representing the damping) and the inclination (representing the stiffness). This data, in combination with that of small strain elastic properties, forms the basis of the analysis.

For Ledsgård, inclusion of the non-linearity reduced the wave speeds and increased the damping. The precise values of these parameters are not published, but the secant shear modulus reduced to 10-50% of the elastic value and the damping ratio increased by 20-100% when degraded (Madshus and Kaynia, 2000).

Several other authors have also utilised the equivalent linear approach in modelling railway critical velocities. It is essentially a compromise between accuracy and complexity, in which the main vibration mechanism is assumed to be quasi-static. Dynamic excitation due to track roughness is not generally included due to much higher computational effort. The general procedure involved in equivalent linear is as follows: soil parameters relating to an initial selected shear strain are selected, and the resulting time-variant strains in the model assessed. An 'effective' shear strain amplitude is then determined, and the next set of soil parameters are selected to relate to this effective strain on modulus and damping degradation curves. This process is repeated until the strains obtained from the model match the assumed strains from which the soil modulus and damping were taken. Generally this process is applied to each layer within the model geometry, as strains will be concentrated within the softer layers.

Alves Costa *et al.* (2010), used a coupled 2.5D FEM-IEM (Finite-element – Infinite element model). Linear elastic analyses were performed iteratively and the stiffness properties were adjusted to match the mechanical properties and the strain level, until a convergence criterion was reached. Hysteretic damping was used in the model. It must be noted that although the approach attempts to approximate non-linear behaviour, the soil response is calculated via a linear elastic method which is incapable of reproducing any change in the soil properties during train passage. Using a 2.5D model for efficiency is limiting in that the soil degradation process is assumed to take place independent of the train position. This means that displacements will always be predicted at lower speeds, as the actual soil strains will not have developed sufficiently high for the assumed degraded parameters to be valid.

Again Ledsgård was used as a case study to validate the model. The results for the equivalent linear analysis matched the site measurements more closely than that of a conventional elastic analysis, with the model showing the degradation region to expand as the train speed increased. A simulation of the stress path followed by a soil element at 4.05 m depth (equivalent to the middle of the soft organic clay layer at the site) during low and high speed train passage can be seen in Figure 2.6. The stress path for the higher train speed shows far greater shear and mean

stresses, and does not show the obvious loading/unloading cycles (from bogie passage) of the slower train. Yang *et al.* (2009) previously carried out a simulation of stress paths using a 2D FE model, with similar large differences in stress and strain found for different train speeds.

Although predictions such as this begin to show the complexity of what may be happening beneath a high-speed train, they are still limited by being based upon elastic analysis methods. An important part of future work in the area of critical velocities is to improve understanding of the strain and stress levels occurring beneath a train passage, as well as to obtain strain and stress dependent lab data so that more efficient equivalent linear and non-linear models can be developed.

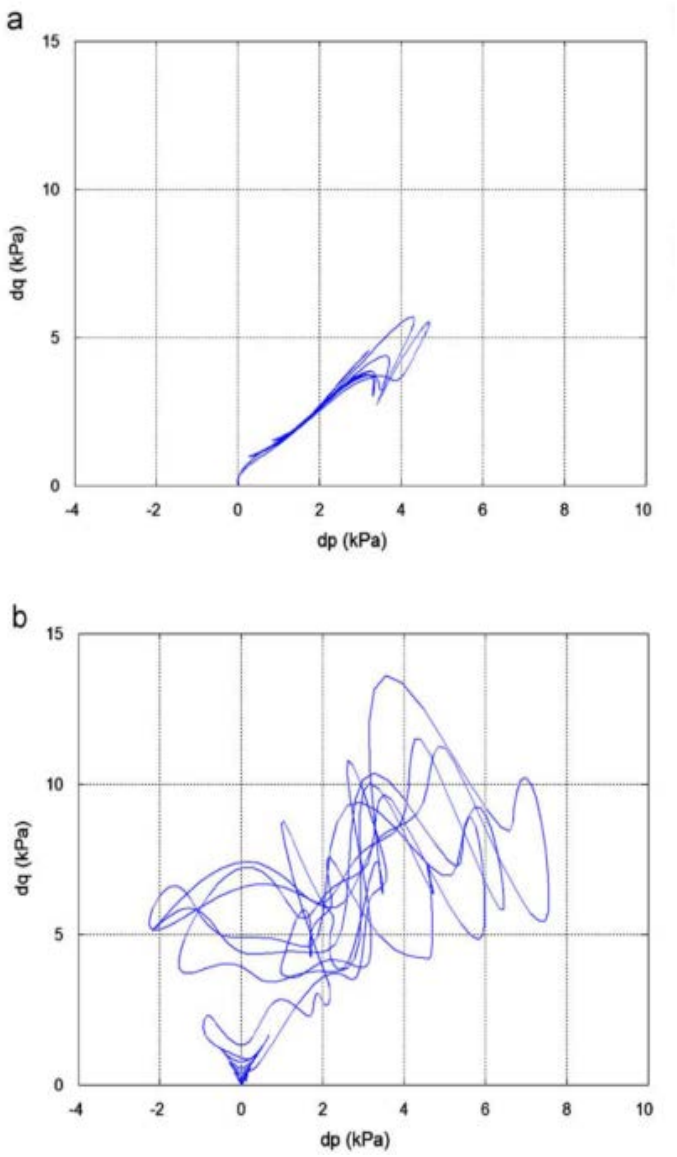

Figure 2.6: Simulated stress path of a point in the soft soil layer at the Ledsgård critical velocity site, with train passage of 70 km/h (a) and 204 km/h (b). dp is the mean stress increment, whilst dq is the shear stress increment (Alves Costa *et al.*, 2010).

Equivalent linear models rely upon the selection of an 'effective' shear strain amplitude (γ_{eff}), which is chosen from a factor, Rr, which is applied to the maximum shear strain (γ_{max}) in the model to reduce it to a value taken to be representative of the entire soil layer:

$$\gamma_{eff} = Rr(\gamma_{max}) \qquad \text{Equation 2-7}$$

Different values for the factor Rr have been found empirically. In seismic analysis a value of 0.65 is usually recommended (Kramer, 1996), with a range of 0.5 to 0.7 applied depending on the situation (Lysmer *et al.*, 1975). Values between 0.2 and 1 have been proposed by other authors, again with the exact value situation dependent (Katayama *et al.*, 1992; Yoshida *et al.*, 2002). The applicability of these values of Rr to the vibration induced by high-speed trains is unknown.

Alves Costa *et al.* (2010) found a value of 0.65 to give a good response for an equivalent linear model of Ledsgård, although this model was more complex than a basic equivalent linear model, as the shear modulus was adjusted according to the effective strain in each element of the 2D cross-section. In contrast, Shih *et al.* (2017) found a value of Rr of 0.2 to be most appropriate for an equivalent linear model of Ledsgård in ABAQUS, with shear modulus adjusted by layer rather than by element. In this model Rr was applied to octahedral shear strains.

Whilst non-linear models have been developed and shown to give excellent agreement to site measurements (Woodward *et al.*, 2015; Kalliainen *et al.*, 2016; Shih *et al.*, 2017), they are extremely complex, computationally expensive and require the sourcing of many parameters. The use of simpler, faster, cheaper equivalent linear models is therefore an area of great interest, should they be proved accurate. This is largely dependent on the selection of appropriate degraded parameters, which will be further assessed in this thesis.

Setting a limiting train speed factor

In the design of new railways or upgrades to existing routes, it is important to be able to predict where critical velocity effects may occur and to take steps to mitigate them. One of the simplest measures is to set a limiting factor, X_{VC}, to apply to the site critical velocity, by which train speeds should be limited to prevent the occurrence of critical velocity effects at a particular site.

A range of methods have has been used to define X_{VC}. A report by British Rail Research (Hunt, 1994) suggested a value of 0.7 for the factor X_{VC}, based on a theoretical study of track behaviour at Stilton Fen and Rainham Marshes. Woldringh and New (1999) proposed a value for X_{VC} of 0.6, as the track displacements for Ledsgård, Stilton Fen and Amsterdam all showed a significant increase in dynamic displacement above this speed (with dynamic displacement being approximately 125% of static displacements at X_{VC} = 0.6, and 150% at X_{VC} =0.7). This is broadly

consistent with the results of dynamic finite element analyses reported by Liang in Powrie *et al.* (2008) (Figure 2.7), which indicated dynamic displacements at 125% above static at X_{VC} = 0.6.

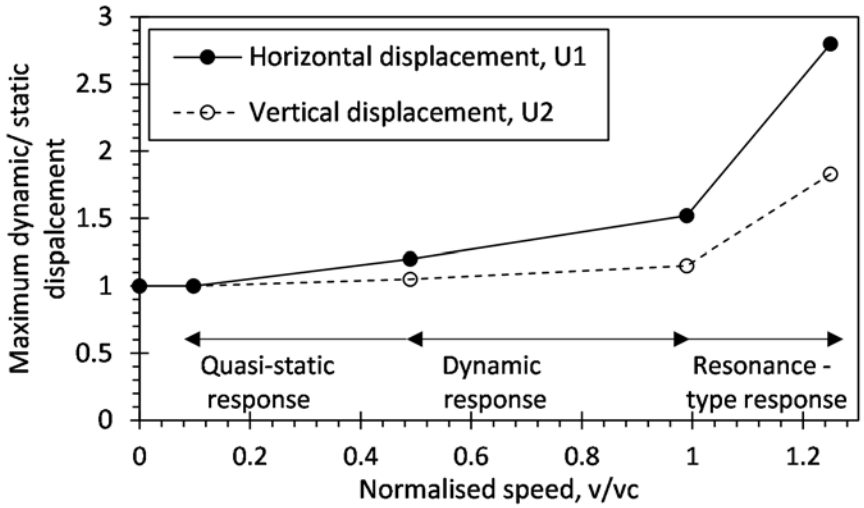

Figure 2.7: Maximum ground displacement vs. train speed. Redrawn from Powrie *et al.* (2008).

Brough *et al.* (2013) used Falling Weight Deflectometer (FWD) tests to estimate the critical velocities at a number of sites. Comparison with the maximum line speeds that Network Rail found practical for those study sites suggested a limiting value of X_{VC} of 0.6 to 0.7. However, there is still significant variation in the value of X_{VC}. For example, some sites in Ireland appeared to run satisfactorily at $X_{VC} > 0.7$, whilst the Network Rail speed limit at Gravel Hole, near Preston, corresponded to $X_{VC} = 0.55$, when based on FWD-derived critical velocity data.

A range of measurement methods have been used to measure track movements at different sites, including lasers, optical methods (digital image analysis), accelerometers and seismometers. It should be noted that, owing in part to uncertainties in signal processing and interpretation at the time, different measurement methods gave some variation in the values of displacement produced; for example, laser based measurements at Stilton Fen were approximately 20% to 40% lower than those derived from accelerometers.

An additional issue in the selection of X_{VC} is that a simple generic rule does not account for axle loads, which are known to have a significant impact on track displacements. Methods proposed to incorporate axle loads are case-specific and time consuming, and so militate against the development of a general rule.

Woodward *et al.* (2016) presented a different approach to setting X_{VC}, based on limiting peak particle velocities (PPV) within the ballast to acceptable levels. They point out that several studies attempted to define at what PPV significant ballast movement and therefore increased track maintenance costs occurs. On the basis of a number of case studies, a limiting ballast PPV of 20

mms^{-1} is proposed, which is linked to critical velocity values for the sites to give a recommended X_{VC} of 0.5 to 0.6.

In conclusion, the selection of X_{VC} largely comes down to the maximum deflections that railway operators can allow, based on considerations of safety and track longevity. Although estimates for X_{VC} do vary, they generally fall in the range of 0.5 to 0.7, with a value of 0.6 appearing to satisfy the widest range of estimation methods. However, the robustness of any site prediction is strongly dependent on the method by which the site critical velocity is assessed. For example with a value of 0.6, an under- or over- estimation of site critical velocity by about 20% would result in a speed limit range equivalent to applying X_{VC} of 0.5 and 0.7. Therefore, future focus and research should not be focused on defining the value of X_{VC}, but rather should on the methods used to estimate the actual site critical velocity.

2.2 Measuring dynamic properties of soils

2.2.1 Soil stiffness and damping

Soil stiffness and damping are key parameters for accurate critical velocity modelling. The shear modulus (G) is the parameter most commonly used, and, as for damping, its value depends strongly on the strain amplitude, as well as factors such as mean principal effective stress, plasticity index, void ratio, over-consolidation ratio and the number of loading cycles (Vucetic and Dobry, 1991; Kramer, 1996).

During monotonic testing, shear modulus, also known as the secant stiffness, reduces progressively with shear strain, γ. Dobry and Ng (1992) used discrete element method simulations to show this is principally because of the slippage or separation of intergranular contacts as shear strain increases. The rate at which the shear modulus degrades with strain is highly variable, depending on the constituents of the soil, as demonstrated for a range of soils presented in Figure 2.8. As strains increase, and the shear modulus degrades, damping tends to increase (Figure 2.9).

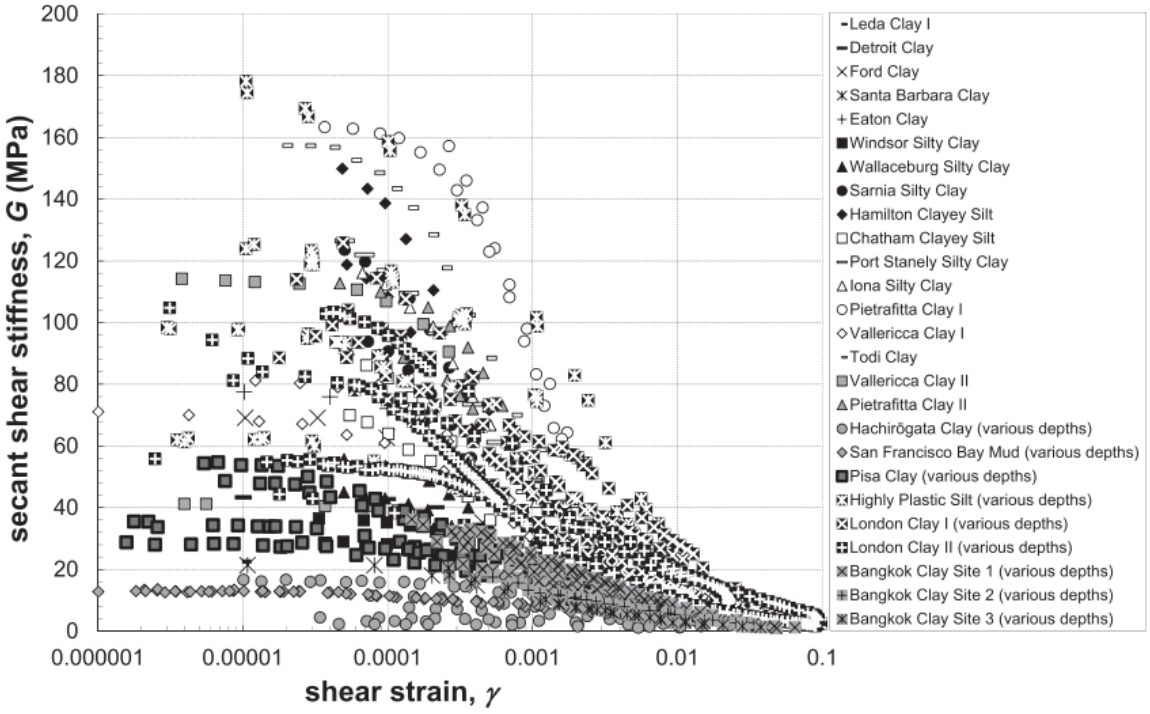

Figure 2.8: Secant shear-stiffness versus shear-strain data for a variety of soil types (Vardanega and Bolton, 2013).

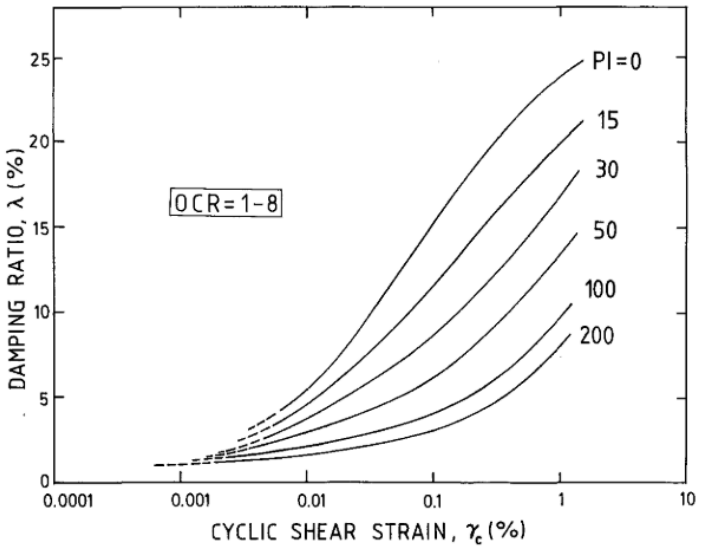

Figure 2.9: Typical damping ratio increase with shear strain, in relation to soil plasticity (Vucetic and Dobry, 1991). OCR 1-8 defines the over-consolidation ratio range for which this damping-strain relationship is considered valid.

The soil behaviour represented by a shear modulus degradation curve ranged from linear elastic to inelastic, as strain levels increase. This behaviour is generally divided into three zones (Jardine, 1992). At very small strains there is thought to be a small linear elastic zone, where the shear modulus is at its maximum value (G_0), and the damping ratio at its minimum value. This is termed Zone 1. The upper strain limit of this range is called the linear elastic threshold shear strain, γ_t^e.

At slightly larger strains there is a recoverable zone, Zone 2, in which the stress-strain relationship is non-linear and hysteretic, but strains remain recoverable upon stress reduction. This stiffness reduction is accompanied by an increase in damping. The upper strain limit of this zone,γ_t^v, is termed the volumetric threshold shear strain. It marks the point at which, if strains exceed it, Zone 3 begins. This consists of significant stiffness degradation, irrecoverable strain development, and further increases in damping along with other plastic inelastic behaviour. The three zones of behaviour are summarised in Figure 2.10.

For testing on soil samples to be considered non-destructive, the strains applied must stay within Zone 1 and Zone 2, and not go beyond γ_t^v. The value of γ_t^v has been found to be between 0.01 % and 0.04 % for clays (Jardine, 1992)

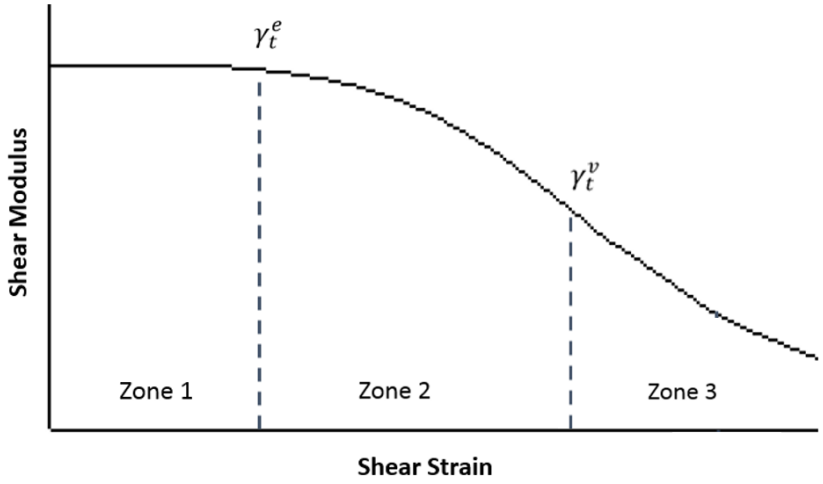

Figure 2.10: Typical shear modulus behaviour with strain

2.2.2 Site and laboratory equipment overview

All modelling requires input parameters, with the quality of the results dependent on how accurate the input data is in relation to the modelled site. There are several ways of obtaining this data, briefly summarised in Figure 2.11. The most simple is to carry out basic desk study surveys of a site, using historical borehole and geology information to estimate typical parameters. This is unlikely to be very reliable and is likely not suitable as the only source of parameter values, except for perhaps very basic scoping models. In situ testing and laboratory testing provide several methods of measuring or inferring more accurate parameter values.

Compared to laboratory work, in situ tests have the advantage of not requiring soil sampling and therefore soil disturbance. They can also usually measure larger volumes of material rather than the few discrete points from which laboratory samples are taken. However, laboratory tests have the advantage of allowing more precise measurement of material properties, as fewer empirical

relations or theoretical analyses are involved. Moreover tests can be carried out at stresses other than those in situ, allowing material non-linearity to be investigated and undrained and drained parameters to be measured.

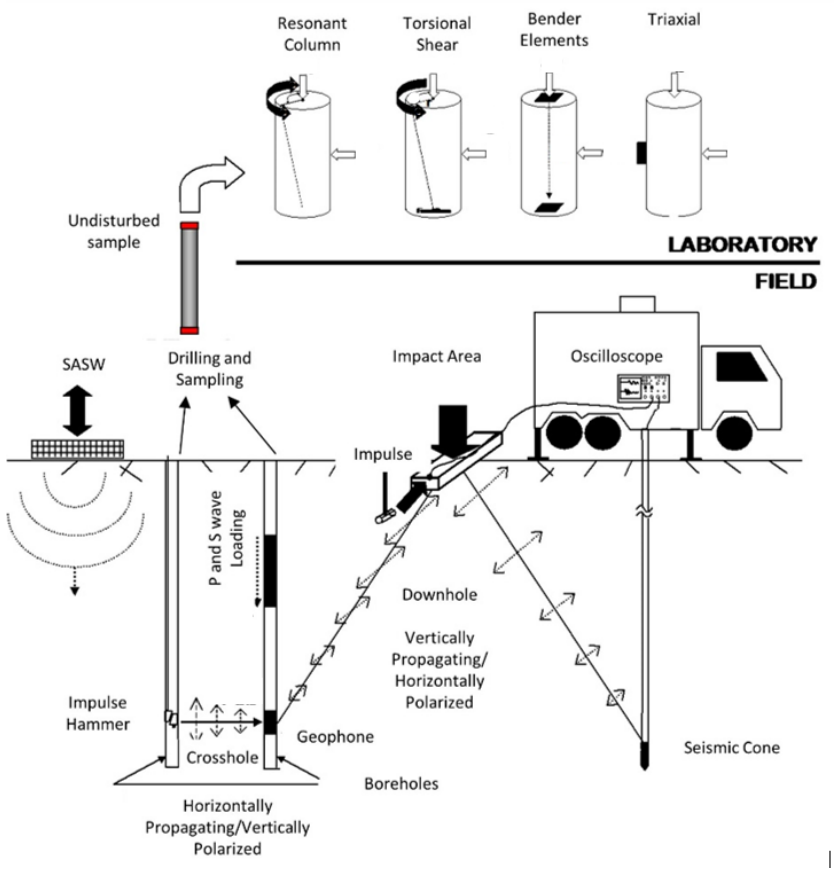

Figure 2.11: Common in-situ and laboratory tests. Modified from Schneider et al. (1999).

Laboratory tests can be used to measure a range of parameters, from geomechanical values such as density, porosity, strength and stiffness, to elastic constants such as Young's modulus and damping values. Wavespeeds can also be directly measured, or derived from other measurements. The shear modulus of a soil can be measured, enabling the S-wave speed to be derived.

Testing in a resonant column allows measurements of shear wave speed and damping, including variation with strain. Shear modulus can be derived from the measured shear wave speed. These tests can be carried out at a range of confining pressures. Triaxial machines are the most commonly used piece of advanced geotechnical testing equipment. Measurements of shear modulus, Young's modulus and Poisson's ratio can be taken. Samples can be consolidated isotropically, as in the resonant column, or with addition axial load, allowing the in-situ conditions to be better replicated.

Bender elements can be fitted in either piece of equipment, allowing measurements of shear wave speed and compressional wave speed. In all laboratory testing it is very useful to test for the same parameter in two or more forms of equipment, to increase the reliability of the results. To do this, tests should be carried out in the same strain range. A summary of the strains at which tests generally operate is shown in Figure 2.12.

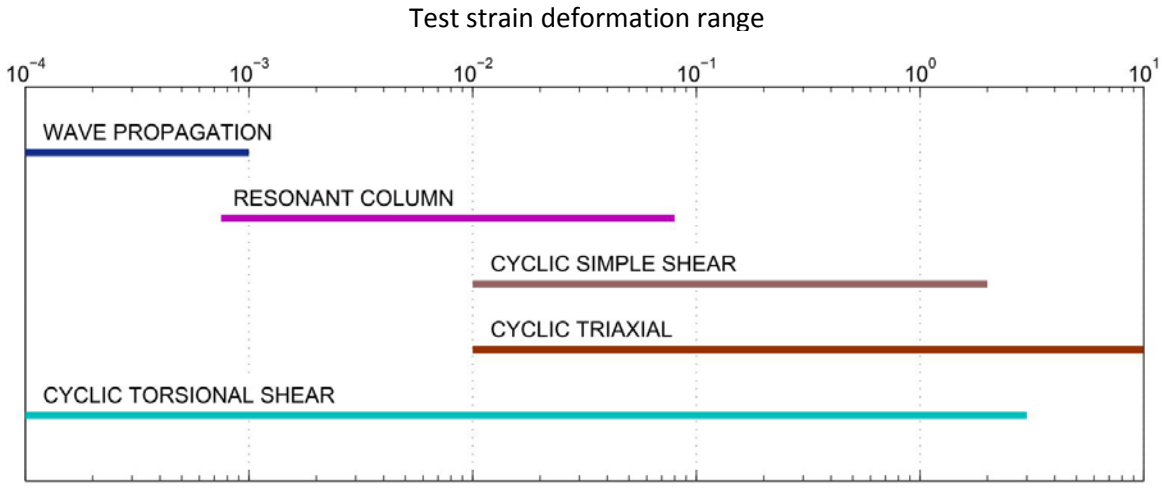

Figure 2.12: Strain deformation range for a variety of dynamic lab tests (Houbrechts et al., 2011).

2.2.3 Anisotropy considerations

The assumption is often made that soils are isotropic, that is their material properties are the same both horizontally and vertically. Due to the way in which soils are deposited over large areas, the forces they have undergone, and therefore the deformations, are essentially one-dimensional. Most anisotropic soils are considered to be cross-anisotropic, meaning that they have a single (vertical) axis of symmetry, with the two horizontal directions being indistinguishable. Cross-anisotropy tends to be more pronounced in soils with flat particles, such as clays, than for more rounded particles such as sands. This is caused by flatter particles tending to settle through water onto their flat faces rather than their edges. Several frameworks are used to attempt to investigate and categorise anisotropy, such as the work of Graham and Houlsby (1983); Hird and Pierpoint (1994); Coop *et al.* (1997); Lings *et al.* (2000). The approach taken in this thesis is discussed in section 4.4.2

Chapter 3 Modelling Background

3.1 MOTIV model theory and past work

3.1.1 Background and theory

MOTIV is a 2.5D semi-analytical model for ground vibration in the wavenumber domain. It was initially developed under the name TGV, by Xiaozhen Sheng at the University of Southampton (Sheng *et al.*, 2004a;b). It was initially developed to predict environmental vibration caused by trains. It has been used to investigate the variation in track displacement with load speed for varying track weight and ground stiffness, with self-consistent results. Modelling results have also been compared with site measurements from the Ledsgård critical velocity site and two non-critical velocity sites (Sheng *et al.*, 2003). Within MOTIV vehicles are described as multiple rigid body systems which only consider vertical dynamics (Figure 3.1). The mass of the vehicle body, bogie and wheelset are represented by M_C, M_B, and M_W respectively, whilst J_C, and J_B represent the moments of inertia of each. Rectangles containing crosses denote suspension units, where k_1 indicates the primary suspension stiffness (and damping) per axle and k_2 the secondary suspension stiffness per bogie (Sheng *et al.*, 2003).

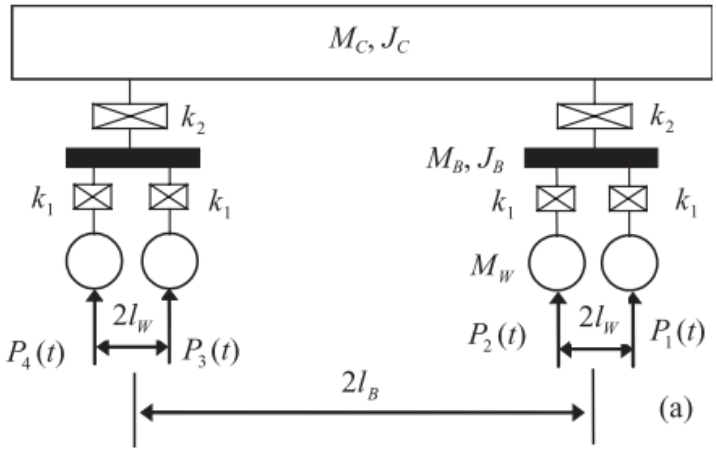

Figure 3.1: Schematics of MOTIV model for bogied vehicle (Sheng *et al.*, 2003).

The track is modelled as multiple beams supported by vertical springs of identical mass, as shown in Figure 3.2, where $P_1(t),\ldots, P_n(t)$ represent the vertical wheel-rail forces for n forces. It is assumed that each wheelset is always in contact with the rails, and that the sleepers and ballast distribute the vertical wheel-rail forces evenly over the track width. The sleeper (the lowest beam) is prescribed a mass per unit length but no bending stiffness. The ballast is modelled as a visco-elastic layer of set lateral width and infinite length, with only vertical ballast stiffness accounted

for. The ground is modelled as a layered elastic half-space using flexibility matrices in terms of wavenumbers k_x and k_y in the x and y directions. The ground layers are parallel, with each formed of isotropic, homogenous material. The flexibility matrices relate the stresses and displacements at the top and bottom of each layer to for a matrix representing the whole ground response. The model is 2.5D, with the model fully described in the 2D cross-section of the track, and the third direction described by wavenumbers. Once set-up, solutions are performed in the wavenumber-frequency domain. Full details of the equations upon which the MOTIV model is based would be impractical to reproduce here, but can be found in (Sheng *et al.*, 1999; Sheng, 2001; Sheng *et al.*, 2003;2004a;b).

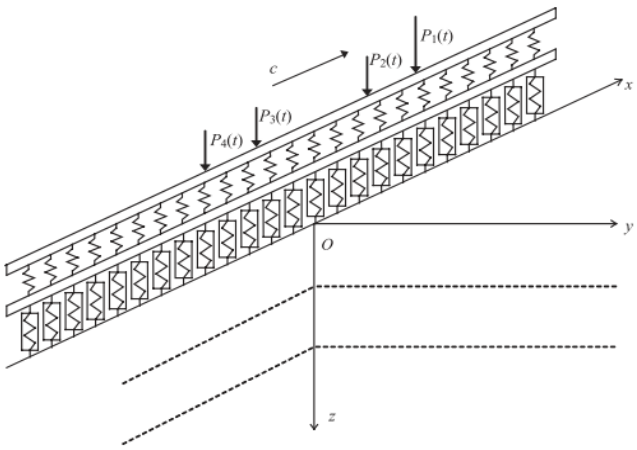

Figure 3.2: Schematics of MOTIV model for track-ground system (Sheng *et al.*, 2003).

The key required inputs for MOTIV are summarised below, with more detail given in further sections:

- Ground parameters for each layer – layer thickness, Young's modulus and Poisson's ratio (or dilational 'P' and shear 'S' wave speeds), damping loss factor (equal to twice the damping ratio).
- Train parameters – train dimensions, train speed, moving axle loads, number of train vehicles. Generally 4 vehicles is found to give good results whilst minimising model run time and computational demand.
- Track parameters – ballast, sleeper pad, sleeper and rail dimensions, mass, stiffness and damping.
- Model size – Model track length (L_x) is a function of the number of train vehicles, and must be sufficient to accommodate entire train without it reaching around and catching its own tail. The model length and width are a function of the wavenumbers prescribed in each direction, further explored in section 3.2.3.

3.2 Parametric study

Initially a parametric study was carried out, using MOTIV, to look at the impact of a variety of soil, track and ground geometry parameters on the model results. The modelling was based around the Gravel Hole case study site, further detailed site information can be found in Chapter 5, although the specific site used is not of importance for the parametric study. Network Rail provided information from their geotechnical investigations on the site. Of particular interest are several boreholes along the track, a cross-section of which is given in Figure 3.3. The site is underlain by a horizon of peat, sitting over layers of stiffer sand, clay and gravel. This peat has a minimum layer thickness of 1.9 m, and deeper horizons of up to 4 m. Peat has a much lower stiffness than traditional foundation materials, and is likely to be the main reason for the critical velocity effects at the site. No borehole information is available perpendicular to the track.

An unusually soft layer either above or between stiffer layers is typical of a critical velocity site, so provides a useful basis of ground geometry for a parametric study. The fastest trains on the site are Class 390's (Pendolinos), a typical UK passenger train. The site was found to experience large track displacements following an increase in line speed from 160 km/h to 200 km/h, forcing the imposition of a speed restriction across the site. Site displacement measurements were taken using geophones, more details in Chapter 5, which will be used to provide a comparative measure for the parametric model results. It is not known whether the site has reached the peak of critical velocity displacements, as data is limited by the range of train speeds on the site.

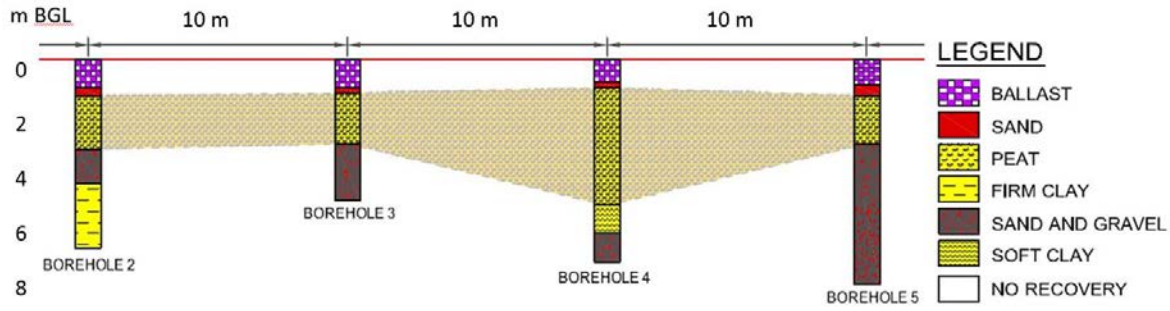

Figure 3.3: Gravel Hole boreholes cross section (After Aspin Foundations Ltd (2013)).

3.2.1 Basic model parameters

Initial track and vehicle parameters

Parameter values typical of UK track were used representing UIC60 rail and mono-block concrete sleepers. Where possible, train parameters specific to Class 390's (Pendolinos) were adopted; otherwise values typical of higher speed passenger trains were used. Where Class 390 or site

specific parameters were not available the RIVAS project was a particularly useful parameter source (an investigation of track and ground vibration, run at the University of Southampton, for tracks representative of the UK (Thompson *et al.*, 2013)). The Class 390 has a loaded weight of 59.2 tonnes at 180% tare weight (Le Pen, 2008) and an unloaded vehicle weight of 46.6 tonnes (Mak, 2014). All parameters are detailed in Table 3.1, with explanatory schematics of dimensions set out in Figure 3.4 and Figure 3.5.

Table 3.1: Default track and vehicle input parameters for MOTIV.

Track parameter	*Value*	*Track parameter*	*Value*	*Vehicle parameter*	*Value*	*Vehicle parameter*	*Value*
Rail mass**	120 kgm^{-1}	Rail pad damping loss factor**	0.2	Axle spacing*	2.7 m	Wheelset mass***	1750 kg
Sleeper mass**	461.5 kgm^{-1}	Rail damping loss factor**	0.01	Bogie spacing*	17 m	Bogie pitching moment of inertia	3000 $kg.m^2$
Ballast mass**	1740 kgm^{-1}	Ballast damping loss factor**	0.04	Bogie to end of vehicle*	2.906 m	Primary suspension stiffness***	258 $x10^3$ Nm^{-1}
Rail bending stiffness**	$1.29x10^7$ Nm^2	Track width**	2.5 m	Car body mass	475 $x10^2$ kg	Primary suspension viscous damping***	4250 Ns/m
Ballast stiffness**	$4.64x10^9$ Nm^{-2}	Ballast width**	3.1 m	Car body pitching moment of inertia	206 $x10^4$ $kg.m^2$	Secondary suspension stiffness***	410 $x10^3$ Nm^{-1}
Rail pad stiffness**	$3.69x10^8$ Nm^{-2}	Track roughness**	FRA Class 3	Bogie mass***	2325 kg	Secondary suspension viscous damping***	$200x10^2$ Nsm^{-1}
Single Axle Load (180% tare axle load)*	145070 N	Single Axle Load (Gross Load)****	134841 N	Wheel Radius**	0.445 m	Hertzian contact type	curved

Sources: * Le Pen (2008), ** RIVAS project (Thompson *et al.*, 2013), *** Mak (2014), ****Priest *et al.* (2012). Note the track roughness is measured from the rails using a track recording vehicle or a corrugation analysis trolley, as a spectrum of the relationship between the roughness level, in dB (re 1µm) and the wavelength in m. It represents small deviations in the rail surface.

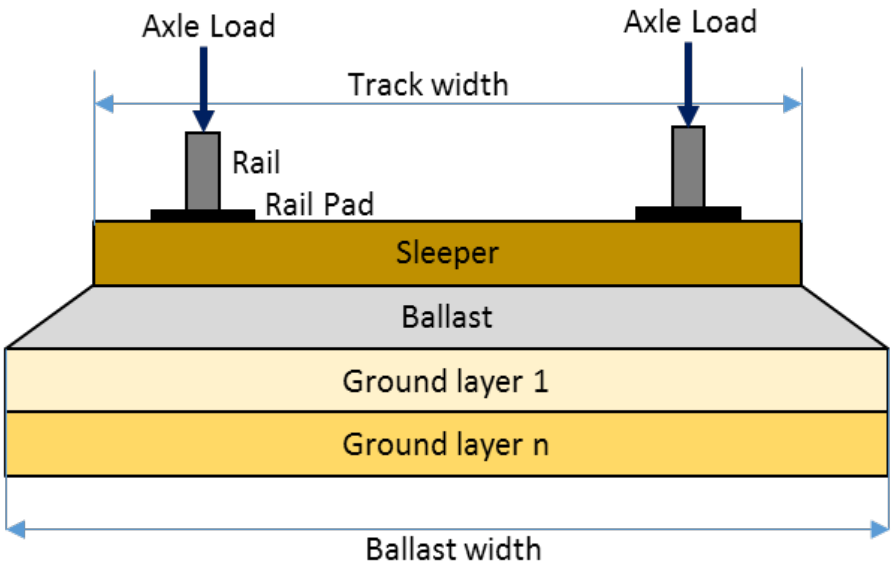

Figure 3.4: Cross-section schematic of track and sub-system components.

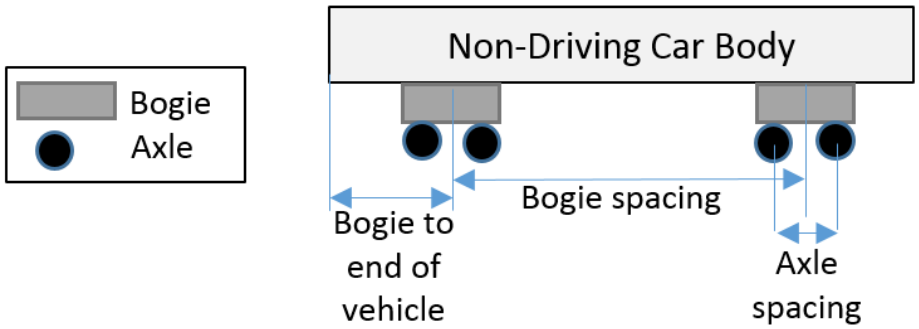

Figure 3.5: Schematic of train vehicle dimensions.

Geometry and loading options

There are three types of ground geometry which can be adopted within MOTIV:

1. A homogeneous half-space,

2. One or more layers of ground of specified thickness above a rigid foundation,

3. One or more layers of ground of specified thickness above a stiffer half-space.

As the soft peat layer is the ground material of interest on the site, three alternative ground geometries were chosen to represent the site (Figure 3.6). The rigid foundation and the stiffer half-space are methods of representing the comparatively stiffer layers of sand, gravel and clay beneath the peat.

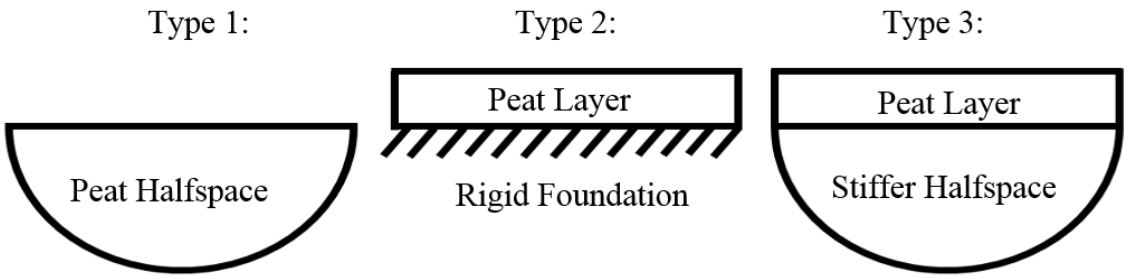

Figure 3.6: MOTIV parametric study ground geometry types.

For the parametric study three loading configurations were used in MOTIV:

1. A single moving load (a moving point load producing quasi-static deflection),

2. A single vehicle (allowing interaction of the displacements from the two wheelsets in a bogie)

3. Four vehicles (representing a train, including dynamic excitation due to track unevenness).

For configuration 3, as well as the moving load, following the recommendations from the RIVAS project using MOTIV (Thompson et al., 2013), excitation frequencies from 0.25 to 120 Hz with 80 logarithmically spaced steps were used. This was coupled with a receiving frequency band of 0.2 to 120 Hz and 400 linearly spaced receiving frequencies.

Load configuration 1 is equivalent to a single axle load, i.e. one quarter of the overall train weight. Load configuration 2 has 4 loads, representing the 4 axles in a vehicle. Load configuration 3 has 16 loads to represent 4 vehicles (an actual Class 390 consists of 9-11 carriages; however it is impractical to include this many in the model due to memory and run time constraints). Each model is run over a range of speeds, with the peak displacement noted from each speed. These peak displacements can then be plotted against speed to produce a critical velocity curve.

Initial ground parameters

Ideally ground parameters would be based on detailed site and laboratory testing of samples from the site, especially as peat is a ground type subject to large variations in its properties. However, no such results are available for Gravel Hole. Limited measurements of the ground wavespeeds made beside the track at the study site provided an initial estimate of the dilational (P) and shear (S) wave speeds for the lower layers of sand and gravel.

In selecting the initial parameters, the limited in-situ wavespeed measurements were used to estimate the wavespeeds for the stiffer halfspace. It was not possible to estimate the wavespeed of the peat from the site measurements, so the shear wave speed was initially set to 53 ms^{-1} (the train speed causing the largest measured movements on the site). The Poisson's ratio was set to

0.11 (Rowe *et al.*, 1984) and the density to 1050 kgm^{-3}, allowing the compressional wave speed and Young's modulus to be derived. The derived Young's modulus of 6.3 MPa is reasonable for slightly clayey peat, with all other ground parameters assigned typical values for that ground type (Table 3.2). The thickness of the peat layer was initially set at 2 m, representative of the range found from the borehole measurements.

Table 3.2: Initial Gravel Hole modelling ground paramters.

	Peat		*Stiffer Halfspace*	
Parameter	*Value*	*Source*	*Value*	*Source*
Density	1050 kgm^{-3}	Rowe *et al.* (1984)	2000 kgm^{-3}	Site SASW
Damping Loss Factor - Constant	0.3	Zainorabidin and Wijeyesekera (2009)	0.1	Bowles (1997)
Young's Modulus	6.3 MPa	Computed	54 MPa	Computed
Poisson's Ratio	0.11	Rowe *et al.* (1984)	0.49	Selected for saturation
S Wave	52.6 ms^{-1}	Site SASW	95 ms^{-1}	Site SASW
P Wave	79.39 ms^{-1}	Computed	768 ms^{-1}	Site SASW

Site SASW refers to seismic measurements taken beside the track (Rushworth, 2014).

3.2.2 Geometries

Type 1 - Halfspace model

Using the initial parameters given in Section 3.2.1, all three ground geometry types were run with all three loading configurations. Figure 3.7 shows the calculated maximum peak-to-trough displacements for running loading configurations 1 (single moving load) and 2 (single vehicle) across ground geometry type 1 -the peat halfspace. The resulting displacement curves are similar in shape to the critical velocity curves produced by Sheng *et al.* (2003) and Krylov (1995), indicating that MOTIV is capable of producing a smooth displacement results graph of an expected shape, even when run above critical speeds. Loading type 1 (a single load) is unable to account for interaction between train wheelsets, thus the calculated displacements were significantly less than those calculated using loading type 2 (a single vehicle), although the critical speeds are similar. This ground geometry has very low stiffness as it does not incorporate any representation of the ground beneath the peat, so displacements are substantially over-estimated. Although this model is useful for carrying out parametric studies, it is too simple to represent the site accurately.

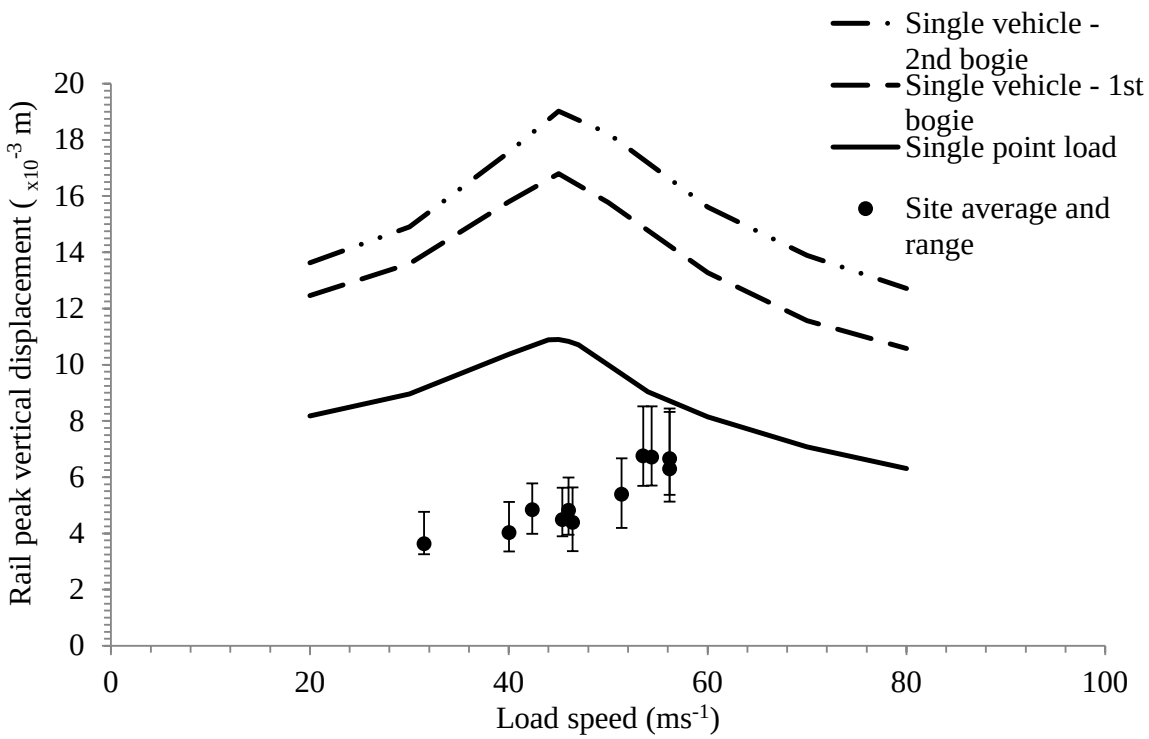

Figure 3.7: Rail displacement vs. load speed curves for a single point load and a single vehicle moving across a peat halfspace. Geophone measurement results for site also presented.

Type 2 – Layer over rigid foundation model

The same initial parameters and loading types were applied to the second ground type – a peat layer over a rigid foundation. The rigid foundation represents the relatively stiffer layers of ground beneath the peat. The thickness of the peat layer on the site varies, from 1.9 m to 4 m and its depth perpendicular to the track is not known. A thickness of 2 m was deemed to be roughly average for the boreholes presented earlier. The shape of the calculated displacement curve for a 2 m peat thickness, Figure 3.8, matches that of the site measurements fairly well, although the gradient is lower.

When the displacement values for this model are compared to those of the peat halfspace it is clear that introducing a rigid ground element beneath the peat has had a considerable effect, with peak displacements for the 2nd bogie in a single vehicle decreasing from approximately 19 mm to 10 mm respectively. This is to be expected, as the rigid foundation beneath the peat will increase the overall stiffness of the system, whilst also being more realistic. Again superposition of displacements between bogies in a single vehicle can clearly be seen. Displacements are still over-calculated when compared to site measurements, especially at low speeds. While the displacements have decreased, the critical velocity has increased significantly compared to the peat halfspace, from approximately 45 ms^{-1} to 77 ms^{-1}.

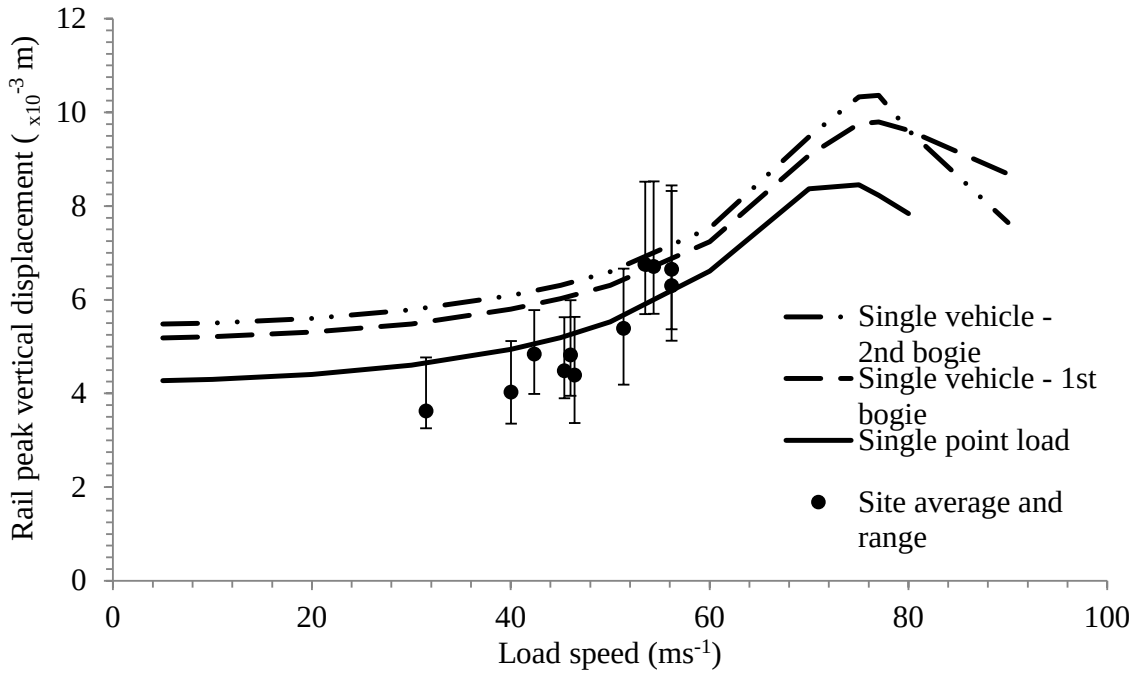

Figure 3.8: Displacement vs. load speed curves for a single point load and a single vehicle moving across a 2 m peat layer over a rigid foundation. Geophone measurement results for site also presented.

As the thickness of the peat layer on the site does vary, this model was repeated with the peat thickness decreased to 1.5 m and increased to 4 m, to quantify the impact on calculated displacements (Figure 3.9). A single point load was used to speed calculation time. A key point to note are the critical speed values, of 83 ms^{-1}, 70 ms^{-1} and 60 ms^{-1} in models with 1.5 m, 2 m, and 4 m respectively, i.e. the critical speed reduces as the peat depth increases. This is to be expected, as the shallower the depth to the rigid foundation the stiffer the overall system will be. Clearly the selection of peat thickness is a key parameter in the calculated results, so for lack of any other data the site average of 2 m thickness will be used from this point onwards.

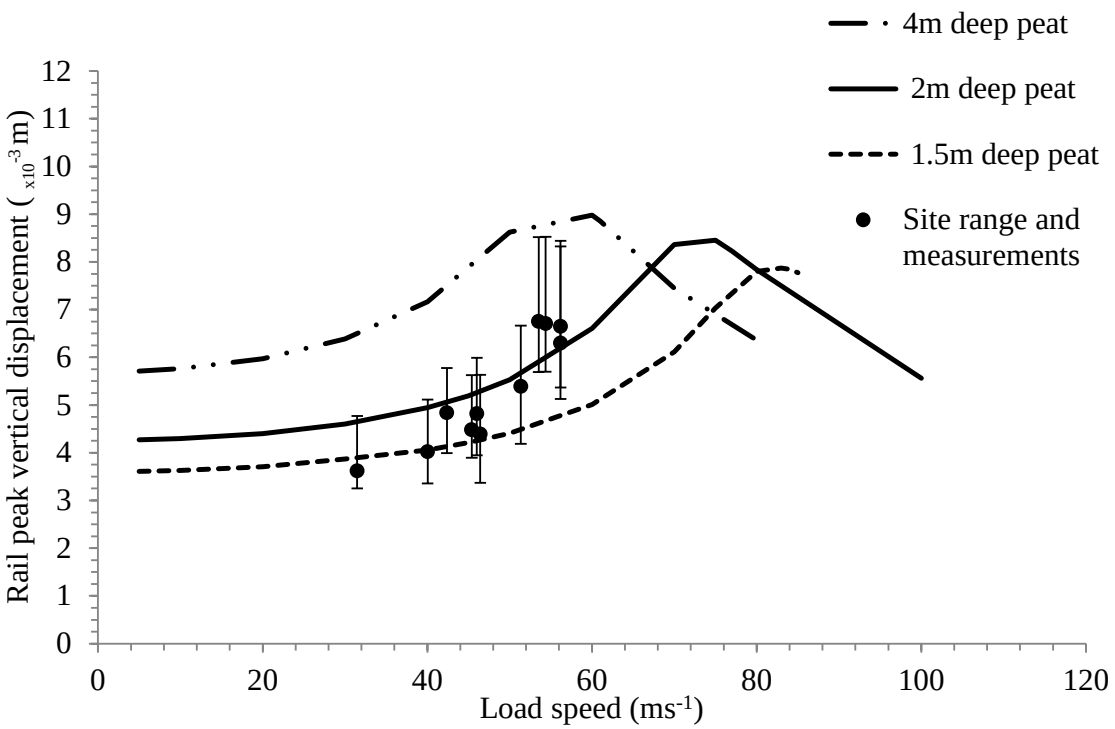

Figure 3.9: Displacement vs. load speed curves for a single point load moving across a peat layer over a rigid foundation, for various depths of peat. Geophone measurement results for site also presented.

The third loading type introduced a full vibration analysis including dynamic excitation, accounting for track roughness as well as the quasi-static loads. Due to computational time it was run at only 4 speeds – 20 ms^{-1}, 50 ms^{-1}, 70 ms^{-1} and 90 ms^{-1}. In this evaluation mode MOTIV calculates the total frequency spectrum of the vibration velocity of the rail. This has two components – quasi-static and dynamic. To allow comparison to site data output is plotted in the form of the 1/3 octave band spectrum of the pass-by response of the rail (Figure 3.10, Figure 3.11, Figure 3.12). 1/3 octave band spectra are commonly used in noise and vibration analysis, both measurements and predictions. They are based upon a logarithmic frequency axis, as that correlates better with the human response to sound and vibration. The site geophone measurements are also able to be presented for the same spectrum for comparison.

At lower frequencies quasi-static forces contribute the majority of the total vertical velocity level, whereas above a certain crossover point at higher frequencies the dynamic forces contribute the most towards the total. The calculated results show that as the load speed increases the frequency at which these components crossover also increases, meaning that the quasi-static forces remain dominant over a larger part of the frequency spectrum. The crossover point increases from 10 Hz at a load speed of 20 ms^{-1} (Figure 3.10) to 25 Hz at 50 ms^{-1} (Figure 3.11) to 35 Hz at 90 ms^{-1} (Figure 3.12). This is important, as traditional track vibration reduction methods, such as reducing track roughness, are not effective for quasi-static excitation. The vertical velocity

level also increases with speed, but drops substantially at 90 ms^{-1}. There does not appear to be an extreme change in vertical velocity level between any of the speeds, more models run at intermediate speeds would allow a better investigation of near-critical train speeds effect on the power spectrum.

Measured geophone data from for a single train travelling at 120 mph (53 ms^{-1}) on the site was converted from the time domain to Power Spectral Density and hence to a 1/3 octave band spectrum using Matlab. This can be compared to Figure 3.11, the model running at 50 ms^{-1}. It produces a good fit, with the pass-by frequencies of the axles clearly visible and matching fairly well.

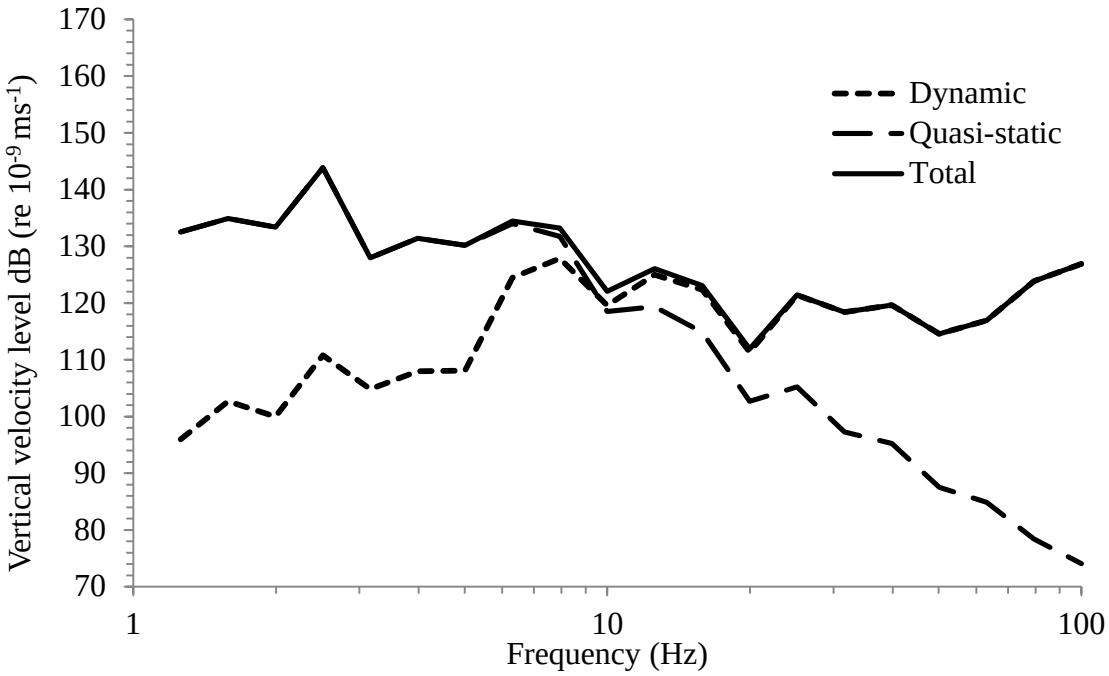

Figure 3.10: 1/3 octave band pass-by response power spectrum of the rail for a full train (4 vehicles) running over a 2 m peat layer over rigid foundation at 20 ms^{-1}.

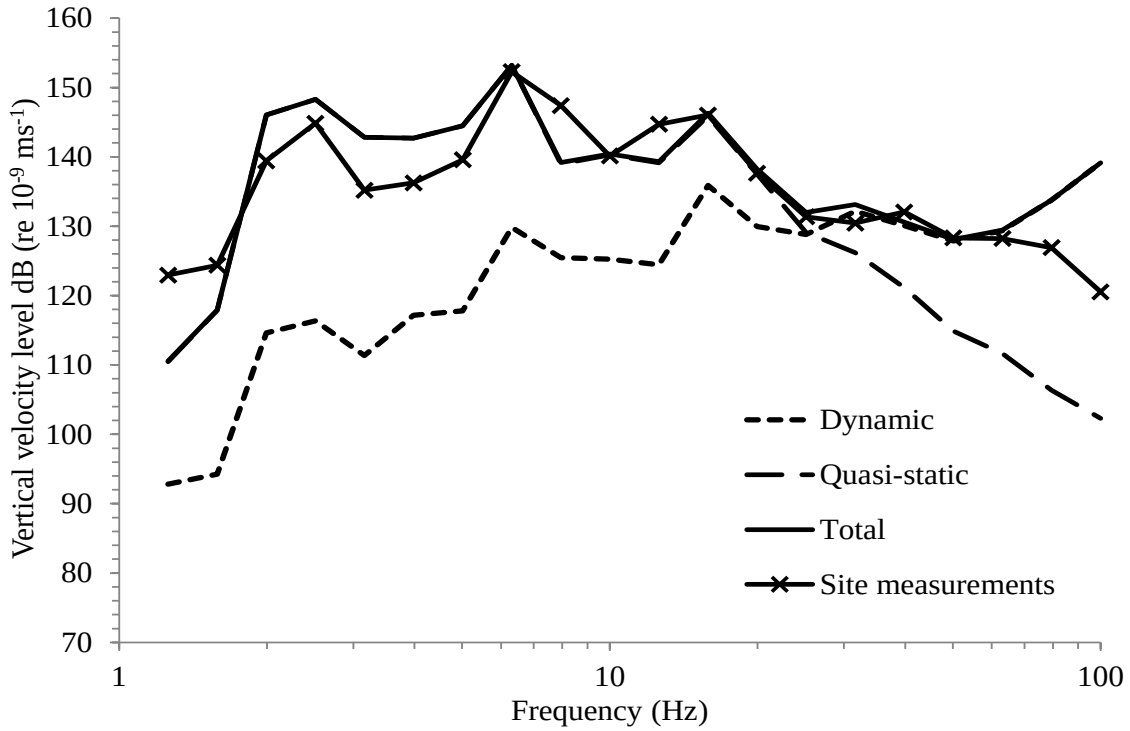

Figure 3.11: 1/3 octave band pass-by response power spectrum of the rail for a full train (4 vehicles) running over a 2 m peat layer over rigid foundation at 50 ms^{-1}. Geophone site measurements also presented.

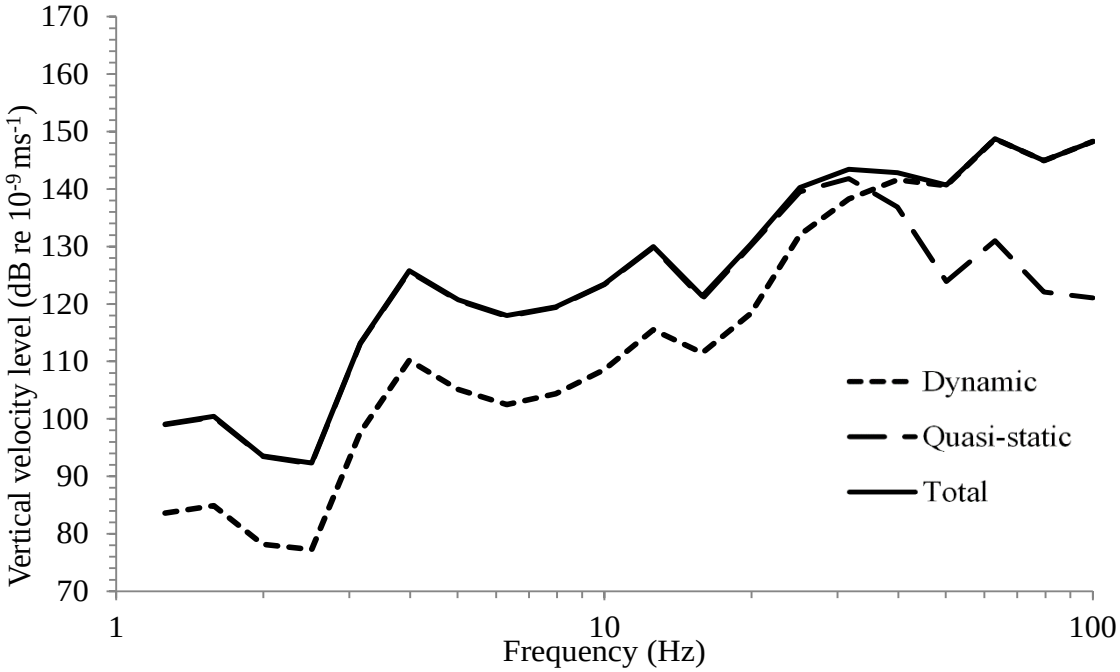

Figure 3.12: 1/3 octave band pass-by response power spectrum of the rail for a full train (4 vehicles) running over a 2 m peat layer over rigid foundation at 90 ms^{-1}.

Type 3 – Layer over stiffer halfspace

This model type is a peat layer over a stiffer halfspace. In this case the halfspace is an alternative to the rigid foundation used previously, as a method of representing the stiffer layers beneath the

peat. The calculated displacements are similar in shape to those from ground type 2, again over-calculating displacements especially at lower speeds (Figure 3.13). This ground type calculates higher displacements and a lower critical speed than the equivalent ground type 2 (rigid foundation) model, which is to be expected as the ground beneath the peat layer is now less stiff. When displacements are compared for comparable models, ground types 2 and 3 are within 9% of each other across all speeds, indicating that the models are beginning to converge with each other for this site.

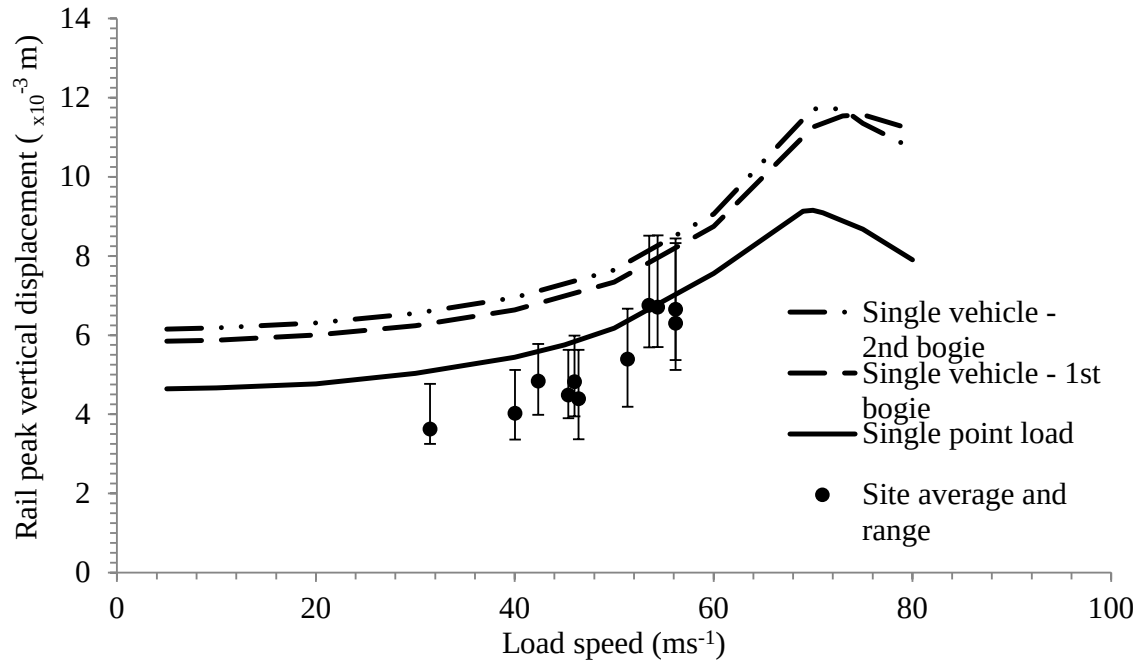

Figure 3.13: Displacement vs. load speed curves for a single point load and a single vehicle moving across a 2 m thick peat layer over a halfspace of stiffer material. Geophone measurement results for site also presented.

Full dynamic analysis results are similar to those calculated by ground type 2. As before the quasi-static component is more important at low frequencies and the dynamic component is more important at higher frequencies. Again the crossover point between the two components increases frequency with increase in speed: 10 Hz at 20 ms^{-1}, 30 Hz at 50 ms^{-1}, 50 Hz at 90 ms^{-1}.

Figure 3.14 plots the calculated results for 50 ms^{-1} against the measured site results recorded at 53 ms^{-1}. A very good match is achieved, with the wheel passing frequencies matching well, although the calculated and measured results vary more at either end of the frequency scale. This ground type predicts the closest results to those onsite for the full train analysis, although ground type 2 is closest to the site measurements for loading types 2 and 3.

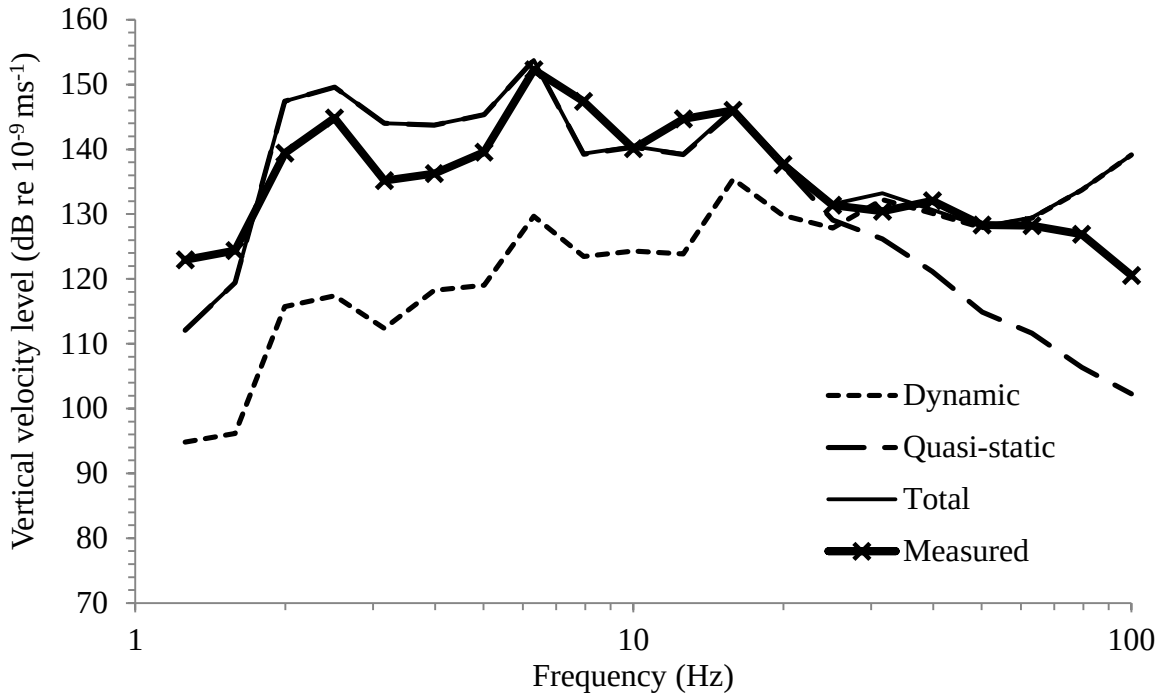

Figure 3.14: 1/3 octave band pass-by response power spectrum of the rail for a full train (4 vehicles) running over a 2 m peat layer over a halfspace of stiffer material at 50 ms-1. Geophone site measurements also presented.

Geometry conclusion

Using the displacements produced by the second bogie of a single vehicle allows easy visual comparison of all ground geometry types (Figure 3.15). It is clear that introducing a stiffened or rigid ground element beneath the peat has a considerable effect, with the full peat half-space (type 1) substantially over-estimating the displacements. Although this model is useful for carrying out parametric studies, it is too simple to represent the site accurately.

Both the rigid foundation and stiffer halfspace based models represent the shape of the displacement curve fairly well, but over-predict displacements. Although the rigid foundation based model acts in a similar way to the stiffer halfspace for this site, it is not recommended for use in future modelling, as it relies on there being a large stiffness disparity between the ground layers.

With ground model type 3, the displacements are consistently around 30% greater than those measured on site, thus the basic parameter estimates used need to be adjusted to match the site. The excessive displacements may be partly attributable to the lack of confinement of the peat layer in the MOTIV model as each layer is considered to be of infinite lateral extent. The inability to represent the varying thickness of the peat horizon along the track evident in the borehole

records may also have had an impact on the results. This ground type is deemed the most applicable for use in future work.

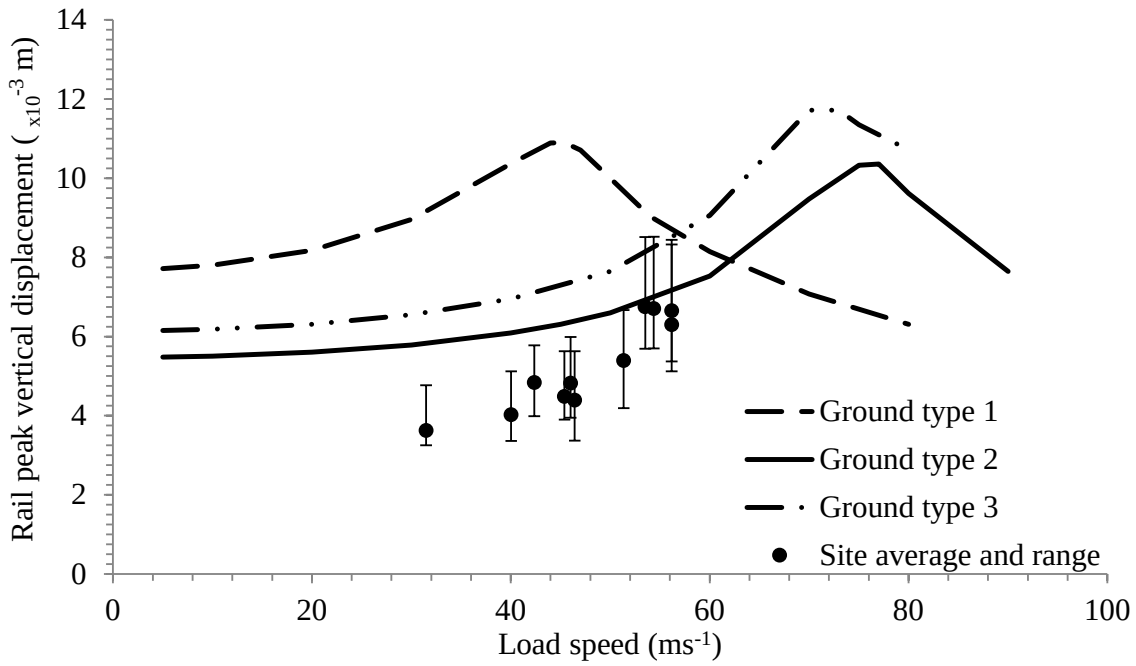

Figure 3.15: Displacement vs. load speed curves for the second bogie of a single vehicle moving across all three ground types. Ground type 1 is a peat halfspace. Ground type 2 is a 2 m peat layer over a rigid foundation. Ground type 3 is a 2 m peat layer over a halfspace of stiffer material. Geophone measurement results for site also presented.

3.2.3 Model dimensions

There are a number of parameters that can be varied within the set-up of the MOTIV model itself. β_{max} is the maximum wavenumber along the track, γ_{max} is the maximum wavenumber normal to the track. They are dependent on the frequency range. However, as a moving static load will be used for most models there is no obvious frequency range. Ultimately the model must have sufficient length in the direction of the track, L_x, to accommodate the entire train without it reaching around and catching its own tail.

$$L_x = \frac{2\pi}{\delta\beta} \qquad \text{Equation 3-1}$$

where $\delta\beta$ is the wavenumber step in the β direction, which is equal to:

$$\delta\beta = \frac{\beta_{max}}{\left(\frac{Number\ of\ grid\ points}{2}\right)} \qquad \text{Equation 3-2}$$

where gridpoints are the number of elements which the ground is divided into in the track direction. There must also be sufficient length perpendicular to the track, L_y, for waves to spread out and decay, as the domain is periodic in space due to the Fast Fourier Transform method used. L_y is calculated as follows:

$$L_y = \frac{2\pi}{\delta\gamma} \qquad \text{Equation 3-3}$$

where δγ is the wavenumber step in the γ direction, which is equal to:

$$\delta\gamma = \frac{\gamma_{max}}{\left(\frac{Number\ of\ grid\ points}{2}\right)} \qquad \text{Equation 3-4}$$

where gridpoints are the number of elements which the ground is divided into in the γ direction, normal to the track. To allow MOTIV to run on a desktop computer it was found necessary to restrict the number of grid points in the β wavenumber domain (along the track) and in the γ wavenumber domain (normal to the track) to 1024. To be able to include four vehicles as a 'Full Train' model, a minimum L_y of (4 x 23.9) = 95.6 m is required, where 23.9 m is the length of a single vehicle. However, an excessively large L_y will mean that the model cannot be run on a desktop computer, and also vastly increase run times. Therefore three β_{max} and γ_{max} values (6,12,24) were trialled to assess their effect on the model output, as they all give more than the minimum length of 95.6 m, see Table 3.3.

Table 3.3: Beta and Gamma max values.

β_{max} and γ_{max} *(rad/m)*	*δβ and δγ (m)*	*L_x and L_y (m)*
6	0.011719	536
12	0.023438	268
24	0.046875	134

Using the peat halfspace model loaded with a single moving load, the rail displacements were found to be well captured by a range of +/- 5 rad/m (Figure 3.16), therefore the smallest value of β_{max} and γ_{max} chosen in this investigation of 6 rad/m would be suitable. The range of β_{max} and γ_{max} values in Table 3.3 produced a maximum difference in predicted peak displacement of 1.1%. To accommodate any growth in the wavenumber range in more complex models, and as it increases calculation time very little over models with 6 rad/m, a value of 12 rad/m for β_{max} and γ_{max} was selected for future models. Run times on a 24 GB RAM laptop with a 2.8 GHz CPU for a model with two ground layers over a halfspace are approximately 1 minute for a single point load or

vehicle at one speed, 10 minutes for a single vehicle load across 20 train speeds, and 3 hours per speed to carry out a full dynamic analysis for 4 vehicles.

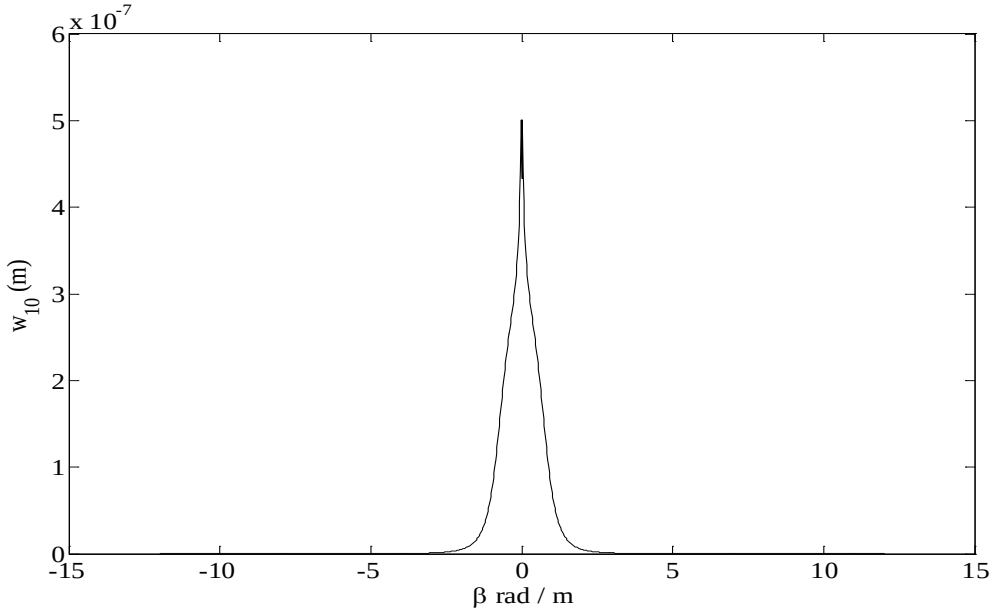

Figure 3.16: Rail displacement vs. wavenumber relationship, peat halfspace with a single moving load.

3.2.4 Track and vehicle parameters

The peat halfspace model, with a single moving point load, was used to assess the importance of a variety of parameters.

Ballast stiffness

A wide range of ballast stiffness values was used in the RIVAS project (Thompson *et al.*, 2013), varying between researchers and sites; for example models for Horstwalde, a site in Germany, used a value of 4.64×10^9 Nm^{-2}, in comparison to a value of 3.15×10^8 Nm^{-2} for Greby, a site in Sweden. This large range indicates the difficulty researchers face in selecting an appropriate value for this parameter. As the track type at the Horstwalde site presented similarities to Gravel Hole, and was used in several other sections of the RIVAS project to represent generic European track, its value was used, although models were run at 25 % and 50 % of this stiffness value to investigate its importance on the model results. These models showed a maximum difference in peak displacement of just 0.28 %. Therefore despite a range of values being used in the RIVAS project, ballast stiffness was considered unimportant to the accuracy of this model. From this point onwards, the original value as recommended in the RIVAS project for the Horstwalde site was used.

Ballast damping

Increasing the damping loss factor value from 0.04, as recommended in RIVAS, to 0.2 had no impact on the resulting displacements, therefore ballast damping was considered unimportant to the accuracy of the model. From this point onwards the original value of 0.04 as recommended in the RIVAS project was used.

Ballast depth and width

Ideally the impact of changing the depth of the ballast and the width of the track-ground interface would be investigated. However, as the MOTIV input routine assumes a 45° ballast slope it was not possible to change one without affecting the other. Consequently, reducing ballast depth to 0.2 m also reduced interface width to 2.9 m, and increasing the interface width to 3.6 m increased ballast depth to 0.55 m. The resulting variations in maximum peak displacement from the original values were a maximum of +4.33 % for the reduced dimensions, and – 8.66 % for the increased dimensions, at a speed of 45 ms^{-1}. Overall, it is thought that the change in displacements can mainly be attributed to the change in interface width either increasing or decreasing the pressure on the ground, and not to the change in ballast depth itself. From this point onwards the original ballast depth of 0.3 m will be used, as this is a standard value for most railways.

Train weight variation

The Class 390 maximum loading is 59.2 tonnes. The base model was re-run with an unloaded train weight of 46.6 tonnes, giving an axle load of 114287 N, as opposed to 145070 N, a load reduction of 21.3 %. The resulting peak displacements were also found to be 21.3 % lower, therefore peak displacements are deemed linearly proportional to loading. As detailed loading information for the case study site is not available, it is assumed trains are running at 50 % loading capacity from this point forwards, i.e. at 52.9 tonnes – an axle load of 129737 N.

3.2.5 Ground parameters

To test further the potential of MOTIV to model critical velocity effects, model type 3 (a peat layer above a stiffer half-space) was re-run with a large number of parameter combinations in an attempt to match more closely the site measurements. The objective was to reduce both the low speed deflections and the critical velocity. However, these two requirements are conflicting. Several parameters may be adjusted to reduce the calculated displacements; first the Young's modulus, density, damping and Poisson's ratio for the peat were varied. When adjusted individually the parameters have differing effects on the resulting displacement curve:

- Increasing Young's modulus reduces the displacements but also increases critical speed
- Increasing density maintains the general shape of the displacement curve whilst reducing the critical velocity and slightly decreasing displacements, owing to its impact on wavespeeds
- Increasing damping reduces the slope of the displacement curve and hence peak displacements
- Increasing Poisson's ratio reduces displacements, especially at lower speeds, with Poisson's ratios of close to 0.5 representing a saturated soil, and hence increasing the P wave speed of that soil.

Secondly the S-wave speed of the stiffer half-space was increased to 130 ms^{-1}. This still lies within the range measured on site and is equivalent to a Young's modulus of 100 MPa, a reasonable value to represent a combination of sands and gravels. A large number of parameter combinations were modelled, with Table 3.4 detailing the parameter combination giving the best fit.

Table 3.4: Refined ground parameters.

Peat Type	*Density (kgm^{-3})*	*Damping Loss Factor*	*S Wave Speed (ms^{-1})*	*P Wave Speed (ms^{-1})*	*Young's Modulus (MPa)*
Peat	1600	0.2	35	1400	5.88
Stiffer Halfspace	2000	0.1	130	768	100

Figure 3.17 shows the resulting displacement curve for the best fit refined parameters. A very close match to the site measurements is achieved. The parameters required to produce this result are generally reasonable. However, the density and Young's modulus are higher than might be expected for peat. This could be partly attributed to the aggregating and averaging out the properties needed to reproduce the measured behaviour for a lens of peat confined by much stiffer, denser materials. It should also be remembered that the site measurements are of a variety of trains of differing weights, whereas the MOTIV calculations are based on only a Class 390's weight.

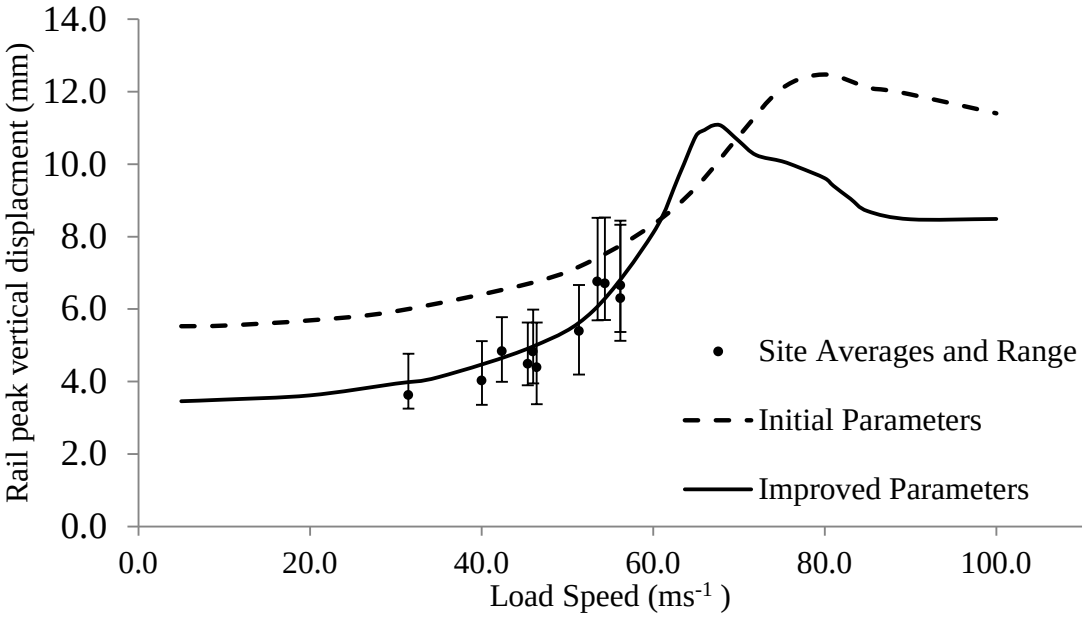

Figure 3.17: Displacement vs. load speed curves for the second bogie of a single vehicle running across ground type 3, using initial estimates and refined parameters. Geophone measurements results for site also presented.

Figure 3.18 shows the displacement of the ground surface for a single vehicle, indicating the wave behind the train. This illustrates the importance of allowing for the superposition of displacements between axles, and also of utilising a sufficiently large model. Note this image does not show the full extent of the model. The results for a full vibration response analysis for the refined parameters match the site monitoring measurements very closely (Figure 3.19). At this speed (53 ms^{-1}), below 30 Hz it is the quasi-static component that is dominant and above this frequency it is the dynamic component. As before this transition frequency increased with the train speed; e.g. it is found to be at 20 Hz at 25 ms^{-1}.

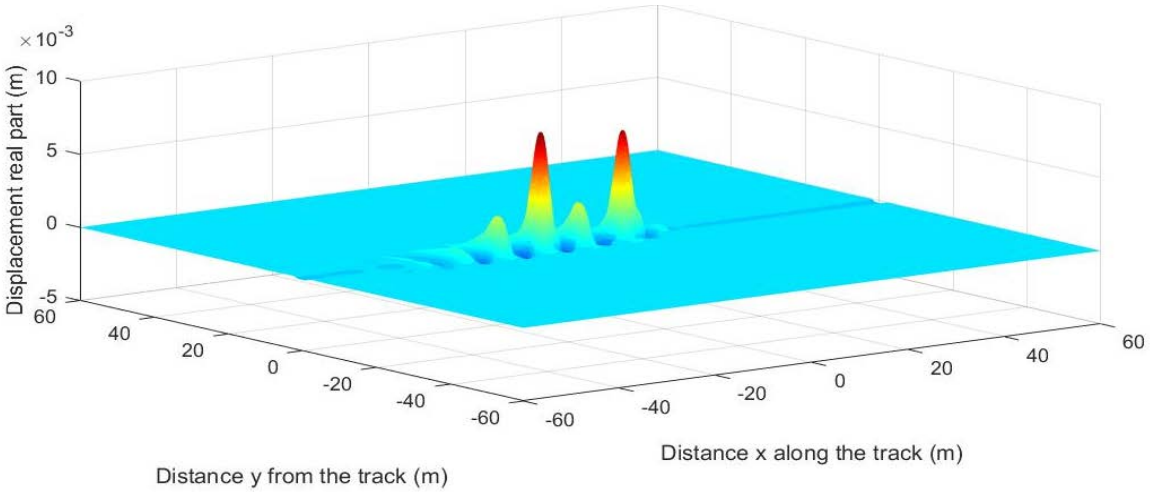

Figure 3.18: 3D plot of ground surface displacement, for a single vehicle travelling at 67 ms^{-1} across a 2 m peat layer (refined peat parameters) above a stiffer half-space.

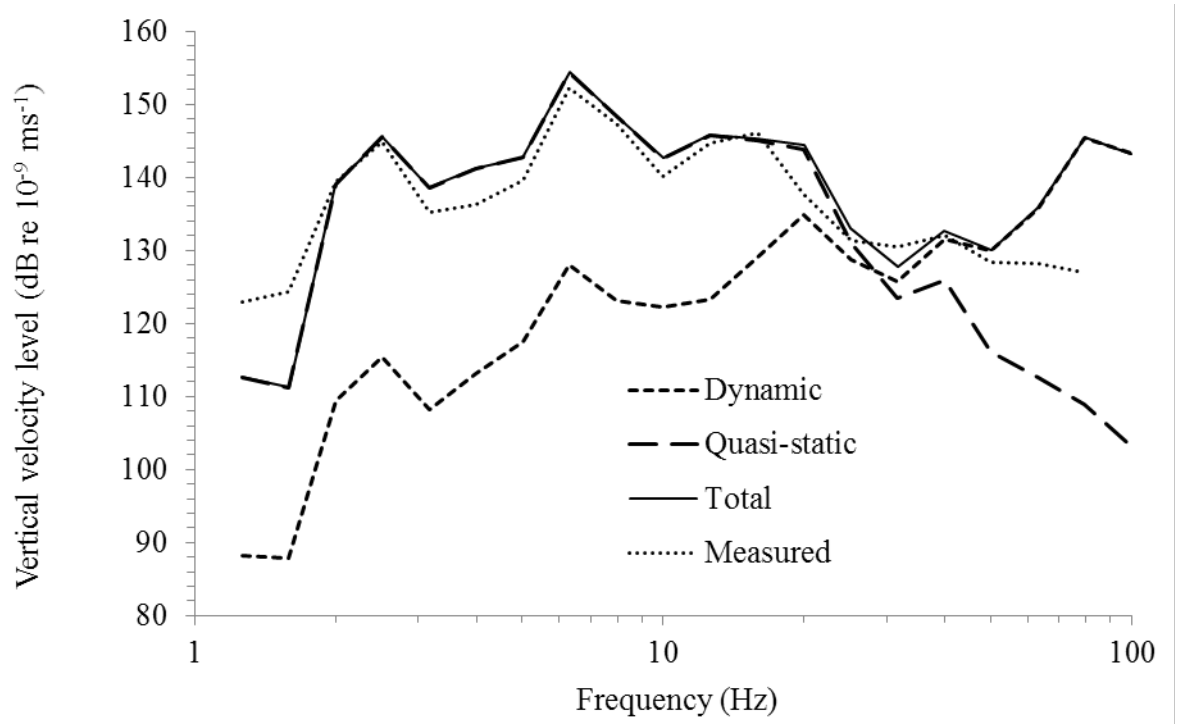

Figure 3.19: Full train pass-by vibration response for 4 vehicles running at 53 ms^{-1} across ground type 3, using refined peat parameters. Site measurements also presented.

3.2.6 Impact of saturation levels

It has been observed that the ground water level at the case study site is extremely high, sitting just above the base of the ballast layer. The high value of Poisson's ratio used in the refined parameters, and the correspondingly high P wave speed are consistent with saturated soil. The properties of peat are highly dependent on its water content; therefore three sets of parameters were chosen to represent three possible levels of saturation:

1) Completely saturated peat,

2) Relatively dry peat, uniformly saturated with a saturation level of 45%,

3) A 1 m thick layer of completely saturated peat overlain by a 1 m thick layer of relatively dry peat.

Peat is a highly variable material, therefore defining specific parameters based upon literature is difficult. Reported values for bulk and dry density of peats range from 500 / 160 kgm^{-3} for pure sphagnum moss (Walczak *et al.*, 2002), to 1040 / 500 kgm^{-3} for Jawa peat (Kalantari *et al.*, 2010) and 1800 / 770 for Irish moss peat (Huang *et al.*, 2016). These values show a significant range, and are all for 'pure' peat samples. As the peat type on the site is unknown, and is likely to have sand, which has a higher density, mixed into it from the neighbouring layers, values towards the middle

of the range were selected. A saturated bulk density of 1300 kgm-^{3} was chosen, still significantly lower than traditional engineering materials. With the dry density assumed to be 450 kgm-^{3}, a density value of 800 kgm-^{3} was selected to represent relatively dry peat, sitting at approximately 40% of the way between the dry and bulk densities. Peat is an extremely absorptive material and so is unlikely to be entirely dry.

As the water content of soil increases, the compressional wave speed for low amplitude vibration increases to a value a little larger than that of water whereas the shear wave speed is unaffected (Schevenels *et al.*, 2004). The earlier shear modulus was therefore kept constant for all three scenarios, at the value used in the earlier refined peat parameter set (1.96 MPa). The Poisson's ratio was adjusted to give P wave speeds as shown in Table 3.5. The stiffer halfspace was unchanged from the previous refined parameter value set.

Table 3.5: Peat parameters for various levels of saturation

Peat Type	*Density (kgm^{-3})*	*Damping Loss Factor*	*S Wave Speed (ms^{-1})*	*P Wave Speed (ms^{-1})*	*Young's Modulus (MPa)*	*Poisson's Ratio*
Saturated	1300	0.2	39	1586	5.88	0.4997
Relatively Dry	800	0.2	49	93	5.10	0.3

The deflections for the three scenarios are shown in Figure 3.20. Clear differences can be seen in the shape and amplitude of the calculated displacement curves. As the degree of saturation increases, the displacements decrease, owing to the reduction in compressibility caused by the presence of water in the pore spaces. These results imply that reducing the saturation level of the peat will tend to increase track displacements.

The critical velocities for the relatively dry and layered soils are very similar, at 79 ms^{-1} and 80 ms^{-1} respectively, with these two cases also producing displacement curves of similar gradient and shape. In contrast the critical velocity for the saturated case is lower at 73 ms^{-1}.

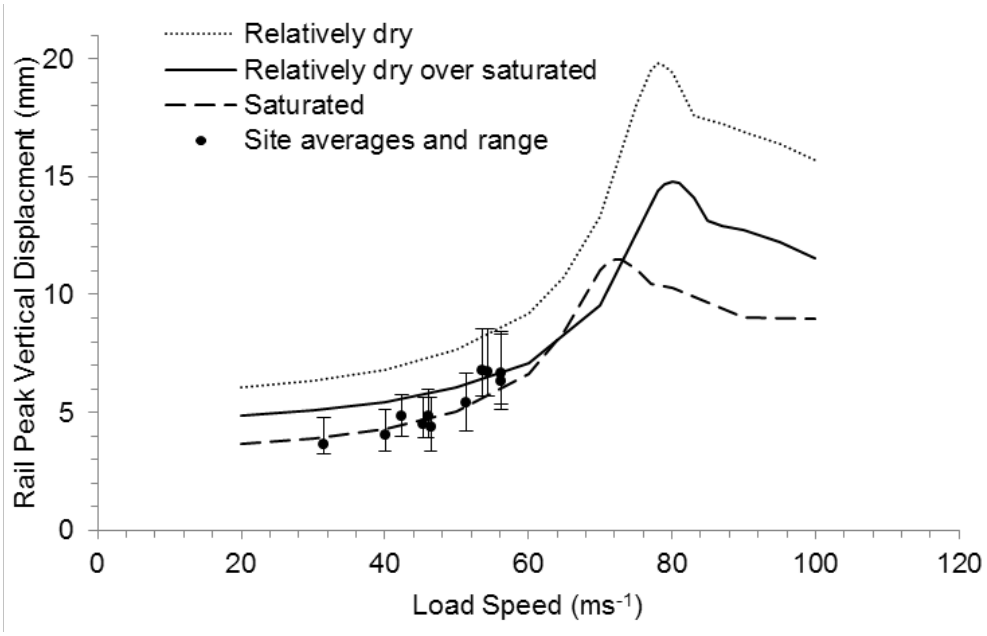

Figure 3.20: Displacements vs. load speed for a single vehicle running across a 2 m peat layer above a stiffer halfspace, using parameters given in Table 4. Geophone measurements are also shown.

The track receptances (i.e. the displacement due to a unit force as a function of frequency) are shown in Figure 3.21 for each soil condition. These results are for a moving load of 53 ms^{-1}. The vehicle wheelset receptance, based on its unsprung mass, is also shown for comparison. A peak in the vertical velocity level is expected at the frequency at which the rail and wheelset receptances cross, known as the vehicle-track coupled resonance (Thompson, 2009). At low frequencies the receptance of the track on the fully saturated soil is less than the others, but above 60 Hz it is higher than that of the other soil cases. Consequently, the coupled vehicle-track resonance is expected to occur at a lower frequency in this case, leading to the higher vibration levels observed in the model for the saturated soil in Figure 3.20. Overall these results suggest that reducing the groundwater level at the site is likely to lead to an increase in critical velocity effects.

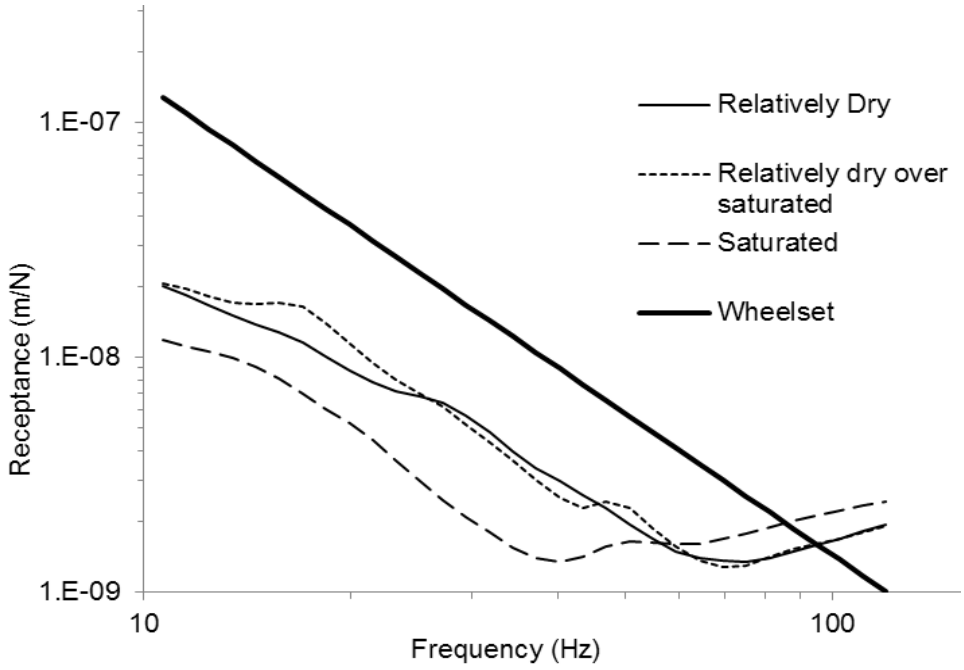

Figure 3.21: Track receptances for different soil conditions, and wheelset receptance

3.2.7 Parametric study conclusion

A study has been presented of critical speed effects using a test site in the UK as a case study. MOTIV, a semi-analytical model of a track coupled to a layered ground, has been shown to run well below, at, and above critical velocities, producing a smooth displacement curve. Three ground geometries were trialled, of increasing complexity. Ultimately a layer of softer ground over a halfspace of stiffer material was deemed the most applicable to the present study and future similar studies.

Initial calculations made using best estimates of ground properties from the site (namely limited borehole and wavespeed data) and the MOTIV model, led to much larger deflections than were measured. Three loading cases, again of increasing complexity, were trialled. The first, a single point load, was unable to account for superposition of displacements from several bogies, so is inappropriate for further use. Models using multiple load points (a single vehicle) produced results fairly close to the site measurements at higher speeds, but the most accurate results were produced when a full dynamic analysis was run to account for both quasi-static and dynamic effects. In this case a close match between the model prediction and the site measurements was found. In general it is recommended that models should incorporate four vehicles, to allow for superposition of displacements whilst minimising model computational cost.

By refining the soil parameters in the model, within a range that is still considered reasonable, close agreement was achieved in terms of the track displacements using a single vehicle loading.

Frequency spectra also showed close agreement when a full dynamic analysis was run. The inability of MOTIV to reproduce the limited lateral extent of the peat layer in reality is proposed as the cause of the somewhat high peat stiffness and density parameters necessary to replicate the measured data.

In terms of parameters that affect the results from MOTIV the following can be concluded:

- Uncertainty over ballast stiffness values is not critical, with values a factor of 10 different to each other producing very similar displacement results.

- Detailed knowledge of site track geometry is essential, as ballast depth and interface width have effects on displacement of a magnitude worth considering.

- Details of train loading levels should be sought where possible, as a linear displacement between loading and displacement is predicted – for example for a Class 390 up to a 20% increase in deflections between unloaded and fully loaded states can occur.

- Site investigations of ground parameters, particularly ground geometry and wavespeeds of softer layers are an important aspect of model accuracy and a required to improve confidence in the input data used.

- More detailed site investigations and laboratory work, such as oedometer and triaxial tests, to give accurate soil parameters are highly desirable.

The need to prioritise sourcing good site specific data, in terms of ground geometry and ground parameters, is clear for MOTIV to be a useful tool in modelling critical velocity effects. The ability of a linear elastic model to provide useful results is entirely reliant on the sourcing of good parameter data. If recommendations can be made as to the most effective methods to select or measure these parameters, then linear elastic models can move a step forward from their current levels of usefulness.

3.3 More detailed modelling

In addition to the initial modelling carried out as part of the parametric study, further modelling took place, again based upon desk-study / non-invasive parameter estimation techniques, to investigate the impacts of varying various parameters and geometries within the model. An arbitrary model numbering system is introduced to aid comparison of different models within this section.

3.3.1 Impact of more detailed model geometry

In order to test the influence of introducing more layers in the models, and also with the aim of appropriate model results with more realistic peat parameters, a more complex ground geometry was developed (T3.9). This can be seen in Figure 3.22, but essentially is based upon the site boreholes (Figure 5.1), with the depth of the track ballast below and adjacent to the sleeper removed, so that only the ground below the ballast surface is included (as the ballast itself is included within the track structure section of the model). This results in the addition of a 0.4 m depth section of ballast-type gravel, and a 0.3 m section of sand above the 2 m layer of peat and the stiffer halfspace.

A fresh desk study was carried out to decide upon ground parameters, based upon linking the borehole descriptions to literature and also involving the in situ wavespeed measurements. The resulting parameter values and their sources can be found in Table 3.6.

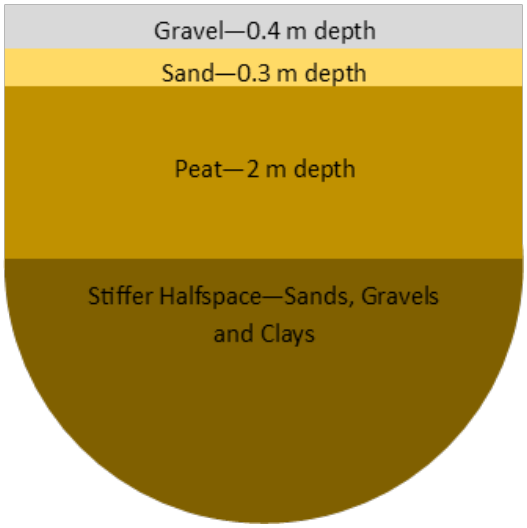

Figure 3.22: Ground geometry for MOTIV model T3.9.

Table 3.6: Soil parameters for MOTIV model T3.9 - multiple layers above a stiffer halfspace.

	Soil Layer Type and Depth			
Parameter and Source	*Gravel (Ballast Type) – 0.4 m*	*Sand – 0.3 m*	*Peat – 2 m*	*Stiffer Halfspace – Sands, Gravels, Clays*
Density (kgm^{-3})	1600	1900	1050	2000
	1500 –Ballast (Le Pen, 2008) 1600- Granite Ballast (Chang *et al.*, 1980) 1590 – Full scale rail rig tests (Ferro, 2016)	Assumed for medium dense sands	1050- (Rowe *et al.*, 1984)	Assumed for deep dense sands, clays and gravels, saturated
Damping Loss Factor	0.04	0.1	0.3	0.1
	0.04 – RIVAS project report (Thompson *et al.*, 2013)	0.1 - (Bowles, 1997)	0.3 - (Zainorabidin and Wijeyesekera, 2009)	0.1 - (Bowles, 1997)
Young's Modulus (MPa)	150	100	3.8	55
	170-180 – ballast (Indraratna *et al.*, 1997) 150-200 – ballast (Aingaran, 2014) 100-350 - ballast (Desai and Siriwardane, 1982) 50-150 – loose gravel, 100-200 – dense gravel (Bowles, 1997)	50-150 loose, 100-200 dense (Bowles, 1997); 80 – silty infrastructure sand (Paderno, 2009)	Derived from other parameters, however value sits within literature ranges of 0.1 – 4 MPa, with higher values expected due to the slight clay content (Rowe *et al.*, 1984; Zainorabidin and Wijeyesekera, 2009; Briaud, 2013)	Derived from other parameters, however value sits within literature ranges: gravel 50-150 loose, 100-200 dense, medium dense clay 15-50 , hard clay 50-100, sandy clay 25-250 (Bowles, 1997)
Poisson's Ratio	0.3	0.3	0.4997	0.498
	0.3 – 0.4 (Bowles, 1997) 0.33 - (Thompson *et al.*, 2013) 0.3 - (Powrie *et al.*, 2007)	0.3-0.4 (Bowles, 1997)	High Poisson's ratio as peat expected to be saturated	High Poisson's ratio as c expected to be saturated
P wave speed (ms^{-1})	355	223	1500	1600
	Derived from other parameters	Derived from other parameters	Derived from saturated Poisson's ratio	Derived from saturated Poisson's ratio
S wave speed (ms^{-1})	189	120	35	95
	Derived from other parameters	Derived from other parameters	Selected to represent peat from various literature (see Young's modulus)	Site measured SASW data

The results of this model (T3.9) can be seen in Figure 3.23, with a very good match achieved between the model and the site measurements. The parameters which produce this result are more realistic for the peat then those used in the previous 'refined' parameters, with a much lower density of 1050 kgm^{-3}, Young's modulus of 3.8 MPa and wavespeed of 35 ms^{-1}, all of which fit well with the literature ranges for very soft materials such as peat. The inclusion of the additional layers also introduces further kinks to the shape of the displacement curve, due to the Rayleigh wave speed dispersing through the different speed layers.

Also shown in Figure 3.23 are the results for running a model using the peat and stiffer halfspace parameters used in model T3.9, but without the layers of sand and gravel above the peat (T3.10). A significant difference in the resultant displacements can be seen, showing that the introduction of just 0.7 m (total) depth of stiffer materials can make a significant difference to a site. This implies that the use of recycling waste ballast for the future use of ground reinforcement could possibly mitigate against critical velocity effects, although this would involve either raising the surrounding track or removing existing ground material, in order to maintain track alignment.

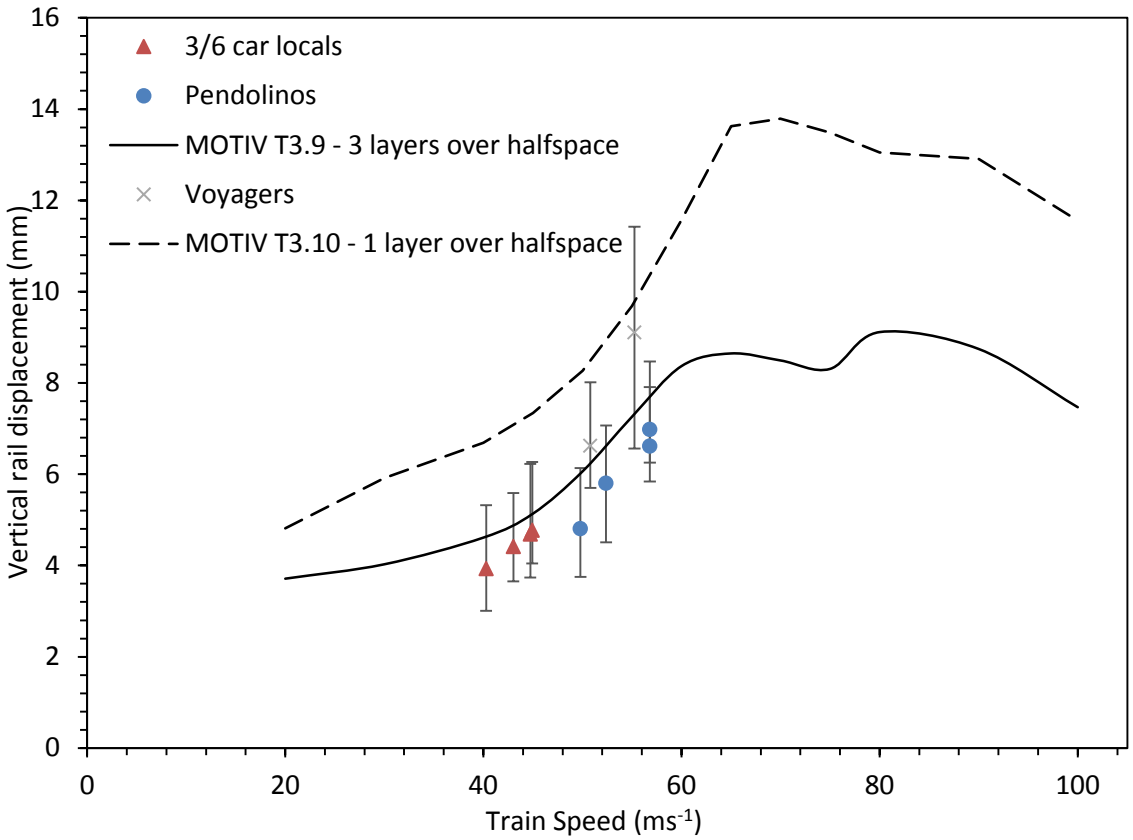

Figure 3.23: MOTIV model T3.9 - 0.4 m ballast-type gravel, over 0.3 m sand, over 2 m peat over a stiffer halfspace of sands, gravels and clays and MOTIV model T3.10 – 2 m peat over a stiffer halfspace of sands, gravels and clays, for a single vehicle.

3.3.2 Impact of thickness of stiffer surface layer

Model T4.4 was used to investigate the impact of varying the thickness of the stiffer sand and gravel layer above the peat. The geometry is shown in Figure 3.24, with the thickness X of the sands and gravels being set at increments between 0 m and 5 m. The ground parameters are based upon the best-fit parameters in section 3.3.1, with the parameters for layer 1 and the halfspace being set equal, see Table 3.7.

The results (Figure 3.25) show the large impact the thickness of a stiffer layer over a soft layer has on critical velocity speeds and displacements. Figure 3.26 summarises the peak displacement for each curve, normalised by the peak displacement for the X=0 m model. For this site model large improvements in displacements can be found, with the introduction of 1.5 m of sands and gravels over the peat reducing peak displacements by half. The additional impact of each increase in X reduces as X increases, with each increase of X after 1.5 m having significantly less impact on peak displacements than X increments below 1.5 m.

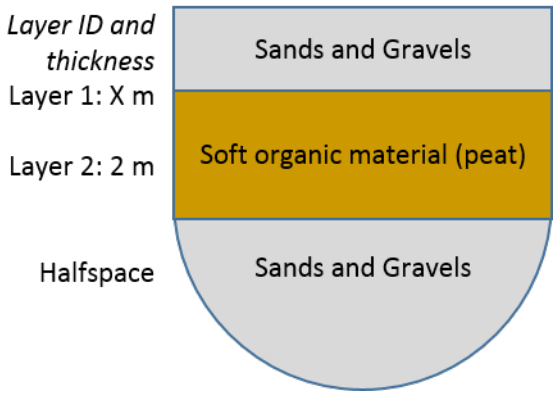

Figure 3.24: Model T4.4 geometry, with upper sand and gravel layer of varying thickness.

Table 3.7: Ground parameters for models T4.4 and T4.5.

Layer	*Density* (kgm^{-3})	*DLF*	*G (MPa)*	*E (MPa)*	*V*	V_S (ms^{-1})	V_P (ms^{-1})
1	2000	0.1	18	55	0.498	95	1600
2	1050	0.3	1.3	3.8	0.499	35	1500
H/S	2000	0.1	18	55	0.498	95	1600

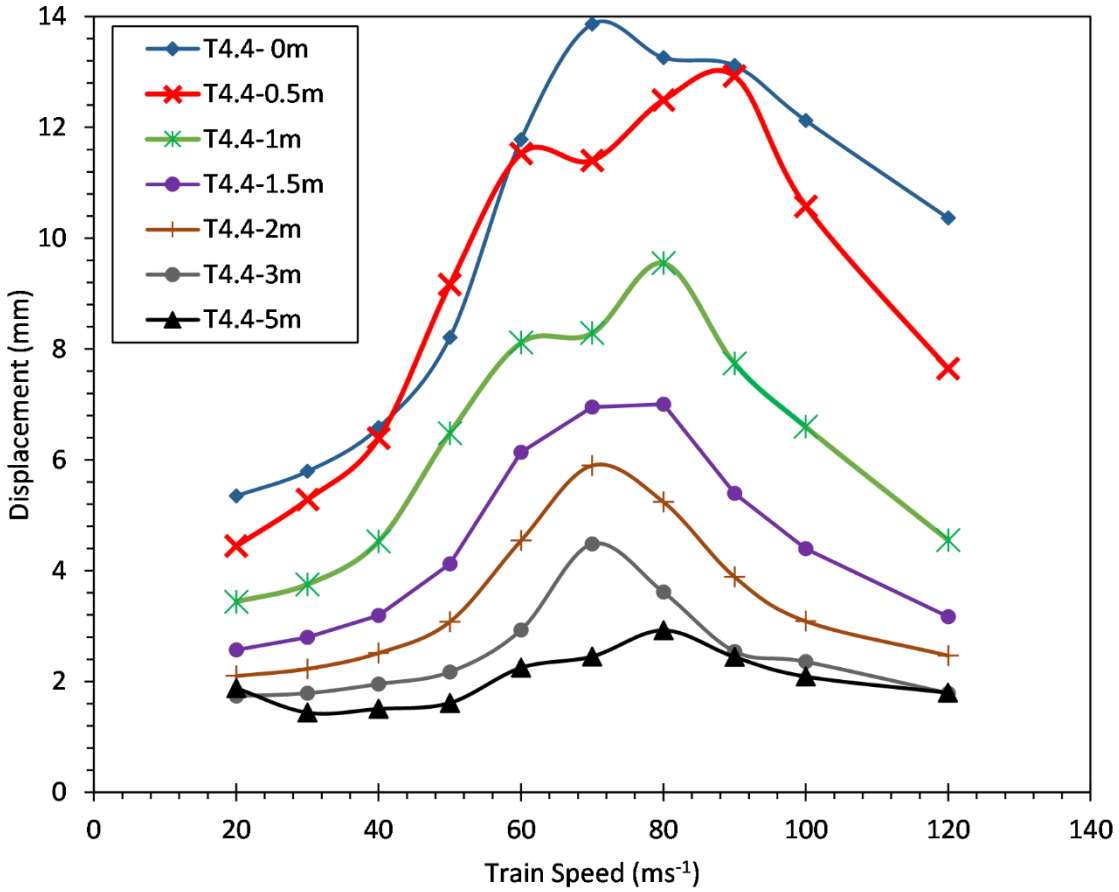

Figure 3.25: Displacement versus speed curves for a sand and gravel layer of varying thickness, over 2 m of peat over a sand and gravel halfspace.

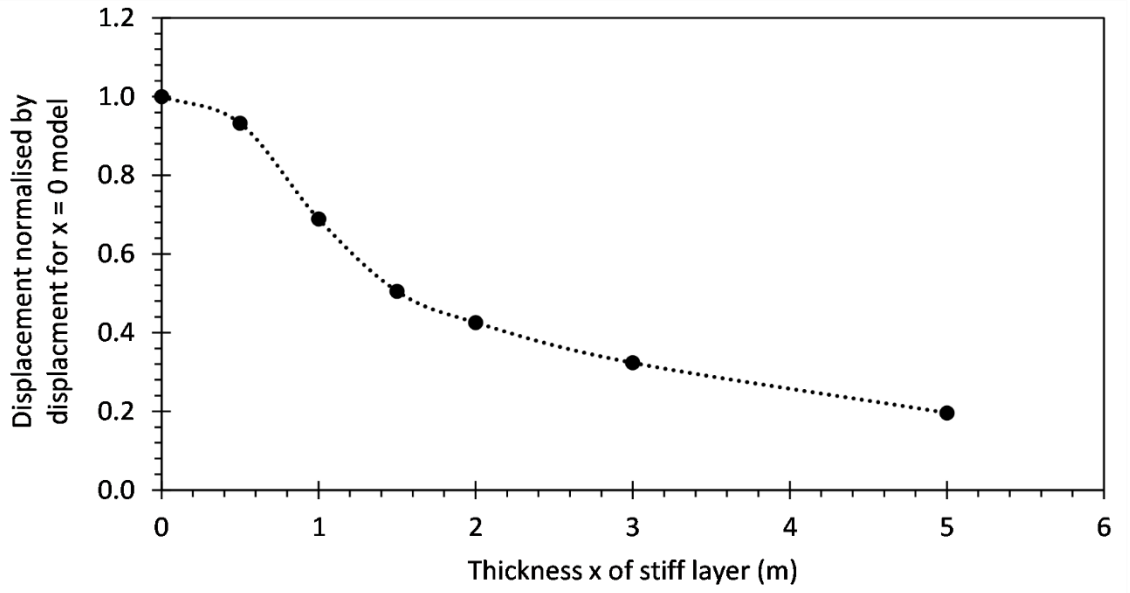

Figure 3.26: Summary of impact of varying thickness (X) of surface layer (sands and gravels), over 2 m of peat over a sand and gravel halfspace.

3.3.3 Impact of thickness of lower softer layer

Model T4.5 was used to investigate the impact of varying the thickness of the peat layer. The geometry is shown in Figure 3.27, with layer 1 and the halfspace set constant. The ground parameters in Table 3.7 were used. The resulting displacement curves show significant increases in predicted displacements for additional peat thickness (Figure 3.28), with the peak displacements for 1 m of peat twice that if no peat were included, and the displacements for 2 m of peat 50% greater than for 1 m of peat.

Figure 3.29 summarises the peak displacement for each curve, normalised by the peak displacement for the X=0 m model. The results sit on an approximately linear scale of increase in displacements with increase of X, up to approximately X = 2.5 m, showing that defining the depth of the softest layers on a site is key to an accurate model.

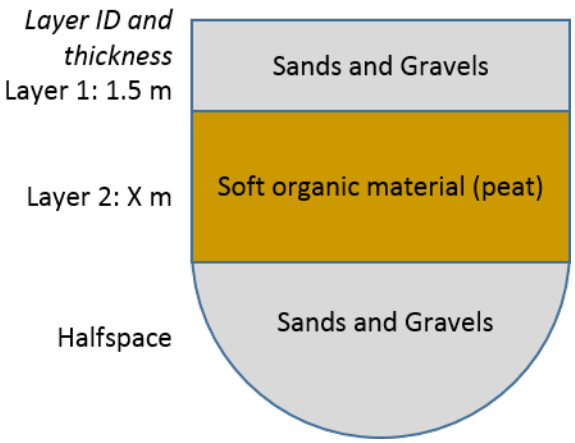

Figure 3.27: Model T4.5 geometry, with peat layer of varying thickness.

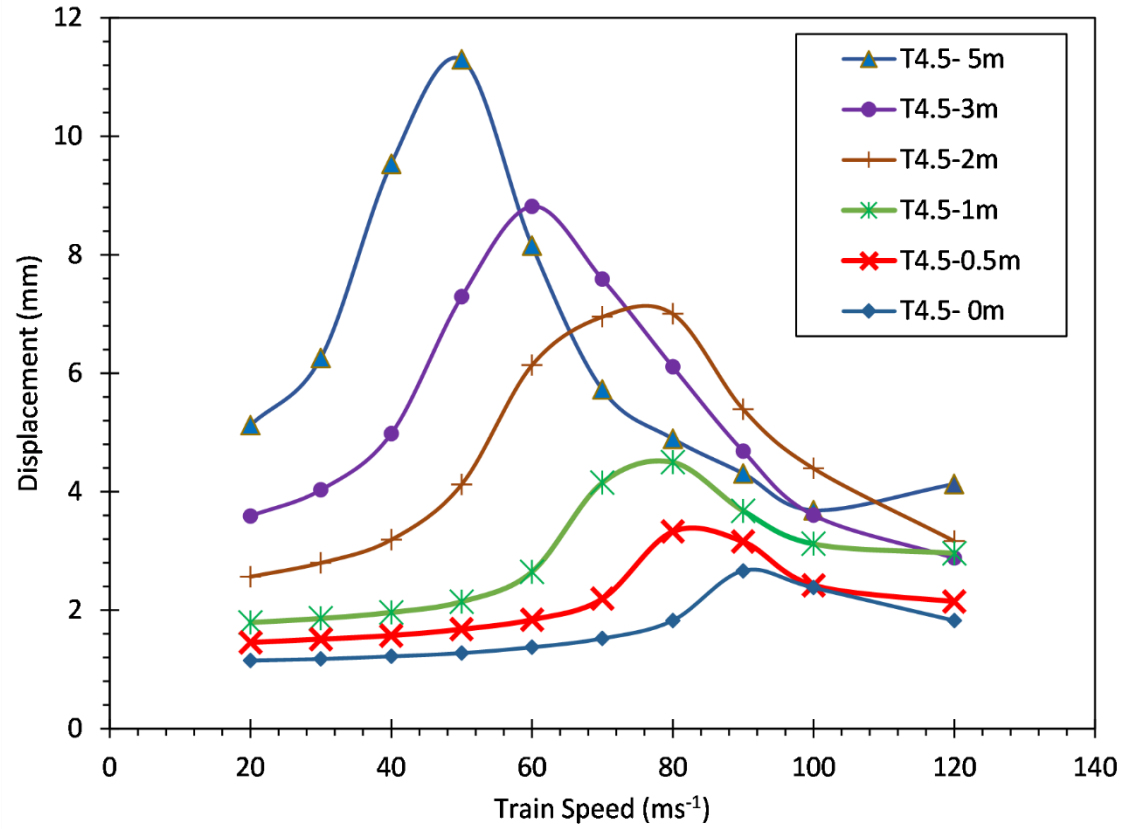

Figure 3.28: Displacement versus speed curves for a peat layer of varying thickness, between 1.5 m of sand and gravel and a sand and gravel halfspace.

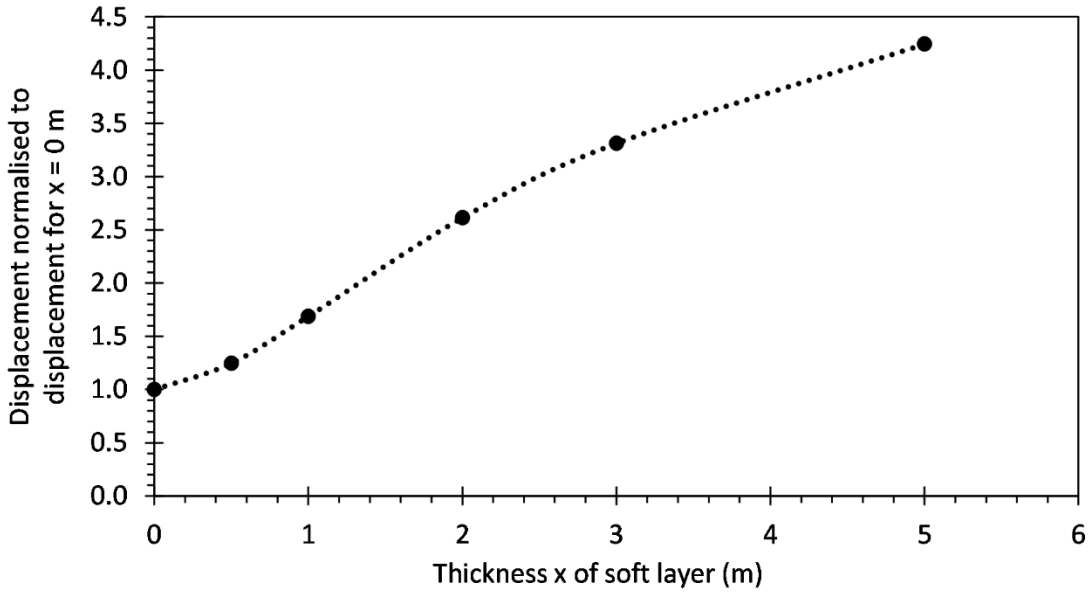

Figure 3.29: Summary of impact of varying thickness (X) of soft peat layer, between 1.5 m of sand and gravel and a sand and gravel halfspace.

3.3.4 Impact of stiffness ratios of soil layers

Model T4.6 was used to investigate the importance of the ratio of stiffness between the soft layer and the material above / below it. The geometry is shown in Figure 3.30, with the depths of all layers, and the parameters for the peat set constant. The ground parameters in Table 3.7 were used, with the damping, density and Poisson's ratio of the sands and gravel layers held constant, whilst the Young's modulus, and so the shear wave speed, was varied. The ratio of the sand and gravel shear wave speeds to the peat shear wave speeds was varied between 1 and 7.

The resulting displacement curves (Figure 3.31) show significant reductions in the peak displacements as the stiffness of the sands and gravels increases, with displacements halved when the sands and gravels have a shear wave velocity 2.5 times that of the peat, compared to a ratio of 1. Figure 3.32 summarises the peak displacement for each curve, normalised by the peak displacement for the lowest ratio (weakest) model. The resulting decreases in displacements are approximately inversely proportional to the shear wave ratio. This suggests that whilst accurately defining the strength parameters of the stiffer layers of the model is key for values of up to around four times the value of the softest layer's strength, accurate definition of stiffer strength values at ratios higher than this become less important to overall model displacements.

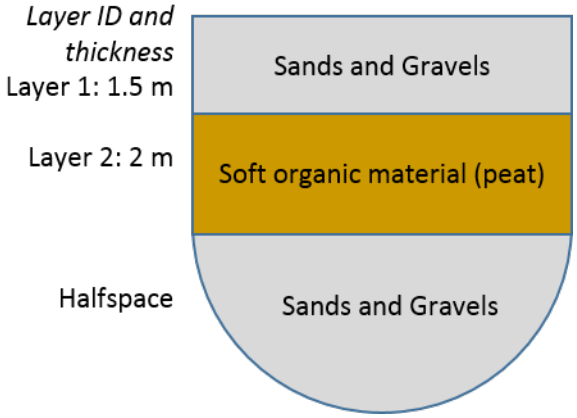

Figure 3.30: Model T4.6 geometry.

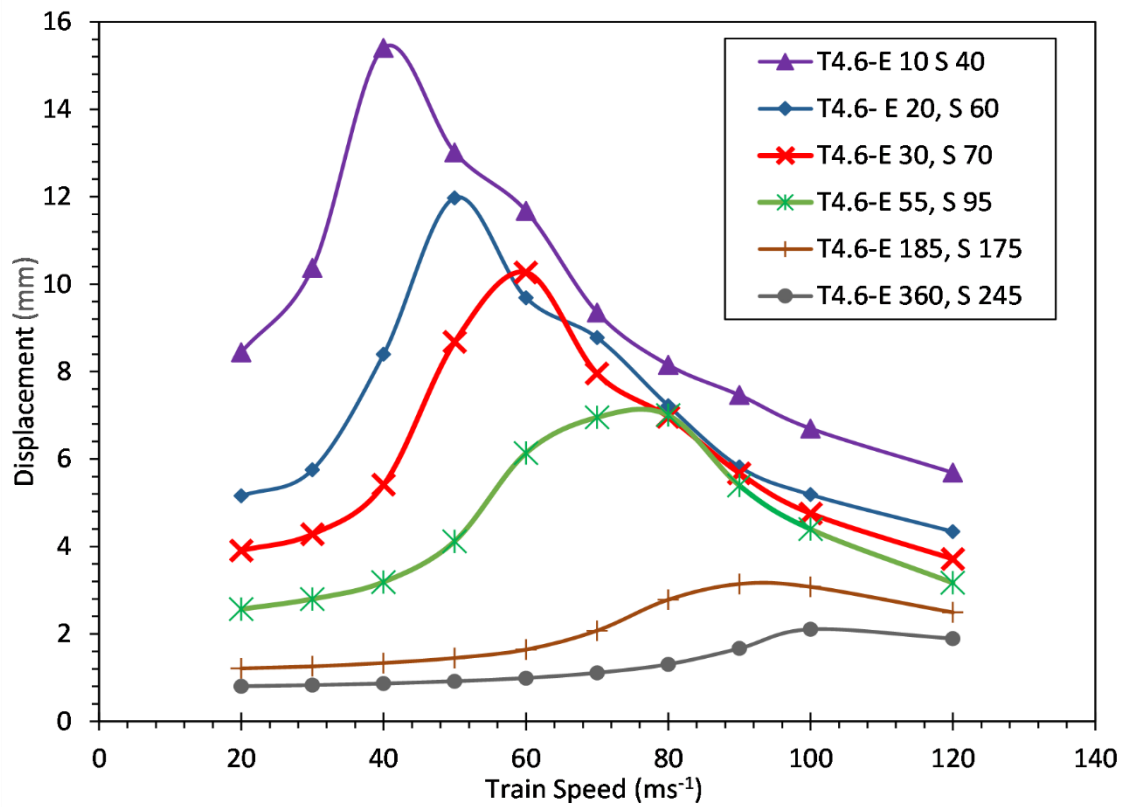

Figure 3.31: Displacement versus speed curves for 1.5 m of sand and gravel over 2 m of peat and a sand and gravel halfspace, for varied values of Young's modulus (E, MPa) and shear wave velocity (S, ms^{-1}) of the 1.5 m layer.

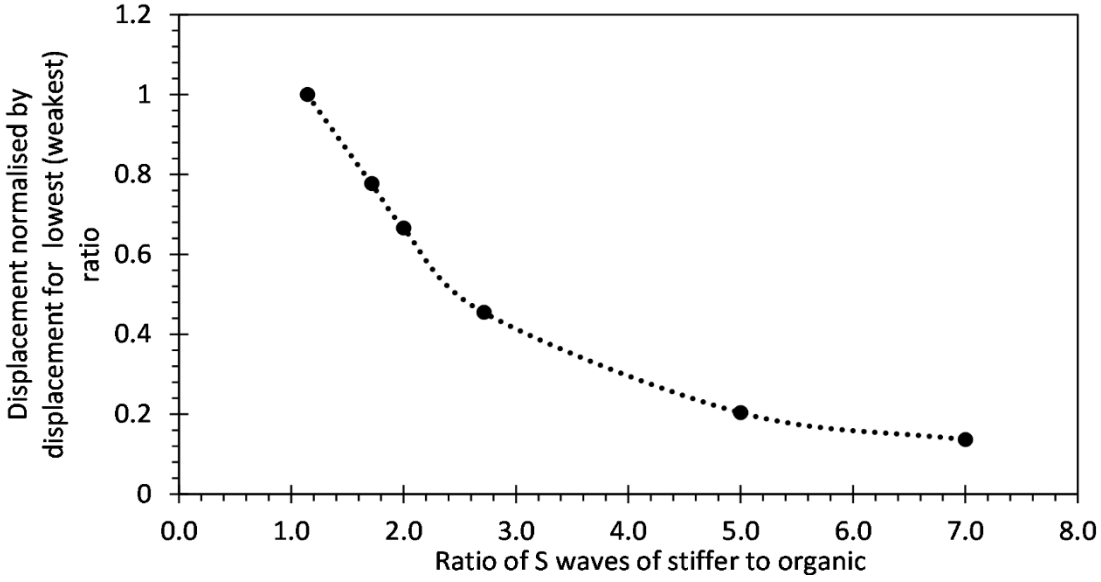

Figure 3.32: Summary of impact of varying ratio of stiffness between the upper stiffer layer, and the softer organic peat layer, for a model of 1.5 m of sand and gravel over 2 m of peat and a sand and gravel halfspace.

3.3.5 Assumptions and compromises

In order to allow the model to run on a desktop computer, the overall size and element density of the model must be restricted, which will have some effect on accuracy. Larger / more intensive models could be run on a supercomputer, but it is proposed that sufficiently good results can be achieved on a desktop computer. This also makes MOTIV a much more useful tool in critical velocity investigation and prediction, due to ease of access.

It is also only possible to represent layers of ground as homogeneous layers of constant thickness, therefore peat layers of varying depth cannot be represented. It must be remembered that the dynamics of the overall train, and the track irregularities, are only considered in the full train model. It is assumed that the FRA 3 roughness class provides a good representation of the likely roughness of the track at the site. Ideally site measurements would be used. It is also assumed that the track geometry conforms to standard UK track geometry, as further information was not available.

Trains are also only modelled at a constant speed, whereas some site measurements found the trains to be slowing across the measurement site. It was not possible to investigate or account for this effect in MOTIV during this project. MOTIV also is not able to model discrete sleeper supports, but instead uses a continuous support of equivalent stiffness. This should not affect the results as the harmonic forces produced by sleeper passage were shown to remain constant if the sleeper-passing frequency is higher than that of vehicle–track resonance (Auersch, 2005).

Chapter 4 Site and Experimental Methods

4.1 In situ site measurements

4.1.1 Penetration tests

There are many forms of in situ tests available to estimate various soil parameters. Tests such as cone penetration tests (CPT) and standard penetration tests (SPT) allow basic strength and deformation parameters to be estimated through relating cone tip resistance or test blowcount with empirical data on soil strength. The resulting data can be useful for modelling. For example Connolly *et al.* (2014b) used soil parameters from SPT testing in a rail scoping model, ScopeRail, for several sites. However, these tests are prone to inaccuracy if large granular particles are present in the soil; moreover great care and skill are required of the test operator. These tests can often be carried out in conjunction with borehole sampling. Boreholes, both new and historic, can provide information on layer depths and geological descriptions of layer components.

Dynamic probe testing, or commonly for railways Super Heavy Dynamic Probe testing (SDHP), involves driving a cone into the ground using a high frequency percussive hammer. The cone is attached to a steel rod, demarcated at 100 mm intervals, allowing the number of blows to drive the cone through 100 mm of ground to be recorded (Southern Testing Ltd., 2016). After every 1 m section a torque reading is taken, and then an additional rod is added. This process is repeated until the cone refuses to penetrate further, or the limit of the depth of interest is reached. In the case of the SHDP the hammer weighs 63.5 kg and is dropped from a height of 750 mm. The number of blows per 100 mm, when plotted against depth, give a visual indicator of the relative stiffness of the ground. It is also possible to correlate the number of blows to those of the Standard Penetration Test and so gain estimates of soil stiffness parameters, through empirical methods, should the general soil type be known.

4.1.2 Seismic measurements

The Spectral Analysis of Surface Waves (SASW) method is an in-situ method, introduced by Heisey *et al.* (1982) and developed further by Nazarian and Desai (1993) and Yuan and Nazarian (1993). It is non-invasive, relatively quick to carry out and relatively inexpensive. However, it is limited to estimating properties for the shallower soil layers. At the test site, surface waves are excited by a ground impact, with two receivers placed at a range of distances from the impact point used to measure the response. The ground is assumed to consist of several uniform layers of different

thicknesses and wave speeds. The impact induces waves in the soil with a range of frequencies. Lower frequencies have a longer wavelength and so travel relatively deeply into the soil. Deeper layers tend to be stiffer and have a lower damping than those above. Conversely higher frequency waves have a shorter wavelength and so stay closer to the surface, where the layers tend to be softer and have higher damping.

The signals recorded by the SASW receivers are analysed, and dispersion curves produced (phase velocity vs. frequency plot or phase velocity vs. wavelength plot). Through this, a wavespeed profile of the shallow ground is built up and a stiffness profile developed, allowing the dynamic shear modulus and damping ratio to be determined. This technique has been used to give parameters for high-speed rail modelling by Kaynia *et al.* (2000) and Degrande and Schillemans (2001), with Triepaischajonsak *et al.* (2011) and Connolly *et al.* (2014a) using a similar technique (Multichannel Analysis of Surface Waves – MASW). MASW is an extension of the SASW method, introduced by Park *et al.* (1999), which uses a multichannel approach, meaning , unlike the two receiver approach of SASW, 24 or more channels are used.

More advanced but invasive seismic tests to measure compressional and shear waves include up-hole, down-hole and cross-hole testing. In up-hole testing an excitation source is located at the base of a borehole and wave arrivals are recorded at receivers on the ground surface, whilst in down-hole testing the locations of the transmitters and receivers is reversed. The tests can be repeated at different depths to build up a fuller profile, and so provide better spatial resolution than SASW, but at greater cost. The cross-hole method uses two or more boreholes, with the transmitters and receivers all being placed within boreholes. Using multiple boreholes makes this method more suitable for estimating damping, but does require horizontal layers.

4.2 Site sampling

4.2.1 Sampling techniques and considerations

Many methods are available to take samples from sites for laboratory testing, from simple hand augers to more complex machine driven rigs. Whichever method is used the two key aims of the sampling regime are identical: to provide samples representative of the ground from which they are taken, and to minimise sample disturbance as far as possible. All works should be carried out in general accordance with BS 5930:2015 'Code of Practice for Site Investigations' (British Standards Institute, 2015) and BS EN ISO 14688-1 ‘Geotechnical investigation and testing’ (British Standards Institute, 2018a).

In order to be representative of the sampling site, samples must be sufficiently large to contain a range of all the particle sizes, fabrics, fissures and fracturing within the ground. It is also important to ensure the retained samples are of sufficient size to be used in the desired laboratory testing equipment.

Sample disturbance can occur during drilling, sampling, transportation, storage or preparation for testing. There are four mechanisms associated with sample disturbance (Clayton *et al.*, 1995):

- Changes in stress conditions,
- Mechanical deformation,
- Changes in water content and voids ratio,
- Chemical changes.

Changes in stress conditions are an unavoidable aspect of soil sampling, as the total stresses are reduced from those in situ to zero in the laboratory storage. Mechanical deformations are caused by the sampling process itself, as the cutting blade distorts the soil, but can also be caused by accidental impacts during transport and storage. If samples consolidate or swell after sampling, this will induce a change in water content and voids ratio, whilst incorrect transportation and storage methods can also induce these effects through vibration and evaporation. If samples come into contact with drilling fluid, or other substances, chemical changes in either the pore water or the soil may occur.

The extent of all forms of disturbance are in some way linked to the soil type, and to time. For example, whilst it is ideal to always minimise the time between sampling and testing, low permeability soils will take longer for excess pore pressures to dissipate, and so may be stored longer before excessive swelling occurs. Conversely, granular soils lose the majority of their strength when total stresses are reduced to zero, and so are very difficult to sample for laboratory testing.

The basis of the classification of soil samples set out by Hvorslev (1949) is still in use today. Three classes of sample are defined. Non-representative samples are those which soil or rock layers have become mixed, and are not particularly useful for any form of site investigation. Representative (disturbed) samples are those which contain soil from a particular stratum, and have not been contaminated by other stratum, but may have been remoulded and have a changed water content. Finally undisturbed samples are those where the soil is subject to minimal disturbance, sufficient to allow laboratory experiments of the approximate physical characteristics of the soil.

Each combination of ground type and sampling procedure is likely to produce samples of a set classification, further detailed in BS 5930 (British Standards Institute, 2015). For samples which are to be used for shear strength or compressibility tests BS 5930 states they should be quality class 1, which requires use of sampler category A. When a sampling regime is being set, BS 5930 should be consulted, and a sampling method which will produce a sufficiently high quality class for the intended use of the samples should be selected wherever possible.

There are two main types of undisturbed soil sampling – tube sampling, and block sampling. In tube sampling a tube is pushed or hammered into the ground, displacing or distorting soil as it does so. This is the most common method of sampling, with the mechanical deformation caused during the boring process being in the form of compaction, remoulding or displacement of the soil. Block sampling generally involves cutting a block shaped sample from the base of a pit. It is less common, as a large pit is required, which can be problematic and expensive for anything but shallow samples, but does have the benefit of not subjecting the sample to shear distortions. Only tube sampling is possible for this work, as block sampling is not possible in the short time available to take samples from live rail sites.

Hvorslev (1949) recommend the use of drilling fluids where possible if the borehole is below the water table, to reduce the total vertical stress changes that occur at the base of the borehole, to minimise base swelling. The faster sampling takes place the less swelling will occur, as water will have less time to enter the soil. Base heave, where the plastic flow of soil occurs upwards into the borehole, due to a combination of decreased vertical stress and a low undrained shear strength, is a common problem in very soft soils. If it occurs, depths in excess of three borehole diameters ahead of the bottom of the hole may experience disturbance (Clayton *et al.*, 1995). Hight and Burland (1990) recommend the use of drilling fluid (a bentonite and water mix) to prevent this, but note that the bore casing must be continuous for this to have effect. Due to issues with disposing of bentonite, the most common form of modern prevention is the use of a continuous casing, which also minimises caving, where soft soils collapse and fall out of the bore side wall into the base of the borehole.

The design of the sampler cutting edge can have a large impact on sampler disturbance. Hvorslev (1949) defined the area ratio of the sampler, calculated from the internal and external diameters of its cutting edge. The lower the area ratio, the better quality, theoretically, the sample produced. It is generally recommended that in soft or very soft soils a low area ratio, or cutting taper angle, is essential.

Baligh (1985) showed that the strains imposed on the centreline of a soil sample as it travels into a sample tube are initially compressive, and then extensive. The magnitude of these strains is

dependent on the tube geometry. In stiff clays this has the effect of increasing the effective stress, and so the strength and stiffness values obtained from laboratory testing should generally be reduced (Chandler *et al.*, 1992). However, Clayton *et al.* (1995) note that the large variability of clays, for example the inclusion of laminations of sands, or fissured planes, mean this effect does not always occur. In normally and lightly overconsolidated clays the opposite occurs, with large decreases in mean effective stress occur during sampling (Hopper, 1992) . Clayton *et al.* (1998) used a numerical model to show that increasing the area ratio, through increased sampler wall thickness, causes a significant increase in the peak compressive strain ahead of the cutting edge, although the peak strain in extensions only saw a slight increase.

Casagrande (1936), Siddique (1990) and Hopper (1992) noted that soft clays should have the outer disturbed layer shaved off as soon as the samples are removed from the borehole. This is to help minimise moisture migration within the sample, as the outer layer of the soil has been shown to have higher pore pressures than the centre immediately after sampling, due to the higher strains experienced during sampling.

In order to minimise sample disturbance, the methods used to preserve and transport samples must also be considered. ASTM D4420 (2007) states that for samples which are to undergo detailed laboratory testing (such as triaxial testing) samples must be preserved and sealed inside moisture proof containers (e.g. wrapped in plastic film and aluminium foil, wax sealed, glass or plastic jars). These containers must then be protected against temperature change, vibration and shock impacts. During transport, samples must be placed inside shipping containers that protect against vibration and prevent the samples from rolling into one another/ the transport vehicle. Wherever possible, for very fragile samples, they should be transported and stored in the orientation from which they were taken, to minimise sample disturbance.

Windowless sampling

The type of sampler available for use on the case study sites within this project is the Tracked Windowless Sampling Rig (WS), see Figure 4.1. This is a tracked hydraulically powered percussive drilling rig, which relies on a hammer unit of 63.5 kg falling over a distance of 750 mm to advance the sampler. The sampler comprises of a 1 m length high tensile steel tube, which has a plastic liner inside for soil core retention. Once the first 1 m run has been completed the sampler is extracted using the drilling rig's built-in hydraulic jacking system. The windowless sample hole can then be progressed by adding a 1 m extension rod and repeating the procedure above. This process can be continued until the target depth has been reached or the sampler refuses, at which point the borehole will be backfilled.

Although this hammering method of driving the sampler tube can lead to high sample disturbance, it remains the most common method for use on railways due to the typical working conditions (small working space, stiff upper ground/track system layers and short working time frames).

BS 5930 (British Standards Institute, 2015) states that due to the plastic liner inserted inside the steel sampler in a WS rig, the cutting shoe wall thickness is about 10 mm, giving an area ratio of between 50 % (largest 100 mm diameter tube) and 115% (smallest 45 mm diameter tube). It suggest a soil quality of class 3 will be produced. According to BS 5930 a class 3 sample should not be used for compressibility, shear strength, density or permeability tests. As this is the only sampling method available for the site, the likelihood of sample disturbance will have to be considered when testing the samples and discussing / using the results. Samples will be trimmed to remove the outer disturbed layers, to minimise the effects of the sampling method.

Figure 4.1: Windowless sampling rig in use AECOM Ltd. (2016)

4.3 The resonant column

4.3.1 Overview and adaptations

Various types of resonant column (RC) apparatus have been in popular use since the early 1960's to measure the dynamic responses of soil and related parameters. The RC is based on the theory of a visco-elastic cylinder allowing the propagation velocity of waves in a soil sample to be derived. This is achieved through monitoring the response of a column of material to excitation at resonance, with the frequency at resonance identified from the plot of acceleration versus frequency. An example response curve is shown in Figure 4.2. The results allow wave velocities, damping and, indirectly, shear modulus to be determined at very small and small strains. Although there were many sources of inaccuracy inherent to the early designs and procedures, these have been reduced over time by various authors such as Wilson and Dietrich (1960), Anderson and Stokoe (1982) and Hardin and Drnevich (1972) , with Drnevich (1978) carrying out extensive work to standardise test procedures.

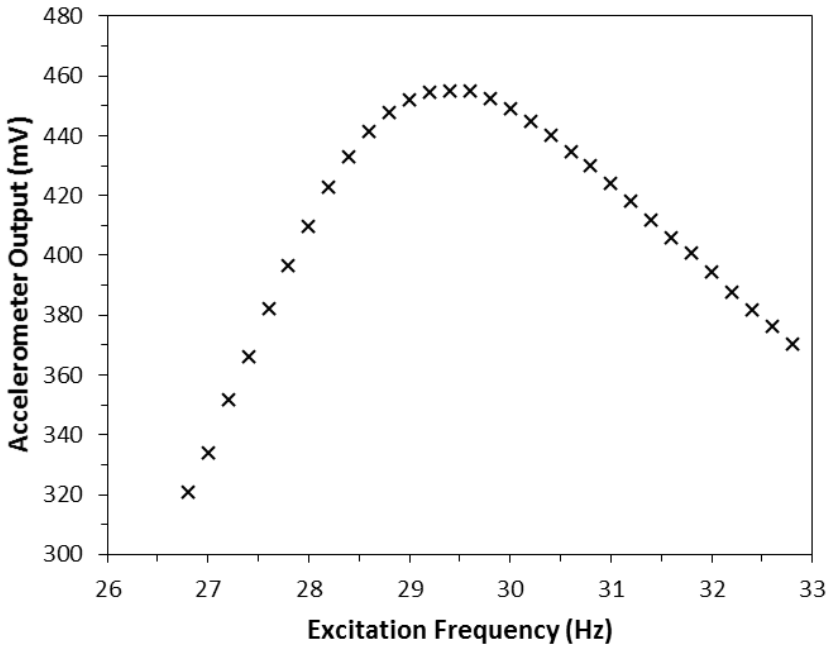

Figure 4.2: Example frequency response curve for a Gravel Hole sample in the RC.

Currently a variety of designs exist, which vary in the types of excitation they can apply to the specimen, with torsion and flexure being the most common and longitudinal the least common. The types of boundary conditions applied to the specimen in a RC also varies. Various excitation modes were investigated by authors such as Wilson and Dietrich (1960)and Cascante *et al.* (1998).

The most common RC is the Stokoe RC (SRC), which is typically used to apply torsional excitation and is of fixed-free configuration. A drive mechanism is attached to the free end of a cylindrical

specimen with its other end being fixed (Figure 4.3). The motion of the free end is measured using an accelerometer and used in the analysis to obtain the resonance frequency of the system (Richart *et al.*, 1970). For analytical purposes the RC is modelled as a single degree of freedom system – i.e. that the sample is treated as a spring and the drive system as a lumped mass (Figure 4.4). The drive mechanism consists of four electromagnets, which the arms of the drivehead that is attached to the sample sit inside.

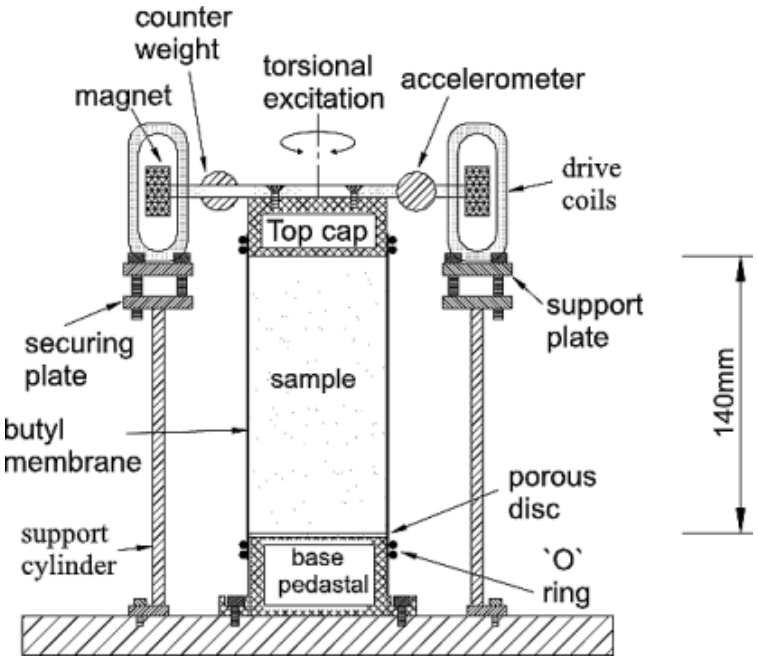

Figure 4.3: SRC – Typical fixed-free apparatus (Priest et al., 2005) – Modified from Stokoe et al. (1999).

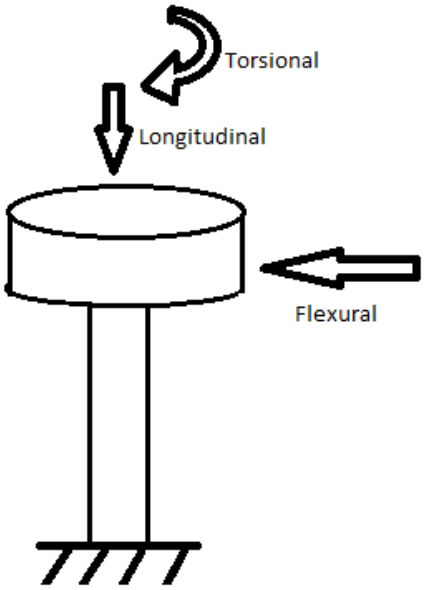

Figure 4.4: Model of RC as a single degree of freedom, fixed-free configuration, with excitation modes shown.

Cascante *et al.* (1998) modified the coil and magnet connections of an SRC so that both torsional and flexural excitation could be applied to the specimen. If all four coils are connected in series the torque required for torsional excitation is produced, whilst using just two coils opposite one another allows a lateral force to be applied to excite flexural motion (Figure 4.5).

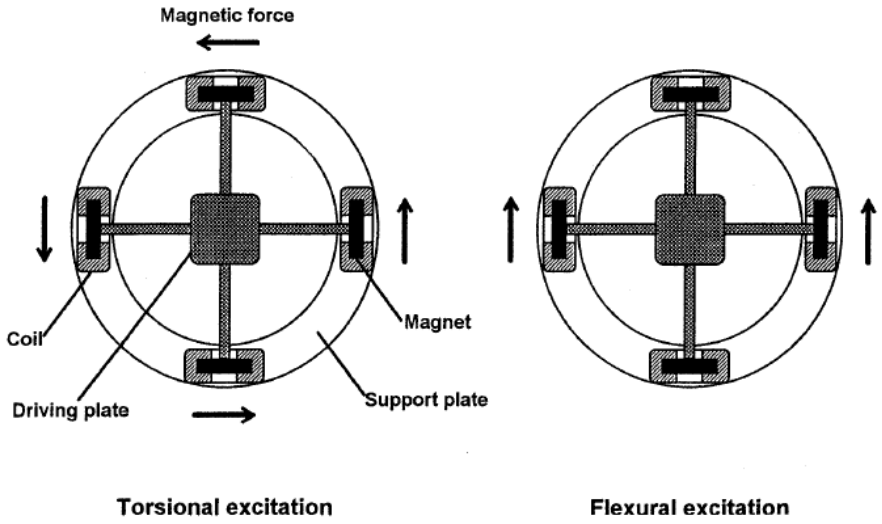

Figure 4.5: Coil and magnet configuration for torsional and flexural excitation. Modified from Cascante *et al.* (1998).

Work done by Hardin (1965) amongst others, showed that if strains in the sample can be assumed to remain small during the testing process then an elastic solution is satisfactory. This allows the soil dynamic properties such as stiffness and damping to be obtained, based on the relationship between the dynamic modulus of the material and the resonant frequency of the column.

Figure 4.6 shows the layout of the RC built for this project, with bender elements (BE) installed into the top and bottom caps. Back pressure is applied through a GDS water pressure controller, whilst sample confining pressure is applied through a GDS air pressure controller. This RC was made from modifying one of the GHRC drive heads designed by Priest (2004), so as to be able to use it on a standard support cylinder. It is therefore very important that care is taken in the calibration stages to check for any additional compliance this may have introduced. These modifications can be seen in Figure 4.7. Four brackets were machined from solid aluminium, to allow the imperial support frame to bolt to the metric drivehead. As the calibration bars and the RC support column to be used in this project have been tested with several times previously, it will be possible to compare the calibration curves for the new modified RC to the previous results. If no new compliance has been introduced the spread of values of I_0 should not be any larger for the modified RC than in previous results.

It should be noted that several authors (Avramidis and Saxena, 1990; Hardin *et al.*, 1994; Priest, 2004) have suggested that compliance issues are worsened by the stiffness of the tested soils. As only fairly soft soils will be used in this project, the amplitudes of any compliance issues are likely to be much smaller. Equally, Chung *et al.* (1984) showed an underestimation of shear modulus when a low confining pressure of 10 kPa was used, suggesting that there was a lack of fixity between the top cap and the top of the sample specimen. The use of dental plaster as an adhesive can give a better coupling between the top cap and specimen, which is useful in the low confining pressure scenario, but also to prevent slippage under torque if very stiff highly bonded soils are to be tested (Clayton *et al.*, 2007).

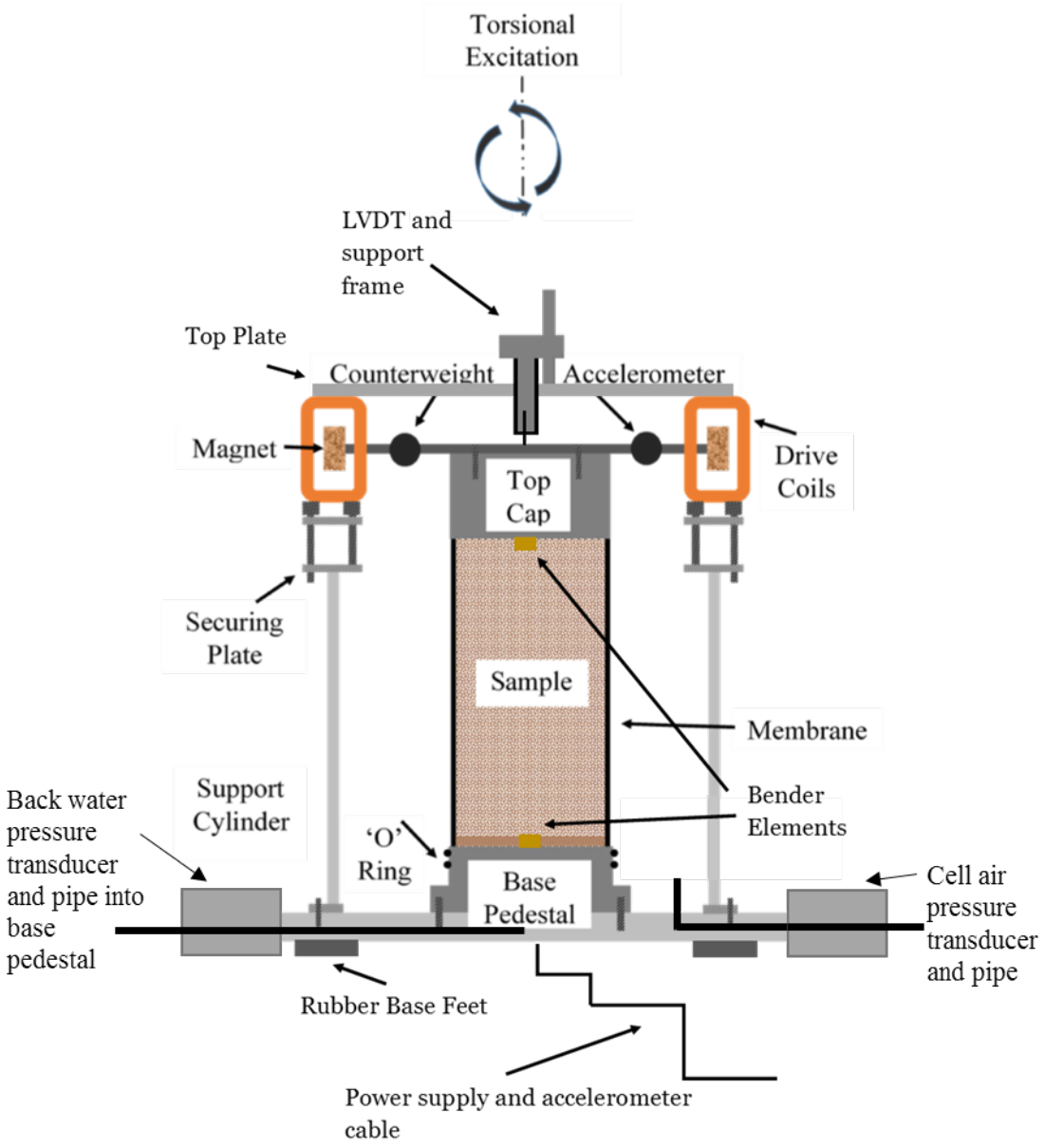

Figure 4.6: Resonant column apparatus schematic, with bender elements installed.

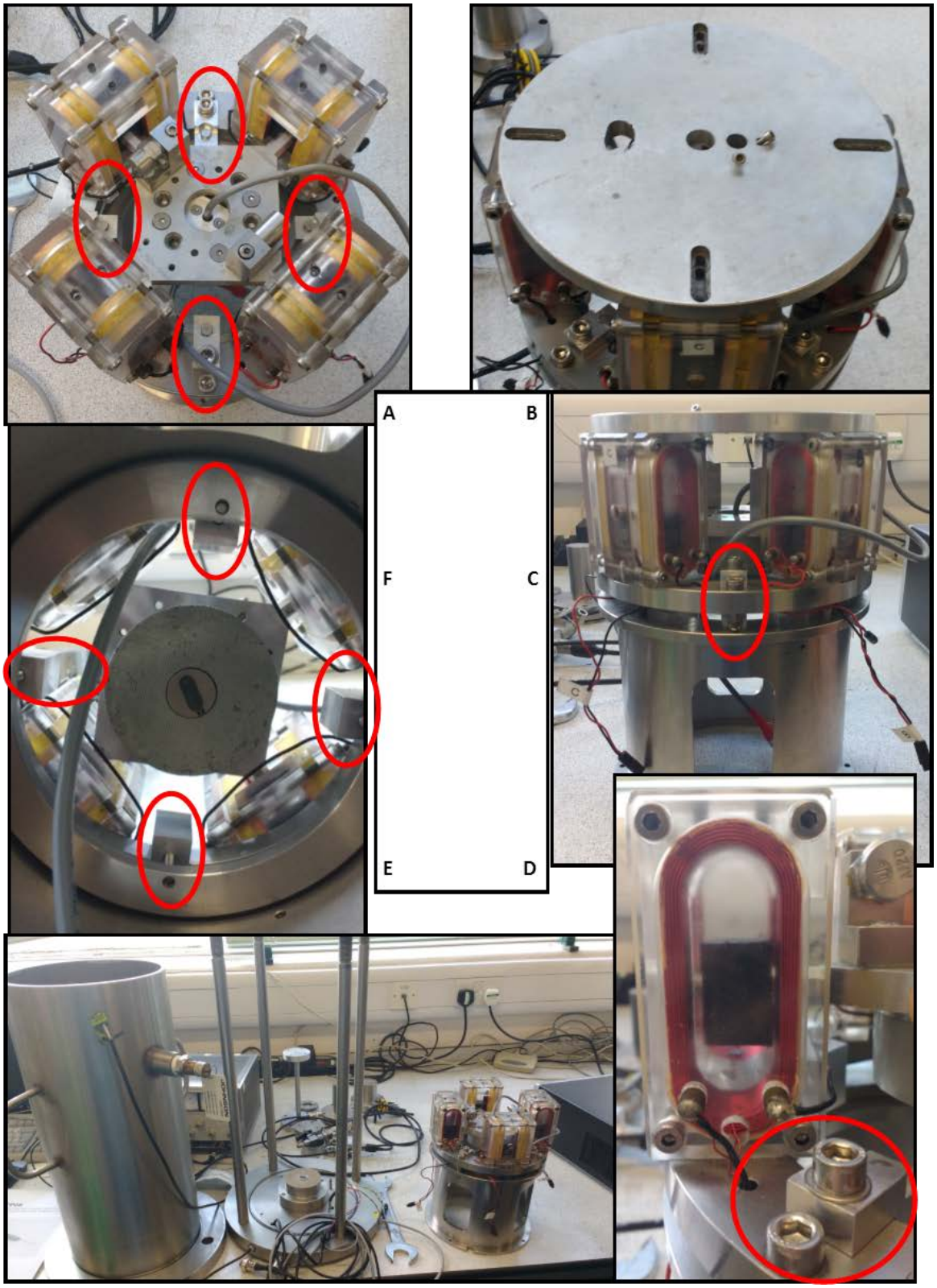

Figure 4.7: The modified RC, showing modification brackets in red. Image A: top view of driveplate without top plate. B: top plate including mount for LVDT. C: Side view of drivehead bolted to support frame. D: Side view of magnet inside coil, embedded in acrylic. E: Left to right – pressure cell, base platen, support cell and drivehead. F: Inside view of top plated with embedded BE.

Considerations for testing on very soft soil

Additional care must be taken when positioning the sample, to ensure the drivehead is sitting perfectly level and central within the electromagnets, as softer soils will consolidate to a greater extent and so be more likely to result in an off-centre drivehead. The drivehead must remain not touching the electromagnet coils for the resonance tests to run successfully. Additionally it may be found that softer samples consolidate so far as to bring the drivehead into contact with the bottom of the electromagnets, any consolidation of more than approximately 6 mm is likely to cause this. In this case the cell should be opened, with the back pressure taps shut, to enable the electromagnet frame to be repositioned.

4.3.2 Theoretical considerations for the resonant column

Torsional vibration and shear wave propagation

The application of different excitation modes propagates different wave types, with the specimen idealised as a solid elastic cylinder. Results from torsional and longitudinal excitation are governed by the wave equation whereas waves from flexure tests are dispersive, with their velocity depending on the frequency of excitation (Kolsky, 1953).

Applying a torsional force allows shear wave speed (V_s) to be measured. The governing equation for a fixed-free apparatus, (Richart *et al.*, 1970) is:

$$\frac{I}{I_0} = \frac{\omega_n L}{V_s} tan \frac{\omega_n L}{V_s} \qquad \text{Equation 4-1}$$

Where I is the mass polar moment of inertia (MPM) of the specimen, I_0 is the MPM of the drive-system, ω_n is the natural circular frequency of vibration of the system and L the specimen length. This assumes the specimen to be completely fixed at the base, and that the drive-system can be idealised as a rigid non-deformable solid mass.

Although the resonant frequency measured in the resonant column is actually the damped natural frequency ω_d it is sufficiently close to the natural frequency ω_n to not give significant errors (Priest, 2004).

Damping in a single degree of freedom system

Two possible methods can be used to determine damping in the resonant column: the logarithmic decrement method from the decay of the free vibration, or through evaluation of the bandwidth

of the peak at resonance using the frequency response function. Both methods assume that the sample can be idealised as a single-degree-of-freedom system subject to viscous damping. The same result should theoretically be found with both methods. In this research the logarithmic decrement method is used.

An example of the free vibration decay method is summarised in Figure 4.8. The system is bought up to the resonance frequency, then the power to the excitation drive system cut and the free–end accelerometer movement recorded as a function of time.

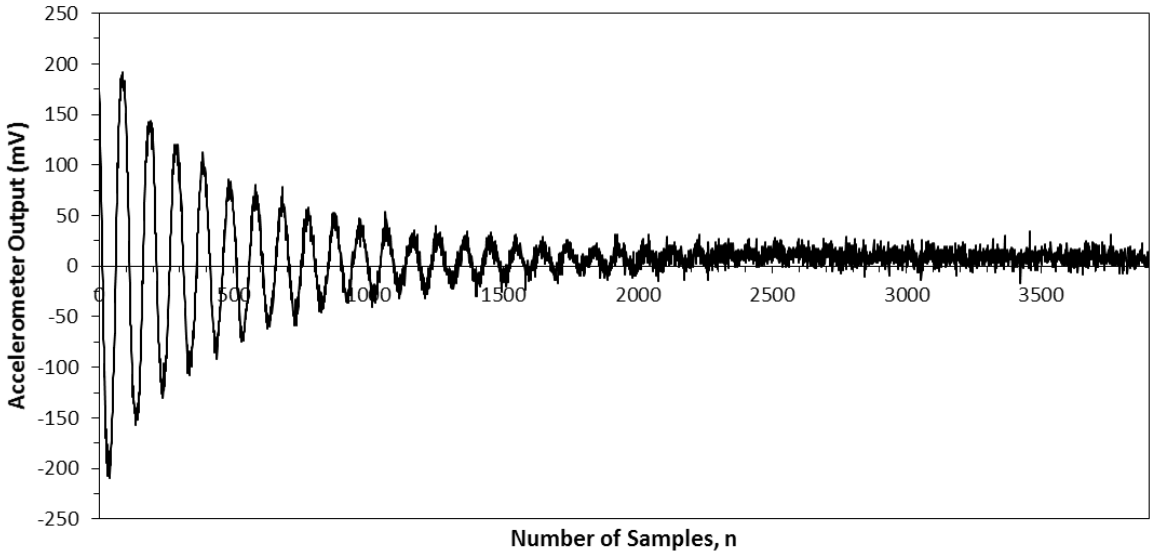

Figure 4.8: Typical free vibration decay plot showing sampling points in detail for a Gravel Hole sample.

The logarithmic decrement (δ) is calculated as follows:

$$\delta = \frac{1}{n} ln \frac{A_1}{A_{1+n}} \qquad \text{Equation 4-2}$$

Where A_1 is the amplitude of vibration for first cycle after the power is cut and A_{1+n} is the amplitude of cycle 1+n of free vibration. The peaks $A_{1,}A_2$ etc are plotted in Figure 4.9. The logarithmic decrement calculation is based upon the decay in amplitude of vibration of any two successive peak amplitudes being a constant ratio (Richart *et al.*, 1970). The damping ratio, D, is derived from the logarithmic decrement as follows:

$$D = \frac{\delta}{\sqrt{(2\pi)^2 + \delta^2}} \qquad \text{Equation 4-3}$$

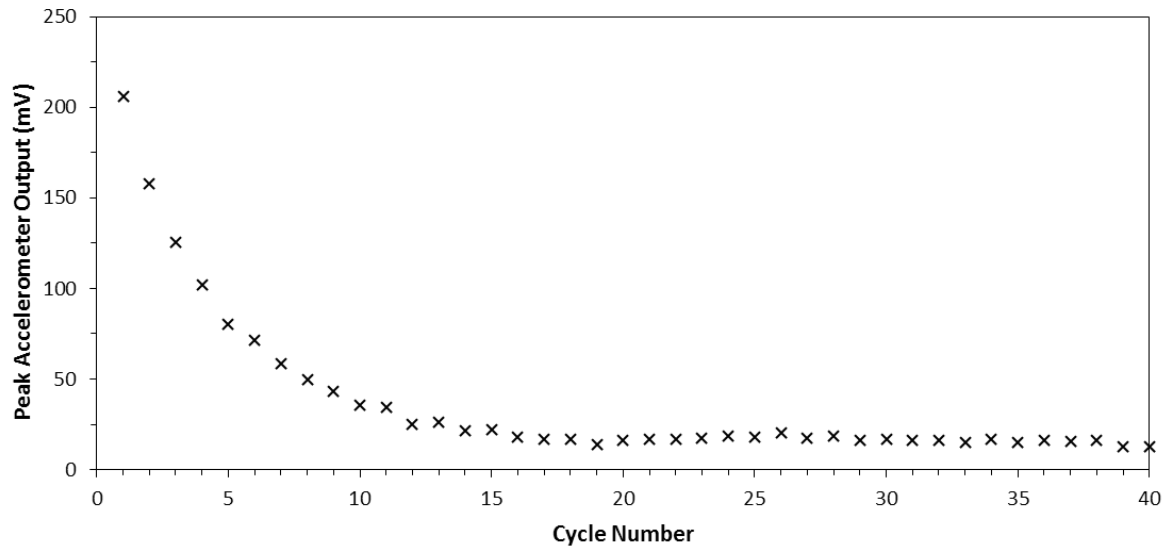

Figure 4.9: Typical free vibration decay plot showing peak accelerometer output per cycle for a Gravel Hole sample.

The half-power bandwidth method, summarised in Figure 4.10 requires data from the accelerometer and the input current at each frequency. A_{max} is the frequency response function amplitude at the resonant frequency f_r , $f_1$and f_2 are the frequencies at $A_{max}/\sqrt{2}$ above and below the resonant frequency. These two points arte equivalent to 3 dB above and below the maximum amplitude, i.e. the half-power points. The damping ratio is found as follows:

$$D = \frac{(f_2 - f_1)}{2f_r} \qquad \text{Equation 4-4}$$

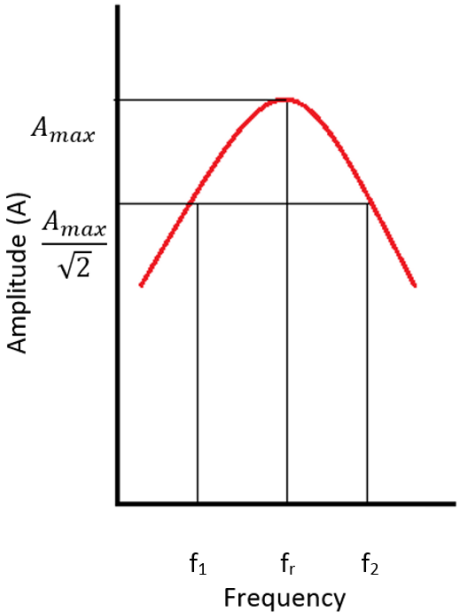

Figure 4.10: Half-power bandwidth method for damping

The damping measured in the RC is a combination of the material damping and the equipment damping. Equipment damping is the term given to the loss of energy in the system caused by the electro-motive force (EMF) induced in the coils. The motion of the magnets moving through the coils, caused by the application of current, induces an EMF in the coils. This EMF is in the opposite direction of the motion of the magnets and so causes a loss of energy in the system, termed back EMF. Several methods have been implemented by various authors to reduce or account for this equipment damping, such as producing correction curves (Laird, 1994; Stokoe *et al.*, 1999), or using a current-mode source rather than the popular voltage-mode source (Cascante *et al.*, 2003; Meng and Rix, 2003).

The drive mechanism to be used in this project was initially designed by Priest (2004), for use in the Gas Hydrate Resonant Column. In the design process several modifications were made to the standard Stokoe design, in order to increase the overall stiffness of the apparatus and to provide better damping measurements. In summary the modifications are:

- Stiffened drive coils, encased in protective acrylic and attached to a support plate at the top,
- Increased driveplate thickness and fixing screw diameter
- Adaptation of the GDS control system to allow all drive coils to be disconnected, to form an open circuit during free vibration decay measurements for damping. This open circuit prevents a back EMF being induced in the coils, meaning the inertial effect that EMF has on the vibrating system is removed. This was shown to substantially reduce the impact of equipment damping on the specimen damping measurements during free-vibration decay.
- Parallel wiring of the coils allows all voltages to be applied at the same time, rather than the small time differences which could occur in the original Stokoe style series wiring.

Consolidation

Consolidation in the resonant column is isotropic, meaning that $\sigma'_1 = \sigma'_2 = \sigma'_3$, as the only external forces applied are the cell pressure and the back pressure. Therefore in the resonant column, the mean principal effective stress p' is equal to the difference between the cell pressure and the pore pressure.

4.3.3 Shear moduli and strain measurement

Measurement of shear modulus

Assuming linear isotropic elasticity and small strains (Hardin and Drnevich, 1972), the shear modulus (G) and Young's modulus (E) can be computed from the measured shear wave speed (V_s) as follows:

$$V_s = \sqrt{\frac{G}{\rho}} \qquad \text{Equation 4-5}$$

$$G = \frac{E}{2(1+\nu)} \qquad \text{Equation 4-6}$$

Where ρ is the specimen density and ν the Poisson's ratio.

RC testing can be used to define the shear modulus at very small strain (G_0) as well as the shear modulus degradation with shear strain. In order to do this, multiple tests are run, with each having a higher applied voltage than the previous. Higher applied voltages result in higher amplitudes of movement and therefore higher strains. Initially the peak frequency is not affected by increasing strain levels, but as shear strain increases the shear stiffness decreases, resulting in the peak frequency of the system reducing, see Figure 4.11. As strain can be calculated from the applied voltage, the accelerometer output and the specimen geometry, the shear modulus vs. shear strain degradation curve can be obtained.

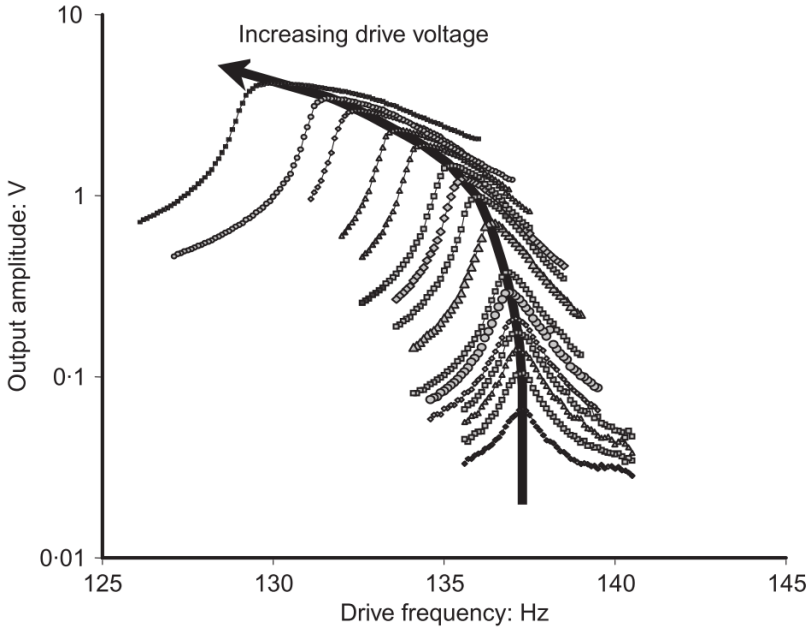

Figure 4.11: Results of Stokoe RC testing on dense Leighton Buzzard sand (Clayton, 2011).

Measurement of torsional strain amplitudes

The magnitude of the resonant frequency, and therefore the shear modulus, is dependent on the shear strain level in the sample during the test. Assuming pure torsion, the shear strain within a cross section is:

$$\gamma = \frac{r\theta}{L} \qquad \text{Equation 4-7}$$

where γ is the shear strain, r is the specimen radius and θ is the angle of rotation, assumed constant along the specimen length (Figure 4.12). At the axis of rotation the strain is zero, increasing to a maximum at the perimeter. ASTM. (2007) states that the average shear strain in the sample occurs at 0.8 r from the centre axis, therefore the average shear strain is:

$$\gamma = \frac{0.8r\theta}{L} \qquad \text{Equation 4-8}$$

The angle of rotation is determined from the accelerometer output, the measured resonant frequency (w_r) and the specimen geometry:

$$\theta = \frac{y}{x} = \frac{Acc}{{w_r}^2 x} \qquad \text{Equation 4-9}$$

Where *y* is the displacement of vibration amplitude, *x* is the distance to the accelerometer from the central axis of the sample and *Acc* is the acceleration amplitude. In the equipment used for this research, *x* was 0.03595 m. The acceleration amplitude is calculated from the accelerometer's peak output. The charge output by the accelerometer is proportional to the drive systems imposed acceleration, that is converted to volts via a charge amplifier. In the equipment used for this research the charge amplifier was set to 15 volts peak to peak output, with the gain set to +/- 2.5 *g* (where *g* is the gravitational constant at the earth's surface). This output is converted to root mean squared voltage (V_{RMS}) by the computer, therefore must be multiplied by $\sqrt{2}$ to be converted to volts. Therefore, the peak accelerometer output, Acc, for this research is:

$$Acc = \frac{\sqrt{2}V_{RMS}}{(15/(2*2.5))}g = 4.62\,V_{RMS} \qquad \text{Equation 4-10}$$

Substituting Equation 4-10 into Equation 4-9, the angle of rotation is:

$$\theta = \frac{Acc}{{w_r}^2 x} = \frac{4.62\,V_{RMS}}{(2\pi f)^2 x} = \frac{3.26\,V_{RMS}}{f^2} \qquad \text{Equation 4-11}$$

Where f is the resonant frequency in Hz. Finally substituting Equation 4-11 into Equation 4-8 the shear strain is:

$$\gamma = \frac{0.8r\theta}{L} = \ 1.30V_{RMS}\, d^2/f^2L \qquad \text{Equation 4-12}$$

Where d is the diameter of the sample.

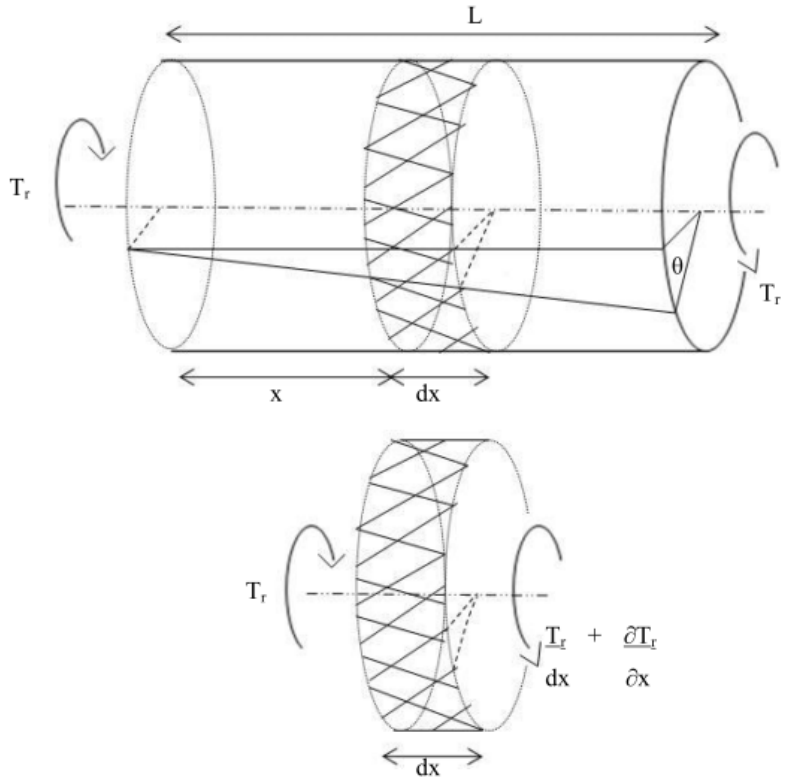

Figure 4.12: Idealisation of wave propagation in a solid elastic cylinder (Otter, 2011).

4.3.4 Resonant column calibration

Calibration of Io

The measured behaviour in the resonant column is a combination of the characteristics of the soil and the apparatus. In order to separate the soil response from that of the apparatus of the mass polar moment of inertia (I_0) of the drive-system must be found. As the drive-system is a complex shape I_0 is best determined through calibration testing of samples with known properties. Aluminium bars (Figure 4.13) are normally used to calibrate as they have known uniform geometric properties and stiffness (Priest et al., 2005; Clayton et al., 2007; Otter, 2011).

For a sample length of approximately 140 mm, typical torsional frequency results are 17 Hz to 25 Hz for soft clay soil (Hardin and Drnevich, 1972) and up to 400 Hz for stiff cemented sands (Avramidis and Saxena, 1990) whilst Cascante et al. (1998) found silica sand to have a flexural resonance frequency of 50 Hz to 100 Hz. The standard aluminium calibration bars have torsional

frequencies of 60 Hz to 270 Hz (Kirby, 2011). Therefore a range of aluminium bars exist which cover most frequencies found in soil samples.

As the samples to be tested in this research were expected to have a low stiffness, and therefore a low resonant frequency, calibration was focused on the use of low stiffness bars. This involved the use of two aluminium bars, one brass bar and one nylon bar, which were produced for previous RC calibration work (Priest, 2004).

I_0 is determined through modelling the sytem as a torsional pendulum with a single degree of freedom (Priest, 2004; Clayton *et al.*, 2007). The calibration bar is idealised as a torsional spring of stiffness k, and the drive-system as a single mass, therefore:

$$\omega_n = \sqrt{\frac{k}{I_o}} \qquad \text{Equation 4-13}$$

where ω_n is the natural circular frequency of the calibration bar. The resonant frequency of the bar is then measured, and additional masses (I_{am}) are added to the drive mechanism. The new resonant frequency is determined for each combination of bar and added mass. Three additional masses were used for each bar, leading to Equation 4-13 becoming:

$$I_{am} = \frac{k}{\omega_n^2} + I_O \qquad \text{Equation 4-14}$$

I_{am} is plotted against $1/\omega_n^2$ for each calibration bar (Figure 4.14). The intercept on the y-axis is given by I_O and k by the gradient of the best fit line. Figure 4.15 shows I_O to vary with frequency, and therefore with bar stiffness. This was also found by Priest (2004); Bui (2009); Rees (2009) and (Otter, 2011). As the derived value of I_O is used to determine the stiffness of the bar in Equation 4-13, the increasing value of I_O is not accounted for.

In order to reduce this dependency the known material properties of the aluminium bars can be used to produce a regression equation allowing an I_O value corresponding to a measured frequency to be calculated.

The torsional governing equation, Equation 4-1, is used, with values of ω_n found from testing the four calibration bars.

$$\frac{I}{I_x} = \frac{\omega_n L}{V_s} \tan \frac{\omega_n L}{V_s} \qquad \text{Equation 4-15}$$

Where I is the mass polar moment of inertia (MPM) of the specimen – in the case of calibration the bar stem, I_x is the MPM of the drive-system (in this case the drivehead, top cap and bar top platen) ,ω_n is the natural circular frequency of vibration of the system, equal to 2πf where f is the

measured frequency in Hz , L= specimen (bar stem) length and V_s is the shear wave velocity of the specimen (aluminium bar stem). I_i is the MPM of a cylindrical component i :

$$I_i = \frac{md_i^2}{8} \qquad \text{Equation 4-16}$$

Where m_i is the mass and d_i is the diameter of the component i.

V_s is calculated using Equation 4-6. As aluminium, the bar density (ρ) is taken as 2700 kgm^{-3} , Young's modulus as $69x10^9$ Pa and shear modulus (G) as $25.9x10^9$ Pa (Mondolfo, 1976).

Substituting calculated and measured values into Equation 4-15 produces values for I_x in relation to the bars resonant frequency. I_0 is simply the subtraction of the MPM of the bar top platen from I_x (Equation 4-17):

$$I_0 = I_x - I_{bar\ top\ platen} \qquad \text{Equation 4-17}$$

A plot of I_0 vs. frequency provides a calibration curve for future testing Figure 4.15, the equation of which is presented on the figure. The calibration bar shear modulus can be back calculated from these values, and compared to the theoretical value, giving an error of between 0.12 % and 0.58 %. This discrepancy has been shown to be caused by equipment compliance issues, such as specimen fixity, support frame fixity and drive mechanism fixity (Clayton *et al.*, 2007). However, the value of the errors measured in this calibration are so low that it can be assumed no compliance issues have been introduced as a result of the equipment modifications discussed previously.

Figure 4.13: Standard aluminium calibration bars.

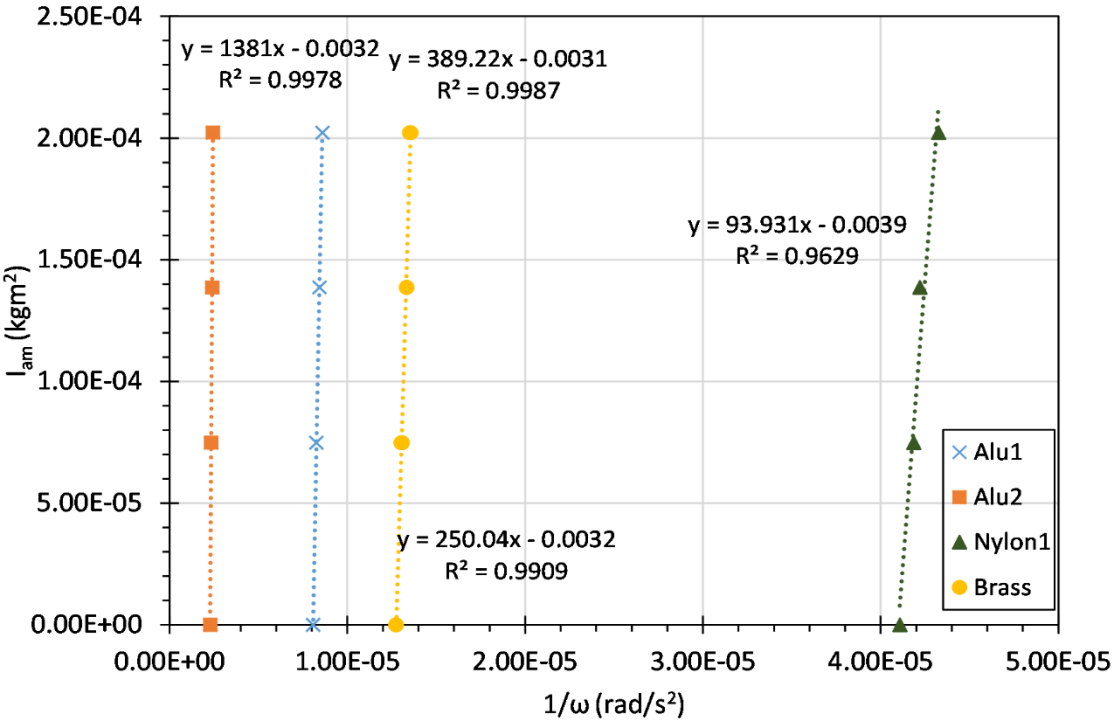

Figure 4.14: Single degree of freedom calibration for RC

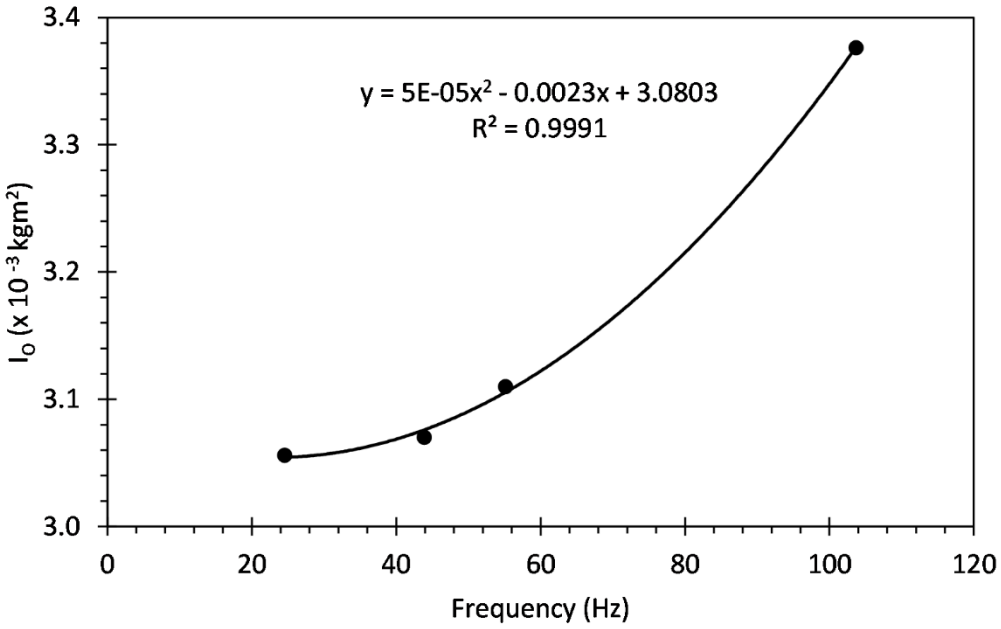

Figure 4.15: Single degree of freedom calibration for RC I_O using regression analysis.

Calibration of pressure and displacement transducers

A GDS STDDPC pressure controller was used to apply back pressure. Pressure transducers fitted at the cell level were used to measure pore pressure (water) and cell pressure (air). All pieces of pressure equipment were calibrated using a 580 series hydraulic Budenberg dead weight calibration machine, from 1 kPa to 700 kPa.

A LVDT (linear variable differential transformer) was attached to the top plate of the RC, to measure sample consolidation during testing. This was calibrated using a micrometer.

4.3.5 Resonant column test procedure

Apparatus assembly

Following specimen preparation to the required dimensions and particle sizes, see Section 4.7, the specimen was transferred onto the RC base platen, and the top platen added. Small pieces of fine grade filter paper were applied to the parts of the sample base that would sit over the pore pressure holes in the base plate. Initial measurements of height and diameter, at several positions, were then taken. The use of dental plaster to secure the specimen was not deemed necessary.

A radial drain filter paper was wrapped around the outside of the specimen, to speed consolidation, which was followed by a latex membrane (Figure 4.16). Silicon grease was used between the membrane and the end platen to ensure an airtight seal. Measurements were then repeated. Next narrow strips of foil were wrapped around the specimen, overlapped at their joints with silicon grease added. This method was used to minimise gas diffusion into the sample from the surrounding air cell pressure. The overlapping and use of grease ensured the specimen was free to expand or contract (Ghiassian and Grozic, 2013). A second latex membrane was then added (Kim and Novak, 1981), with several o-rings being places over both end platen.

The support column and drive head was then carefully positioned and the column bolted to the base of the cell. Next the drivehead was positioned, ensuring it was centred on the top cap, the magnets aligned within the coils, both horizontally and vertically and the top cap bolts fitted. The accelerometer was connected, followed by the coil-stiffening top plate being attached. The LVDT was then clamped in place through the top plate, the BE and power wires connected, the cell put in place and sealed.

Figure 4.16: RC sample assembly - radial drain followed by latex membrane, greased foil strips and a second latex membrane.

Test procedure

The following procedure was carried out for all samples, after the apparatus was assembled:

- Completion of a saturation stage – raising back pressure and cell pressure concurrently, ensuring cell pressure was greater than back pressure by at least 5 kPa, until the desired back pressure was reached. The sample was left to saturate at these pressures until back volume changed ceased and a B check showed saturation was complete (Skempton, 1954; British Standards Institute, 1990b).
- Completion of first consolidation stage – increasing the cell pressures until the desired effective stress was reached for the first test pressure, while holding the back pressure to measure the change in sample volume. The amount of volume change was monitored and used to calculate an estimate of the specimen radius at any point, in conjunction with the axial LVDT measurements. When axial displacements ceased and further back volume changes were extremely small, the consolidation stage was considered complete.
- Completion of BE test – shear and compressional waves excited across a range of input strains, with the resulting wave speeds recorded.
- Completion of resonance tests – starting with the smallest applicable voltage, a broad sweep test was performed to define the approximate resonance peak. This was followed by a fine sweep to measure the frequency to within 0.1 Hz. The input and output strain were recorded, as well as the resonant frequency. The fine sweep was then repeated at the next input voltage, and continued until the resulting resonant frequency began to change. From this point onwards, after each increase in applied voltage the resonant

frequency at the smallest applicable voltage was re-measured. If this value did not change then testing proceeded to the next increase in applied voltage. When the re-measured low strain value began to reduce testing was stopped at that pressure. This process was carried out for both torsional and flexural measurements, although only torsional measurements are discussed in this report.

- Completion of damping measurements – both flexural and torsional damping measurements were taken using the free decay method, repeated three times for each.
- Additional consolidation, resonance and damping stages were then followed until testing at all desired pressures had taken place.
- After the testing at the final pressure, the RC was dissembled with the back pressure valve shut. Sample dimensions were measured both with and without membranes, and the final density and moisture content measured.

4.3.6 Assumptions

The equations of motion from which parameters are derived from resonant column tests make several assumptions, including that the apparatus behaves as a single-degree-of-freedom system, and that during resonance only the sample and attached devices vibrate. Under torsional excitation it is assumed that plane transverse sections of the rod remain plane as stress waves travel through them, with any rotation occurring horizontally around the longitudinal sample axis. Assuming no other deflection or vibration mode is induced and that stress acts uniformly across the cross-section of the specimen then measurements can be made anywhere on the drivehead (Clayton *et al.*, 2007). The wavelengths of the stress waves must also be larger than the bar diameter to ensure they travel down it without dispersion (Kolsky, 1953).

In soil samples the physical formation of the specimen and the varying voids within it mean the stress does not act uniformly. Care must also be taken to consolidate samples before testing, as it is assumed no consolidation occurs due to the testing vibrations. It is also necessary that the confinement of the specimen is higher than the axial stress induced to ensure no tension is applied to the specimen.

In order for a RC test to be deemed non-destructive, and so to allow several measurements to be made, e.g. at a variety of stress states, the recorded strain amplitudes must be less than 10^{-4} rad (ASTM., 2007).

4.4 The triaxial machine

4.4.1 Overview and adaptations

The triaxial machine is one of the most commonly used pieces of geotechnical laboratory equipment. A triaxial machine can apply isotropic (cell) pressure to a specimen, as well as a back pressure and an additional axial pressure from a ram load (see Figure 4.17). There are several key stages to most triaxial tests – saturation, consolidation and shearing. The shearing may be a small probing test, designed to cause recoverable deformation of the specimen, or a large shear that is destructive.

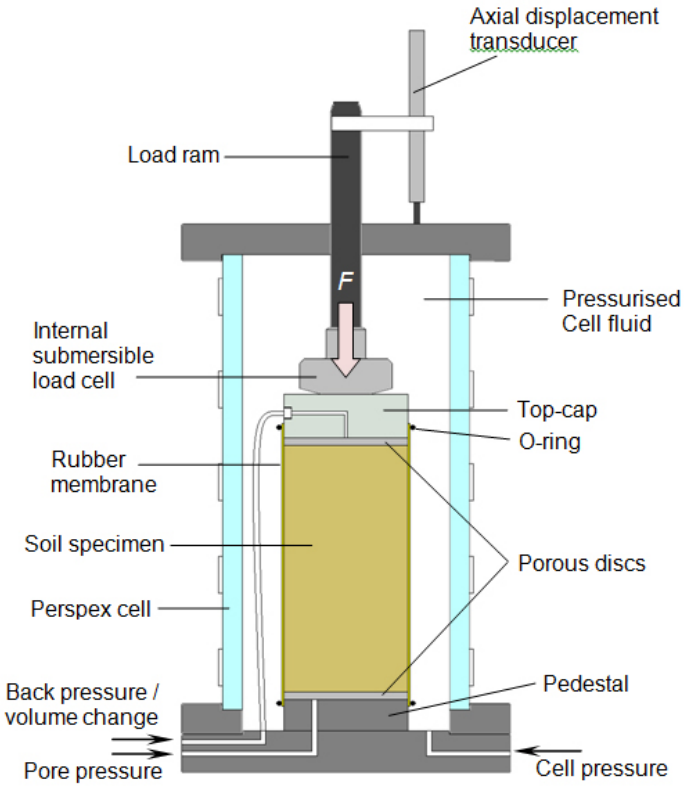

Figure 4.17: Typical triaxial machine setup (Rees, 2016)

Three main forms of triaxial testing exist, each being used for separate purposes. The fastest and simplest triaxial test is the unconsolidated undrained test, which tends to be performed on cohesive soils. The specimen is loaded with only total stresses controlled and recorded, allowing the undrained shear strength C_U to be determined. The second test is the consolidated drained test, which can take a long time to complete testing due to the drained conditions. This test allows effective stress control, with strength parameters such as those within the critical state framework to be defined. The final test form, consolidated undrained, allows the same parameters as in consolidated drained testing to be defined, but at a faster shearing rate and

therefore a faster test time. This is because the pore pressure change inside the specimen is recorded during shearing.

Consolidated drained testing was carried out to measure the shear modulus degradation curve with strain, which can be compared to the results of the RC for similar strains. Horizontal bender elements were also fitted, to measure the horizontal modulus.

Strain measurement

Axial strains were measured globally, using a large scale LVDT on top of the cell, which monitors the deformation of the whole sample. Local axial strains were measured using two small scale LVDTs positioned on opposite sides of the sample, across its centre line. Radial strains were measured using a small scale local radial LVDT, attached to a radial belt which was glued to the sample membrane with two hinges. This measured the radial deformation about the centre line. The three local LVDTs, in addition to the horizontal bender elements, are shown in Figure 4.18

Figure 4.18: LVDT and bender elements (blue) set up on triaxial specimen.

4.4.2 Derivation of parameters

In triaxial testing the stress variables used are the mean effectives stress, p', and the deviator stress, q. They are related to the vertical and horizontal effective stresses, σ_v' and σ_h' by:

$$\begin{bmatrix} p' \\ q \end{bmatrix} = \begin{bmatrix} 1/3 & 2/3 \\ 1 & -1 \end{bmatrix} \begin{bmatrix} \sigma_v' \\ \sigma_h' \end{bmatrix} \quad \text{Equation 4-18}$$

The corresponding strain variables are the volumetric strain ε_p and the distortional strain ε_q. They are related to the vertical and horizontal strains, ε_v and ε_h , referred to as $\varepsilon_a$and ε_r respectively during this triaxial testing, as follows:

$$\varepsilon_q = \frac{2}{3}(\varepsilon_a - \varepsilon_r) \quad \text{Equation 4-19}$$

$$\varepsilon_p = \varepsilon_a + 2\varepsilon_r \quad \text{Equation 4-20}$$

A full description of a cross-anisotropic elastic material required five independent parameters:

$$\begin{bmatrix} \delta\varepsilon_{xx} \\ \delta\varepsilon_{yy} \\ \delta\varepsilon_{zz} \\ \delta\gamma_{yz} \\ \delta\gamma_{zx} \\ \delta\gamma_{xy} \end{bmatrix} = \begin{bmatrix} \frac{1}{E_h} & \frac{-\nu_{hh}}{E_h} & \frac{-\nu_{vh}}{E_v} & . & . & . \\ \frac{-\nu_{hh}}{E_h} & \frac{1}{E_h} & \frac{-\nu_{vh}}{E_v} & . & . & . \\ \frac{-\nu_{vh}}{E_v} & \frac{-\nu_{vh}}{E_v} & \frac{1}{E_v} & . & . & . \\ . & . & . & \frac{1}{G_{hv}} & . & . \\ . & . & . & . & \frac{1}{G_{hv}} & . \\ . & . & . & . & . & \frac{2(1+\nu_{hh})}{E_h} \end{bmatrix} \begin{bmatrix} \delta\sigma'_{xx} \\ \delta\sigma'_{yy} \\ \delta\sigma'_{zz} \\ \delta\tau_{yz} \\ \delta\tau_{zx} \\ \delta\tau_{xy} \end{bmatrix} \quad \text{Equation 4-21}$$

where ε_{xx} and ε_{yy} are horizontal direct strain, ε_{zz} is vertical direct strain, σ'_{xx} and σ'_{yy} are effective horizontal stress, σ'_{zz} is effective vertical stress, γ_{yz} and γ_{zx} are the shear strain in the vertical plane, γ_{xy} is the shear strain in the horizontal plane, τ_{yz} and τ_{zx} are the shear stress in the vertical plane, τ_{xy} is the shear stress in the horizontal plane, E_h is the horizontal Young's modulus, E_v is the vertical Young's modulus, ν_{hh} is the horizontal to horizontal Poisson's ratio, ν_{vh} is the vertical to horizontal Poisson's ratio, ν_{hv} is the horizontal to vertical Poisson's ratio and G_{hv} is the vertical shear modulus.

A triaxial test carried out on a cross-anisotropic soil cannot apply shear stresses, or measure shear strains, hence only the top left-hand corner of the compliance matrix Equation 4-21 can be investigated (Lings *et al.*, 2000). For triaxial cell conditions $\delta\varepsilon_{xx} = \delta\varepsilon_{yy} = \delta\varepsilon_h$ and $\delta\sigma'_{xx} = \delta\sigma'_{yy} = \delta\sigma'_h$, therefore Equation 4-21 can be simplified to:

$$\begin{bmatrix}\delta\varepsilon_v\\ \delta\varepsilon_h\end{bmatrix}=\begin{bmatrix}\frac{1}{E_v} & \frac{-2\nu_{vh}}{E_v}\\ \frac{-\nu_{vh}}{E_v} & \frac{1-\nu_{hh}}{E_h}\end{bmatrix}\begin{bmatrix}\delta\sigma'_v\\ \delta\sigma'_h\end{bmatrix} \quad \text{Equation 4-22}$$

A combination of Equation 4-19, Equation 4-20 and Equation 4-22, with the addition of F_h, the horizontal modulus, allows a complete description of the soil behaviour to be written in terms of G' K' and J':

$$F_h = \frac{E_h}{1-\nu_{hh}} \quad \text{Equation 4-23}$$

$$E_v = \frac{9G'K'J'}{6G'K' + G'J' + 3K'J'} \quad \text{Equation 4-24}$$

$$\nu_{vh} = -\frac{1}{2}\frac{3G'K' + 2G'J' - 3K'J'}{6G'K' + G'J' + 3K'J'} \quad \text{Equation 4-25}$$

$$F_h = \frac{-18G'K'J'}{12G'K' - 4G'J' - 3K'J'} \quad \text{Equation 4-26}$$

where J' is a coupling modulus parameter (Graham and Houlsby, 1983) ; K' is a bulk modulus parameter and G' is a shear modulus parameter (Atkinson *et al.*, 1990).

In constant p' (drained) stress probes, the shear modulus, G' is evaluated as follows:

$$G' = \frac{1}{3}\left(\frac{\delta q}{\delta\varepsilon_q}\right)_{\delta p'=0} \quad \text{Equation 4-27}$$

In constant q (drained) stress probes, K' and J'_{pq}can be evaluated from:

$$K' = \left(\frac{\delta p'}{\delta\varepsilon_p}\right)_{\delta q=0} \quad \text{Equation 4-28}$$

$$J' = \left(\frac{\delta p'}{\delta\varepsilon_q}\right)_{\delta q=0} \quad \text{Equation 4-29}$$

In constant p (undrained) stress probes, the shear modulus, G* is evaluated as follows:

$$G^* = \frac{1}{3}\left(\frac{\delta q}{\delta\varepsilon_q}\right)_{\delta p=0} \quad \text{Equation 4-30}$$

where G* is an undrained shear modulus parameter (Graham and Houlsby, 1983). Horizontal bender elements fitted to the triaxial sample allow measurement of G_{hv}. Some work, e.g. Coop *et*

al. (1997) has tried to show continuity between the dynamic G_{hv} and the static G* measurements. This is unlikely, as if the soil is anisotropic the two parameters are independent (Lings *et al.*, 2000).

4.4.3 Triaxial calibration

GDS advanced pressure controllers were used to apply back and cell pressure. Pressure transducers fitted at the cell level were used to measure pore pressure, cell pressure and back pressure. All pieces of pressure equipment were calibrated using a 580 series hydraulic Budenberg dead weight calibration machine, from 1 kPa to 700 kPa. This equipment was also used to calibrate the 5 kN load cell. All LVDTs were calibrated using a micrometer, across their target measurement range.

4.4.4 Triaxial test procedure

The test methods set out in BS 1377-8:1990 (British Standards Institute, 1990b) were followed.

- Completion of a saturation stage – raising back pressure and cell pressure concurrently, ensuring cell pressure was greater than back pressure by at least 5 kPa, until the desired back pressure was reached. The sample was left to saturate at these pressures until back volume changed ceased and a B check showed saturation was complete (Skempton, 1954; British Standards Institute, 1990b).
- Completion of first consolidation stage – increasing the cell pressure and ram load until the desired stress conditions were reached for the first test pressure, while holding the back pressure to measure the change in sample volume. When axial displacements ceased and further back volume changes were extremely small, the consolidation stage was considered complete. The radial LVDT was monitored during consolidation, to ensure no radial strains occurred.
- Drained constant p' probe cycle and constant q probe cycle completed. Probe size was adjusted according to sample strength. Time for the sample to regain equilibrium was given between probes.
- Undrained constant p probe cycle and constant q probe cycle completed.
- Horizontal bender element tests carried out
- Consolidation to next test pressure carried out, and all stages repeated until all probes at all test pressures were complete
- Final large shear carried out, to a target axial strain of 15 %, at a rate of 0.5 % strain per hour (Gasparre, 2005).

Consolidation

Two types of consolidation method are possible in the triaxial. Samples can be consolidated isotropically, as in the resonant column, with simply an effective cell pressure applied, or with addition axial load, allowing the in-situ conditions to be better replicated. This is known as K_O consolidation, as it involves estimating the in situ earth pressure coefficient of the soil, K_O, to ensure no radial strains are developed during consolidation.

4.5 Bender elements

4.5.1 Theory and past use

The used of BEs to measure G_O is a method first presented by Shirley and Hampton (1978). A BE is a piezo-electric transducer which generates a voltage as it bends, or conversely bends as voltage is applied to it. By placing BEs at either end of a soil specimen a transmitter-receiver set-up is produced. The transmitter element is excited by an input waveform voltage from a function generator, which bends the element, forcing a shear wave to propagate through the soil specimen. This wave bends the receiving element upon arrival, which generates an electrical waveform signal that can be displayed by a digital oscilloscope. This allows the time for the wave to pass the length of the specimen to be recorded. As G_O is a function of the shear-wave speed, it can then easily be deduced from the recorded time and distance between the elements. An example BE set-up within a triaxial cell is shown in Figure 4.19.

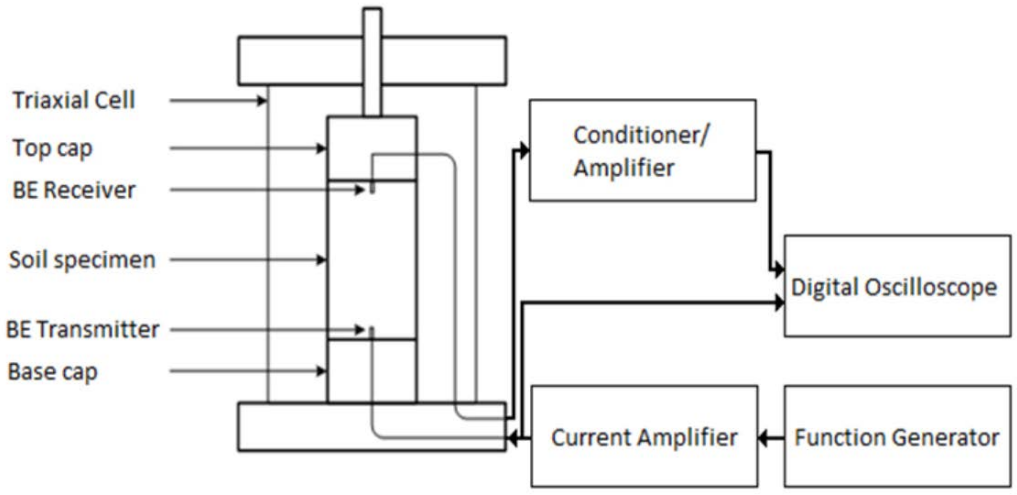

Figure 4.19: Typical BE set-up within a triaxial cell (Camacho-Tauta *et al.*, 2012).

Testing with BEs is a very flexible technique, as it can be set up inside many existing pieces of laboratory equipment. For example, in the case of the RC, the specimen top and bottom caps

require little modification. It is also non-destructive, allowing many tests to be carried out on the same specimen. The BEs installed within the RC end caps for this research are shown in Figure 4.7.

Since the 1980's several authors have tested BEs alongside RCs to assess the validity of BEs as a technique. Dyvik and Madshus (1985) , for example, found the results from the two techniques to agree well when measuring G_O for several clays. Since then the use of BEs together with RCs, as well as with other techniques, has steadily increased. Horizontal BEs are also fitted to the sample in the triaxial cell, Figure 4.18, to allow measurement of G*, the horizontal modulus.

The key parameters in the accuracy of the resulting wavespeed value are the distance of wave travel, and the time measurement. The distance is generally taken to be the distance between the tips of the two BEs. However, determining the arrival wave (and therefore time) at the receiving element is fairly subjective and this has been considered by many authors. The importance of this is compounded by the generally small sample size to which BEs are fitted, leading to the magnification of errors in distance or time measurements.

Proposed methods for determining wave travel time include arrival time of the first output inflection (Start-to-Start), the arrival of the first peak (Peak-to Peak) and a cross-correlation method, which assesses the position of the maximum amplitude of the output and input signals. The start-to-start method looks for the time (t_0) between the start of the source signal and the start of the major cycle of the receiver signal. It is necessary to ignore the initial arrival of the signal which often contains a weak cyclic movement, before the main first movement arrives. In the peak-to-peak method the travel time is taken to be that between the peak of the source signal and the first peak of the receiver signals first main cycle. A common cross-correlation method is that of Viggiani and Atkinson (1995), which uses the function $CC_{yx}(\tau)$ to measure the correlation between the receiver signal, $X(t)$, and the source signal, $Y(t)$, versus the time shift(τ):

$$CC_{yx}(\tau) = \lim_{T\to\infty} \frac{1}{T} \int_T X(t)Y(t+\tau)dt \qquad \text{Equation 4-31}$$

Where T is the total duration of the time record of the test.

An example of all three time determination methods is presented in Figure 4.20.

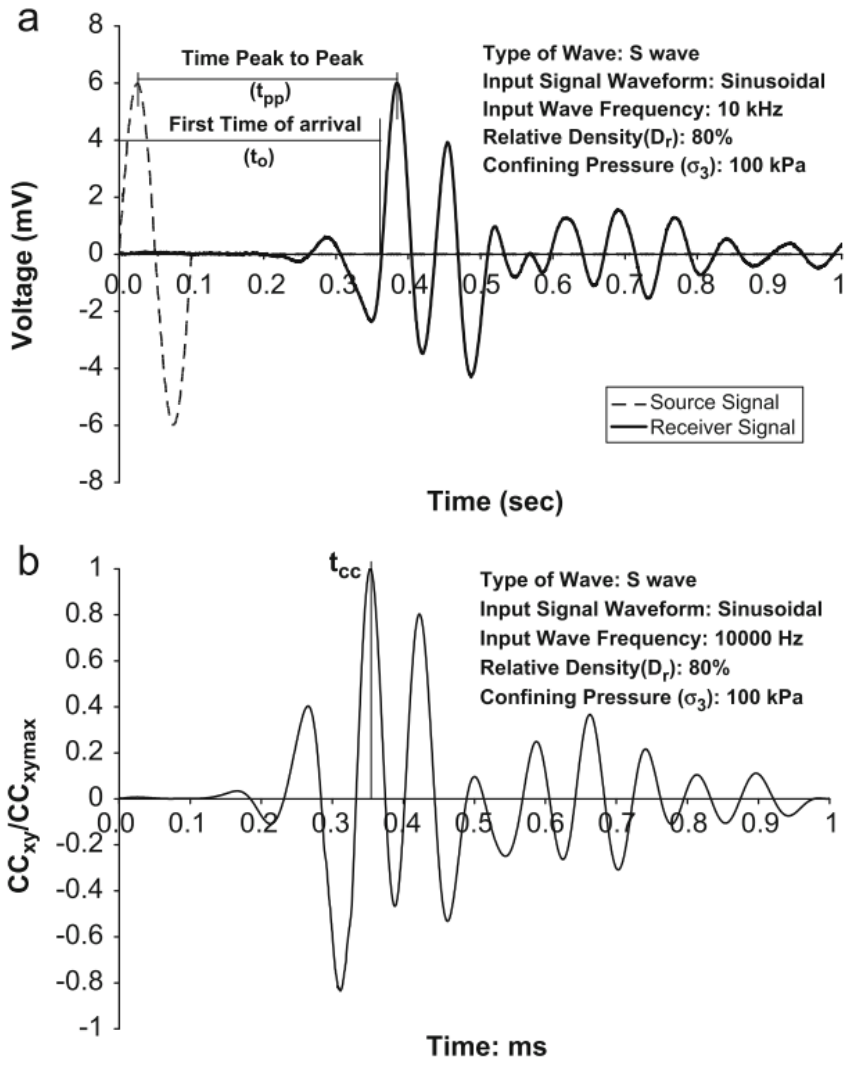

Figure 4.20: An example of start-to-start (time of first arrival) ,peak-to-peak and cross-correlation measurement methods for BE signals (Kumar and Madhusudhan, 2010).

Many authors (including Viggiani and Atkinson, 1995; Arulnathan *et al.*, 1998; Lee and Santamarina, 2005; Leong *et al.*, 2005) have analysed the validity of the various measures. A review of the international interpretation of G_O using BEs (Yamashita *et al.*, 2009) suggested that the most consistent methods of travel time determination are the start-to-start and peak-to-peak methods. Kumar and Madhusudhan (2010) found the values of G_O to compare well between RC and BE measurements using the peak-to-peak and cross-correlation methods.

Another investigative study, (Youn *et al.*, 2008) used clean sand to compare RC and BE techniques, as unlike in cohesive soils, G_O does not tend to increase with frequency (Iwasaki *et al.*, 1978; Kim, 1991). BEs were inserted into a Stokoe RC and two types of sand were tested, each in both dry and saturated conditions. The strain range used, which can be adjusted via the excitation voltage, fell below the elastic threshold strain (< 10^{-3} %). A variety of methods of wave travel time were

investigated, through comparison of numerical and experimental results, as well as by comparing shear wave speed values obtained by BE and RC methods, with the tests and models covering a frequency range of 0.1 Hz to 10,000 Hz. It was concluded that the most preferable input wave form is that of a sine wave, rather than a square wave. This coincides with the findings of authors such as Yu and Richart (1984) and an international test on BE interpretation (Yamashita *et al.*, 2009). For all dry sand specimens very good agreement was found for the shear wave speed between the RC and BE methods.

It should be noted that, even when a single method is used, the results are highly subjective to the experience and view of the person deciding upon which peak to use. In his Rankine lecture Clayton (2011) presented the range of resulting shear wave velocities produced when four independent engineers were asked to estimate start-to-start and peak-to-peak travel times for a set of matching data. The resulting variation in shear modulus for start-to-start estimates ranged between ± 5.4% for a 10 kHz signal and ± 15.4% for a 2.5 kHz signal. The additional use of the cross-correlation method can be used to counter-act some of the human error within BE testing.

BEs also provide a useful tool for comparison with the results of wave speed measurements in the standard RC. They have already been used in producing a parameter set for the critical velocity site Ledsgård in Sweden, in conjunction with a cyclic triaxial machine and various seismic wave analysis methods (Kaynia *et al.*, 2000).

4.5.2 General test procedure

Due to a lack of official testing standard, the recommendations of Clayton (2011) were followed. These include:

- The use of multiple wave travel time methods. Both peak-to-peak and first-arrival methods will be used. If these methods do not compare well then the cross-correlation method will be applied.
- Limiting the lowest permissible amplitude signal-to-noise ratio to 10
- Limiting the sample time to less than 1/100th of the travel time between transmitter and receiver

4.6 Additional laboratory techniques

4.6.1 Transport, storage and logging of window samples from field work

After extraction of the cores from the site, each plastic sample tube had its end caps sealed, using a combination of wax, cling-film and tape, to maintain moisture content. Sample tubes were marked clearly with sample origin, depth and orientation. The tubes were stored within a robust container that did not allow them to move around during transport, and cushioned them from large vibrations, and stored in a temperature controlled room after transportation.

In the laboratory, each tube was logged using the following process:

- Tube ends removed, and casing split along length, using specialist core cutter knife to prevent blade digging into sample.
- Whole sample photographed, including orientation and depth from which it came.
- Whole sample length visually examined for changes in soil type
- Full soil description carried out along sample length, with sections for testing, of at least 160 mm, left undisturbed, and other sections used for fall cone Cu testing, density ring testing and general soil classification examination including gravimetric moisture content.

To protect the sample and maintain moisture content, each sample selected for future testing was re-enclosed in a section of the split sample tubing, which had been cut to length, sealed in wax at the joints and the ends, and wrapped in alternating layers of cling film and foil. Care was taken to ensure sample orientation remains known. Samples were stored in a temperature controlled room.

This methodology is based upon the British Standards for soil identification and classification (British Standards Institute, 2018a;b).

4.6.2 Additional index testing

Liquid and plastic limits

Also known as Atterberg limits, this involved two simple tests to determine both the liquid and plastic limits of remoulded samples of cohesive materials. The plastic limit (ω_P) tests involved rolling a soil sample with the tips of the fingers on a glass plate, and finding the moisture content at which longitudinal and transverse cracks appear at a rolled diameter of 3 mm. The liquid limit (ω_L) is defined as the moisture content at which, using a cone penetrometer, a cone penetration of 20 mm is achieved. From these values the plasticity index (I_P) can be found:

$$I_P = \omega_L - \omega_P$$ Equation 4-32

These values are used to classify soils for comparison against test data from other similar soils. Further details can be found in BS1377-2 (British Standards Institute, 1990a).

Undrained shear strength

Estimates of the undrained shear strength of the sample were made using a fall cone test. This involved measuring the penetration of a cone of known geometry and weight into the sample. The relevant test standard is ISO 17892 (ISO., 2017). The undrained shear strength of the undisturbed specimen in its tested state (C_{ufc}) in kPa is:

$$C_{ufc} = cg\frac{m}{i^2}$$ Equation 4-33

Where c is a factor, equal to 0.8 for a 30° cone, g is the gravitational constant equal to 9.81 ms^{-2}, m is the mass of the cone in grams and i is the average cone penetration in mm for the sample.

As these measurements were taken against the cut face of the undisturbed samples, rather than to samples which have been reconstituted into cone test cups, the strength parameters may not be as reliable. They do however provide a useful method for identifying the depths at which soil strengths change within the boreholes.

Organic content testing

A selection of samples that were believed to have a significant organic content were tested, following the procedure set out in BS EN 12879 and BS EN 13039(British Standards Institute 2000a;b). The basic procedure is to select several representative samples from each soil of interest, which are placed within crucibles, with the initial moisture content measured. Each crucible is dried in a 105 °C oven, before the moisture content is re-measured. This provides a measurement of the total solids and total water content. The crucibles are then places within a high-temperature (450°C) furnace, which causes the volatile (organic) solids to ignite. This allows calculation of the organic solids of the original material, by weight.

4.7 Sample preparation

For the RC ASTM guidelines (ASTM, 2007) on specimen size were followed. The key parts of the guidelines are: a specimen diameter of 35 mm or greater, a specimen length to diameter ratio of between 2 and 3, and a largest particle size of less than 1/10th of specimen diameter, except when specimen diameter is 70 mm or greater in which case largest particle to be less than 1/6th

of specimen diameter. All site samples therefore required a diameter of 70 mm and a height of between 140 mm and 210 mm, with a largest particle size of 11.7 mm.

For the triaxial machine the same specimen size requirements as specified above for the RC were followed, to maintain the level of comparability between tests. For each sample the following data was recorded: a visual description and the origin of soil, the soil state - undisturbed or remoulded, the specimen preparation procedures, the initial and final specimen mass, the specimen dimensions, the void ratio, the moisture content from a representative sample of specimen cuttings and the degree of saturation. Each specimen was trimmed to size, removing the outer disturbed material, using a thin sharp blade, with the sample site orientation maintained.

Chapter 5 Gravel Hole Case Study Site

5.1 Site background and stratigraphy

Background

Gravel Hole is a case study site operated by Network Rail on the UK classic network (the West Coast Main Line). It was found to experience large track displacements following an increase in line speed from 160 km/h to 200 km/h, forcing the imposition of a speed restriction across the site. Mixed rolling stock uses the line, with the fastest trains being Class 390's (Pendolinos). Remediation measures in the form of piling beneath the track have since been introduced.

Stratigraphy

Network Rail provided information from their geotechnical investigations on the site. Of particular interest are several boreholes along the track, a cross-section of which is given in Figure 5.1, as summarised in Table 5.1. They show the site to be underlain by a horizon of peat, sitting over layers of stiffer sand, clay and gravel. This peat has a minimum layer thickness of 1.9 m, and deeper horizons of up to 4 m. Peat has a much lower stiffness than traditional foundation materials, this is likely to be the main reason for the large track movements. Borehole results were only available along the line of the track; no information was available in the direction perpendicular to the track. No further information was available as to the type of peat, or other organic material, identified in the boreholes.

Topology

BGS surface geology mapping shows the site to sit within a zone of sandstone overlain by deposits of Devensian till (British Geological Society, 2016). This corresponds well with the BGS boreholes near to the site, as summarised in Figure 5.2, which shows the historic borehole records which are the closest available to the site in all directions. The ground is shown to be formed from similar layers of sandy clays, clayey sands and gravels, adding evidence to the assumption that the peat layer on the site is a finite horizon. The site specific boreholes cannot show the length or width of the peat horizon, but the historic boreholes show that it at least does not exceed approximately 0.6 km in size. The site location and topology is detailed in Figure 5.3. The site sits at the bottom of a slight basin, with several streams and brooks in the area, as well as a drainage ditch, which follows the line of the adjacent fields and passes beneath the track. These factors perhaps explain why the site has anecdotally been reported to have a very high water table.

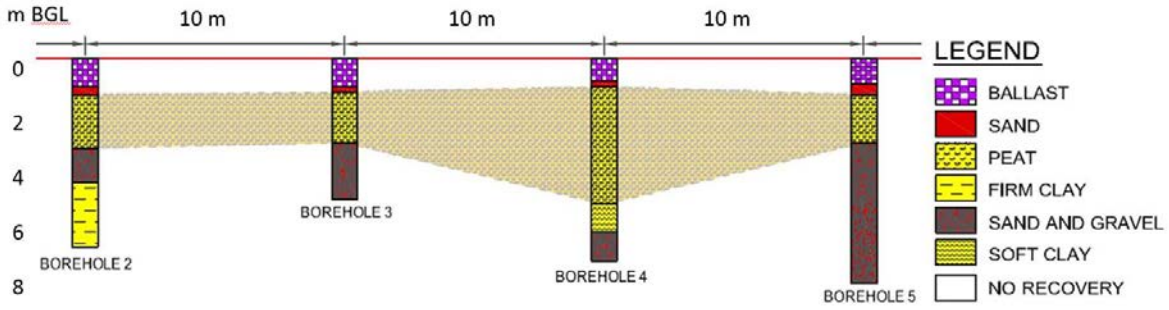

Figure 5.1: Gravel Hole boreholes cross-section (After Aspin Foundations Ltd (2013)).

Table 5.1: Summary of Network Rail Gravel Hole borehole measurements, after Aspin Foundations Ltd (2013).

Ground Type	*Ground Description*	*Borehole Results (m below sleeper surface)*			
		No.2	*No.3*	*No.4A*	*No.5*
Gravel	Grey subangular coarse GRAVEL of granite. Ballast	0 to -1	0 to -1	0 to -0.8	0 to -0.9
Sand	Brown fine to medium SAND	-1 to -1.3	-1 to -1.2	-0.8 to -1	-0.9 to -1.3
Peat	Dark brown slightly sandy slightly clayey spongy PEAT	-1.3 to -3.2	-1.2 to -3	-1 to -5	-1.3 to -3
Sand	Loose to medium dense dark grey slightly peaty gravelly fine to medium SAND	-3.2 to -4.4	-3 to -5	-	-
Clay	Firm to stiff brown and grey very sandy CLAY	-4.4 to -6.7	-	-5 to -6	-
Gravel	Medium dense grey brown coarse GRAVEL	-	-	-6 to -7	-3 to -5
Sand	Brown slightly gravelly medium to coarse SAND	-	-	-	-5 to -7.5

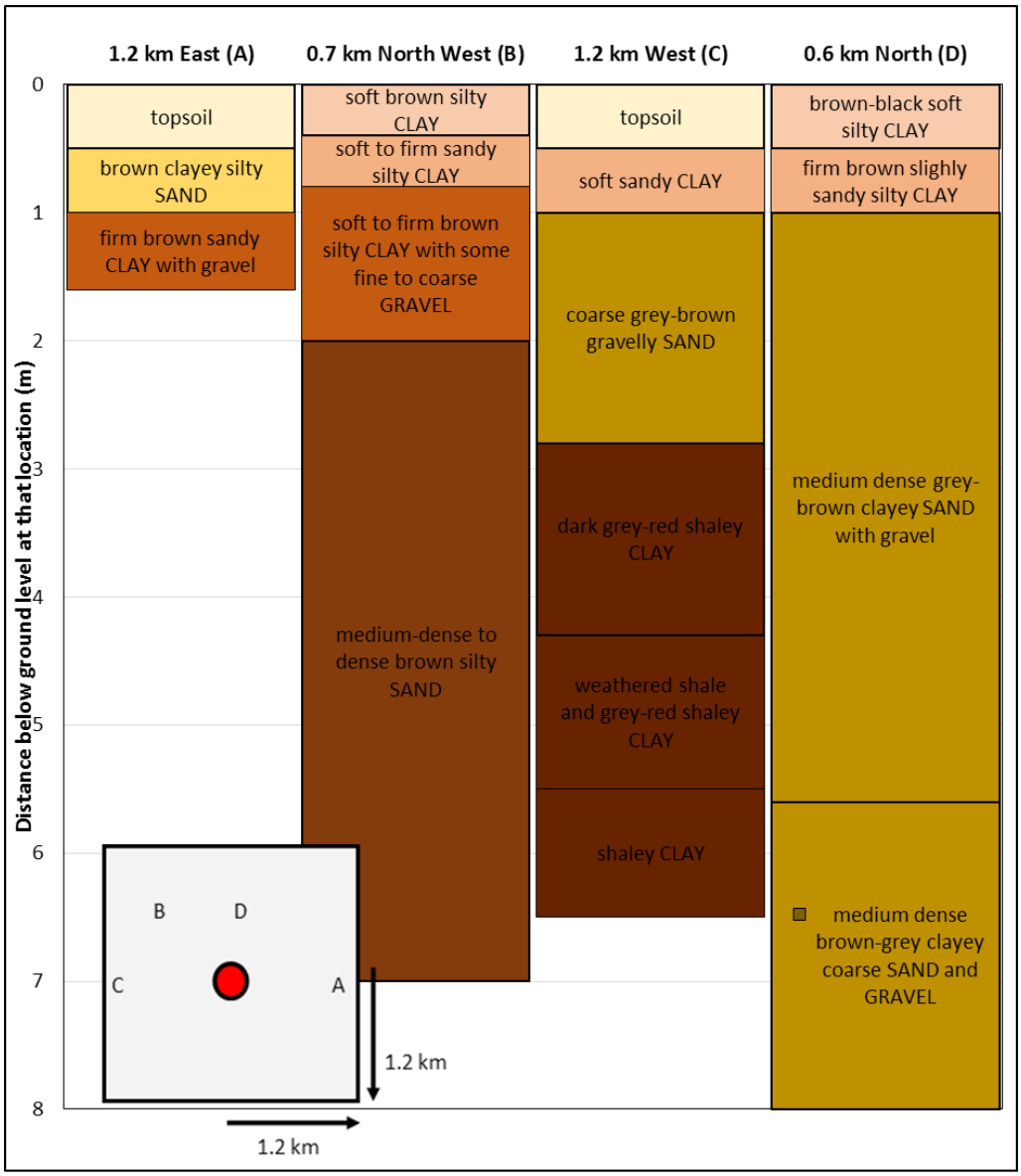

Figure 5.2: Summarised borehole results at various distances surrounding Gravel Hole (British Geological Society, 2016). Includes location map of boreholes relative to site (red dot).

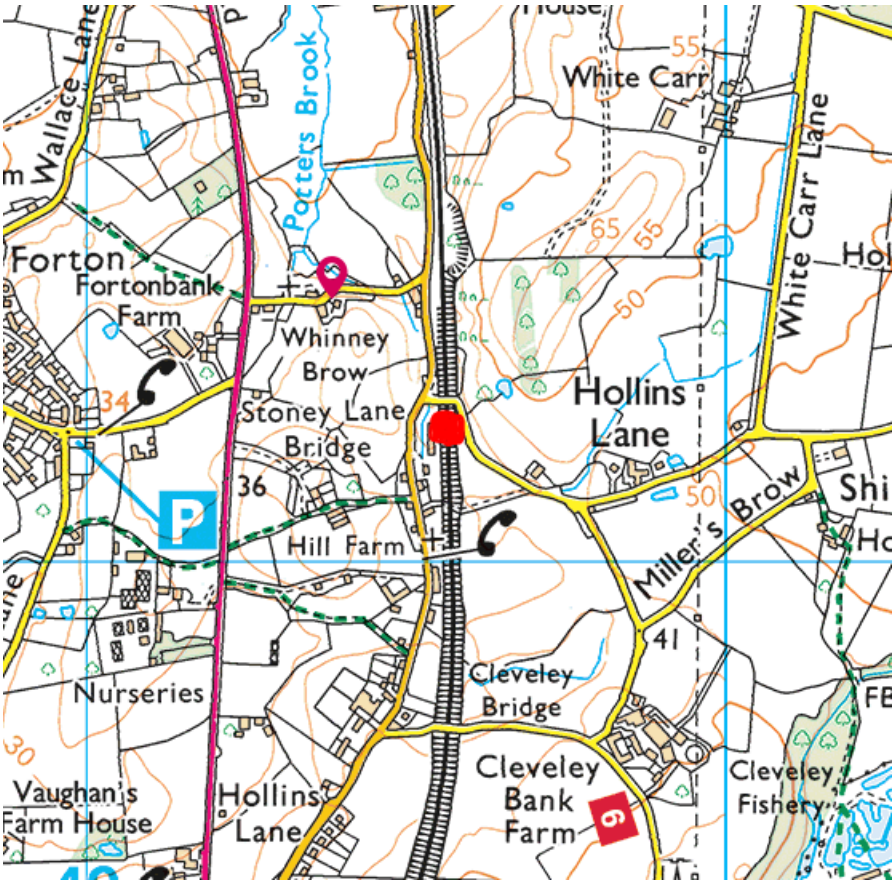

Figure 5.3: Gravel Hole local contouring, red dot indicates site (Ordnance Survey, 2016).

5.2 Site measurements and sampling

5.2.1 Track and ground movement

Researchers within the School of Engineering at the University of Southampton carried out monitoring of track movements at the site using geophones, small seismic devices which output a voltage proportional to velocity. The signal is then filtered and integrated to obtain the displacement. The monitoring and analysis methods used are described in Bowness *et al.* (2006). Geophones were attached to nine alternate sleepers allowing movements over an 11 m length of the track to be recorded. Figure 5.4 shows the site with geophones installed.

Figure 5.4: Gravel Hole site with geophones installed.

Vertical deflection measurements were taken on three visits, one before remediation took place and two after. The pre-remediation measurements will be focussed on in this work. The pre-remediation visit recorded the passage of 11 trains, of varying class and having between 3 and 11 cars. Figure 5.5 shows typical processed geophone data in the form of vertical displacement against time. Owing to the high-pass filtering applied before integration, the trace apparently contains both upward and downward displacements, as the filtering process 'loses' the origin point of the track. In reality the motion of the sleepers is predominantly downwards. The parameter of interest, which is obtained correctly from the analysis, is the peak-to-peak displacement amplitude under each axle passage, which in this example is more than 6 mm.

The variation in average measured track displacements with speed for the nine geophones monitoring the site is shown in Figure 5.6. There are various types of traffic shown, with the LocoPlus26 being a freight train with 26 carriages of unknown load. For modelling purposes the data from the Pendolinos and local trains are used, as the load and axle spacings of the Voyagers are quite different to these, and are also far less common on the route. A Pendolino travelling at 53 ms^{-1} (122 mph) produced a displacement of 7 mm.

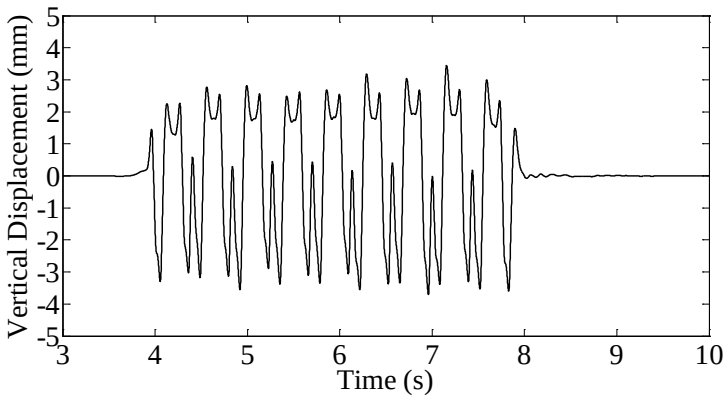

Figure 5.5: Geophone trace showing vertical displacement of a sleeper when passed by a 9-car Class 390 (Pendolino) at 195 km/h (54 m/s).

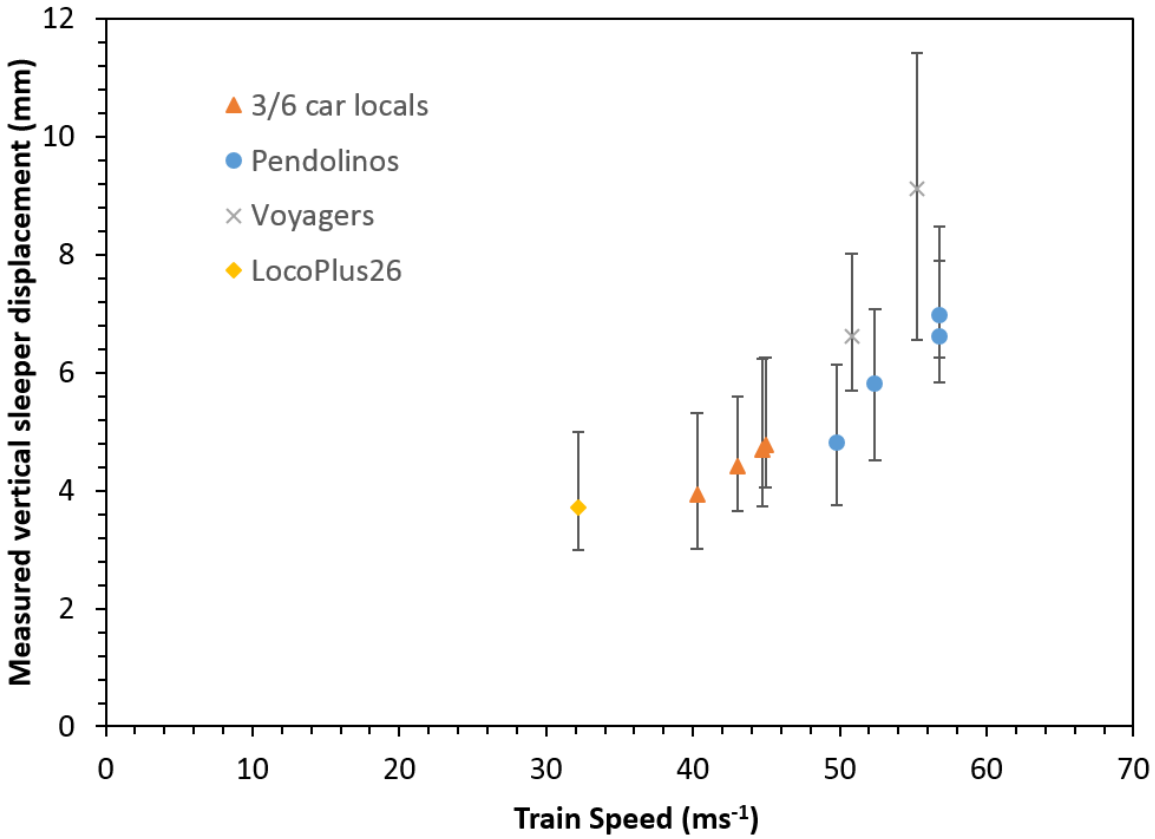

Figure 5.6: Averaged measured displacements and speed for all geophones at Gravel Hole, pre-remediation. Train type and range of displacement per train also shown.

5.2.2 Seismic testing

Limited SASW tests were carried out beside the track, summarised in Table 5.2 (Rushworth, 2014). These measurements are very difficult to analyse and so it was not possible to define wavespeed measurements for the peat. These measurements do however provide a useful initial estimate of the dilational (P) and shear (S) wave speeds for the lower layers of sand and gravel.

Table 5.2: Gravel Hole wavespeed measurements (Rushworth, 2014).

Ground Layer	*Value*				
Top Depth (m)	0	0.1	0.4	1.1	4.4
Bottom depth (m)	0.1	0.4	1.1	4.4	Inf.
Density (kg/m^3)	2000	2000	2000	2000	2000
P- Wave Speed (ms^{-1})	768	768	768	768	768
S- Wave Speed (ms^{-1})	40	95	200	95	900

5.2.3 In situ sampling

Sampling process

A Windowless Sampling (WS) rig and a Super Heavy Dynamic Probe (SHDP) were used to examine the site in a night possession (Figure 5.7)[1]. Two boreholes were taken from directly below the track, one at a chainage chosen to target the previous maximum peat depth and one slightly beyond the extent of the previous boreholes on the down line. Initially the up line was targeted, however it was not possible to break through a very tough layer at the base of the ballast, believed to be the polyurethane 'Xitrack' layer installed as a previous remediation method (Woodward *et al.*, 2014). A large amount of water was also sitting on top of this layer, implying permeability problems, which may be exacerbating the site displacement problems.

The WS was applied to 2 bores to a depth of 6 m, sufficient to pass through the entire depth of the peat horizon, according to previous boreholes, to allow the depth of the peat horizon, and other layers, in the sampled locations to be classified. The SDHP was deployed below the base of the WS rig bore, to test up to 10 m depth. Sample tube diameters were kept as large as possible, beginning at 100 mm and decreasing as necessitated by depth. Following regulations (Section 4.2) sample tubes were immediately sealed on site, and transported in padded boxes to the temperature-controlled lab for storage.

Figure 5.7: Sampling at Gravel Hole.

[1] Site work was undertaken by contractors to the authors specification, with the author present on site.

Sampling results

In total 10 1 m length samples were extracted, from 2 bores (denoted GHS1 and GHS2), as the first 1 m on site was dug by hand as a trial pit. The process set out in 4.6.1 was followed for logging and storing samples. The overall sampling process was very successful with 9 samples suitable for lab testing recovered from GHS1 and 6 from GHS2. Figure 5.8 shows a summary of the borehole results (detailed results presented in Appendix Table 8.1 and Table 8.5).

The borehole results are not as expected, with the ground described as peat in the previous boreholes not appearing, but instead layers of soft silt are present. It is possible that as the previous boreholes were taken from the adjacent line that a peat horizon is present there that was not present on both lines, but due to the close proximity of the lines it seems more likely that the soft organic silt was misidentified by the engineer logging the previous boreholes on site.

If the soft organic silt is presumed to correspond to the peat of the previous boreholes then strong similarities are shown in the layer's thickness, and its variation across the boreholes. The layers of sand and gravel below this soft layer also correspond well with the previous boreholes.

Many of the silt layers had a strong odour of plant decay, with mould spores having grown on the outsides of the samples inside their tubes, in the 3 weeks between sealing the sampling tubes and re-opening in the lab for logging. No mould occurred on the deeper clay, gravel and sand samples, indicating a strong organic presence in the silts.

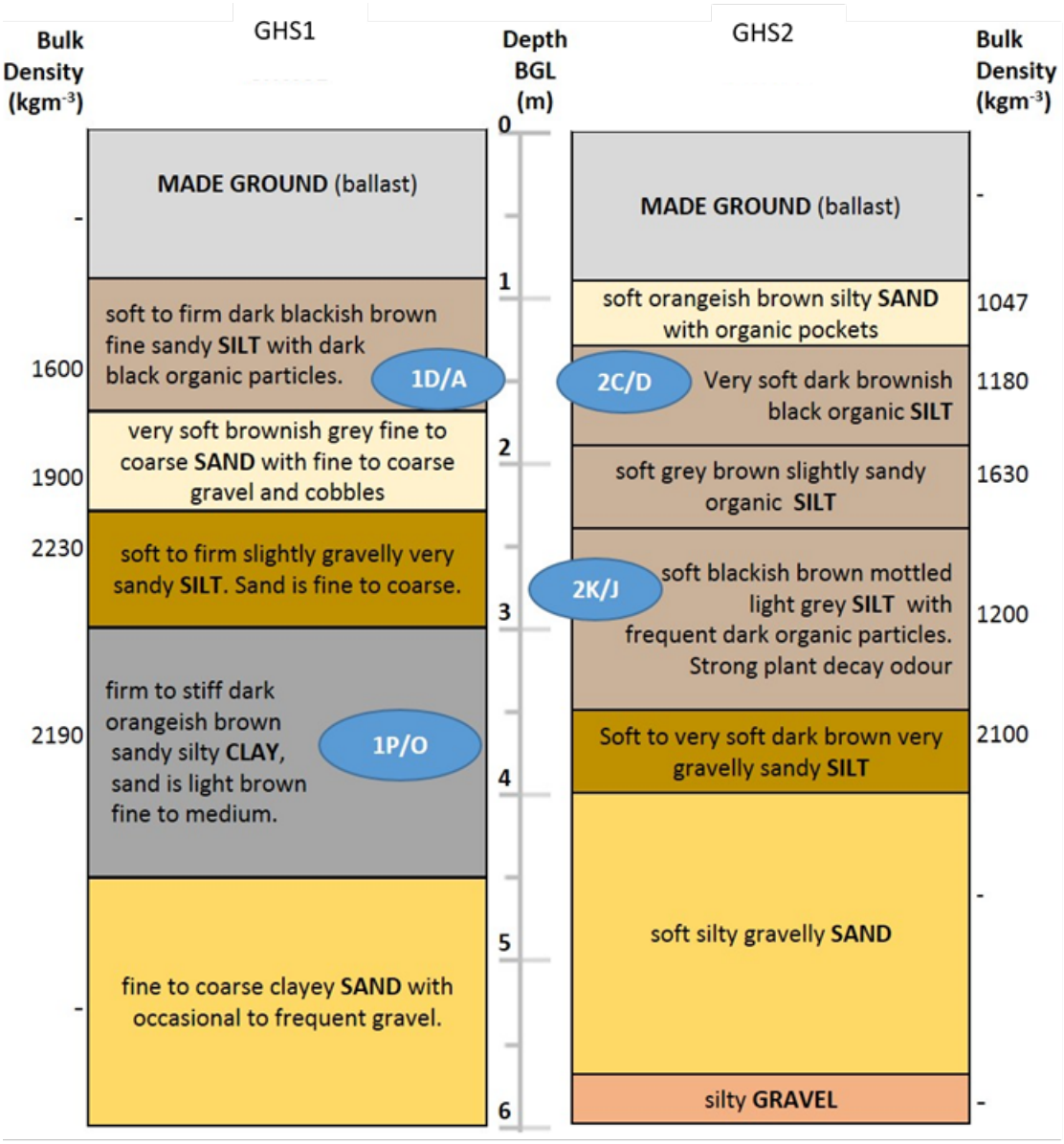

Figure 5.8: Summary of Gravel Hole window sampling results. Note sample iDs in blue ovals are further discussed in section 5.3.1.

Some estimates of undrained shear strengths (Figure 5.9) were taken in the laboratory. A limited number were taken as tests could only be carried out on sections which had remained intact inside the sampling tubes and that were not set aside for use as future lab testing samples. The results show fairly low strengths for the soft silt material 1 m to 3 m below ground level. The granular layers below 4 m were non-cohesive so could not be tested for shear strength.

The blowcount from the SDHP (blows per 100 mm of travel) were converted to SPT equivalence (blows per 300 mm) to allow estimation of relative density, assuming that the ground beneath the base of the boreholes continued to be non-cohesive (Figure 5.10). The results for GHS2 show a lower blowcount than GHS1, continuing the general trend of softer materials in GHS2. In general,

a relative density of medium dense is shown, which roughly corresponds to an expected density of 1750 kgm^{-3} to 2100 kgm^{-3}.

Figure 5.11 shows the variation in density with depth, based upon 50 mm density ring tests completed in the lab. There is some variation in density between the two boreholes, with GHS1 consistently denser. It should be noted that the determination of density from density rings is subject to some error in very variable soils such as these. A large variation with depth is found, with the densities in GHS2 being especially low, with values generally between 1100 kgm^{-3} and 1400 kgm^{-3} for the first 3.5 m below ground level. In geotechnics a typical soil is normally expected to have a density of approximately 2000 kgm^{-3}, almost twice the lowest value measured in GHS2. Low density soils tend to be soils which have a low stiffness, and so are the most likely to be the cause critical velocity problems on the site.

The variation of moisture content with depth is also shown in Figure 5.11. As with density, a significant difference is found between the boreholes, with the denser GHS1 having far lower moisture content than GHS2, in which the values are also more consistent. Greater variability is found for GHS2, with unusually high moisture content present, most likely a result of the organic material in the soil. The presented moisture contents are gravimetric, meaning that for values of greater than 100 % the weight of the water in the soil is greater than the weight of the dry soil.

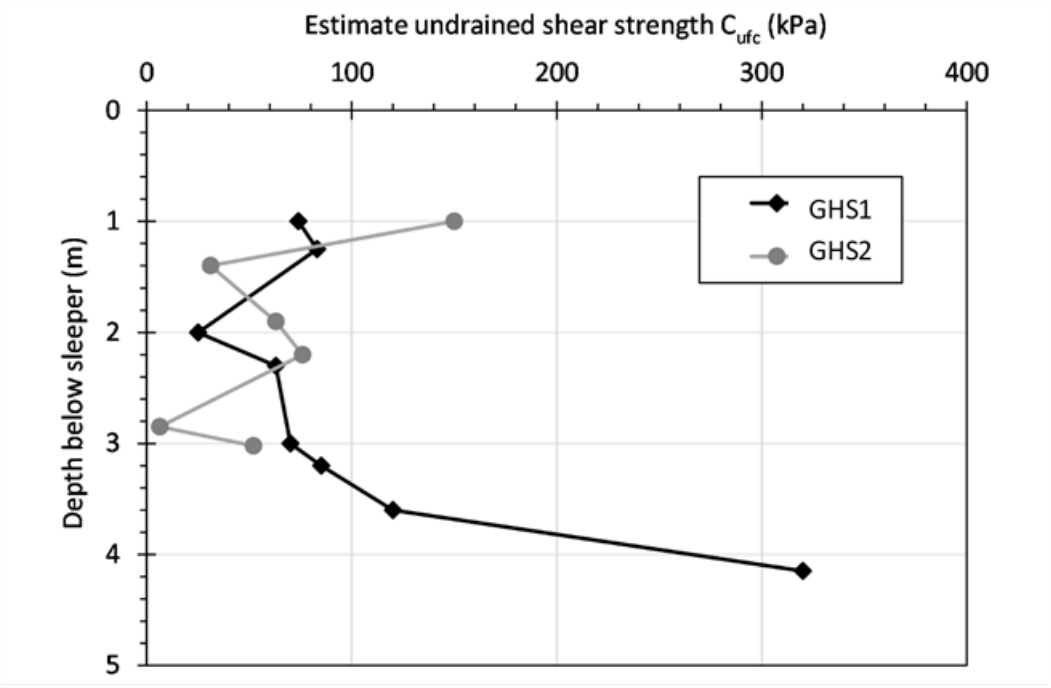

Figure 5.9: Estimate undrained shear strengths from drop cone tests for Gravel Hole borehole samples.

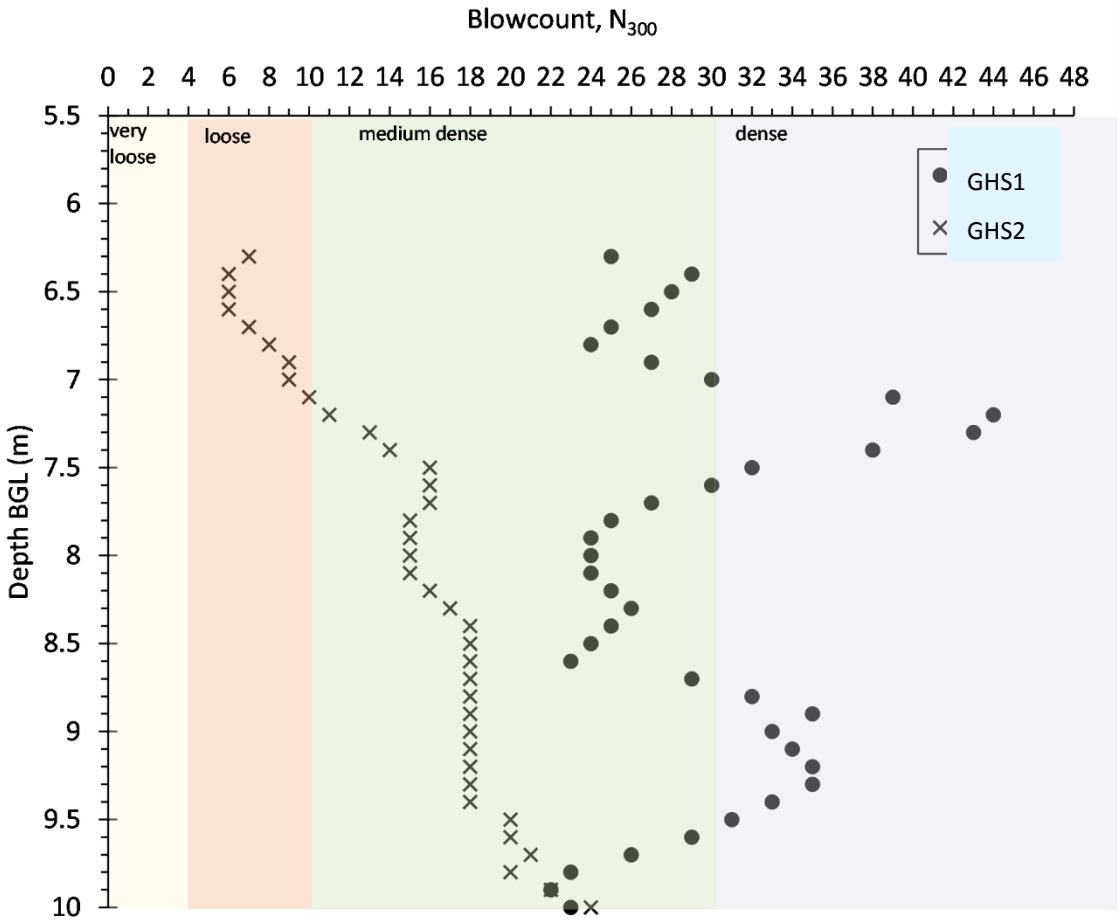

Figure 5.10: SHDP results for Gravel Hole, converted to N_{300}, overlaid with relative densities for non-cohesive soils (Terzaghi and Peck, 1948; USACE., 1994).

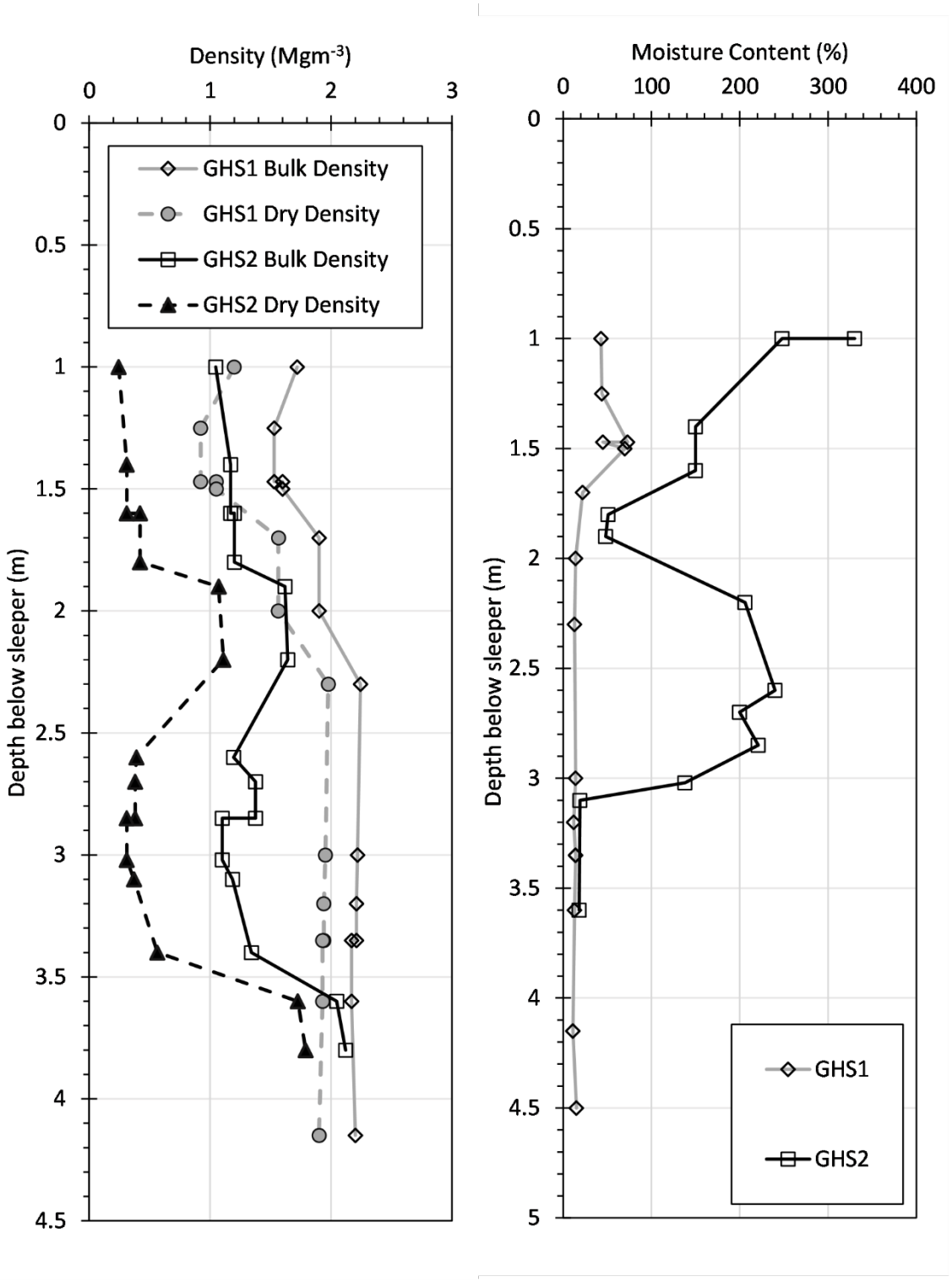

Figure 5.11: Gravel Hole borehole density and gravimetric moisture content variation with depth.

5.3 Laboratory testing regime for site samples

5.3.1 Sample selection

To be deemed suitable for lab testing samples must be of around 100 mm diameter (to allow trimming to 70 mm), have a minimum height of 150 mm and be undamaged. 15 samples suitable for lab testing were retrieved from the bore and samples from the four most geotechnically interesting layers were selected for laboratory testing, the locations of which are marked on Figure 5.8. Samples were selected where two similar adjacent sections suitable for lab testing were retrieved, meaning pairs of samples could be tested in each piece of equipment, resulting in a total of eight samples to be tested. The samples selected, their borehole location, soil description and initial parameters are set out in Table 5.3, with the reference code for the sample names set out below the table. The similar sample pairs are generally from the lowest density, softest layers, with samples GH2K/J, GH2C/D and GH1A/D being organic silts whilst pair GH1O/P is a clay. The densities for the silt soils are far lower than for the clay, with the moisture content unusually high.

To give some indication of the inhomogeneous structure of the samples, images of the exterior of a selection are shown in Figure 5.12. The clay sample GH1P appears to show less variability externally than the silts. Cross- sections for a range of the samples after testing are shown in Figure 5.13. Strong variability is shown in appearance, particularly in the silt samples. The cross-section of sample GH2J is taken before the sample was trimmed from the site diameter of 100 mm to the required diameter of 70 mm. The darker exterior ring indicates the oxidation that has occurred during storage, with fast oxidation rates common in materials with high organic content. The cross-sections for samples GH2C and GH2K are particularly unusual, and whilst it has not been possible to examine the cause of this, it is believed to be due to the high organic content of the material.

Whilst it is impossible to get two identical natural soil samples, the density and moisture content values for the pairs of samples show reasonable similarity, see Table 5.3. It should be noted that these parameter measurements were based upon just one or two density ring samples, so will be subject to error. Further initial testing was not possible due to the need for sufficiently large undamaged samples to be left remaining for the RC and triaxial testing. Samples GH1D, GH1O, GH2C, GH2K were assigned to be tested in the RC, whilst their pairs GH1A, GH1P, GH2D, GH2J were assigned to the triaxial machine.

Table 5.3: Gravel Hole lab sample initial parameters.

Sample Id	*Bore depth BGL (m)*	*Soil Description*	*Initial bulk density (kgm^{-3})*	*Initial moisture content (%)*	*Initial dry density (kgm^{-3})*
GH2K	2.68 - 2.84	soft blackish brown mottled light grey SILT with frequent dark organic particles. Strongly oxidised very dark brown around outside.	1350	200	450
GH2J	2.45 - 2.68		1150	240	330
GH2C	1.41 - 1.58	very soft dark brownish black SILT with occasional pockets of light brownish orange sand and frequent organic black particles, rootlets and decayed leaf skeletons	1170	240	300
GH2D	1.58 - 1.75		1200	150	420
GH1A	1.25 - 1.42	soft to firm dark blackish brown fine sandy SILT with dark black organic particles of up to 4 mm	1600	55	1050
GH1D	1.52 -1.7		1530	70	930
GH1O	3.17 - 3.34	firm dark orangeish brown sandy silty CLAY, sand is light brown fine to medium.	2210	14	1940
GH1P	3.38 - 3.56		2170	14	1930

*Number in sample ID denotes source bore, GH denotes source site (Gravel Hole), A-P denotes sample position within bore, see sample register in Appendix A for reference.

Figure 5.12: Selection of Gravel Hole samples for testing. Top row from left: GH1D pre-test, GH1D post-test, GH2K pre-test. Bottom row from left: GH1P pre-test, GH2D pre-trim, GH2C pre-test.

GH2C

GH2C

GH2K

GH2J Pre-trim

GH2D

GH1D

Figure 5.13: Gravel Hole samples cross-sections.

5.3.2 Testing stresses and procedure

For maximum applicability of results, laboratory tests should be carried out at pressures and effective stresses representative of those that the soil undergoes on the site. The pressures applied to the sample in situ are made up of those from the cumulative ground layers above it, the track structure (ballast, sleepers, rail) and the static weight of the train. The water table depth also impacts the effective stress.

Ground pressures

As the water table was not reliably measured during sampling, a range of water table depths were selected. In situ stresses were calculated as follows, for sample from depth z:

Vertical stress due to the ground σ_{vg} (kPa) for all layers above depth z:

$$\sigma_{vg} = \sum_{i=n}^{n} \left[\{\rho_n \, t_n\} \left(\frac{9.81}{1000} \right) \right] \qquad \text{Equation 5-1}$$

where ρ_n is the density of soil layer 1 (kgm^{-3}) and t_n is the thickness of each ground layer (m) and *n* the number of ground layers.

$$\sigma'_{vg} = \sigma_v - \mu \qquad \text{Equation 5-2}$$

where σ'_{vg} is the vertical effective stress (kPa) and μ is the pore water pressure (kPa) found from:

$$\mu = \gamma_w (z - h) \qquad \text{Equation 5-3}$$

where γ_w is the unit weight of water, z is the depth of the soil sample and h the height of the water table below the ground.

Train pressure

The common industry idealisation of the pressure distribution beneath the sleeper, as shown in Figure 5.14, is calculated as follows:

$$\sigma_{max} = \frac{3 \, F_{max}}{bL} \qquad \text{Equation 5-4}$$

Where σ_{max} is the maximum pressure beneath the sleeper, F_{max} is the maximum railseat load per rail, b is sleeper width and L is sleeper length – calculating the pressure area, assuming a rectangular sleeper (Esveld, 2001; AREMA, 2003) . The 'w' shape of this pressure distribution is due to the ballast not having uniform load transfer properties, due to variations in particle sizes and particle contact.

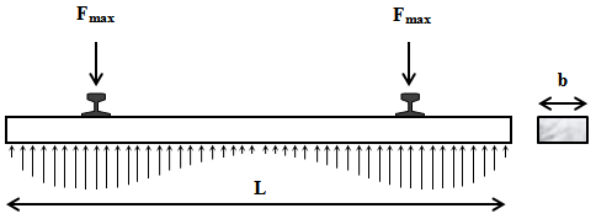

Figure 5.14: Idealised pressure distribution beneath the sleeper. Figure from Abadi (2015), after AREMA (2003).

However, the target pressure to be calculated is for depth z below the ground, and not for directly beneath the sleeper. In the absence of further precedent, the pressure calculated for directly below the sleeper (Equation 5-4) is assumed to distribute through the soil at a rate of 2:1 from the edge of the sleeper on all sides (i.e. the stress area moves out 2 m laterally for every 1 m of extra depth). This is the most commonly used method for simplifying load spread in rail practise (Sadeghi, 2012). This results in the following relationship:

$$Pressure\ Area = \{(4z) + L\} * \{(4z) + b\} \qquad \text{Equation 5-5}$$

where pressure area is in m^2. Therefore the vertical stress, in kPa, due to train loading at depth z (σ_{vtl}) is equal to:

$$\sigma_{vtl} = \left({}^{(3F_{max})}/_{Pressure\ Area}\right)\frac{9.81}{1000} \qquad \text{Equation 5-6}$$

where the railseat load (F_{max}) is equal to the half of the axle load (kg), and the pressure area (m^2) is the area over which the pressure is applied, at the depth of interest. The adaptation of Equation 5-4 for use at depth is a conservative estimate of pressure, i.e. it will tend to more over-estimate than under-estimate the in-situ pressure.

For these calculations, railseat load per rail is taken as the half of the wheel load, which is itself half of the axle load, resulting in a railseat load of 7397 kg for Pendolionos. No dynamic loading effects are included, as the majority of the pressure at depth comes from the ground layers, not the train itself.

Rail and sleeper pressures

For simplicity pressures due to rail mass (σ_{vr}) and sleeper mass (σ_{vs}) were assumed to be evenly distributed by the sleeper, and so evenly distributed over the relevant pressure area for the depth of interest. Each sleeper is assumed to carry the rail which spans halfway between that sleeper and the next - at 0.65 m sleeper spacings, this is equivalent to a total rail mass of 78 kg per sleeper. Each sleeper weighs 300 kg.

Finally, the target vertical effective stress for a sample at depth z is:

$$\sigma'_v = \sigma'_{vg} + \sigma_{vtl} + \sigma_{vr} + \sigma_{vs} \qquad \text{Equation 5-7}$$

The results are the target effective stresses for resonant column testing, which are also converted to mean effective stress and axial stress for triaxial testing. Following this method stresses for testing were calculated (Table 5.4). In addition to the stresses calculated from assumed water levels, several higher stress levels were also chosen, to represent the possibility of a future surcharge being applied to the area. Note that due to the isotropic nature of the resonant column, the vertical effective stress σ'_v is equal to the mean effective stress p'.

Table 5.4: Calculated in situ stresses and target testing stresses for Gravel Hole samples.

Sample ID	*Mean Sample Depth BGL (m)*	*Assumed water table depth below surface (m)*	*Target vertical effective stress σ'_v (kPa)*	*Target mean effective stress p' – triaxial (kPa)**	*Target axial stress q – triaxial (kPa)*
GH10/P	3.40	0.5	35	-	-
		2	50	-	-
		3	60	-	-
		-	75	-	-
		-	150	-	-
		-	250	-	-
GH2C/D	1.55	0.5	17	11.3	8.5
		2	32	21.3	15.8
		3	42	28	21
		-	75	50	37.8
GH2J/K	2.80	0.5	23	15.3	11.5
		2	38	25.3	19
		3	48	32	4
		-	75	50	37.5
		-	125	83.3	62.5
GH1A/D	1.50	0.5	19	12.7	9.5
		2	34	22.7	17
		3	44	29.3	22
		-	75	50	37.5
		-	150	100	75

*In the RC isotropic loading is applied therefore for RC $\sigma'_v = p'$.

5.4 Laboratory test results

5.4.1 General index and organic content testing results

In addition to density, moisture content and drop cone strength measurements (section 5.2.3), liquid and plastic limit tests were carried out on the selected samples, after RC / triaxial tests were complete. Only samples GH1O/P (firm sandy clay) were found to be sufficiently plastic so as to allow successful testing. These samples were found to have a plastic limit of 14 %, a liquid limit of 25 % and a plasticity index of 11 %. When plotted on a plasticity chart (Figure 5.15) this soil is classified as a low plasticity clay. The in-situ moisture content was approximately 14%, sitting close to the plastic limit.

It was not possible to carry out successful tests on the other samples, which are all a variety of silt. Samples GH2C, GH2D, GH1D, GH1A , GH2K and GH2J are all classified as non-plastic organic silts. It was found that samples GH2C and GH2K have a very small clay content, giving them a small amount of plasticity, which was still too low to measure and therefore still qualifies as non-plastic.

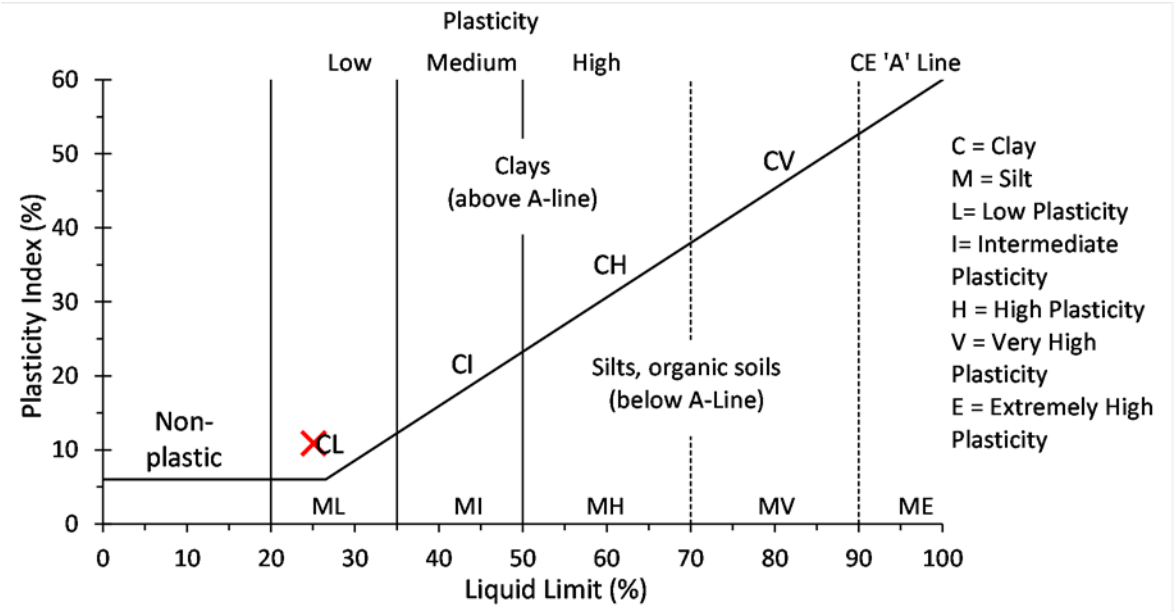

Figure 5.15: Gravel Hole sample GH1O/P plasticity classification chart. Modified from BS5930 (British Standards Institute, 2015).

Organic content

Tests for organic content – total solids and volatile solids, were carried out, following BS EN 12879 and BS EN 13039(British Standards Institute 2000a;b). Tests were carried out on GH2C, GH2D, GH2K and GH2J, as they appeared to have the highest organic content, with tests repeated on 2 sections of each sample, then averaged. The results (Table 5.5) generally classify the soils as highly

organic, with one test on sample GH2K having a volatile solids content slightly below the marker for highly organic. This high level of organic matter may explain why a peat material rather than an organic silt was named in previous boreholes.

Table 5.5: Organic content results for Gravel Hole.

Sample	*Total Solids (%)*	*Proportion of Volatile Solids in Total Solids (%)*	*Proportion of Volatile Solids in Dry Weight (%)*	*Average Volatile Solids in Total Solids (%)*	*Average Volatile Solids in Dry Weight (%)Θ*	*Organic Term**
GH2C	43.7	28.3	28.3	28.0	28.0	High
	44.1	27.6	27.6			
GH2D	48.1	31.9	31.9	17.1	31.7	High
	48.0	31.5	31.5			
GH2J	33.2	37.9	37.9	31.7	38.7	High
	32.8	39.5	39.5			
GH2K	34.5	17.1	17.1	38.7	17.2	Medium
	33.6	17.2	17.2			

*High if value Θ >20, Medium if Θ 6 to 20 (BS EN ISO 14688-2 (British Standards Institute, 2018b)

5.4.2 Resonant column / bender element results

Resonant column testing, including vertical bender elements, was successfully carried out on four Gravel Hole samples. Tested samples were 70 mm in diameter and 140 mm in length. The first samples (GH1O and GH1D) underwent testing at all planned test pressures (Table 5.4). Samples GH2C and GH2K were tested at four out of their planned five pressures.

Due to the range of sample densities height change due to consolidation varied, with a non-linear response to consolidation pressure, as shown in Figure 5.16. GH2C and GH2K required the electromagnet frame to be repositioned for the higher pressure consolidation stages. Once consolidated to 75 kPa, sample GH2C (very soft silt) had reduced in height by 10.5 mm, a significant change of 8 %. In contrast the higher density, stiffer clay sample GH1O had changed by just 0.5 mm (0.4 %) at the final pressure.

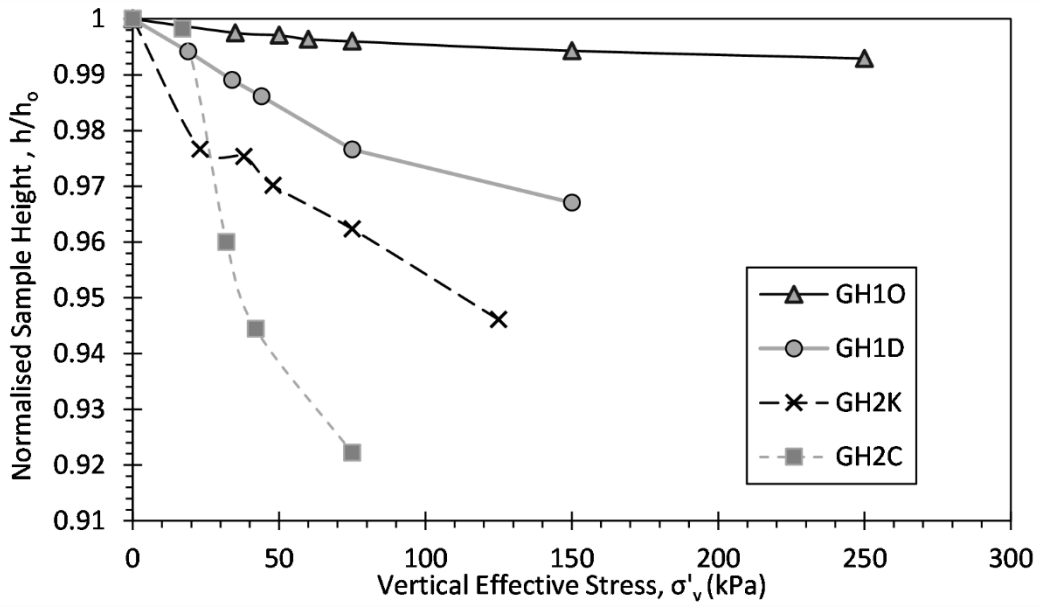

Figure 5.16: Height change with vertical effective stress during consolidation for all Gravel Hole RC samples, normalised by initial sample height

Shear modulus

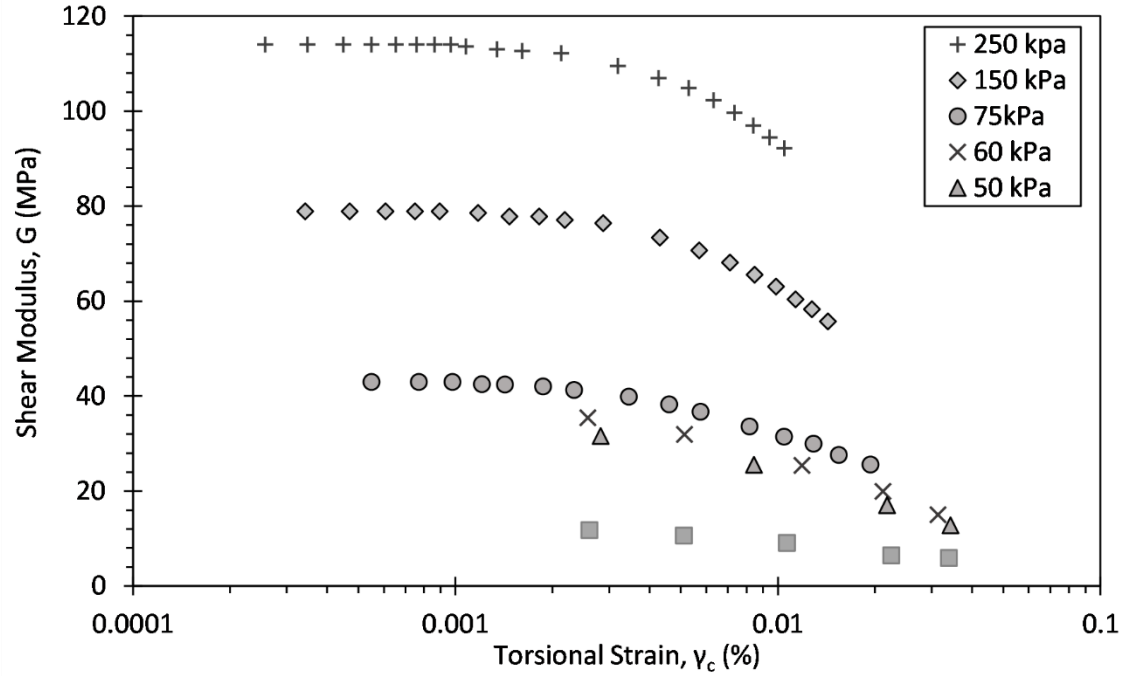

Figure 5.17 (GH1O – firm clay), Figure 5.18 (GH1D – soft to firm sandy silt), Figure 5.19 (GH2K – soft silt) and Figure 5.20 (GH2C – very soft silt) present the shear moduli degradation with torsional strain for the respective samples. The small strain shear moduli ranges from highest in GH1O to lowest in GH2C. The shear moduli measured for the lowest density samples are very low, with sample GH2C having a small strain modulus of just 5 MPa at the lowest test pressure. The three silt samples do vary in modulus; however, all of these values still sit in a very low range,

with a maximum small strain shear modulus of 10 MPa, at the lowest test pressure, for all silt samples. This sits within the typical strength ranges for soft silts.

Normalising the measured shear modulus from the resonant column by the small strain shear modulus for each pressure is used to evaluate the variance in the rate of shear modulus degradation with strain, see Figure 5.21. The stiffest sample (GH1O- clay) shows greater rates of degradation and at lower strains than other samples. For example, averaged across the testing pressures, at distortional strain levels of 0.01% the shear moduli of the samples showed reductions to: GH2K- 98%, GH2C – 93%, GH1D – 87%, GH1O – 77%.

Due to the high-organic nature, colouring and odour of samples GH2K and GH2C it is also reasonable to compare these strength measurements to those of other organic soils of similar moisture content, particularly amorphous peats. Whilst organic materials are inherently highly variable these other measurements can still provide a useful comparison framework. Boulanger *et al.* (1998) reported G_O values of 7 MPa to 11 MPa for isotropic effective stresses of 66 kPa to 200 kPa for peats with a water content of 152 % to 240 %. Kramer (1993) reported G_O values for peats of 0.15 MPa to 11 MPa for very low isotropic effective stresses of 1.5 kPa to 12.5 kPa. The G_O measurements for samples GH2K (Figure 5.19) and GH2C (Figure 5.20) correspond well with these previous peat measurements.

Both the soft and very soft silt samples (GH2C and GH2K) show relatively similar increases in shear moduli with pressure. In contrast, the measured modulus of the clay sample (GH1O) increases with pressure at 10 times the rate of the soft silt samples (based upon a basic linear gradient fit to the linear section of plot Figure 5.22). Sample GH1D, whilst also being a silt, is firmer and has a much higher sand content and lower moisture content than the other silt samples, increases its modulus with pressure at a rate approximately four times faster than GH2C and GH2K. The low rate of increase in modulus with pressure of the soft organic silt samples means that soils which may normally be considered at a great enough depth to have a reasonable shear modulus may have a very low value.

The strain applied to a sample is a function of the input voltage, with greater voltage required to induce a certain strain in a stronger sample than a weaker one. Initially samples were tested cautiously up to 0.03% strain (GH1D - Figure 5.18). After this samples were tested at increasingly higher strains, repeating low strain tests between each higher strain test, to check that the small strain shear modulus was still recoverable. The point at which the shear modulus begins to degrade defines the upper strain limit of Zone 1, the point at which the small strain shear modulus is no longer recoverable when re-tested defines the upper end of Zone 2 and beginning of Zone 3 (section 2.2.1).

The upper limit of Zone 1, the strain beyond which the shear modulus begins to degrade, decreases with increased confining pressure, and is approximately: 0.009% to 0.01% for GH2K (Figure 5.19), 0.003% to 0.004% for GH2C (Figure 5.20), 0.0015% to 0.004% for GH1D (Figure 5.18) and 0.001 % to 0.0015% for GH1O (Figure 5.17). A trend of the upper limit strain being lower for clay samples than for the silts is found. The higher limit strain values for GH2K compared to GH1D also agree with the findings of Kallioglou *et al.* (2008), that increased organic content of cohesive materials increases the strain value at which the shear modulus begins to degrade. It is also interesting that the boundary of Zone 2 appears significantly higher for the silts than the clay sample, with the former being approximately 0.06 % to 0.08 %, and the latter around 0.02 % to 0.04%. These values for the clay correspond well to previous findings for clay (Jardine, 1992).

As testing pressure increases so does the input voltage required to induce a certain strain in the sample. For certain sample and pressure combinations the RC is unable to apply enough voltage to induce sufficiently high strains to reach the end of zone 2, the upper limit of recoverable strain. It is noted beneath each shear modulus degradation curve whether this strain limit was met.

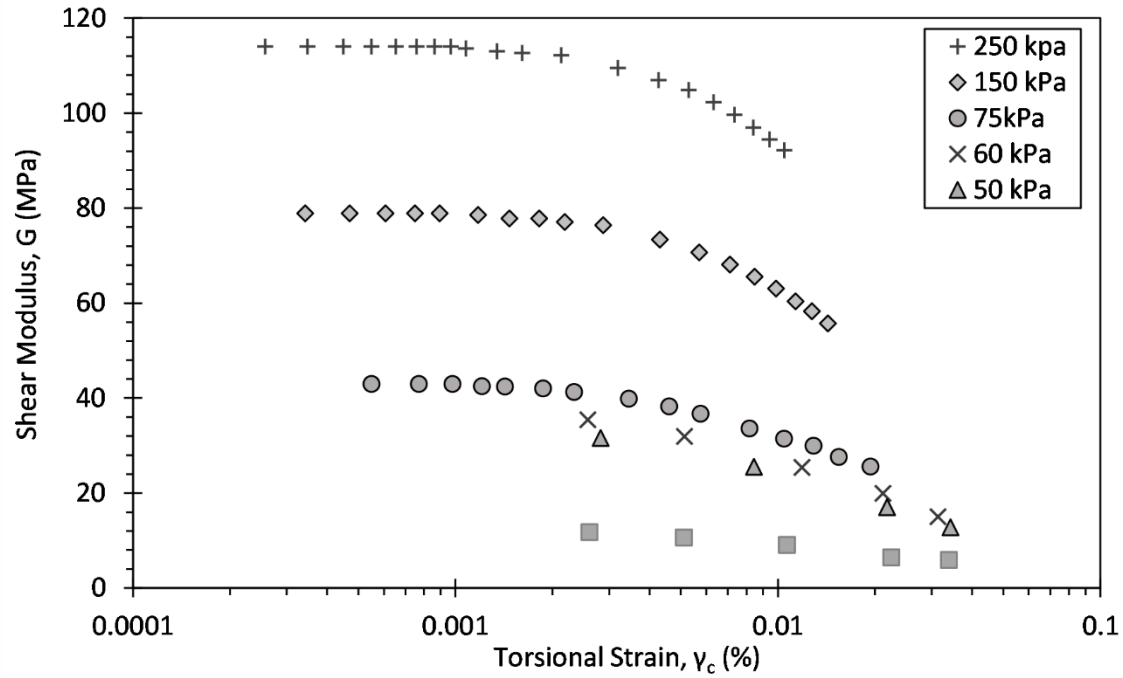

Figure 5.17: Shear modulus degradation with strain for sample GH1O during torsional excitation in the RC, at a range of vertical effective stresses. Strain limit not met for 150 kPa and 250 kPa due to lack of power.

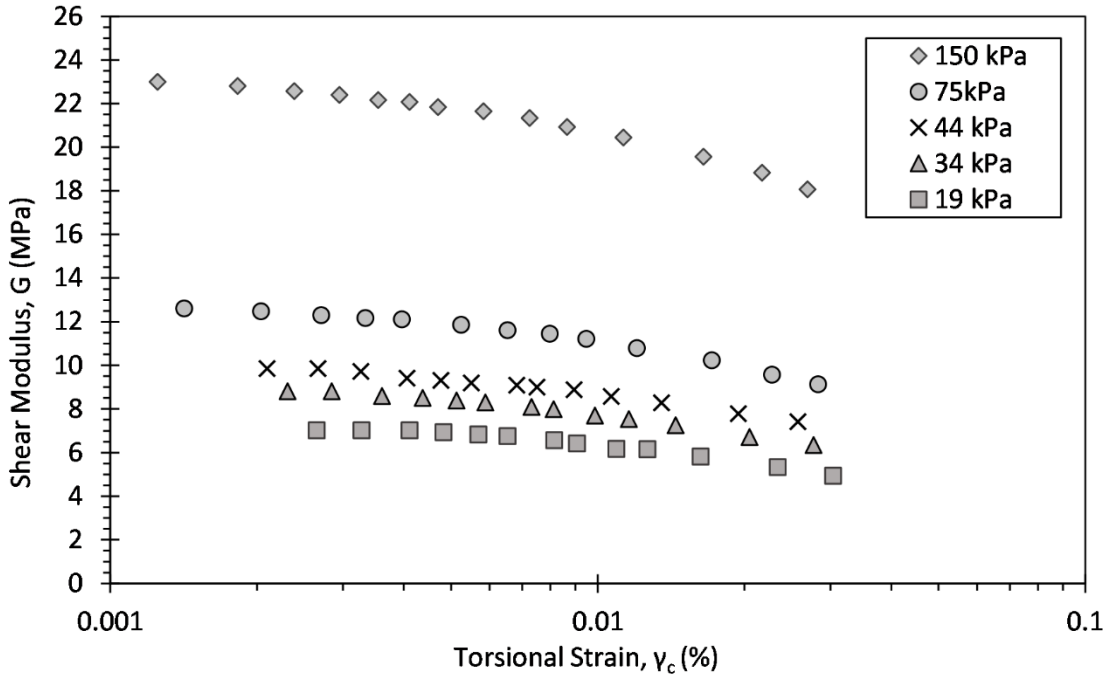

Figure 5.18: Shear modulus degradation with strain for sample GH1D during torsional excitation in the RC, at a range of vertical effective stresses. Strain limits not met.

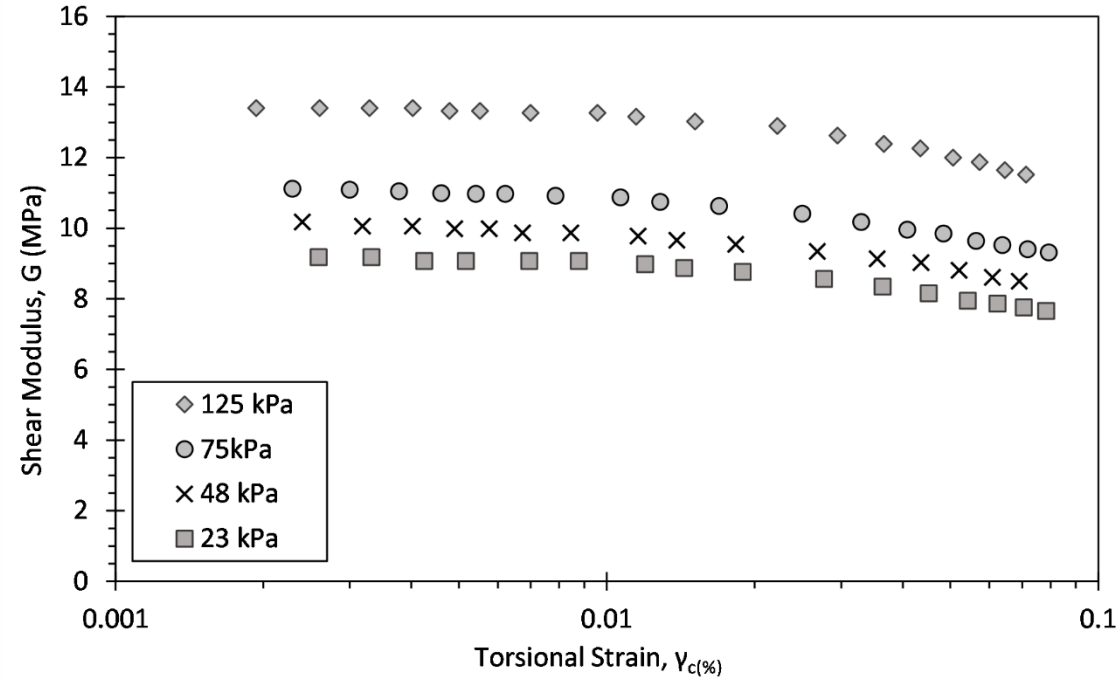

Figure 5.19: Shear modulus degradation with strain for sample GH2K during torsional excitation in the RC, at a range of vertical effective stresses. Strain limit met for all but 75 kPa and 125 kPa.

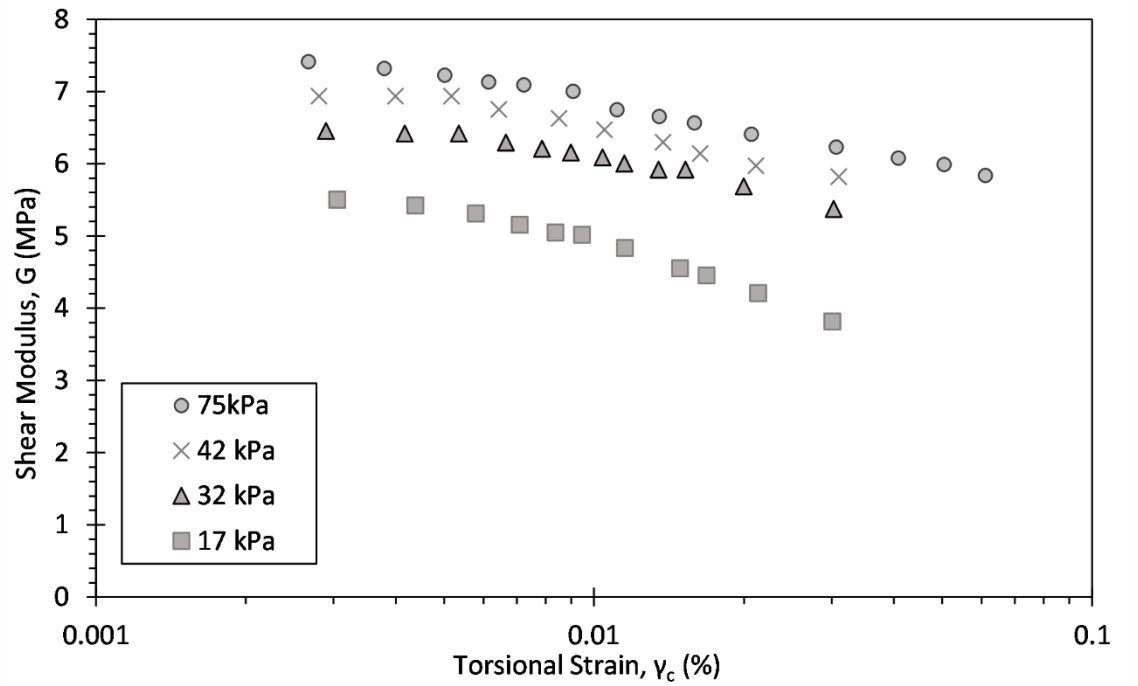

Figure 5.20: Shear modulus degradation with strain for sample GH2C during torsional excitation in the RC, at a range of vertical effective stresses. Strain limit met for 75 kPa.

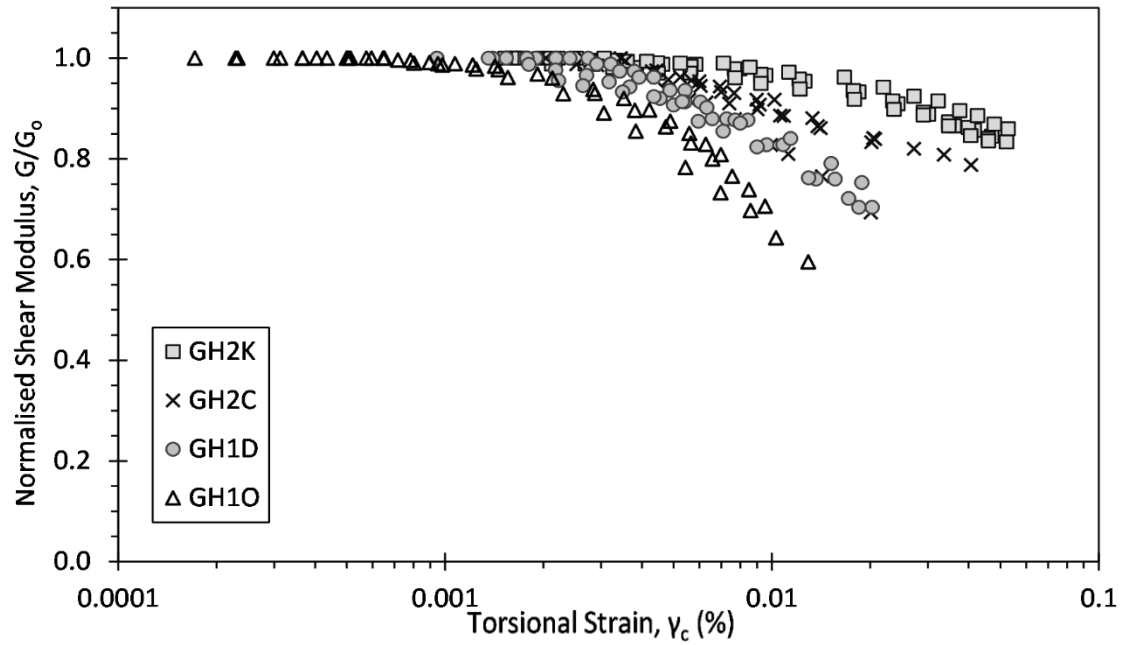

Figure 5.21: Normalised shear modulus degradation with strain for all Gravel Hole samples in the RC, for a range of vertical effective stresses, normalised by small strain shear modulus at the start of each test.

Figure 5.22 also presents the shear modulus derived from the shear wave speeds measured using the vertical bender elements in the resonant column. These results match the resonant column results very well. The differences between resonant column and bender element values are detailed in Table 5.6. Overall the largest variances, of up to 14.5%, are found in sample GH2C. However, the lack of homogeneity in this sample, as shown in the cross-sections in Figure 5.13,

may go some way to explaining this. Whilst the resonance method excites the entire sample and so gives a modulus for the bulk, the bender element method is exciting waves through mainly the centre of the sample. Therefore, the large inhomogeneity in some of these samples will affect these measurements.

The bender elements measure compressional (P) wave velocity as well as shear (S) wave velocity, although the P wave velocity is harder to identify due to its higher speed and greater sensitivity to noise in the equipment. As the samples are saturated the P wave velocity should be a measurement of the wave being passed through the pore water of the sample. This is affected by the soil type, the effective stress and the chemical makeup of the pore water. Water has a P wave velocity of approximately 1450 ms^{-1}, with very organic soils expected to have a much lower velocity than this (300 ms^{-1} to 700 ms^{-1}) whilst clays usually range from 1100 ms^{-1} to 2500 ms^{-1} (Mavko, 2005). The P wave velocities measured in the Gravel Hole samples (Table 5.7) agree well with the expected values, with the most organic samples having the lowest P wave velocities.

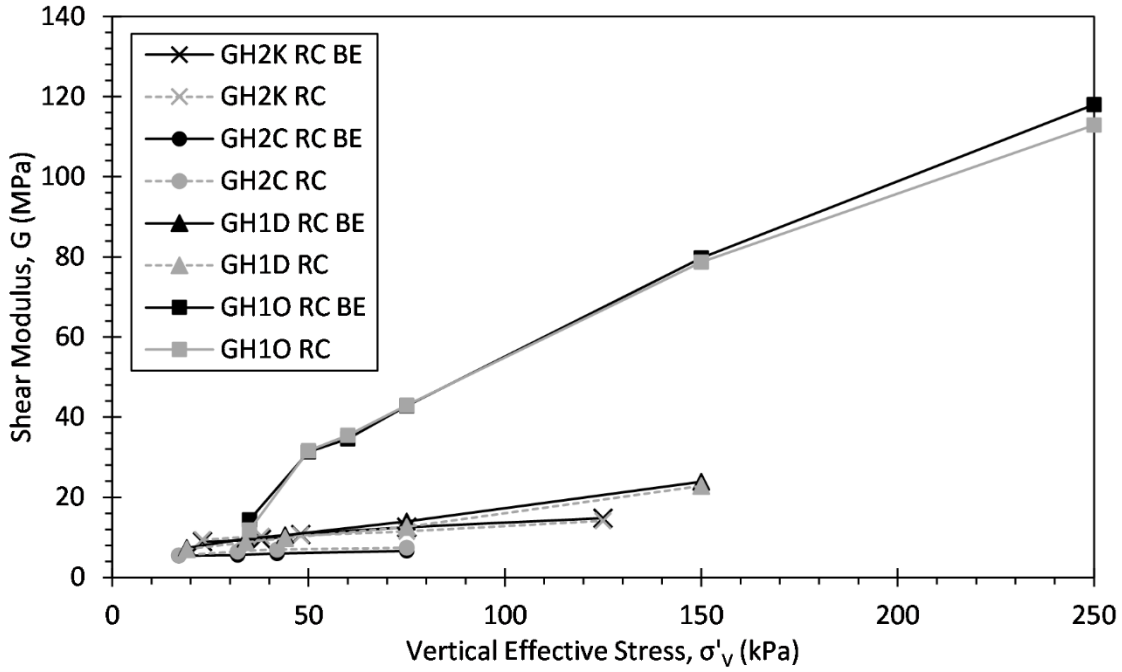

Figure 5.22: Comparison of shear modulus derived from both torsional excitation and BE in the RC, for all Gravel Hole samples for a range of vertical effective stresses.

Table 5.6: G_O values for all Gravel Hole Samples, from both resonant column and bender element techniques.

Sample ID	*Vertical Effective Stress, σ'_v (kPa)*	*RC G_O (MPa)*	*RC BE G_O (MPa)*	*Difference between RC and BE G_0 (%)*	*Sample ID*	*Vertical Effective Stress, σ'_v (kPa)*	*RC G_O (MPa)*	*RC BE G_O (MPa)*	*Difference between RC and BE G_0 (%)*
GH2K	23	9.4	8.9	5.5	GH1D	19	7.0	7.3	4.2
	38	10.2	9.5	7.9		34	8.8	9.6	8.8
	48	10.5	10.7	1.89		44	9.8	10.5	6.9
	75	11.5	12.5	8.33		75	12.6	14.0	10.5
	125	14.1	14.8	4.84		150	22.8	23.9	4.7
GH1O	35	11.8	14.4	19.8	GH2C	17	5.5	5.4	1.83
	50	31.6	31.3	0.8		32	6.5	5.6	14.1
	60	35.5	34.6	2.6		42	6.9	6	14.5
	75	43.0	42.8	0.5		75	7.4	6.6	11.6
	150	78.7	79.7	1.26					
	250	112.9	118	4.4					

Table 5.7: Compressional and shear wave speeds measured in the RC using bender elements.

Sample ID	*Vertical Effective Stress, σ'_v (kPa)*	*V_S (ms^{-1})*	*V_P (ms^{-1})*	*Sample ID*	*Vertical Effective Stress, σ'_v (kPa)*	*V_S (ms^{-1})*	*V_P (ms^{-1})*
GH2K	23	80	415	GH1D	19	69	1307
	38	82	420		34	79	1312
	48	87	427		44	82	1309
	75	94	424		75	94	1330
	125	102	436		150	123	1354
GH1O	35	80	751	GH2C	17	68	340
	50	119	1394		32	78	330
	60	125	1386		42	71	367
	75	139	1390		75	74	385
	150	189	1398				
	250	230	1405				

Damping

Damping was also successfully measured for all the samples, see Figure 5.23 (GH1O), Figure 5.24 (GH1D), Figure 5.25 (GH2K) and Figure 5.26 (GH2C). Damping ratios for samples GH1O (clay) and GH1D (sandy silt) are higher than for GH2D and GH2C (soft to very soft silts) and increase faster with strain. In general for each sample the measured damping ratios seem to be similar across the test pressures, differing most at the smallest strain levels. The damping ratios sit within expected ranges for these types of soils. No clear relationship is shown between confining pressure and damping. This is in agreement with the testing of Kallioglou *et al.* (2008) on organic cohesive materials.

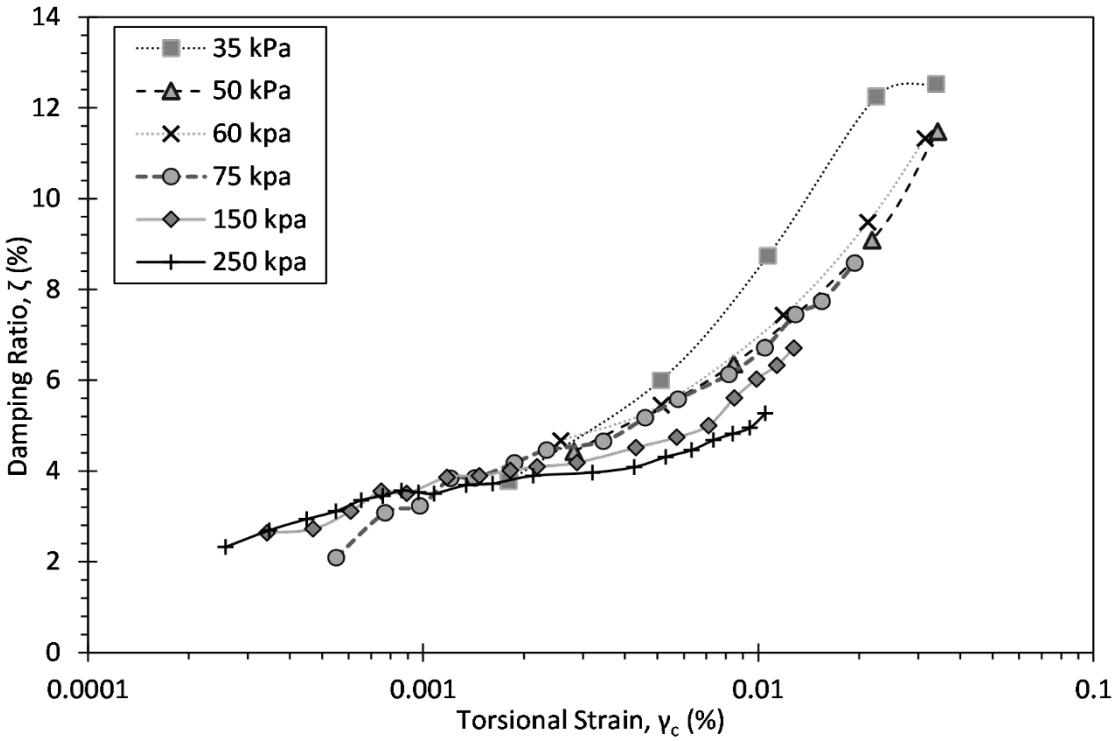

Figure 5.23: Relationship between damping and strain for sample GH1O, during torsional excitation in the RC, for a range of vertical effective stresses.

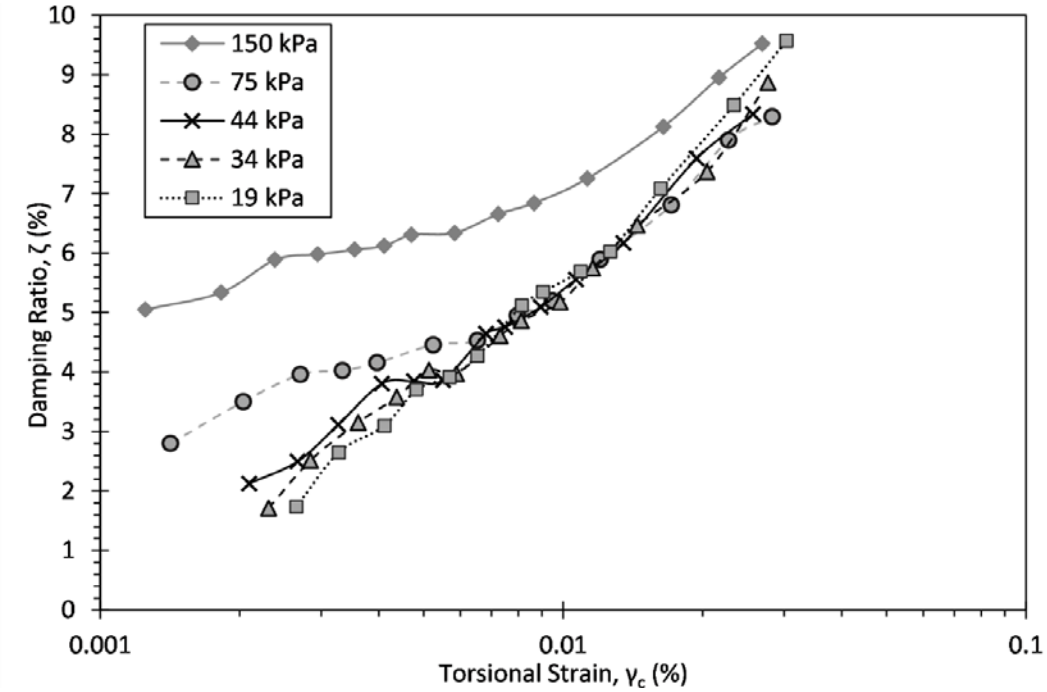

Figure 5.24: Relationship between damping and strain for sample GH1D, during torsional excitation in the RC, for a range of vertical effective stresses.

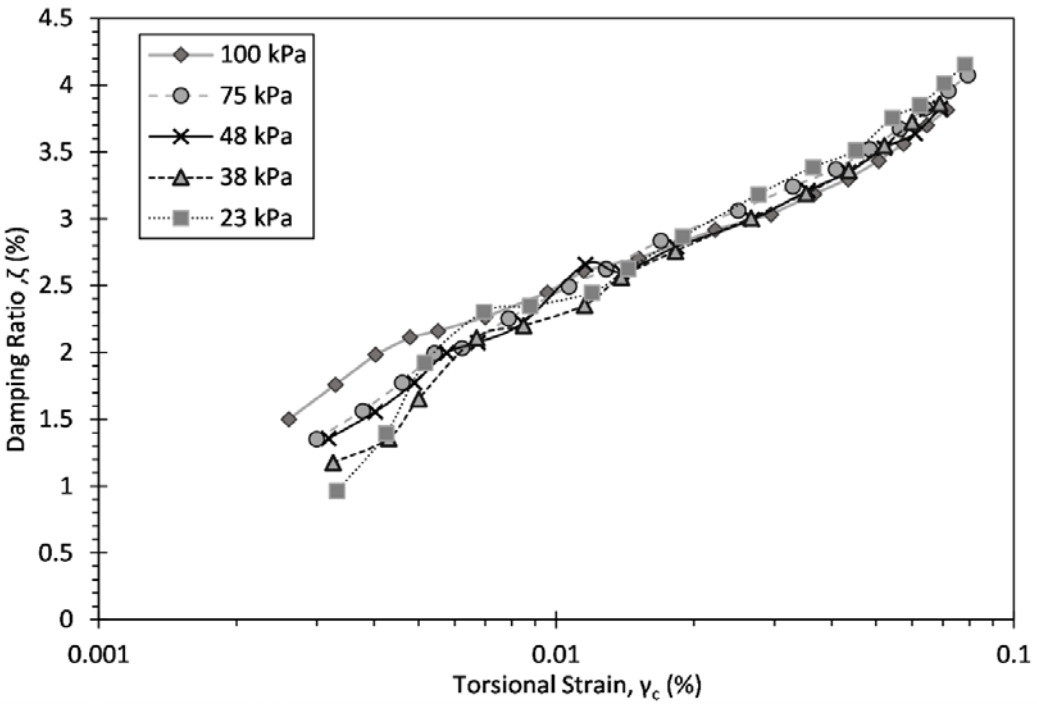

Figure 5.25: Relationship between damping and strain for sample GH2K, during torsional excitation in the RC, for a range of vertical effective stresses.

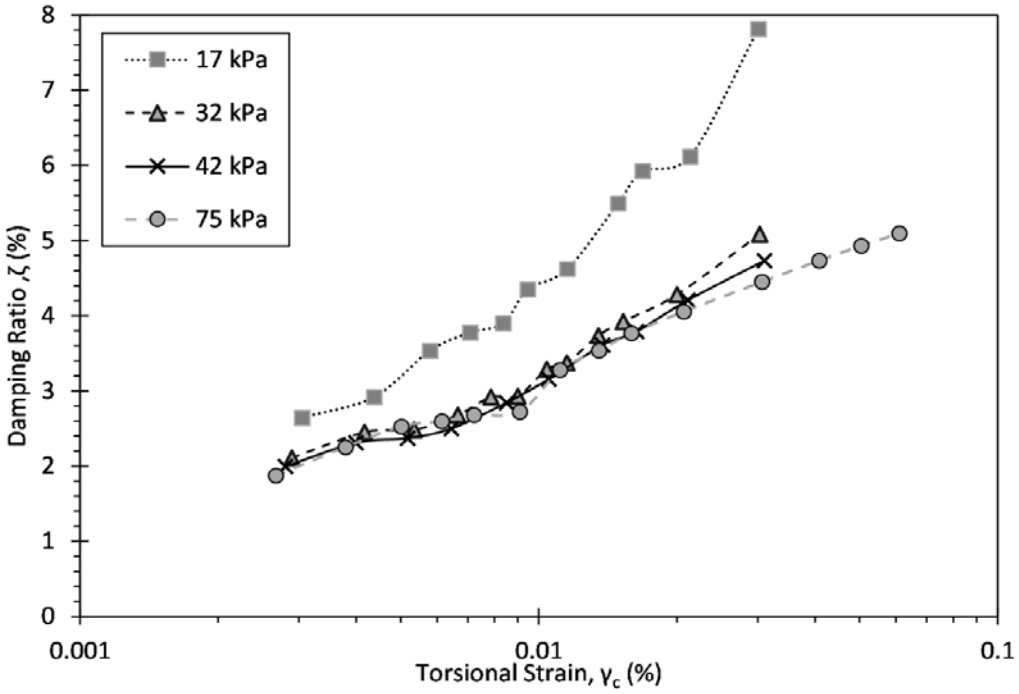

Figure 5.26: Relationship between damping and strain for sample GH2C during torsional excitation in the RC, for a range of vertical effective stresses.

5.4.3 Triaxial / bender element results

GH1P was consolidated isotropically, and tested with constant σ'_v and constant σ'_h probe tests. This enables a more direct comparison to the resonant column, as the consolidation method is the same, and allows simpler analysis of results. The remaining three samples were to be consolidated along the K_O line, and tested with constant p' and constant q probes. Problems were found with the initial GH1A sample to be tested with this method as, despite using advanced pressure controllers, the drift in pressure and ram load were too large for the very low effective stresses being targeted and so no meaningful results were gained.

To improve this a GDS remote feedback module (RFM) was fitted to the cell pressure controller and a differential pressure transducer (DPT) to the cell. Taps were taken close to the cell from the cell pressure and pore pressure lines, and plumbed into the DPT. The output from this transducer was therefore a constant cell level reading of p', the mean effective stress. The RFM enabled the GDS software to be programmed to control a target p', rather than a target cell pressure. For a target constant p' this reduced total drift to ± 0.75 kPa, from the ± 2 kPa being achieved beforehand. Two different startup files enabled the GDS software to be run in either 'traditional' mode, controlling the cell pressure and back pressure, or 'RFM' mode, controlling the mean effective stress and back pressure.

Samples GH2J and GH2D were saturated and consolidated along the K_O line to each target mean effective stress, with drained and undrained constant q and constant p' probes being carried out at the target stress points. An example stress path, for sample GH2J, is presented in Figure 5.27. The ratio of q to p' required to meet K_O conditions averaged 0.74, close to the value of 0.75 predicted beforehand (section 4.4.4). It should be noted that whilst excellent control of the load ram was found in the constant q probes, with a cycle range of ± 0.025 kPa around the target pressure, the control of p' in the constant p' probes was less effective. A total movement away from the target p' of 1.5 kPa was found for each probe. Therefore the movement away from the target p' for all probes sits in the range of 0.6% to 8.8%. The impact of this movement is more significant for the low target stresses in these tests, and would be of negligible impact for more common higher stress triaxial tests. This movement is caused by the pressure controller software not wanting to exceed the set target pressure, therefore having a tendency for the measured pressure to sit just below the target pressure.

Stress and strain data was recorded at a high resolution, with measurements being logged every 2 to 5 seconds during probes, resulting in between 3000 and 10000 data points per probe load. Load and unload cycles for constant p' probes generally showed fairly good regain of strain (Figure 5.28) upon unload. In general, global axial strains were smaller than local axial strains, due to end platen effects (Figure 5.29). In constant q tests volumetric strains also showed a decrease upon unloading (Figure 5.30).

The size of each probe was adjusted in an attempt to balance expected soil stiffness with distortional strains within a target range of up to approximately 0.1%. For a very soft sample such as GH2D, this necessitated probes in the range of 2.5 kPa to 5 kPa (Figure 5.31). Larger probes may have been possible at the higher pressures, as distortional strains of 0.05% were found at the highest pressure, however as these strains were sufficiently large to calculate shear modulus the applied probe sizes were not increased.

In order to evaluate the shear moduli, polynomial curves were fitted to the stress-strain data. The differentiation of the polynomial gave an evaluation of the tangent moduli across strain levels. An example is presented in Figure 5.32, including error bars for the measurements of stress and strain, as calculated in 4.4.2. The polynomial order was selected in order to give the best match to the overall curve, with particular focus on the lower strain sections – applying a linear relationship artificially flattens the small strain results, which would affect the small strain shear modulus estimate.

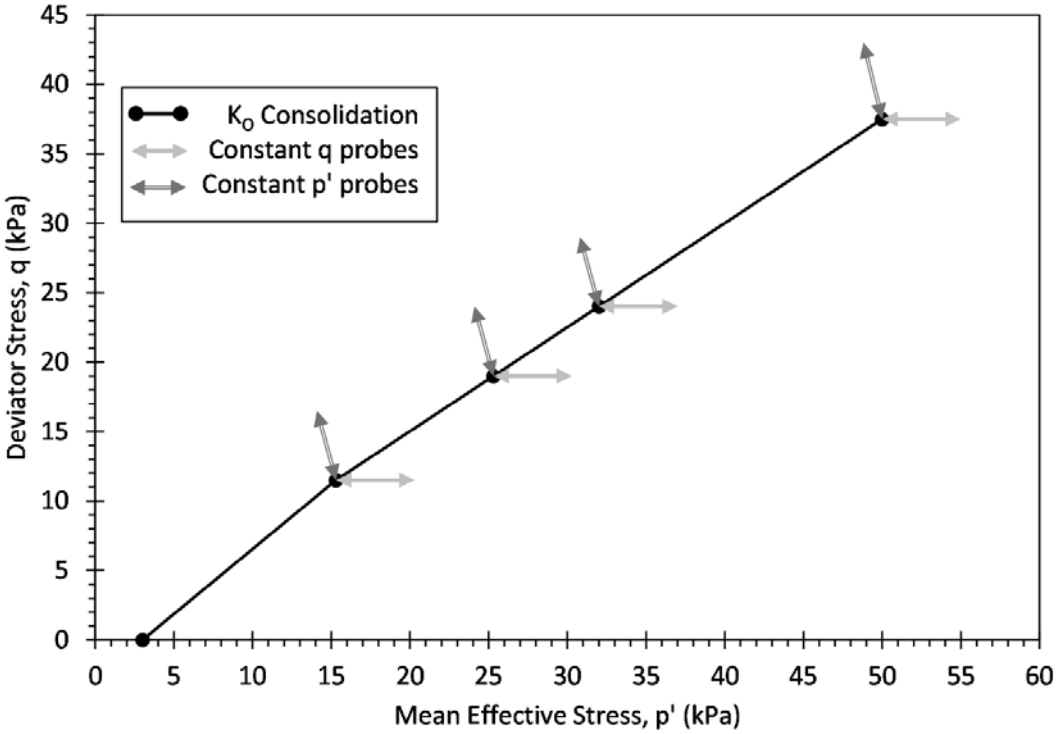

Figure 5.27: Example of K_O consolidation and stress probe paths for sample GH2J in the triaxial machine.

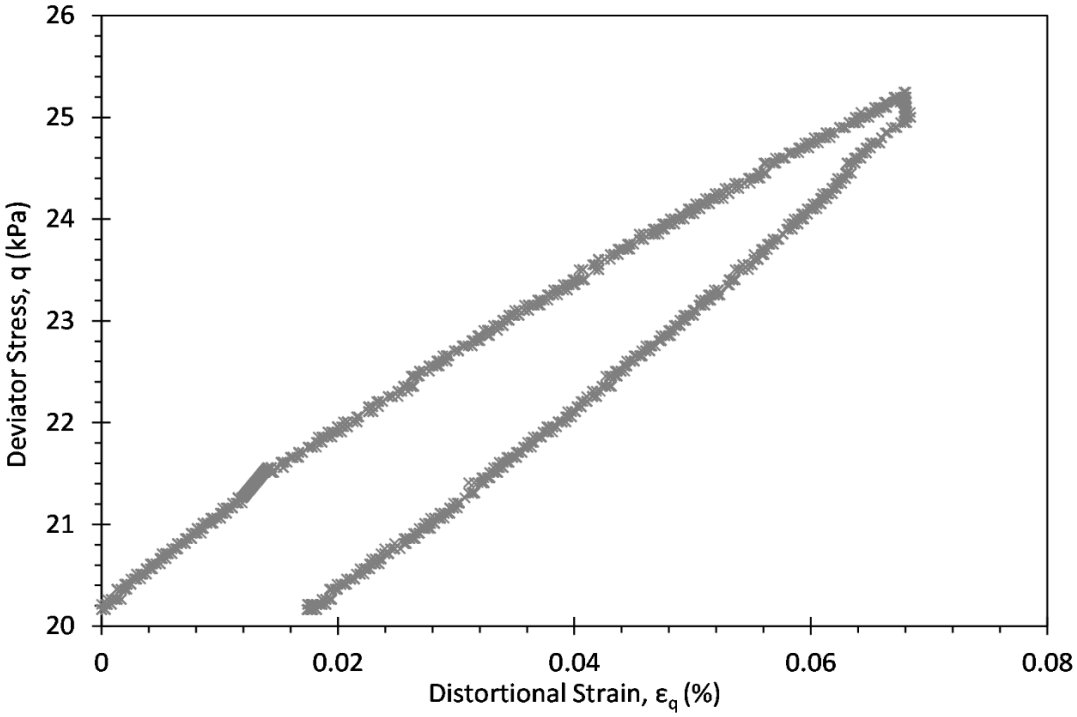

Figure 5.28: Example stress strain data for a constant p' probe (42 kPa) on sample GH2D.

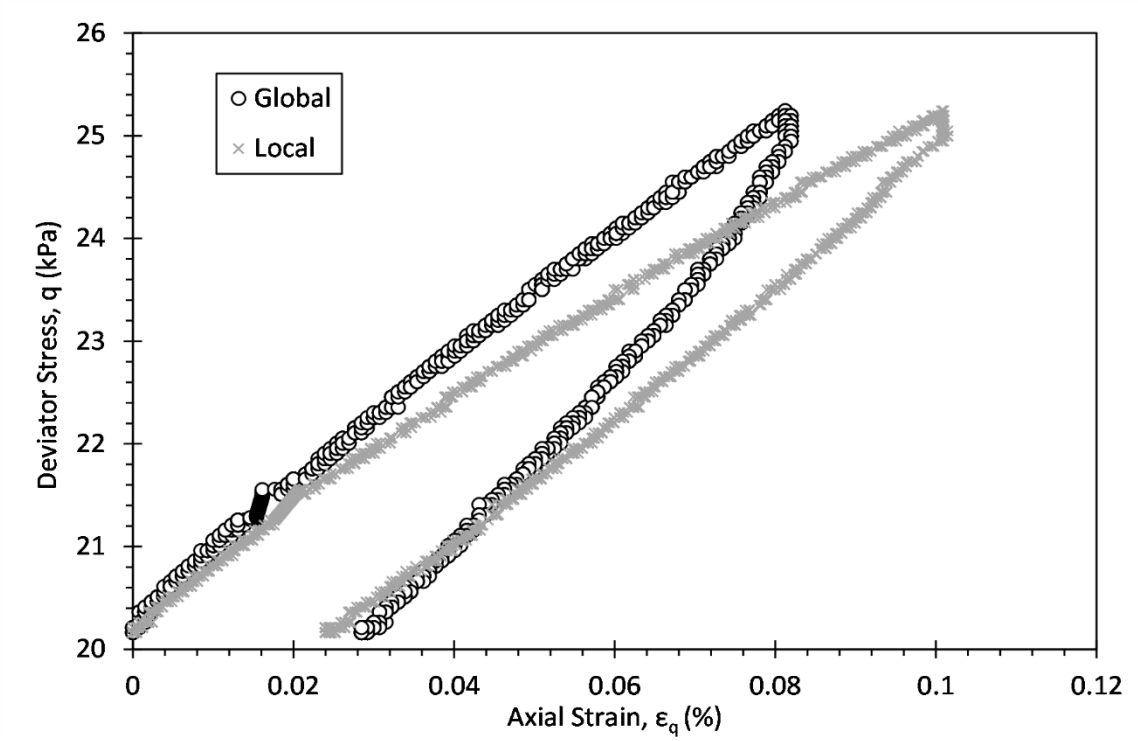

Figure 5.29: Example stress strain data for a constant p' probe (42 kPa) on sample GH2D, showing variance in global and axial strain levels.

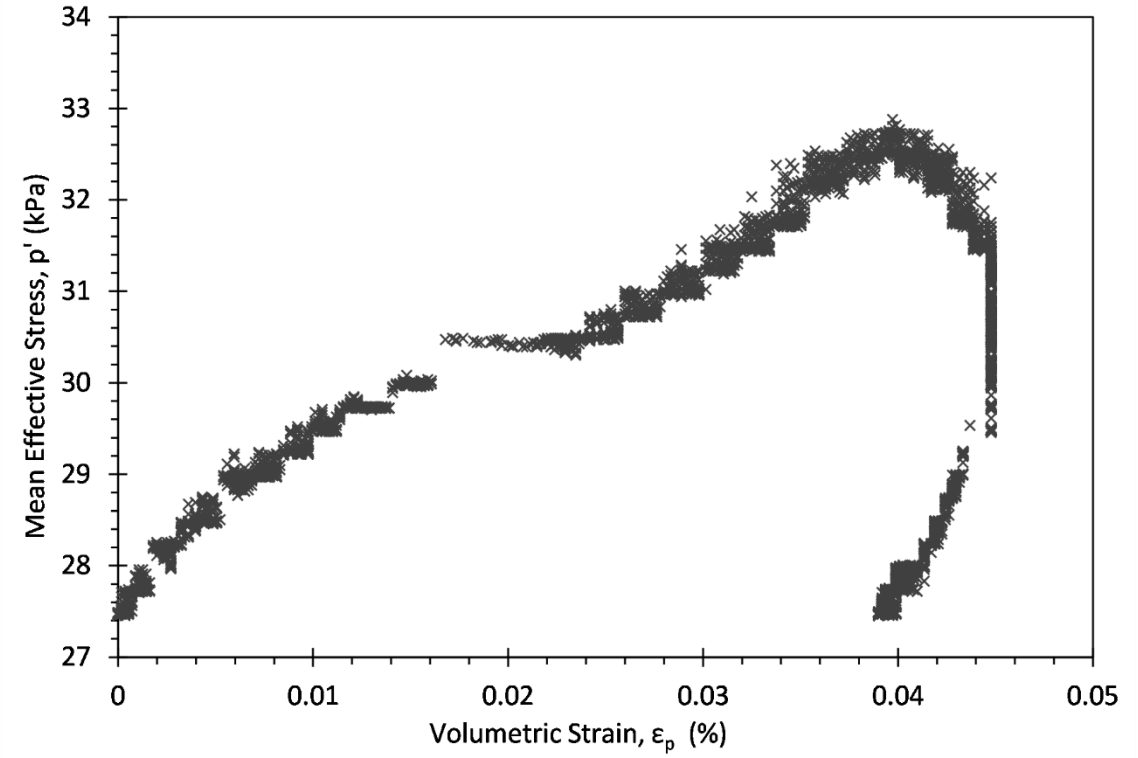

Figure 5.30: Example stress-strain curve for a drained constant q probe (42kPa) on sample GH2D.

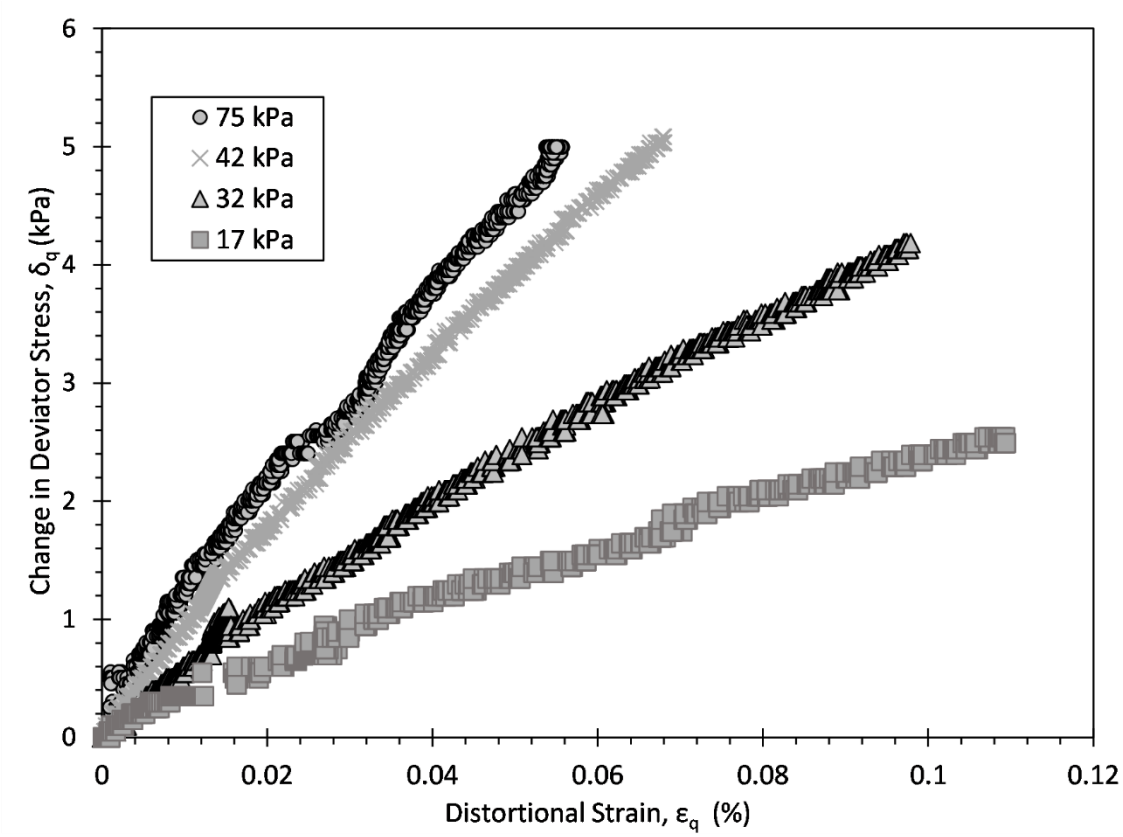

Figure 5.31: Resulting distortional strain for sample GH2D during increasing q, constant p' probes, at a range of mean effective stresses.

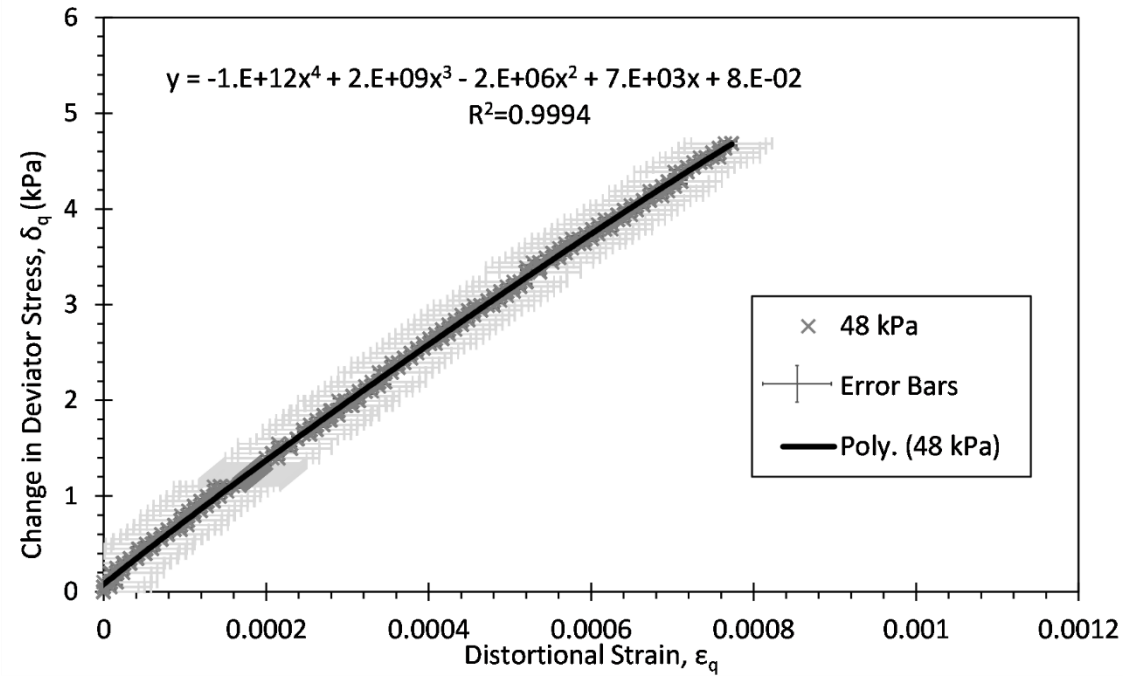

Figure 5.32: Example of stress-strain curve fitting to enable derivation of shear modulus, for sample GH2D during a constant p', increasing q probe at p'=48 kPa. Error bars for deviator stress and distortional strain measurement also shown (+/- 0.25 kPa q ; +/- 0.005% strain).

Shear moduli - isotropic tests (GH1P)

Sample GH1P was consolidated isotropically, i.e. just using increased cell pressure, with no additional ram load. Constant vertical and horizontal effective stress probes were then carried out, and the shear moduli evaluated. The results of this are presented in Figure 5.33, alongside data from the similar sample pair GH1O tested in the RC. In order to compare the RC results to the triaxial data (both isotropic and K_O consolidated) and to other published data, conversion of the RC shear strain measurement (torsional strain γ_c) to the more common direct strain measurement (distortional strain ε_q) is required. The Mohr circle of strain gives:

$$\gamma_c = \varepsilon_v - \varepsilon_h \qquad \text{Equation 5-8}$$

where ε_v is the vertical direct strain and ε_h is the horizontal direct strain. During modelling of soil displacements due to train loading, the soil displacement is overwhelmingly vertical, therefore it is reasonable to assume ε_h is zero. Therefore, for the purposes of critical velocity modelling, utilising the relationship between direct strain and distortional strain (Equation 4-19):

$$\varepsilon_q = \frac{2}{3}(\varepsilon_v - \varepsilon_h) = \frac{2}{3}(\varepsilon_v) = \frac{2}{3}(\gamma_c) \qquad \text{Equation 5-9}$$

The threshold strain beyond which the shear modulus begins to degrade (Zone 2) appears to decrease with increasing pressure, ranging from approximately 0.001% to 0.0009% in the resonant column, and 0.0008% to 0.00007% in the triaxial. However, the threshold strain in triaxial results is strongly dependent on which order polynomial is selected, and so should be treated with caution.

A plot of G_O versus mean effective stress can be used to ease visual comparison between triaxial and resonant column measurements (Figure 5.34). The two data sets match well, especially when considering that they are two natural samples and so are not identical.

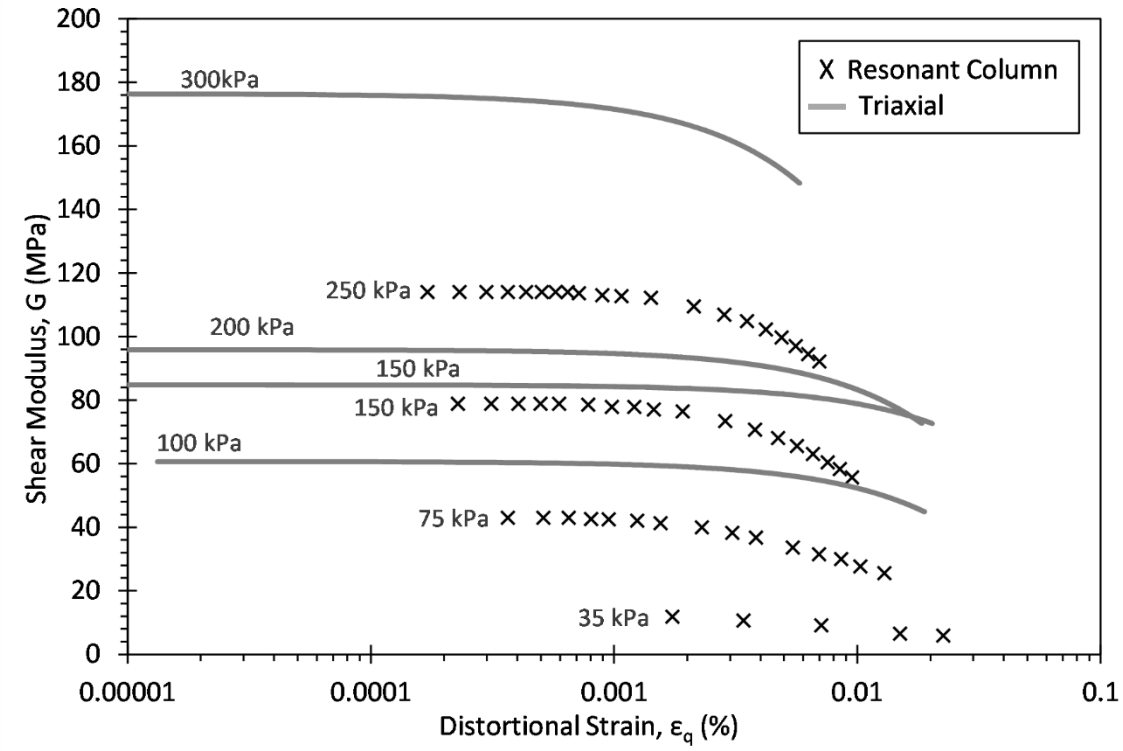

Figure 5.33: Relationship between shear modulus and strain for similar samples GH1O (RC) and GH1P (Triaxial) tested at a range of mean effective stresses.

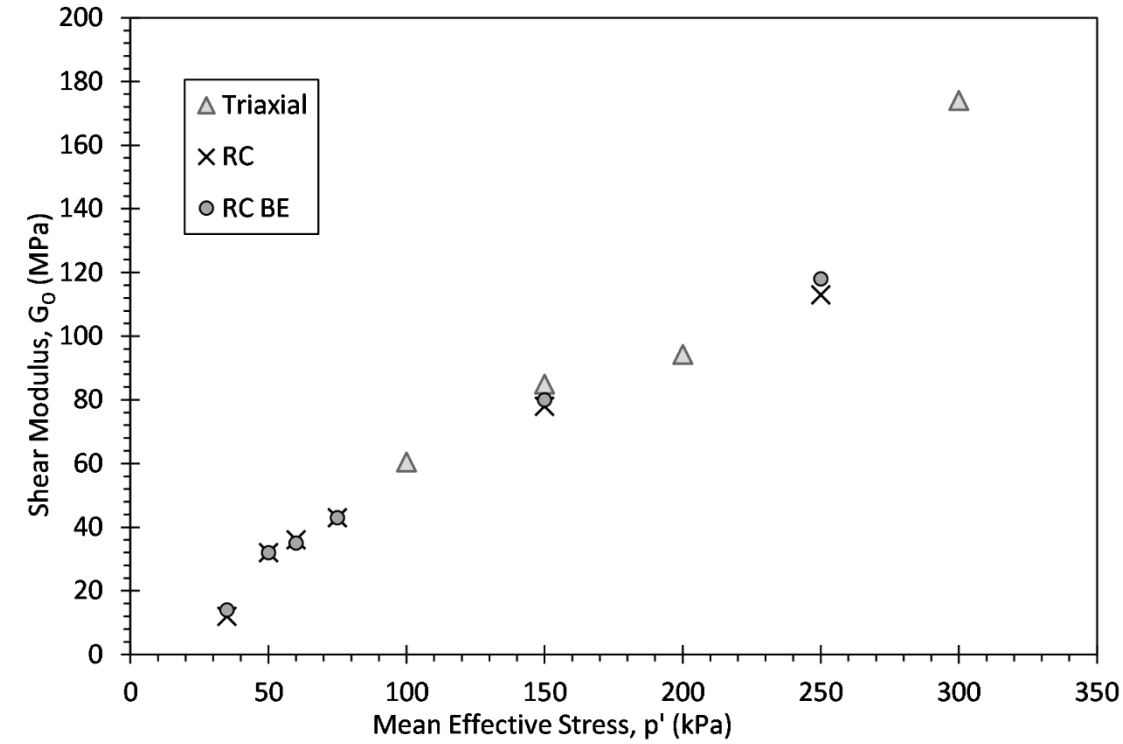

Figure 5.34: Summary comparison of G_O for similar samples GH1O (RC and RC BE) and GH1P (Triaxial) tested at a range of mean effective stresses.

Shear moduli - K_O consolidated (GH2J, GH2D)

The shear moduli degradation curves for samples GH2J (Figure 5.35) and GH2D (Figure 5.36) follow the same overall relationship as their resonant column counterparts, with GH2J having higher shear moduli than GH2D. However, when compared to the resonant column and bender elements results (Figure 5.37), it can be seen that the triaxial results are far lower in moduli, although the rate of increase of modulus with pressure is similar.

These triaxial shear moduli results are particularly low. There are several possible reasons for this, and for the difference between the resonant column and triaxial results. Firstly, as mentioned there was some drifting controlling p' so the assumptions of the analysis, that p' remains constant, were not quite met. Secondly, the consolidation methods differ, with the K_O consolidation in the triaxial applying an axial ram load in addition to a cell pressure. The resonant column applies a single isotropic load (cell pressure), which is higher than the cell pressure in the triaxial machine, so that the overall vertical effective stress in both pieces of equipment are identical. For these samples the average final height and radius, compared to the original dimensions, were 93.5% and 94.1% in the resonant column, and 91% and 99.6% in the triaxial.

Although the resonant column and triaxial samples were not identical, they were similar, and so the general impact of the differing consolidation method is as expected – greater height compression in the triaxial, lesser height compression but greater radial compression in the resonant column. Whilst these differing methods of consolidation (K_O versus isotropic) clearly have an impact on the way that samples consolidate, very little published data is available to define the impact of the different methods, and so it is not possible to factor this in when comparing moduli measurements from the different sources.

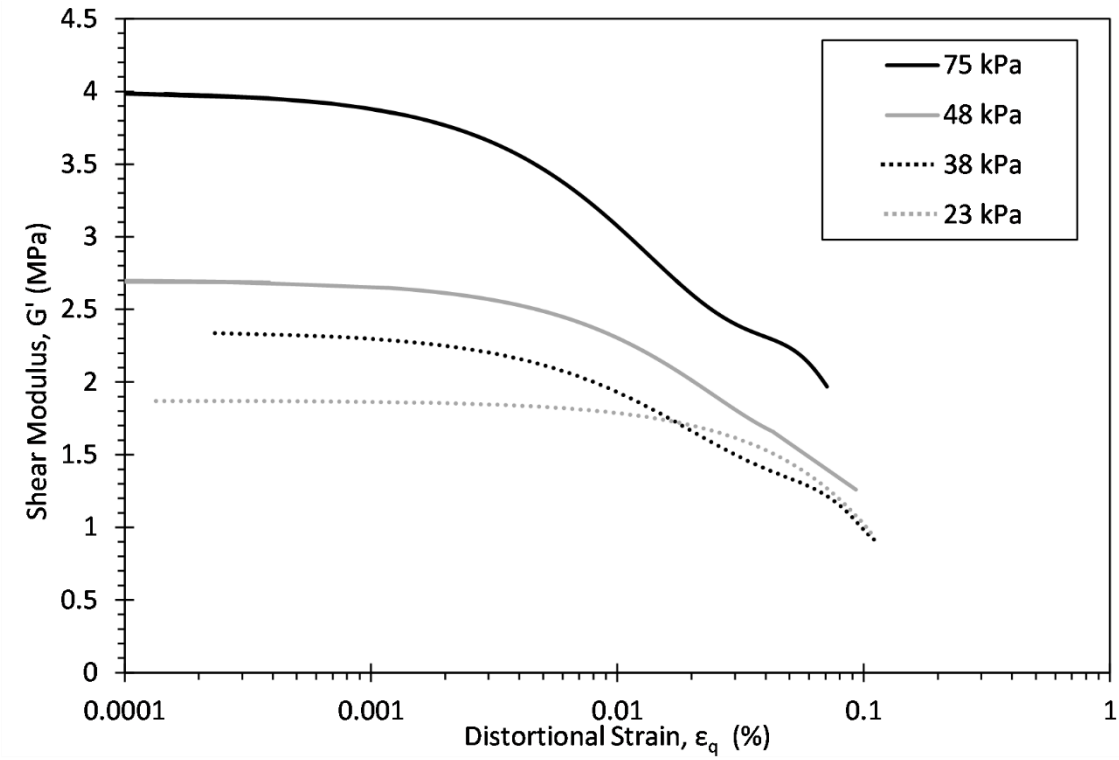

Figure 5.35: Shear modulus degradation with strain for sample GH2J from constant p', increasing q triaxial probes, at a range of mean effective stresses.

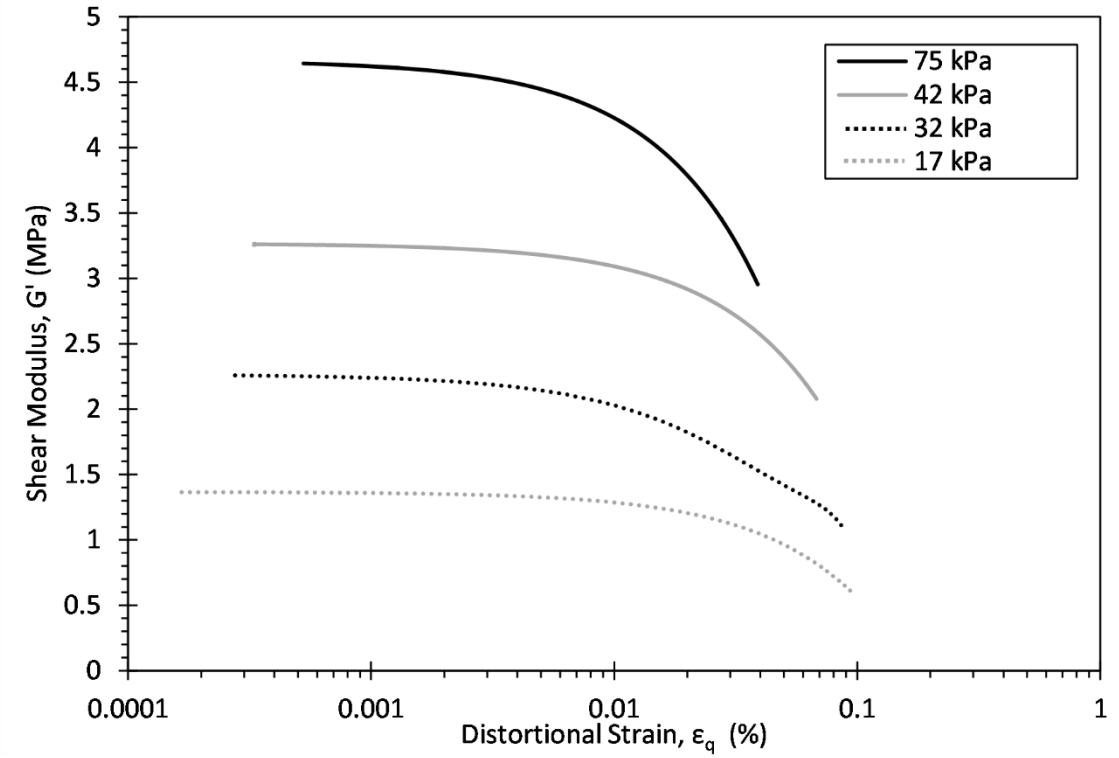

Figure 5.36: Shear modulus degradation with strain for sample GH2D from constant p', increasing q triaxial probes, at a range of mean effective stresses.

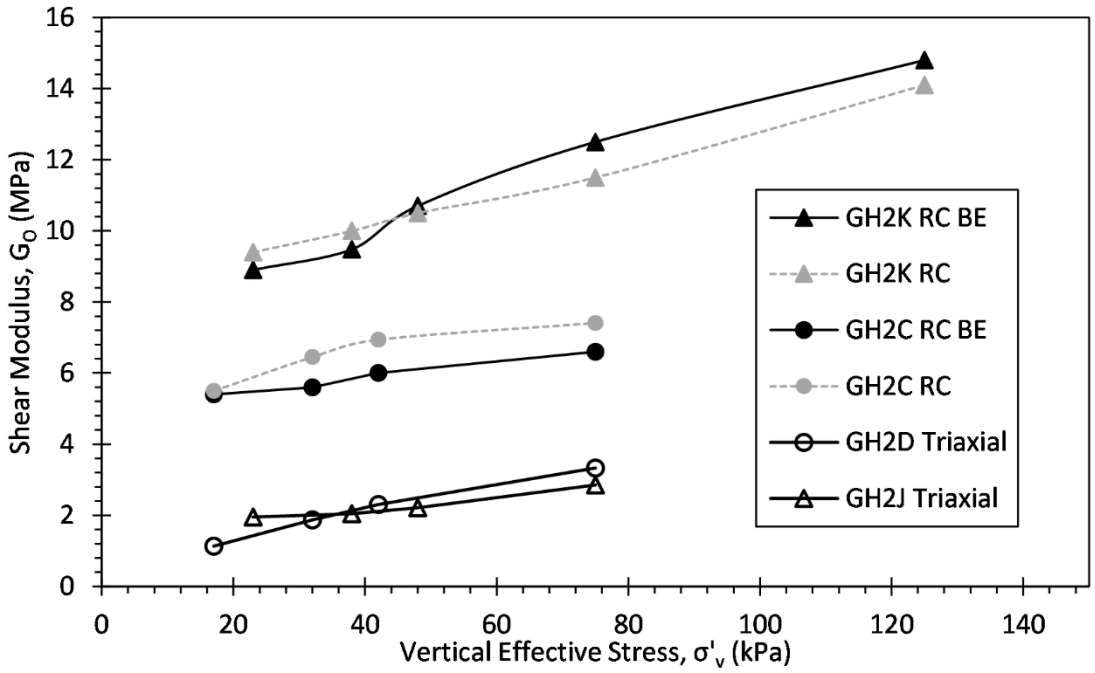

Figure 5.37: Comparison of relationship between very small strain shear modulus and vertical effective stress, for samples tested in the RC, RC BE and triaxial machines. Samples GH2K and 2H2J are considered similar, as are GH2C and GH2D.

Poisson's ratio

To calculate Poisson's ratio from the constant horizontal effective stress probes for sample GH1P, the differential of a linear trendline fitted to local axial and radial strain data is used (Figure 5.38). This derives a single value of Poisson's ratio v'_{hh} from each stress test, see Figure 5.39. v'_{hh} is the Poisson's ratio for horizontal stress on horizontal strain. A strong trend of increasing Poisson's ratio with stress level is found. These values range from 0.013 to 0.032.

Poisson's ratios for samples GH2D and GH2J are derived from the method set out in section 4.4.2, see Figure 5.40 and Figure 5.41. These constant p' and constant q probes measure $v'_{vh,}$ the Poisson's ratio for vertical stress on horizontal strain. The results for sample GH2J show some variation with stress level, but are generally very consistent, decreasing with strain from approximately 0.5 to 0.35. The results for sample GH2D are more variable, with no clear relationship between pressure and Poisson's ratio. This may be due to poor measurement of radial strain during certain probes – for the lowest pressure (17 kPa) test the radial strain measurement was particularly erratic, perhaps due to the low confining pressure and very small resulting movements. However, there still seems to be a general trend value of 0.5 to 0.45. Overall these values sit within expected ranges for saturated silts and clays (Bowles, 1997).

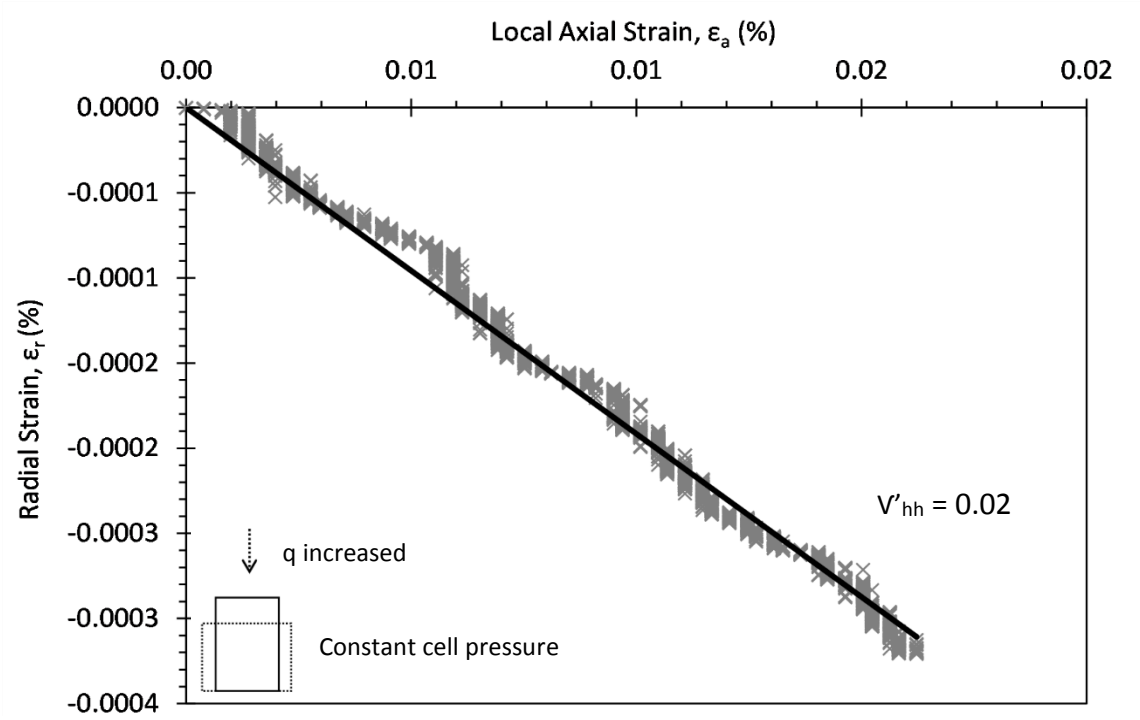

Figure 5.38: Example application of a linear trendline to axial and radial strain data, to allow estimation of Poisson's ratio from constant σ'_h, increasing σ'_v triaxial probes for sample GH1P.

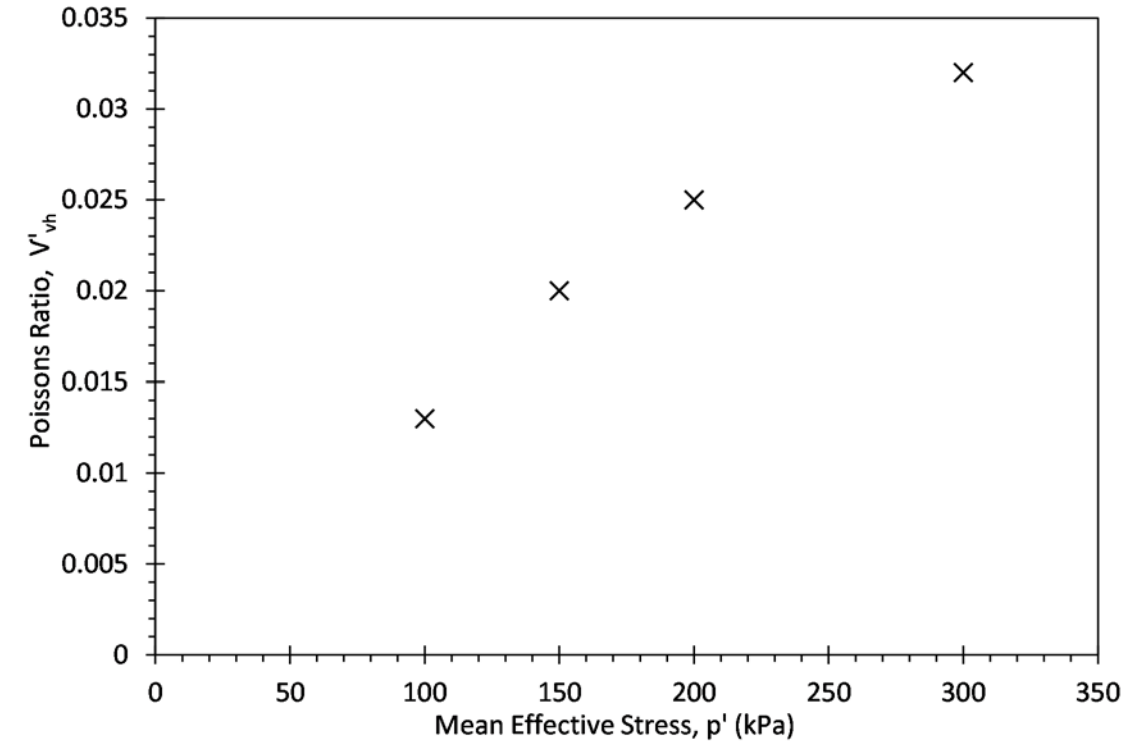

Figure 5.39: Relationship between Poisson's ratio and mean effective stress for sample GH1P tested with constant σ'_h, increasing σ'_v triaxial probes.

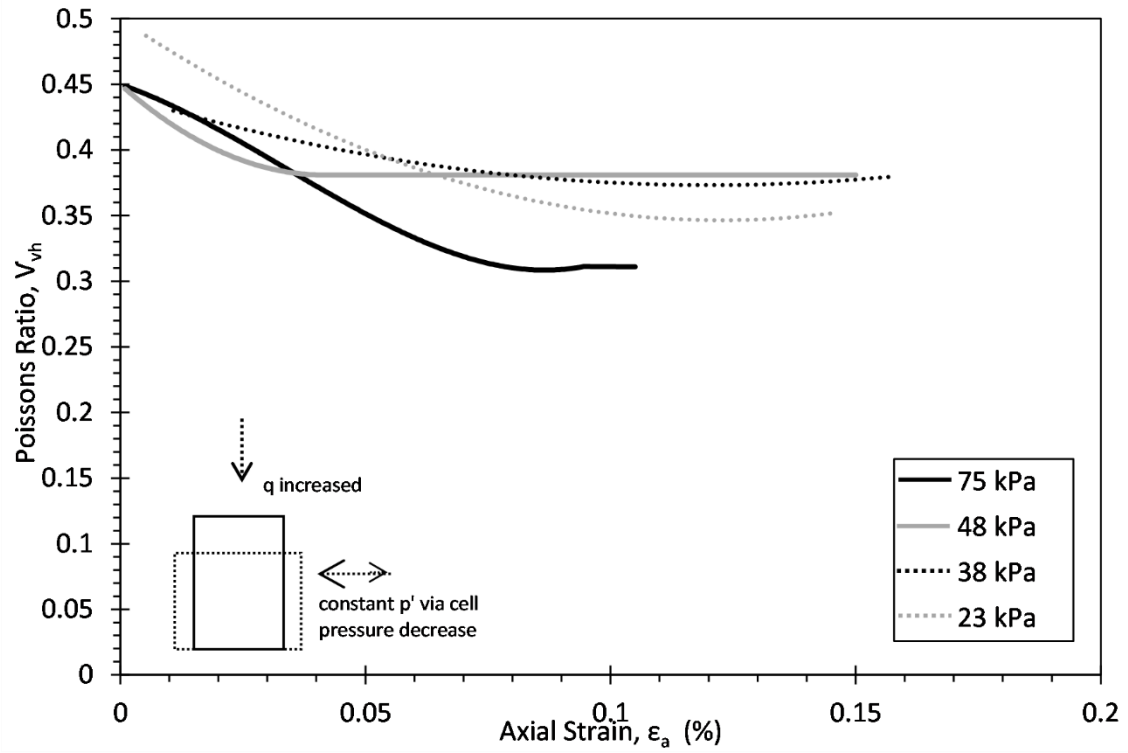

Figure 5.40: Relationship between Poisson's ratio and axial strain, for sample GH2J tested with constant p', increasing q triaxial probes.

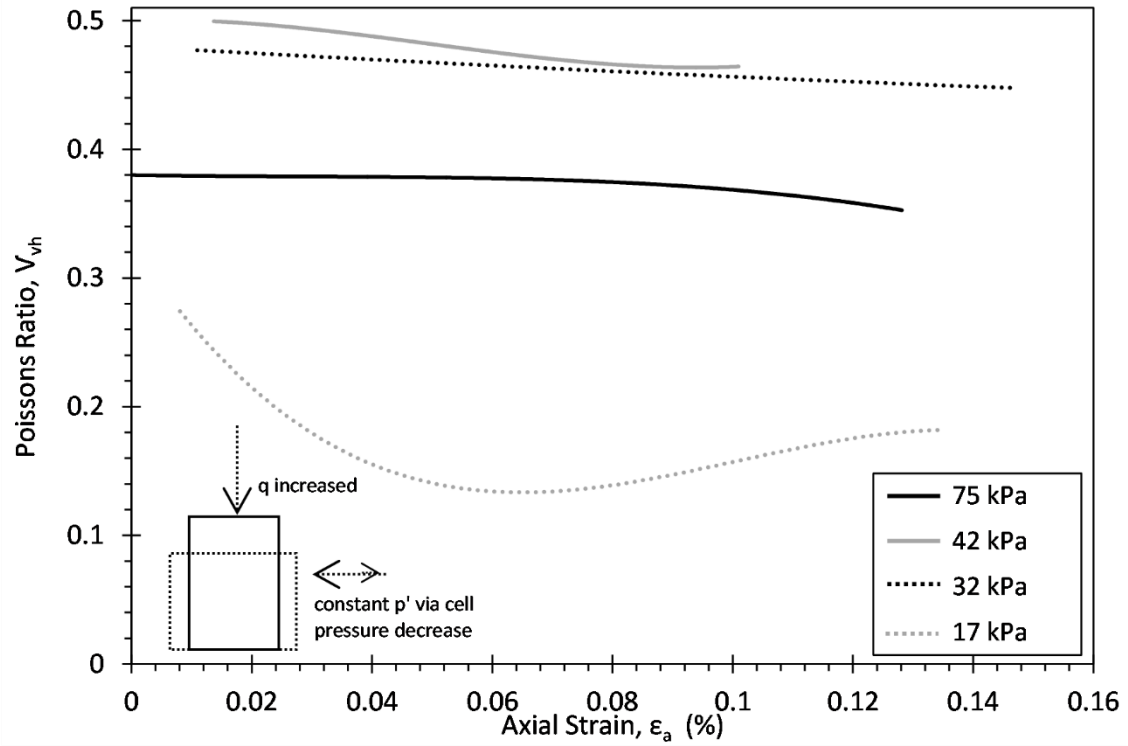

Figure 5.41: Relationship between Poisson's ratio and axial strain, for sample GH2D tested with constant p', increasing q triaxial probes.

Peak undrained strength

After probes at the largest consolidation pressures were complete, large strain shear tests were carried out. Global axial strains of 15 % were targeted at a rate of 0.5 % per hour. Peak strengths, and the axial strains at which these occurred, were measured as in the example Figure 5.42. The peak undrained strength, C_u, is equal to half of the peak deviator stress. The peak undrained strengths, the related strains, and the pressures at which they were measured are presented in Table 5.8. The strength of sample GH1P (clay) is a factor of 10 higher than samples GH2D and GH2J (silt), although GH1P was tested at a higher pressure.

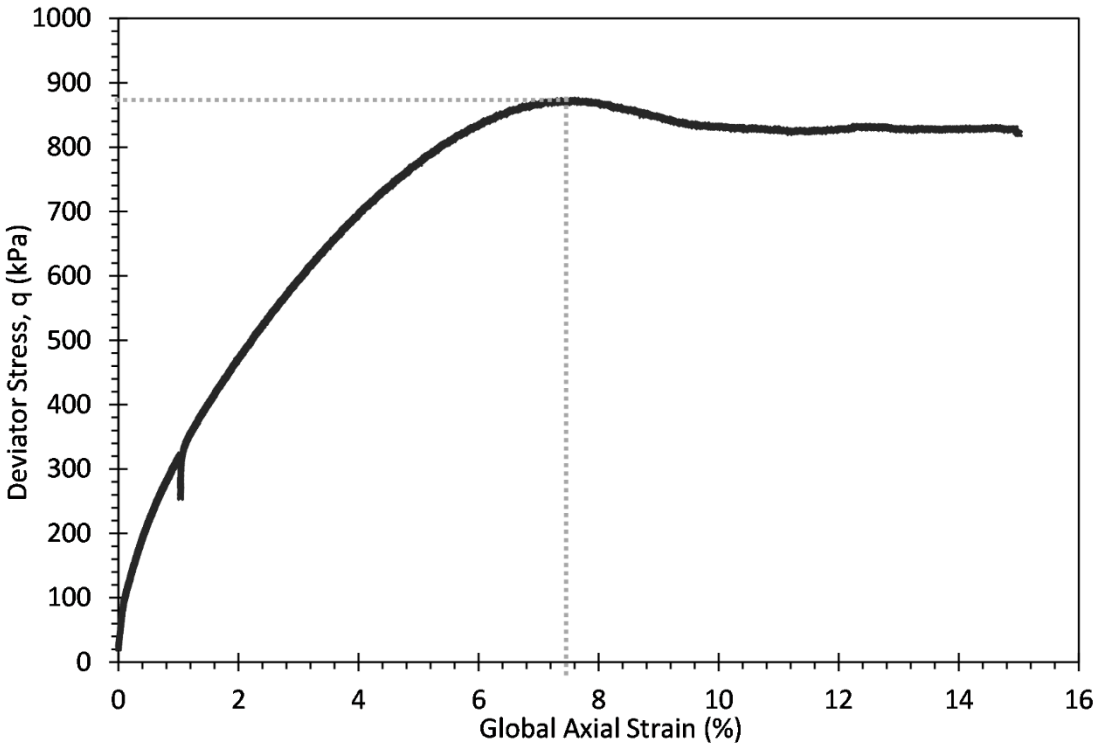

Figure 5.42: Peak undrained strength calculation from large shear test - GH1P. Peak strength is equal to half the peak stress.

Table 5.8: Peak undrained strengths - triaxial tests

Sample ID	*Mean Effective Stress, p' (kPa)*	*Vertical Effective Stress, σ'_V (kPa)*	*Peak Undrained Strength (kPa)*	*Peak Axial Strain (%)*
GH1P	300	300	435	6.75
GH2J	50	75	50	5.15
GH2D	50	75	40	2.45

G* and G_{hv}

Some work, see section 4.4.2, attempted to show continuity between dynamic and static measurements through comparing dynamic G_{hv} measurements, from bender elements, with the static G* measurements derived from an undrained constant mean stress triaxial test. In samples GH2J and GH2D successful horizontal bender element measurements were taken, allowing derivation of the vertical shear modulus G_{hv}, as well as undrained probes, allowing derivation of G*, a shear modulus parameter proposed by Graham and Houlsby (1983).

A comparison of the small strain stiffness results is presented in Figure 5.43. There is no strong relationship presented between the two sets of results, although G_{hv} is consistently lower than G*. It should be noted that no relationship would be expected unless the soil was isotropic, as in an anisotropic soil these two parameters are independent. It should also be noted that G* is a modulus of the bulk material, as the entire sample is tested, whereas G_{hv} passes shear waves through a relatively small section of the sample. As these samples show great variability across their length and width it is reasonable to expect only limited correlation between the measurements.

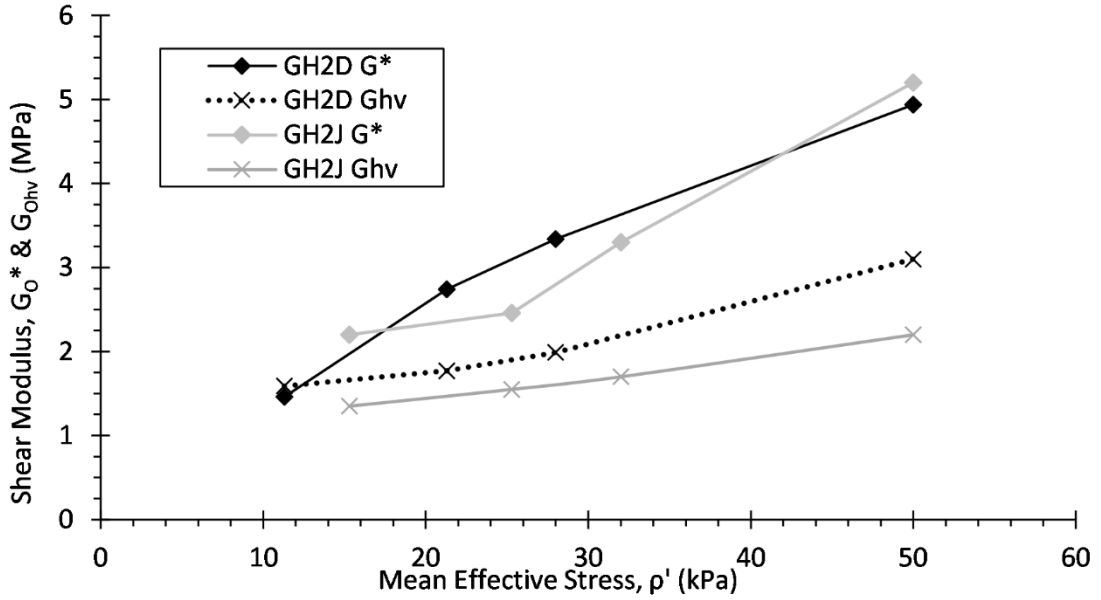

Figure 5.43: Comparison of the small strain shear moduli parameters G*, derived from undrained triaxial tests, and G_{hv}, derived from bender element tests, presented for a range of test pressures.

5.4.4 Comparison of results from both methods

Normalisation of the derived shear moduli by the small strain modulus enables comparison of the degradation rates between the resonant column and the triaxial samples, see Figure 5.44 and Figure 5.45. In general the gradients of the degradation curves are similar across the methods,

with the threshold strains being lower for the triaxial than the resonant column, as previously discussed.

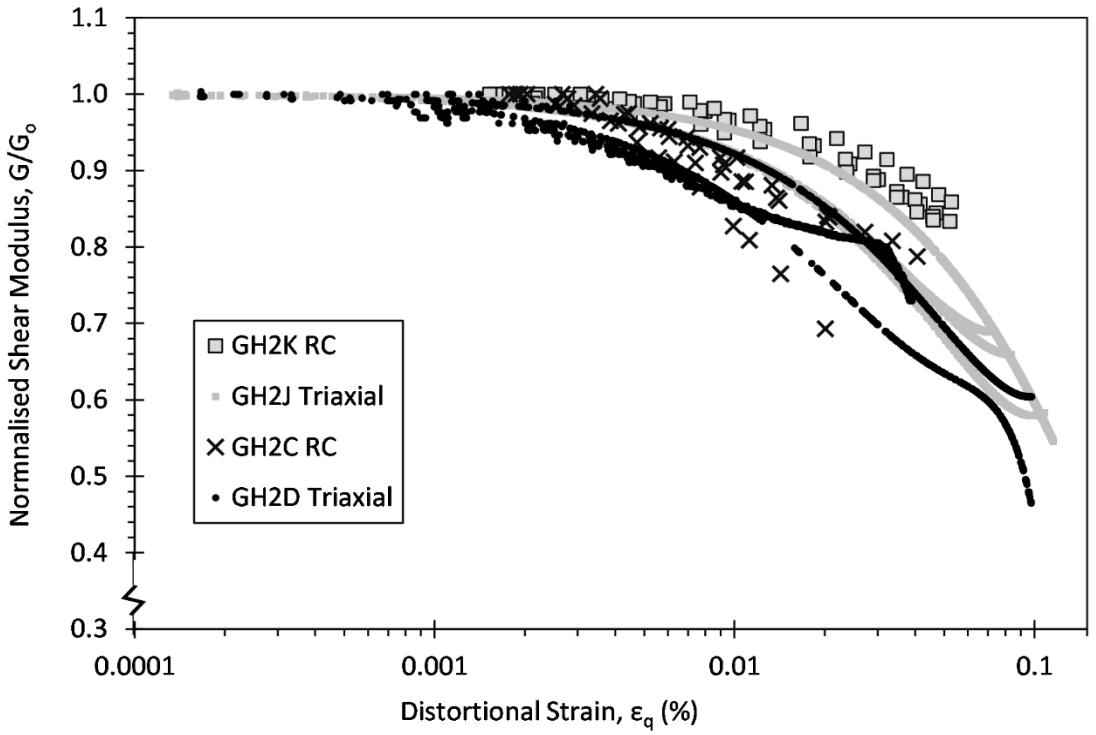

Figure 5.44: Normalised shear modulus degradation with strain for similar Gravel Hole sample pairs GH2K + GH2J and GH2C + GH2D, in the RC and triaxial machines. Results shown are for a range of mean effective stresses.

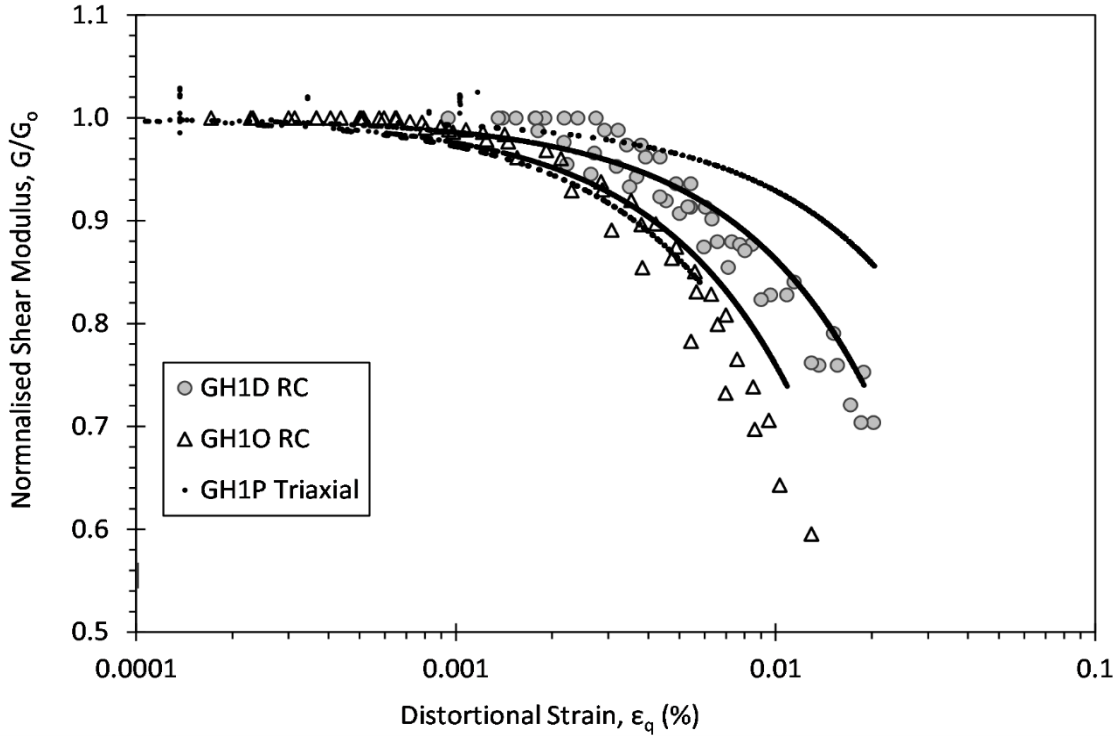

Figure 5.45: Normalised shear modulus degradation with strain for similar Gravel Hole sample pairs GH1P+ GH1O and sample GH1D, in the RC and triaxial machines. Results shown are for a range of mean effective stresses

As the samples have only been tested up to relatively small strains, comparison to published data for modulus degradation rates at higher strains is necessary. As the plasticity index for GH1O/P is known, the normalised shear modulus degradation can be compared to degradation rates measured for clays of different plasticity indexes (Figure 5.46). The measured plasticity index for GH1O/P is 10.9 %, the measured degradation curves do not appear to match the literature curves for this plasticity index, instead showing faster degradation, especially in the RC. The pressure at which the literature data curves were measured is not known, nor the specific types of clay tested. The difference in curves may be due to the substituents of GH1O/P, it is not a pure clay, or due to differences in the measurement of strain.

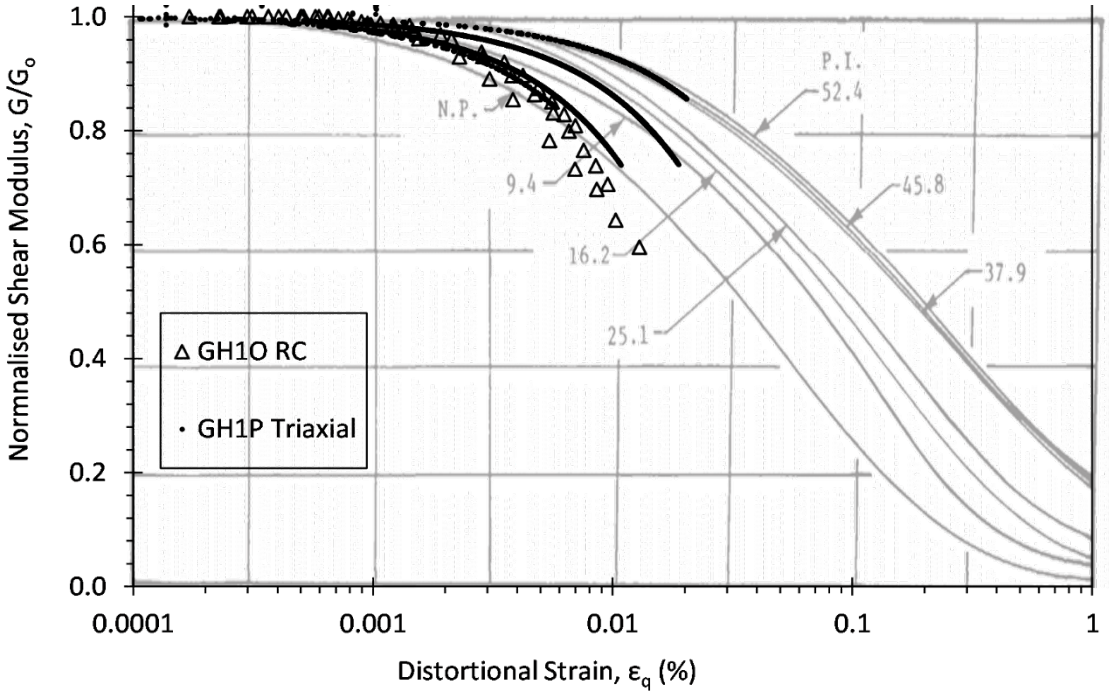

Figure 5.46: Normalised shear modulus degradation with strain for GH1O/P clay samples, shown for a range of effective stresses. Also shown are typical normalised shear modulus with strain relationships for various clay plasticity indexes, after Zen *et al.* (1978). GH1O/P PI is 10.9%.

There is only limited published data on degradation rates for silts, especially organic silts. A useful summary of data measured from offshore silty clays is presented by Sun *et al.* (1988). When the Gravel Hole silt samples are compared to this data (Figure 5.47) similarity is found in the shapes of the degradation curves, whilst some difference remains in the strain levels. Again, this could be due to differences in strain measurement methods, or due to the sand and organic content of the Gravel Hole samples, which was not present in the offshore silty clays.

Kallioglou *et al.* (2008) used a RC to investigate the shear modulus degradation of several peat samples, which are compared to measurements by other authors of Sherman Island peats

(Wehling *et al.*, 2003) , high plasticity inorganic clays (Vucetic and Dobry, 1991) and 'standard' clay (Sun *et al.*, 1988). When the organic Gravel Hole RC samples are compared to these results (Figure 5.48) the highly organic samples GH2K and GH2C match the previous authors results well, agreeing with the findings of Kallioglou *et al.* (2008) that highly-organic soils exhibit higher linearity at lower strain levels than for inorganic materials, showing some similarity to high-plasticity clays. The exact organic content of GH1D is not known, but it is far lower than for the other two samples presented in Figure 5.48, explaining its lower linearity.

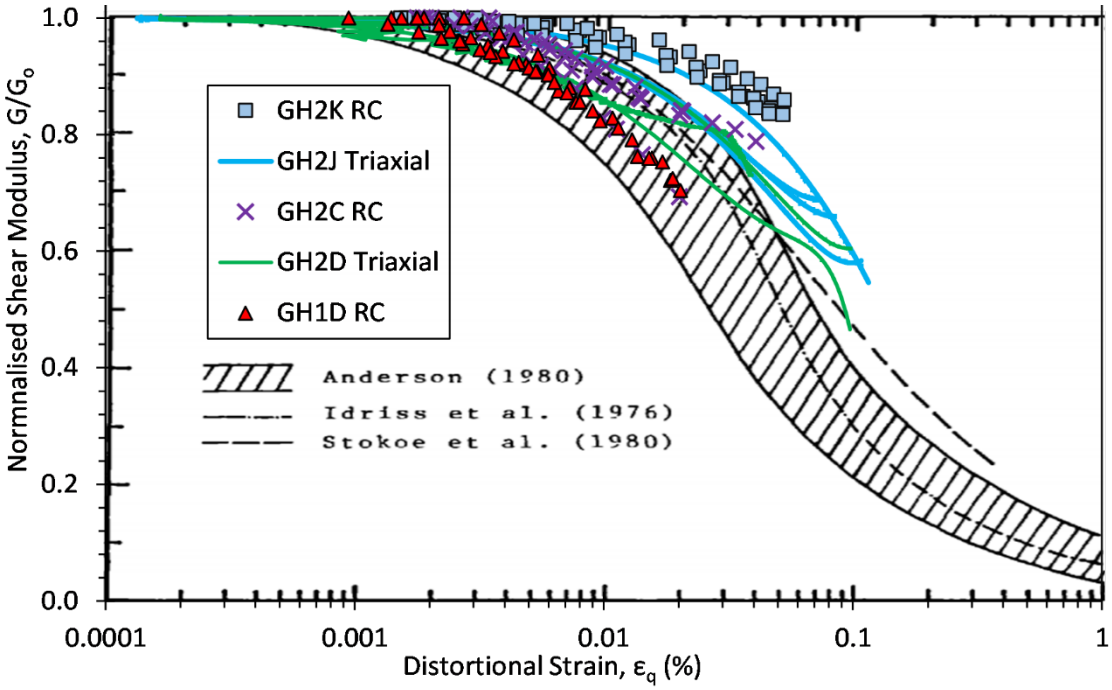

Figure 5.47: Normalised shear modulus degradation with strain for Gravel Hole silt samples, for a range of effective stresses. Also shown are typical normalised shear modulus with strain relationships for various offshore silty clay samples, from Sun *et al.* (1988), summarising data from Idriss *et al.* (1976); Anderson (1980); Stokoe *et al.* (1980).

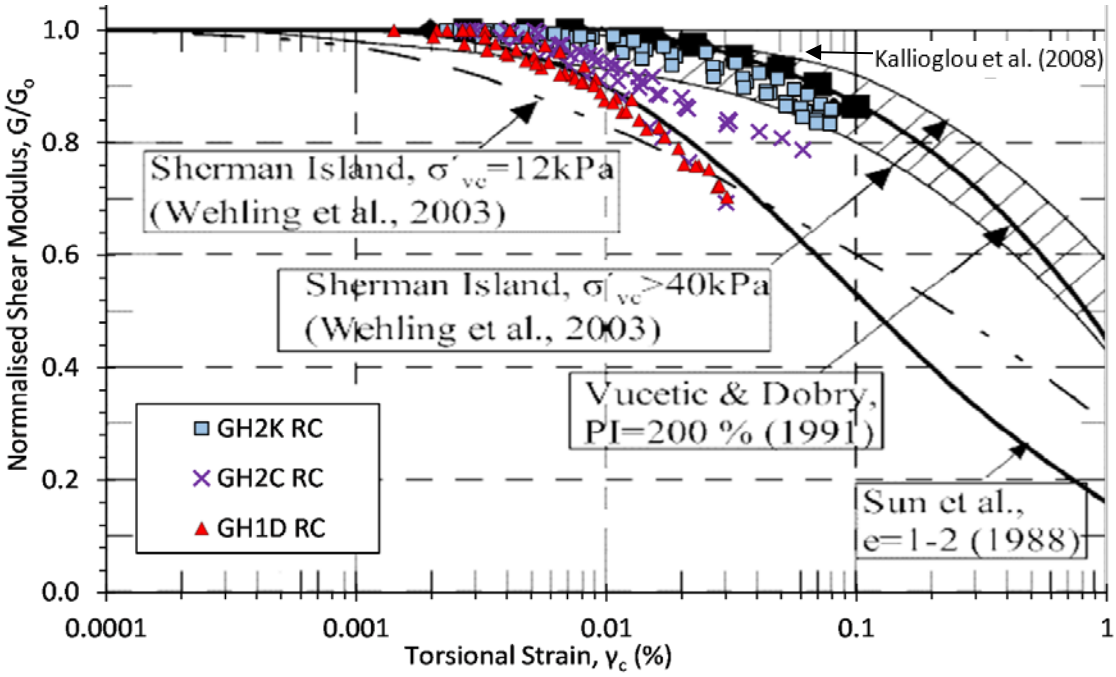

Figure 5.48: Shear modulus degradation of samples GH2K, GH2C and GH1D compared to those for a variety of materials. Modified from Kallioglou *et al.* (2008).

Damping ratio variation with strain tends to vary less broadly between soil types than shear modulus degradation. A comparison of all Gravel Hole damping measurements to published data for clays (Figure 5.49) shows all the data to fit within the published data, and to fit similar curves. Whilst this data is for clays, the curves which appear to best match the measured samples damping will be selected as needed, due to a lack of other published data on organic silt damping at higher strains.

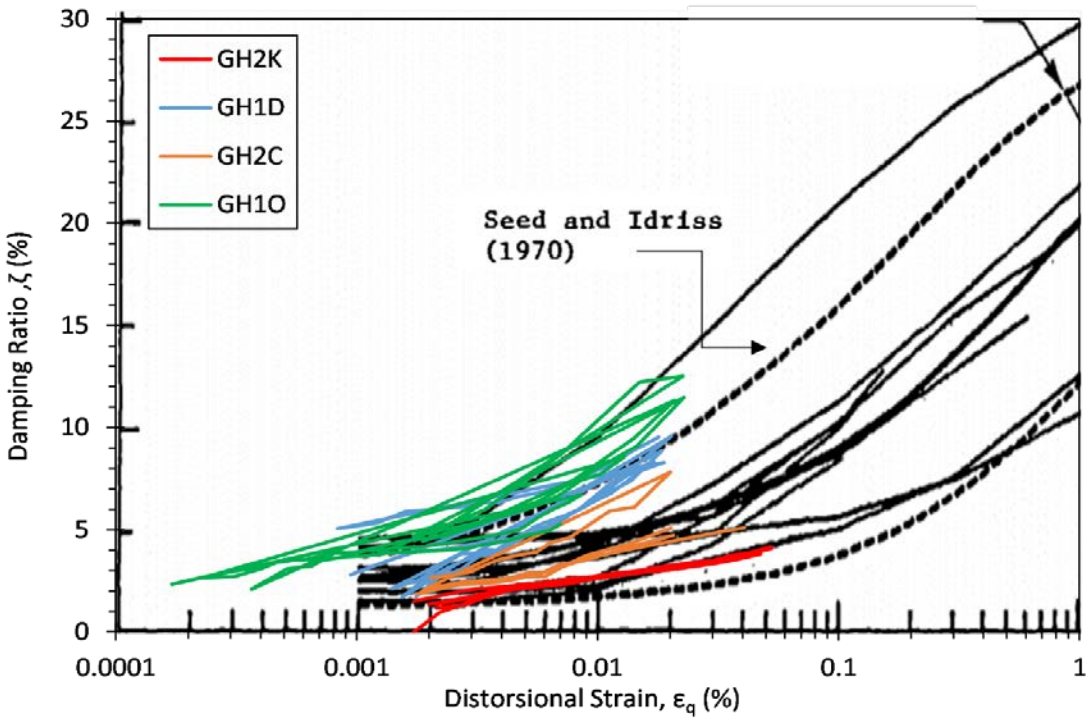

Figure 5.49: Measured damping for Gravel Hole RC samples, compared to typical clay damping ratios modified from Sun *et al.* (1988) and Seed and Idriss (1970).

5.5 Modelling with laboratory parameters

5.5.1 Parameter selection and incorporation of strain

The water level on the site was not reliably measured as insufficient time was available during the 6 hour track closure to wait for levels to stabilise in the bores. In GHS2 a strike of 2.3 m was recorded, with the water level still rising, in GHS1 strikes at 1 m and 2 m were recorded. Lab tests were carried out with assumed water levels of 0.5 m, 2 m and 3 m below the surface. For modelling purposes, the water level is assumed to be at 1.25 m below the surface, therefore results are taken from halfway between the 1st and 2nd testing stresses of 0.5 m and 2 m.

As discussed, large variation has been found between the shear moduli measured in the RC and the triaxial machine. As damping is an important element for modelling purposes, which has only been measured in the RC, and as there seems to be no clear relationship between the RC and triaxial moduli, all parameters for modelling will be based upon the RC results.

An estimation of soil geometry was made based upon the two newest site boreholes, focusing on dividing the first 5 m of ground into 3 layers accounting for key density and strength changes (Figure 5.50). Below this a halfspace was applied, as previous modelling has shown the upper ground layers to have the greatest effect on the accuracy of critical velocity modelling. Whilst additional layers may further increase accuracy they would have a detrimental effect on

computational power and time. For this model geometry it is possible to run MOTIV relatively quickly for displacement and strain results on a desktop computer. Care was taken to define even small layers of 0.7 m thickness, due to the importance shown in earlier modelling of any variation in upper layer stiffness.

Layer 1 represents the ballast type ground. Whilst 1 m of this was measured in the boreholes, 0.3 m of this is built into the track model of MOTIV, therefore only 0.7 m is represented in the ground geometry. Layer 2 represents the very soft to soft highly organic silts. As the soft material varies in thickness across the two boreholes, as well as the previous 4 boreholes, an estimated layer thickness of 2.5 m was selected. This is a difficult parameter to select accurately due to the large variation in depth of the soft layers found in the two recent boreholes and all previous boreholes, implying a layer of great variability. Layer 3 represents the firmer clay ground found beneath the organic silt in several of the boreholes, with a stiffer halfspace of sands and gravels below this.

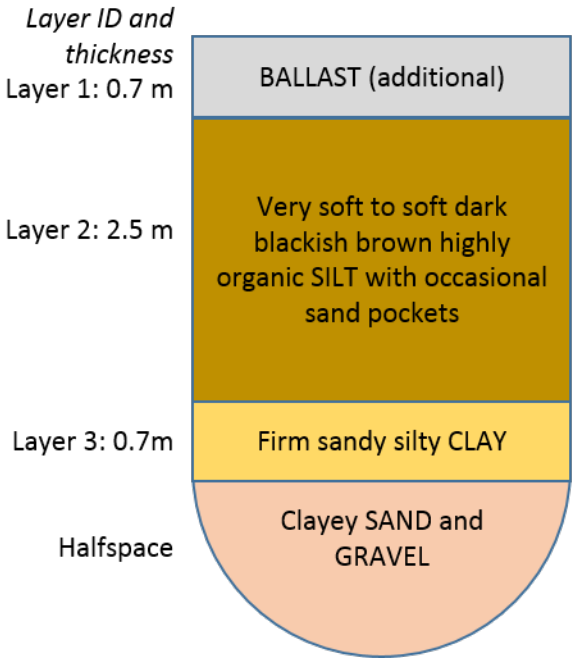

Figure 5.50: Gravel Hole modelling geometry based on site boreholes.

Initially parameters were selected as small strain values. The average of samples GH2C, GH2K and GH1D was taken as representative of layer 2, with sample GH1O corresponding to layer 3. Initial parameters for density, damping and modulus for layer 1 and the halfspace were selected from typical ranges in literature, see section 3.3.1, with the remaining parameters derived from these values. The density for the halfspace was selected from the densities estimated by the SHDP testing, which sits well within literature values. Values of Poisson's ratio were also taken from literature, accounting for the expectation of the water table sitting below layer 1. For the

halfspace a Poisson's ratio between typical sand and gravel values (0.3 to 0.4) and typical saturated clay values (0.45-0.5) was selected (Bowles, 1997).

For the purposes of selecting values from the laboratory damping and shear modulus results, small strain values were taken as those in zone 1, before shear modulus degradation begins with strain. In order to select damping for each sample, the average of the damping measured across the small strain range was taken. This generally consists of the region of lower gradient in each damping plot, as damping increases more rapidly as shear modulus degrade with strain. Any values of high variability at very low strains were ignored. For example, for sample GH1O the shear moduli appear to degrade from approximately 0.0015% torsional strain. On the GH1O damping results larger variability is shown below 0.0008 % torsional strain, therefore small strain damping was taken as the average of the damping between torsional strains of 0.0008 % and 0.0015 %.

For layers 2 and 3 values for density, shear modulus (and shear wave speed) and damping were taken directly from the laboratory measurements. The measured shear and compressional wave speeds were then used to derive the Poisson's ratio of these layers. Note that the damping loss factor (DLF) used in the modelling is equal to twice the damping ratio measured in the laboratory. All selected and derived values for the small-strain, non-degraded (ND) parameters are defined in model ID GH-ND1, Table 5.9

Table 5.9: Gravel Hole post-laboratory modelling parameters

Model ID	ε_q*(%)*	*Layer*	*Layer Size (m)*	*Density (kgm^{-3})*	*DLF*	*G (MPa)*	*E (MPa)*	*V*	V_S *(ms^{-1})*	V_P *(ms^{-1})*
GH-ND1	ND	1	0.7	1600	0.04	57.2	148.7	0.3	189	355
	ND	2	2.5	1200	0.041	6.8	20.1	0.4818	75	400
	ND	3	1	2100	0.075	19.8	59.1	0.4967	97	1200
	ND	H/S	H/S	2000	0.06	51.8	150.2	0.45	161	534
GH-B1	0.02	1	0.7	1600	0.12	25.7	66.7	0.3	127	234
	0.02	2	2.5	1200	0.124	5.5	16.2	0.4818	68	363
	0.02	3	1	2100	0.24	8.6	25.7	0.4967	64	790
	ND	H/S	H/S	2000	0.06	51.8	150.2	0.45	161	534
GH-B2	0.066	1	0.7	1600	0.22	17.1	44.5	0.3	103	193
	0.066	2	2.5	1200	0.228	4.0	11.9	0.4818	58	309
	0.066	3	1	2100	0.34	3.0	9.0	0.4967	38	469
	ND	H/S	H/S	2000	0.06	51.8	150.2	0.45	161	534

Model ID	ε_q(%)	Layer	Layer Size (m)	Density (kgm^{-3})	DLF	G (MPa)	E (MPa)	V	V_S (ms^{-1})	V_P (ms^{-1})
GH-B3	0.015	1	0.7	1600	0.1	27.9	72.6	0.3	132	247
	0.1	2	2.5	1200	0.24	3.6	10.8	0.4818	55	293
	0.014	3	1	2100	0.18	11.7	35.0	0.4967	75	926
	ND	H/S	H/S	2000	0.06	51.8	105.2	0.45	161	534
GH-B4	0.014	1	0.7	1600	0.1	28.5	74.1	0.3	133	249
	0.2	2	2.5	1200	0.267	3.0	8.8	0.4818	50	267
	0.01	3	1	2100	0.18	12.5	37.4	0.4967	77	951
	ND	H/S	H/S	2000	0.06	51.8	150.2	0.45	161	534
GH-B5	0.06	1	0.7	1600	0.2	20.0	51.9	0.3	112	210
	0.15	2	2.5	1200	0.255	3.3	9.8	0.4818	52	278
	0.05	3	1	2100	0.34	6.0	18.0	0.4967	53	655
	ND	H/S	H/S	2000	0.06	51.8	150.2	0.45	161	534
GH-B6	0.06	1	0.7	1600	0.1	27.9	72.6	0.3	132	247
	0.04	2	2.5	1200	0.169	5.0	14.7	0.4818	64	342
	0.01	3	1	2100	0.18	12.5	37.4	0.4967	77	951
	ND	H/S	H/S	2000	0.06	51.8	150.2	0.45	161	534
GH-B7	0.06	1	0.7	1600	0.2	20.0	51.9	0.3	112	210
	0.15	2	2.5	1200	0.255	3.3	9.8	0.4818	52	278
	0.05	3	1	2100	0.34	6.0	18.0	0.4967	53	655
	0.006	H/S	H/S	2000	0.07	44.0	127.7	0.45	148	491

Further models are based on the use of values representing degraded soil parameters, at higher strains. Measured torsional strains (γ_c) from the RC are converted to distortional strains ε_q. An adaptation of the MOTIV programme[2] allows output of the vertical strain in the soil, with speed and depth below the track. This calculates strain from the peak soil displacements at the track centreline for each speed. As the horizontal strains are very small beneath the axle loads, where maximum soil displacements occur, distortional strain is assumed to be equal to vertical strain (Equation 5-9).

In order to select parameter values for a strain of $\varepsilon_q = X$, for layers 2 and 3 values are selected directly from the lab results, if X falls within measured strain values. For layer 1 and the halfspace, normalised degradation curves are applied to the original small strain values. For layer 1 (ballast)

[2] Provided by Dr E. Ntotsios, University of Southampton.

the average degradation at strain X for a range of gravels is applied (Figure 5.51) with a similar process applied for damping (Figure 5.52). For the halfspace a value towards the upper end of the sand band on Figure 5.51 was selected, as the ground is a mixture of both sand and gravel, and clay which has a slower rate of degradation. For layers 2 and 3, to select values of strain X which fall outside of the laboratory measurements reference was made to the closest matching curves of similar materials, as shown in Figure 5.47, Figure 5.48 and Figure 5.49 .

The input strain (the strain value from which degraded parameters were taken) and the output strain are compared. However, a factor must be applied to the peak output strain to give an overall effective output strain value for each layer. Starting from an initial estimate, the effective output strain is then used as the input strain for that layer for the following model, until input strains and effective output strains converge for each layer. A 4 vehicle moving load was used for all models.

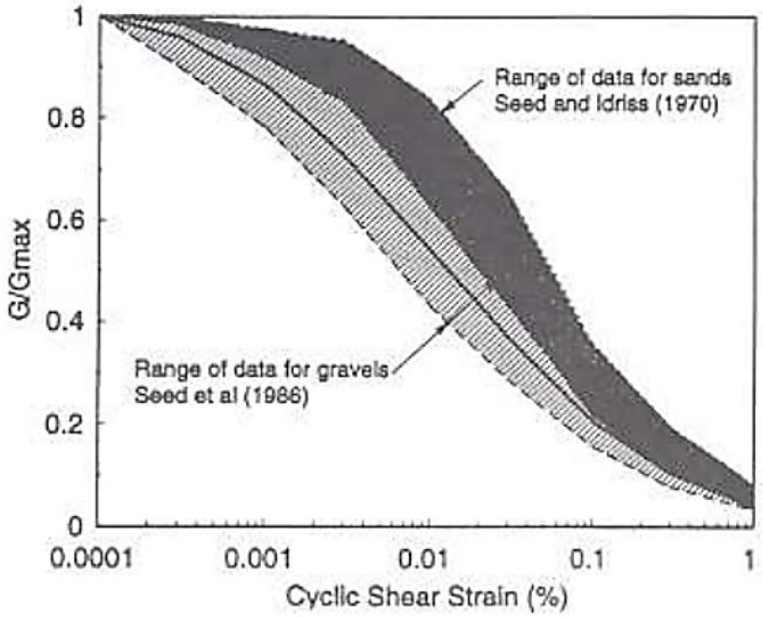

Figure 5.51: Typical G/ G_O versus strain relationship for sands (Seed and Idriss, 1970) and gravels (Seed *et al.*, 1986) as summarised in Rollins *et al.* (1998).

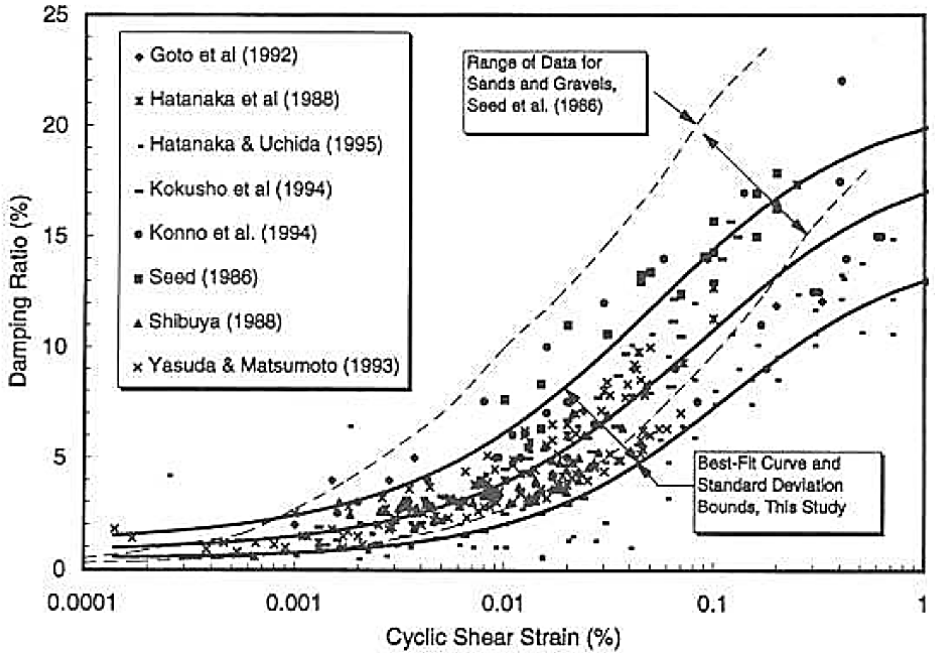

Figure 5.52: Damping variation with strain from a range of investigations, as summarised in Rollins *et al.* (1998).

5.5.2 Results – non-degraded and degraded parameters

Initially modelling was carried out using small-strain, non-degraded parameters (ND1, Table 5.9). The resulting peak strain and sleeper displacements are presented in Figure 5.53 and Figure 5.54 respectively. Peak strains occur at the critical velocity, with a maximum strain of 0.18% in layer 2, the soft silt. The strains are largely centred in the soft silt layer, in a relatively narrow band around the critical velocity. The displacement curve does not match the site measurements at all, with the displacements being far too low and the critical velocity being far too high, as expected.

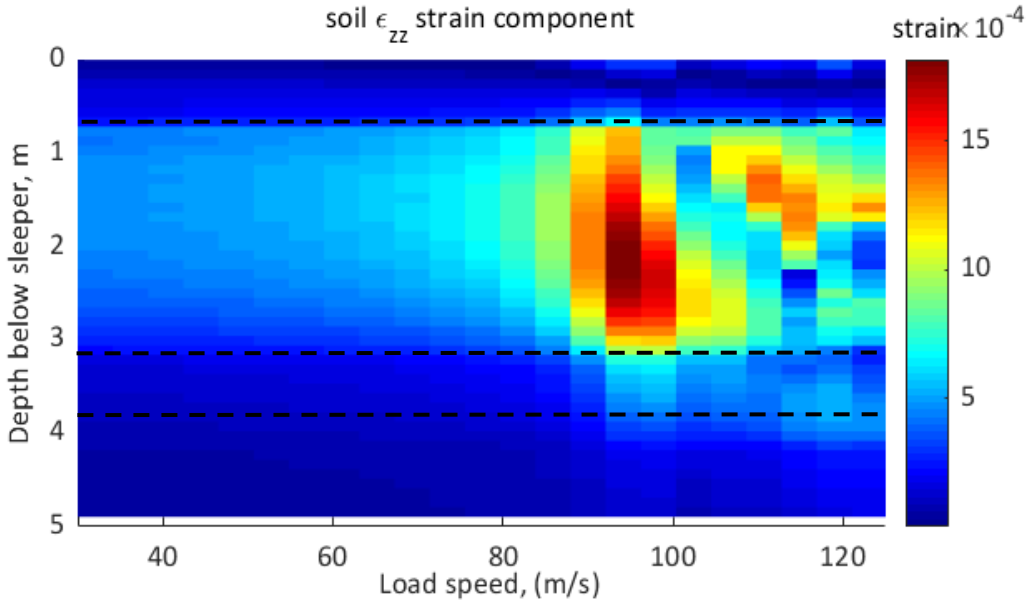

Figure 5.53: Vertical strain variation with load speed and depth, for model ND1, with layer boundaries marked.

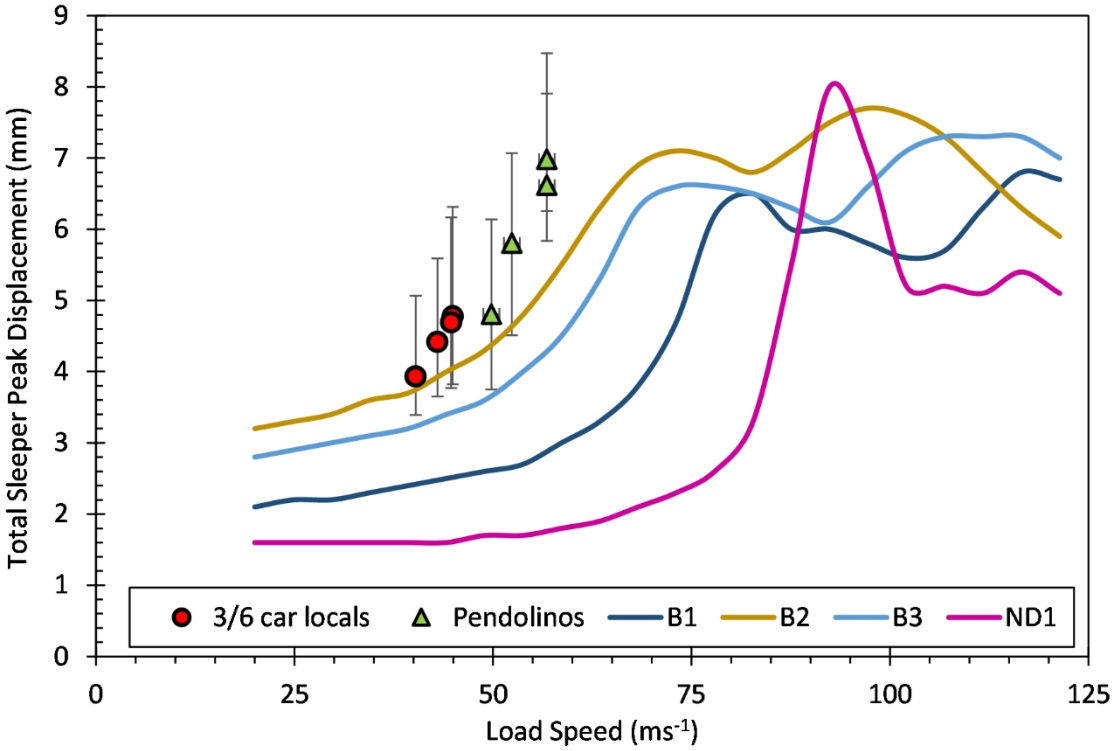

Figure 5.54: Total peak sleeper displacements with load speed for Gravel Hole models ND1, B1, B2 and B3, with site measurements for reference.

A range of models were run, with their parameters set out in Table 5.9. No degradation was applied to the halfspace as the strains below 4 m depth are very small. Initially the same strain levels were applied to all layers, to build up some reference results, so that a plot of peak output strain versus input strain could be developed (Figure 5.55). Whilst the lines are not linear, due to a dependence on the strains applied to the other layers in each model, this plot does aid in selecting target strains to achieve desired output strains for each layer. As discussed in section 2.1.3, the factor Rr to be applied to the peak output strain in order to compare to input strain is a matter of debate. Lines relating to the common value of 0.65, and the value of 0.2 found more recently by Shih *et al.* (2017) are plotted on Figure 5.55. Peak strains are selected from the first critical velocity peak, rather than the measured site peak speed of 57 ms^{-1}, as it is not known whether that is the top of the site critical velocity curve.

The resulting displacement versus speed curves for all models are presented in Figure 5.54 and Figure 5.56. As the assumed input strains increase, causing shear modulus degradation and increases in damping, the critical velocities decrease, the displacements increase, and the gradients of the displacement curves reduce. Models B5 and B6 have strains which all converge to the same Rr for each layer, with model B5 matching an Rr value of 0.65, whilst model B6 matches an Rr value of 0.2 (Figure 5.56). The soil parameters in model B6 are stiffer than in B5, as they are less degraded, resulting in a displacement curve which, although a reasonable match in shape, is far too low in displacements and too high in critical velocity compared to the site measurements.

The highest strains for model B6 (Figure 5.57) are still closely centred within the soft silt layer 2, with a peak strain of 0.17 % at the first critical velocity peak of 78 ms^{-1}.

Model B5, which uses more degraded parameters, produces a far closer match to the site measured displacements. This model applies an input strain of 0.15 % to select the soft silt degraded parameters, in comparison to the 0.04% applied in model B6. This means an input shear modulus of 3.3 MPa in B5 compared to 5 MPa in B6, and a damping loss factor of 26 % and 17 % respectively. Not only are the displacements for the softer model B5 a far better match to site displacements, but the highest strains (Figure 5.58) occur across a wider area in the soft silt and towards the clay below.

To assess the impact of applying degradation to the halfspace, model B5 (Rr = 0.65) was repeated, but with halfspace degradation included. The results of this are presented as model B7.
Figure 5.56 shows no significant impact on displacement through the introduction of an applied degradation in the halfspace, with no significant impact also made on the soil strains. Input, peak output and effective output strains for all models are detailed in Table 5.10.

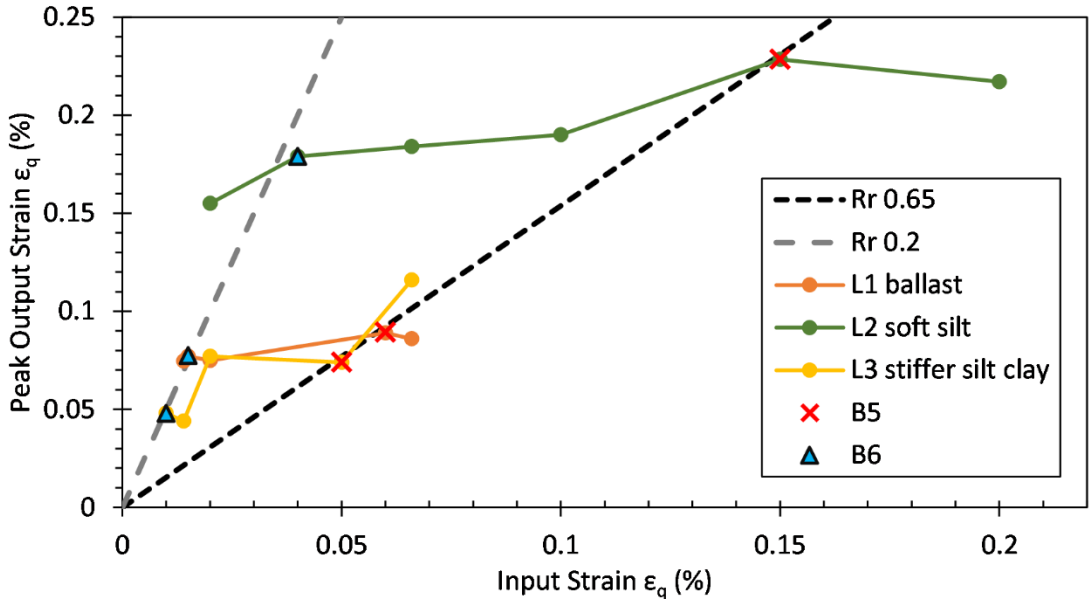

Figure 5.55: Output strain versus assumed (input) strains for Gravel Hole models.

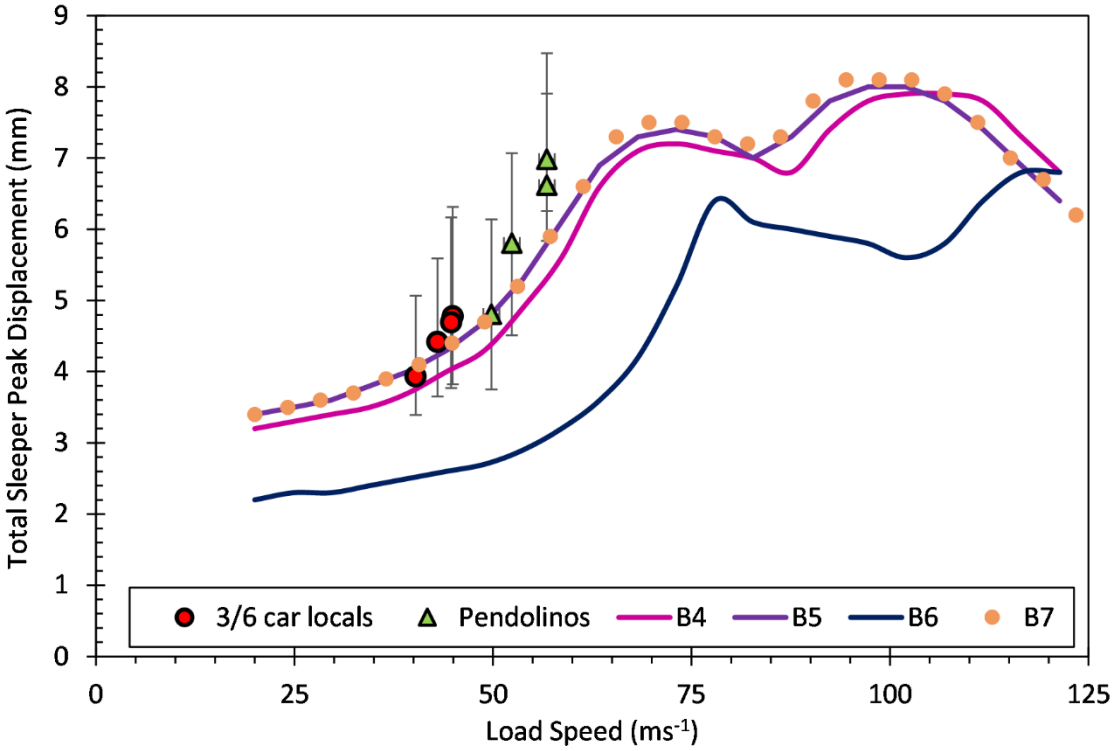

Figure 5.56: Total peak sleeper displacements with load speed for Gravel Hole models B4, B5, B6, and B7, with site measurements for reference.

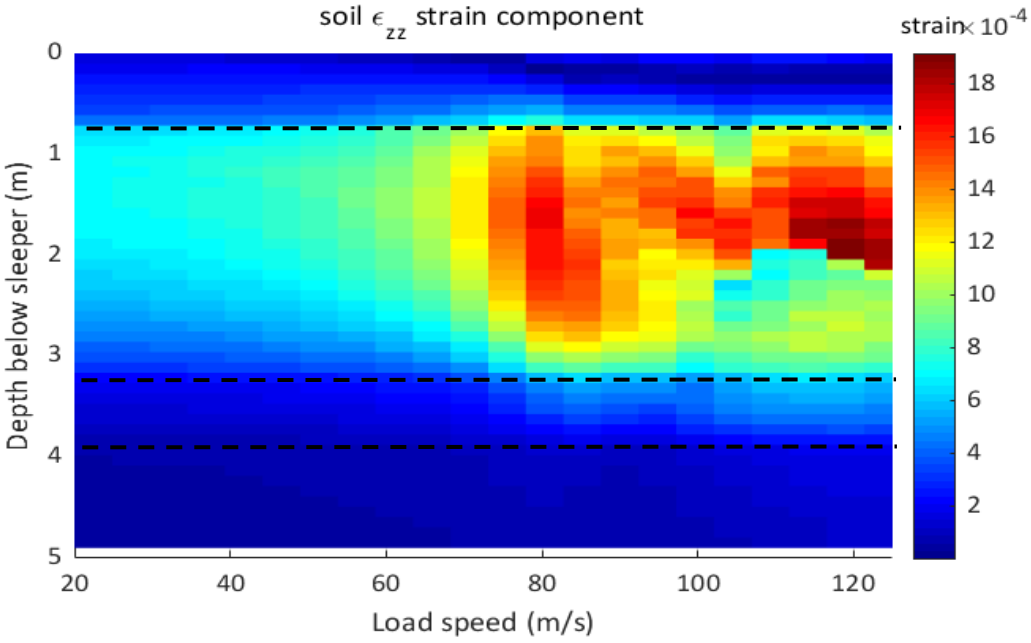

Figure 5.57: Vertical strain variation with load speed and depth, for model B6, with layer boundaries marked.

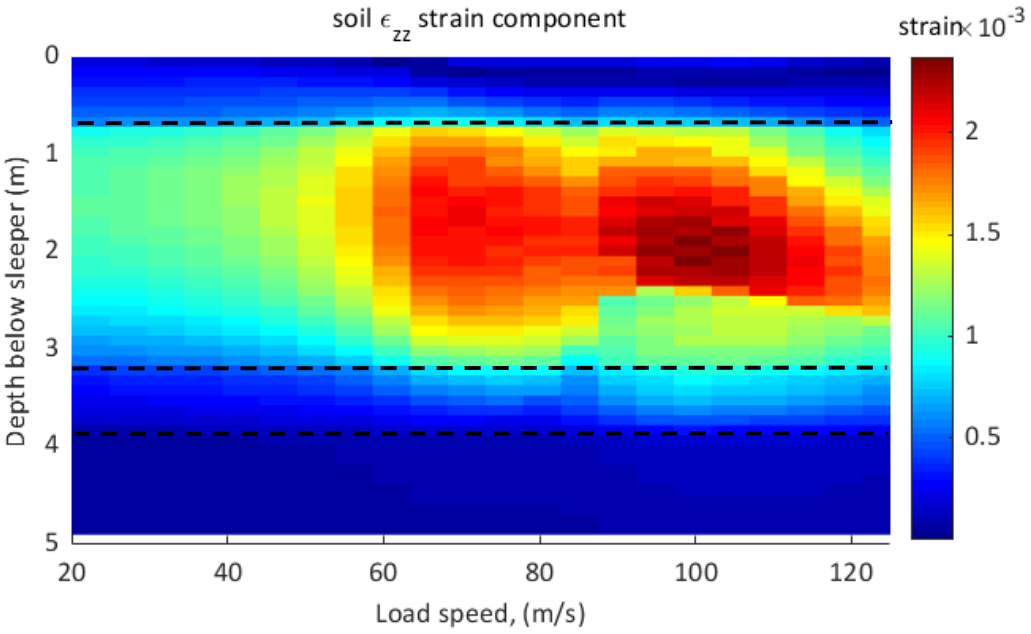

Figure 5.58: Vertical strain variation with load speed and depth, for model B5, with layer boundaries marked.

Table 5.10: Input and output strains for Gravel Hole models.

Model ID	*Layer*	*Input ε_q(%)*	*Peak Output ε_q(%)*	*Effective Output ε_q for Rr 0.2 (%)*	*Effective Output ε_q for Rr 0.65 (%)*
GH-B1	1	0.02	0.075	0.0150	0.049
	2	0.02	0.156	0.0311	0.101
	3	0.02	0.077	0.0154	0.050
	H/S	ND	0.013	0.0026	0.008
GH-B2	1	0.066	0.075	0.0150	0.049
	2	0.066	0.156	0.0311	0.101
	3	0.066	0.077	0.0154	0.050
	H/S	ND	0.013	0.0026	0.008
GH-B3	1	0.015	0.076	0.0152	0.049
	2	0.1	0.190	0.0380	0.123
	3	0.014	0.044	0.0088	0.029
	H/S	ND	0.010	0.0020	0.006

Model ID	*Layer*	*Input ε_q(%)*	*Peak Output ε_q(%)*	*Effective Output ε_q for Rr 0.2 (%)*	*Effective Output ε_q for Rr 0.65 (%)*
GH-B4	1	0.014	0.075	0.0149	0.048
	2	0.2	0.217	0.0433	0.141
	3	0.01	0.039	0.0077	0.025
	H/S	ND	0.009	0.0019	0.006
GH-B5	1	0.06	0.089	0.0179	0.058
	2	0.15	0.229	0.0457	0.149
	3	0.05	0.074	0.0148	0.048
	H/S	ND	0.009	0.0019	0.006
GH-B6	1	0.06	0.077	0.0155	0.050
	2	0.04	0.178	0.0356	0.116
	3	0.01	0.048	0.0096	0.031
	H/S	ND	0.012	0.0023	0.008
GH-B7	1	0.06	0.090	0.0181	0.059
	2	0.15	0.209	0.0418	0.139
	3	0.05	0.074	0.0148	0.048
	H/S	0.006	0.011	0.0023	0.007

5.6 Discussion of site testing and modelling

The site testing programme for this case study was very successful, providing a large range of measurements from a variety of sources. However, it also shows the difficulties in selecting which sources to use, and the limitations from which some suffer.

The importance of directly measuring density, through in-situ probes, or preferably extracting samples, is shown when the in situ seismic measurements are considered. These measurements rely on an assumption of soil density, which for unusual sites such as this is extremely inaccurate. In this case the actual density of the softest layers is only 59 % of the typical assumed density of 2000 kgm^{-3}. Whilst seismic measurements are non-invasive, their ability to estimate the depths of soil layers, especially in the most important upper surface layers, appears too limited to be of use, especially when the sensitivity of the models to these values is considered.

The huge variability in the boreholes taken on the site, both for this work and previously, imply very uneven soil stratigraphy. This makes it extremely difficult to select a model geometry to represent the site, especially for the most important softest layers. Whilst having to select a single value for a layer that ranges from 0.75 m to 4 m in thickness may not be of huge influence in

certain geotechnical projects, it is of great importance in critical velocity modelling. This is especially so on a site such as this where the most variable layer is of significantly lower density and stiffness, when modelling has shown the addition of even 0.5 m thickness can have a large impact on model results.

The use of SHDP, or similar penetration testing apparatus, could prove a useful tool in the modelling of future sites. Whilst the estimation of soil strength from these measurements is difficult for unusual soils, as it is entirely reliant on correlations to previously measured data, they do provide a reasonable estimation of the thickness of soil layers of varying density on the site. As these methods are faster, cheaper and less invasive than drilling boreholes they may provide a useful method for defining a suitable model geometry. For sites where the underlying materials are of a well-known material then correlations between blow count and density can be made fairly accurately.

The first one or two metres of ground beneath the track appear to have a disproportionately large impact on the predicted displacements. When modelling this site, introducing just 0.7 m of sand and gravel over the soft 2 m layer reduced peak displacements by over 40%. Another set of models assessed the impact of the thickness of a generic stiffer layer over the softer layer, and found thicknesses of 1.5 m reduced peak displacements by 50%. An additional model sought to investigate the importance of the stiffness ratio between the soft layer and the stiffer ground around it. In this case it is suggested that once the ratio reaches a value of 4 it is no longer necessary to further define the parameters for the stiffer layer, as additional stiffness increases beyond this will only have small impacts on the displacement.

As expected, the unusual organic soils on this site respond in a different way in the laboratory testing to ‘normal’ engineering clays. Whilst the organic soils have low small-strain strengths, the strain at which the shear modulus begins to degrade is higher, although once it begins the rate of degradation is more rapid than for a typical clay. It was not possible to define the plastic or liquid limits of the organic silts, an additional example that the unusual soils on critical velocity sites require detailed laboratory testing, rather than just selection of parameters from typical curves aided by comparison metrics such as the plasticity index.

The RC proved a relatively fast and effective method for defining the shear modulus and damping of the samples at a range of strains. Additional care must be taken when testing on very soft compressible soils, to ensure the RC system remains aligned. The addition of bender elements to the RC proved a very useful method of defining the compressional wave speed, and so the Poisson’s ratio, whilst also providing additional shear wave measurements. The comparison of these shear wave measurements to those from the RC itself appear to provide a method of

holistically testing the inhomogeneity of the sample. The speeds for the samples that were known to be more homogeneous compared very closely, whilst those for the very inhomogeneous samples differed slightly. It is proposed this is due to the RC measuring the entire bulk of the material whereas the bender elements mainly focus through the core of the sample.

The method of consolidation appears to have a great impact on the samples. Sample pair GH1O (RC) and GH1P (triaxial), were both consolidated isotropically, and show a good match in shear modulus between the two pieces of equipment. The remaining sample pairs were consolidated isotropically in the RC and along the K_O line in the triaxial. This appears to have had a large impact on the measured shear moduli, with the triaxial measurements being consistently considerably lower than for the RC. As damping measurements are required for modelling, the values from the RC were selected for modelling.

Comparisons for samples GH2D and GH2J of the vertical shear modulus G_{hv}, derived from triaxial horizontal bender elements, with G*, derived from triaxial undrained probes, do not show a strong similarity. This is not unreasonable considering the theoretical equivalence of G_{hv} and G* is based upon an assumption of isotropic homogeneity, which is unlikely in these highly variable samples.

Modelling was successfully carried out based upon the parameters measured in the laboratory, for a range of strains. The results appear to show that consideration of strain degradation is essential for critical velocity modelling, with peak strains of up to 0.2% predicted in the soft layer at critical velocity. The strains from which input parameters were selected were varied for each of the model layers, aside from the halfspace where strength degradation has been shown to have little effect on the predicted displacements, due to the low strains. Strains were found to be largely focused in the softest layer, increasing rapidly as the load speed approaches critical velocity.

A factor Rr was applied to the predicted peak strains from the models, in order to assess required input strains. It is interesting that for this site the more common Rr factor of 0.65 appears to provide a reasonable match to site displacements, whilst the Rr factor of 0.2 found appropriate by Shih *et al.* (2017) for an equivalent linear model of Ledsgård predicts displacements smaller displacements and higher critical speed than those measured on site. The necessary simplification of a very complex site geometry, alongside the decision to select shear moduli from the RC testing rather than the triaxial testing may have affected this.

Another factor may be the rates of degradation of modulus and damping parameters for different soils, as increasing strain results in decreased shear modulus, which tends to increase

displacements whilst conversely increased damping tends to decrease displacements. The product of the shear modulus and the damping at a selected strain can be considered to be a parameter called the effective damper rate (D_E) (Shih *et al.*, 2017). For some soils the rates of decrease in shear modulus, and increase in damping mean that the resulting range of D_E with strain is less than the range of either of the individual components, making the input strain a less important parameter. For other soils the changes in normalised modulus and normalised damping with strain vary greatly from each other. If the normalised damping increases faster than the normalised shear modulus decreases, the resulting normalised D_E varies more greatly with strain than the shear modulus alone. In this case the selection of input strain is of greater importance.

It is noted that for all models and parameters for this site the peak strain experienced at critical velocity appears to always sit within the 0.15 % to 0.2 % range. This corresponds to the peak strains predicted by the modelling and lab measurements for the Ledsgård critical velocity site. If the Rr factor can be defined with greater confidence then this implies that for predicting critical velocity displacements and speeds for future sites, where no current critical velocity displacements are measured or take place, input strains for the softest soil layers should be selected for a peak output strain of 0.15 % to 0.2 %. Without a basic target such as this, even if lab testing were carried out for a future rail site it is impossible to define where on the strain degradation curves parameters should be selected.

This site exemplifies the difficulties in using 2.5D models to represent unusual site geometries, as ideally a model would reproduce a soft layer which varies in thickness both parallel and perpendicular to the track. The impact of a defined horizon of soft soil within a model, rather than a uniform layer, is unknown. Whilst this is an area for future work, there is an argument that, with the selection of suitable parameters, 2.5D models can at least provide displacement predictions which are on the conservative side. The requirement to have layers which extend infinitely across the model will make them more likely to safely over-predict rather than under-predict displacements, as long as a suitable layer thickness is selected.

Chapter 6 Fishbourne Case Study Site

6.1 Site background and stratigraphy

Background

At a site near Fishbourne station in southern England, a long-running monitoring programme has been carried out by the University of Southampton as part of the Track 21 programme. This has comprised a variety of work, including a study using a combination of geophones and videos with digital image correlation (DIC) to monitor track displacements near a level crossing (Le Pen *et al.*, 2014).The site has also been used for noise and vibration monitoring. The site is also regularly traversed by Network Rail's track recording car, recording site track roughness measurements. A range of traffic passes the site, with a maximum line speed of 70 mph (113 km/h).

Stratigraphy

BGs surface geology mapping shows the site to sit on the boundary of the Lambeth Clay group and the London Clay formation, overlain by River Terrace deposits (sand, silt and clay) or deposits of gravel, sand, silt and clay (British Geological Society, 2016). This corresponds well with the historic BGS boreholes near to the site, as summarised in Figure 6.1, which shows the historic borehole records closest to the site in all directions. The area consists of generally soft clays with some silt and sand content, increasing in stiffness and chalk content with depth, overlying the London Clay formation.

Topology

The site sits within a very wide flat basin, with the closest watercourse being a stream running adjacent to the far end of the site (Figure 6.2). No further information on ground water levels is known.

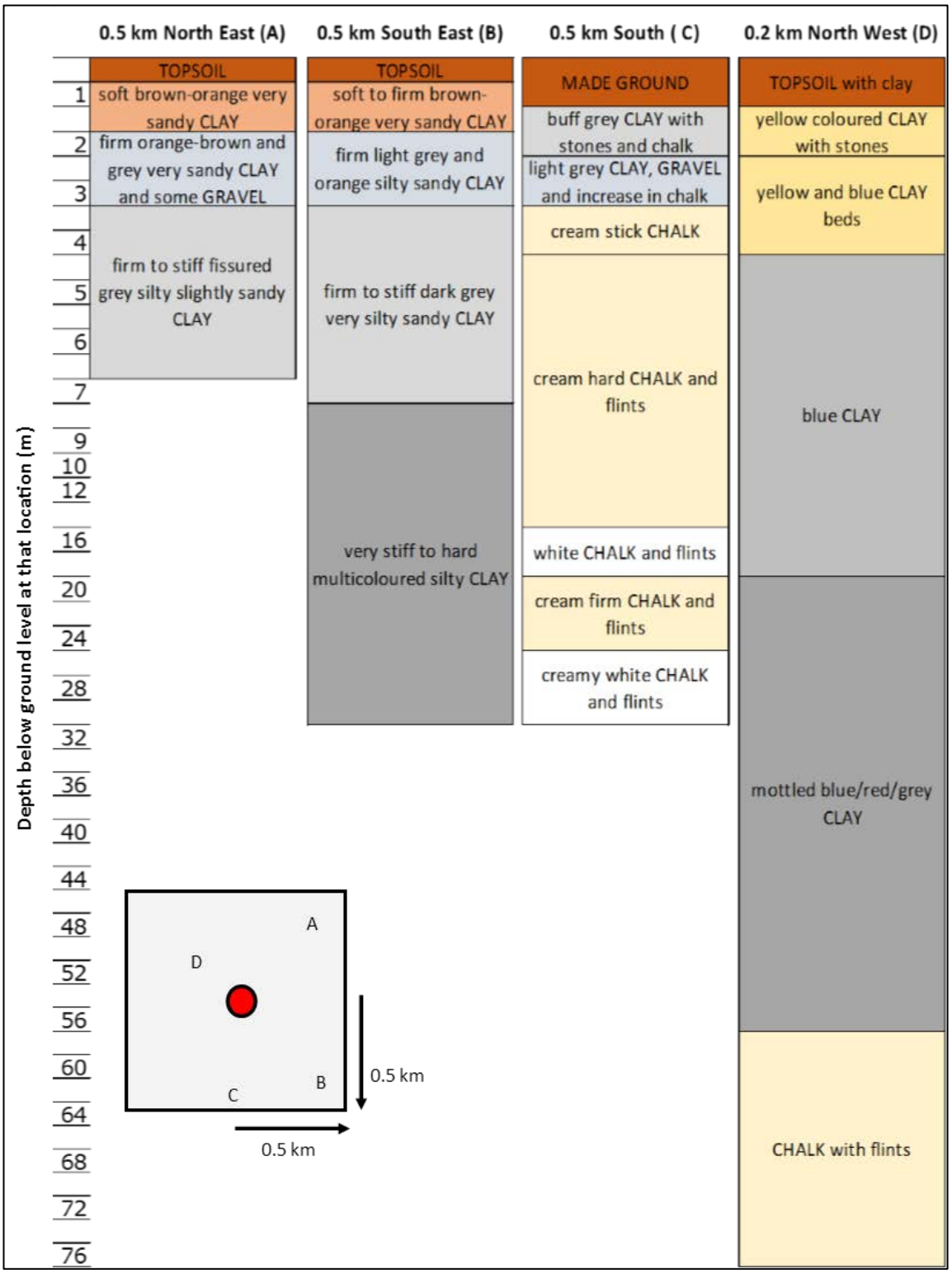

Figure 6.1: Summarised borehole results at various distances surrounding Fishbourne (British Geological Society, 2016). Includes location map of boreholes relevant to site (site shown by red dot).

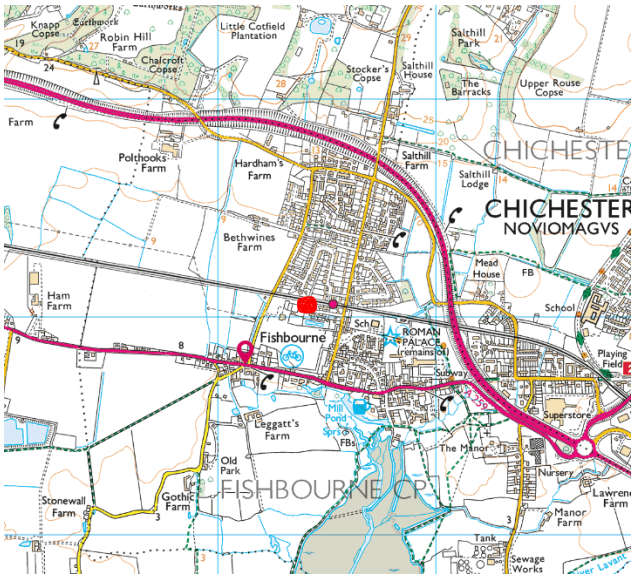

Figure 6.2: Fishbourne local contouring, red dot indicates site (Ordnance Survey, 2016).

6.2 Site measurements and sampling

6.2.1 Track and ground movement

Some track displacement measurements have been taken using geophones, but these are deemed unsuitable for comparing to models as they were taken close to the level crossing, and also span a very limited range of train speeds. Although the site displacements do not currently exhibit 'critical velocity' type behaviour, it is useful as an 'intermediate' type site, as there is the possibility that there are soft clays beneath the site, which may cause issues if the line speed were raised to typical classic network 'high' speeds in the future.

6.2.2 Seismic testing

Work carried out by Wiseman (2015) for the University of Southampton used the MASW method to estimate shear wave velocity and stiffness profiles for the site. The initial MASW results were refined through several processes, lastly being used in MOTIV to predict ground vibration response, with the values then adjusted until a best fit with the measured train pass-by data was achieved (Table 6.1). Wiseman notes that the effectiveness of the coupling between the accelerometer and the ground with the mounting method used has not been assessed. The site measurements took place during inclement weather conditions, which may have also had an effect on the results. The depths of different ground layers are very difficult to determine with any accuracy in these seismic measurements.

Table 6.1: Fishbourne ground properties from MASW and MOTIV analysis (Wiseman, 2015)

Layer	*Depth (m)*	*Damping Loss Factor*	*P-wave speed V_P (ms^{-1})*	*S-wave speed V_S (ms^{-1})*
1	1.0	0.05	1400	140
2	2.5	0.05	1400	80
Halfspace	-	0.05	2000	350

Taking a Poisson's ratio of 0.5 (assuming the clays are saturated) an estimate of the Young's modulus and undrained shear strength (C_u) of each layer of Wiseman's model can be made, see Table 6.2. These estimates can be compared to those obtained in the laboratory. In order to estimate C_u the below relationship was assumed, for overconsolidated London Clay type materials (Butler, 1974):

$$C_U \cong {}^{E}/_{400} \qquad \text{Equation 6-1}$$

Table 6.2: Estimated of ground strength and Young's modulus parameters based on the wavespeed measurements and modelling predictions of Wiseman (2015) for the Fishbourne site.

Layer	*Depth (m)*	*S-wave speed V_S (ms^{-1})*	*Young's Modulus E (MPa)*	*Undrained shear strength Cu (kPa)*
1	1.0	140	39	98
2	2.5	80	13	32
Halfspace	-	350	245	613

Whilst the estimates of wavespeeds can potentially be utilised as input parameters for models, dispersion plots are the best method to compare the available site seismic measurements to the output from MOTIV models. A Fourier transform is used to transform the response for each frequency at 1 m spacings to the wavenumber domain. This results in a triple axis plot of wavenumber, frequency and amplitude of response. The plot presents the propagating modes of the Rayleigh waves in the measured ground, with each line (formed from high peaks of amplitude) representing a wave type associated with a cross-sectional mode of the layered ground Thompson (2009).

Using the dispersion plot to estimate wave speed (phase velocity, c in ms^{-1}) of a wave at a particular frequency (f in Hz) a line is constructed from the origin to a point on the dispersion curve and the relevant wavenumber (k in $radm^{-1}$) measured:

$$c = \frac{\omega}{k} = \frac{2\pi f}{k} \qquad \text{Equation 6-2}$$

where ω is the circular frequency ($rads^{-1}$). The group velocity (c_g) is the inverse of the slope of this curve:

$$c_{g=}\ \partial\omega/\partial\, k$$ Equation 6-3

Figure 6.3 shows the dispersion plot from the seismic measurement at Fishbourne. The resulting output is not particularly clear, Wiseman (2015) notes that results for wavenumbers above 3 radm^{-1} are difficult to interpret due to the spatial resolution of the measured data which causes aliasing to occur at high frequencies.

To increase the usability of the dispersion plot, the response amplitudes are normalised by the maximum value at each frequency, resulting in a plot with far clearer ground wavespeeds (Figure 6.4). A surface wave is seen between 10 and 30 Hz, with a wavespeed of approximately 100 ms^{-1}. A second surface wave between 20 and 60 Hz has a wavespeed of approximately 125 ms^{-1}, and possibly extends into the upper wavenumbers. Results at higher frequencies relate to the ground layers nearer the surface, results at lower frequencies relate to deeper ground layers. Therefore it appears from this dispersion diagram that some wavespeeds in the upper layers are faster than the wavespeeds in the lower layers, although the unreliability of measurements above 3 radm^{-1} should be remembered.

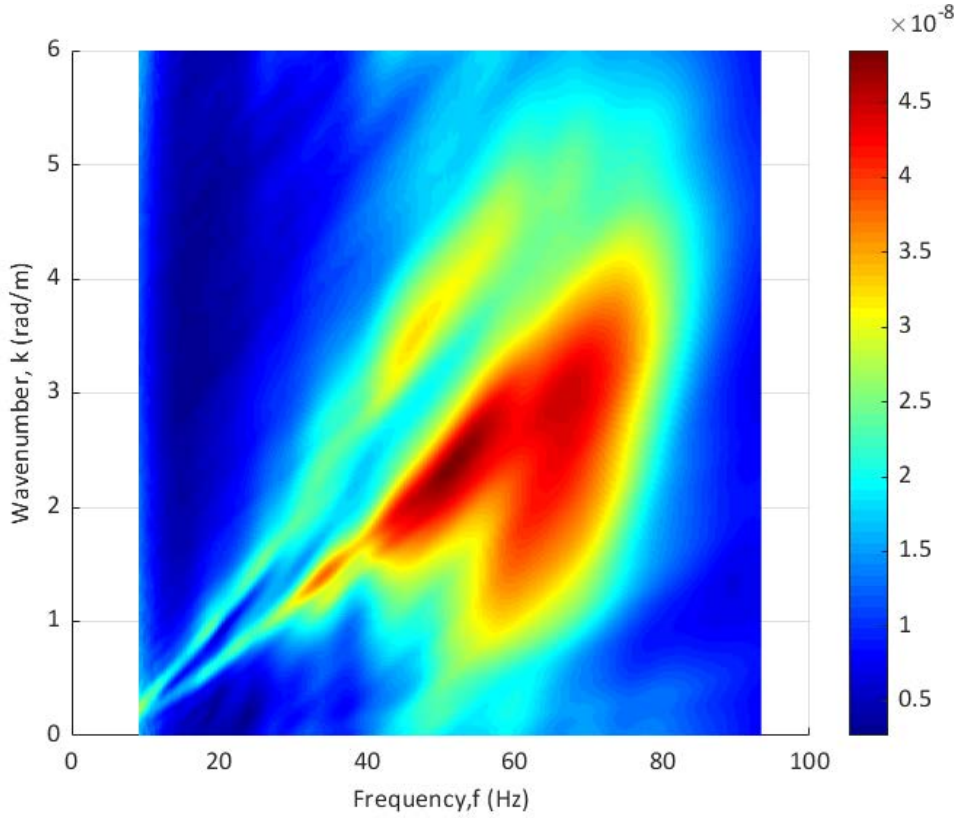

Figure 6.3: Soil dispersion plot for Fishbourne based on site seismic measurements. Scale for amplitude of Z-axis response shown. After Wiseman (2015).

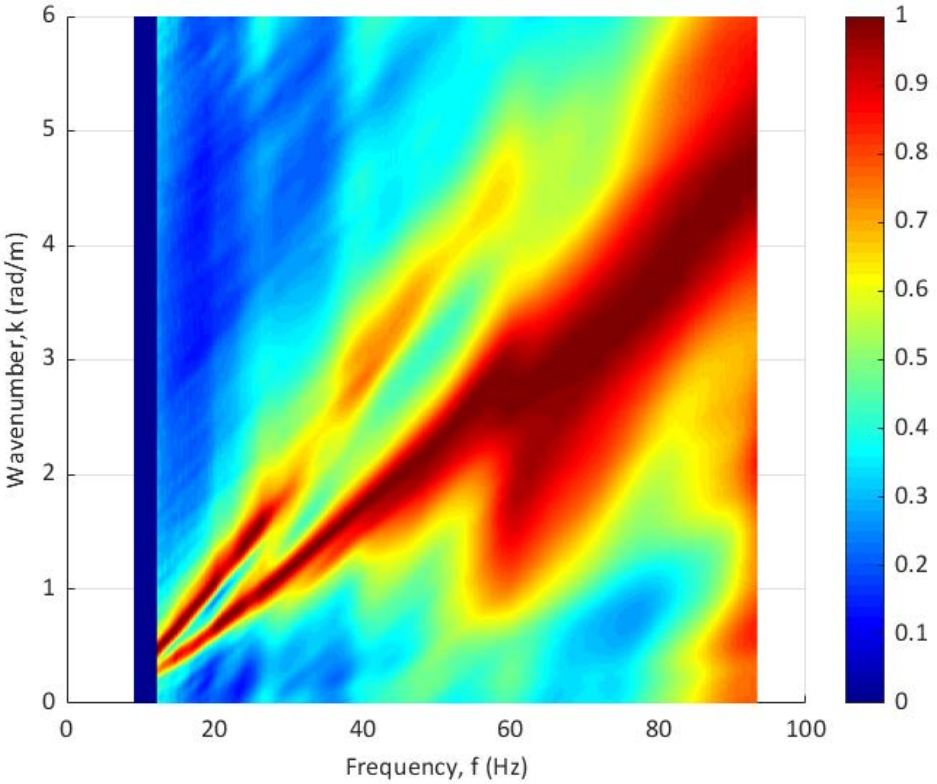

Figure 6.4: Soil dispersion plot from Fishbourne seismic measurements, normalised by the maximum amplitude in each frequency. Scale for comparative amplitude of Z-axis response shown. After Wiseman (2015)

6.2.3 In situ sampling

Sampling process

A Windowless Sampling (WS) rig and a Super Heavy Dynamic Probe (SHDP)[3] were used to examine the site conditions. Two locations were targeted, on the sports ground adjacent to the track, at distances of approximately 5 m and 10 m from the track (Figure 6.5). The WS rig targeted 2 bores of 6 m depth, with samples of 1 m length being extracted throughout. The SDHP was deployed adjacent to the WS rig bore, to test up to 10 m depth.

To minimise sample disturbance solid sample tube liners were used. Sample diameters were kept as large as possible, with the majority of sample tubes being kept at 100 mm diameter. Following regulations (Section 4.2) sample tubes were immediately sealed on site, and transported in padded boxes to the temperature-controlled lab for storage.

[3] Site work was carried out by contractors to the authors specification, with the author present.

Figure 6.5: Fishbourne site sampling location. Rail track behind hedge along yellow line.

Sampling results

In total ten 1 m length samples were extracted, from two bores (denoted FBS1 and FBS2) as the first 1 m on site was dug by hand as a trial pit. The process set out in 4.6.1 was followed for logging and storing samples. The overall sampling process was very successful with ten lab testing suitable samples recovered from FBS1 and six from FBS2. Figure 6.6 shows a summary of the borehole results (detailed results presented in Appendix Table 8.4 and Table 8.5). The general soil types agree with those found in the nearby BGS boreholes (Figure 6.1), generally consisting of clay which increases in stiffness with depth. Similar results are found from both boreholes, both in soil type and layer thickness, implying fairly uniform stratigraphy below the site. There are a variety of clays present, ranging from softer grey mottled orange clay to stiffer dark brown clay, with some smaller silt layers. The increase in soil stiffness below 3 m BGL agrees with the site seismic measurements Table 6.1).

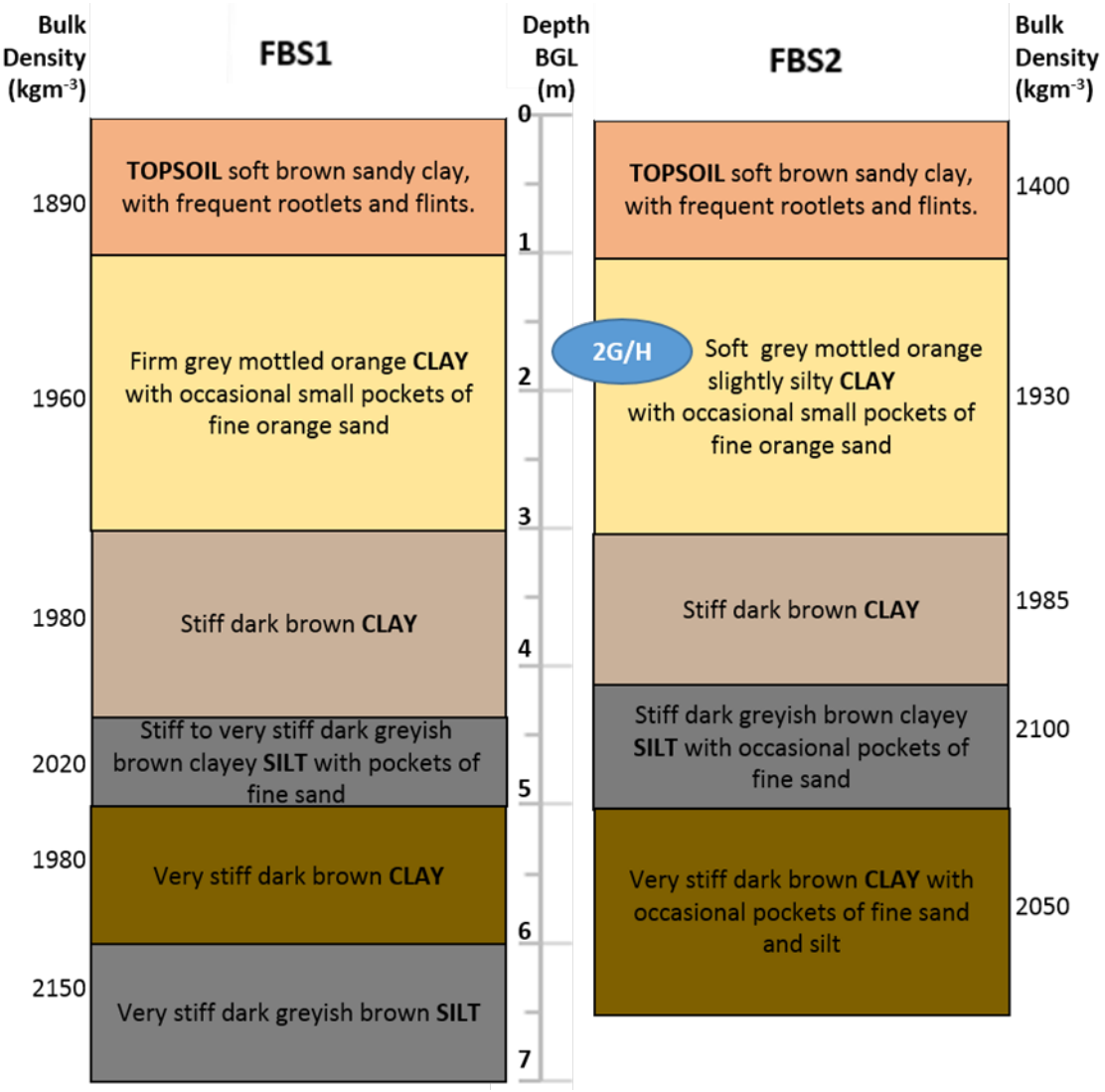

Figure 6.6: Summary of Fishbourne boreholes

Estimates of undrained shear strengths (Figure 6.7) from drop cone tests also show an increase in stiffness below 3 m, correlating well with the borehole results in terms of layer depths. Whilst these strength measurements are not particularly accurate for numerical use, they provide a useful comparison of the strength variation with depth. The estimates of undrained shear strength from the seismic measurements (Table 6.2) compare reasonably well for layer 1 and the halfspace, although the extremely soft seismic layer 2 strength measurement is not represented in the lab measurements.

The SHDP results (Figure 6.8) appear to relate well to the depths of divisions between the soil layers found in the boreholes, with a higher blow number indicating a stiffer soil. Relatively little published work is available to relate SHDP blow count to the soil strength. Huntley (1990) produced guidelines for a relationship for clay, which have been applied to these SDHP results, however they do not agree particularly well to the borehole results. The stiffnesses derived from the SHDP appear to underestimate stiffness compared to the borehole sampling

results, especially for below 3 m depth. As Huntley's SDHP correlation is based on the results for one type of clay from one site it is unsurprising that they do not correlate strongly in this case.

Figure 6.9 shows the variation in density with depth, based upon 50 mm density ring tests completed in the lab. There is some variation in density between the two boreholes, with FBS1 being denser down to 2.5 m BGL and FBS2 denser below 2.5 m BGL. Moisture contents across the boreholes are fairly uniform, generally sitting in the 25-30 % range for the clay soils and 15 to 25 % for the silt soils. These densities sit within expected ranges for clays (Bowles, 1992).

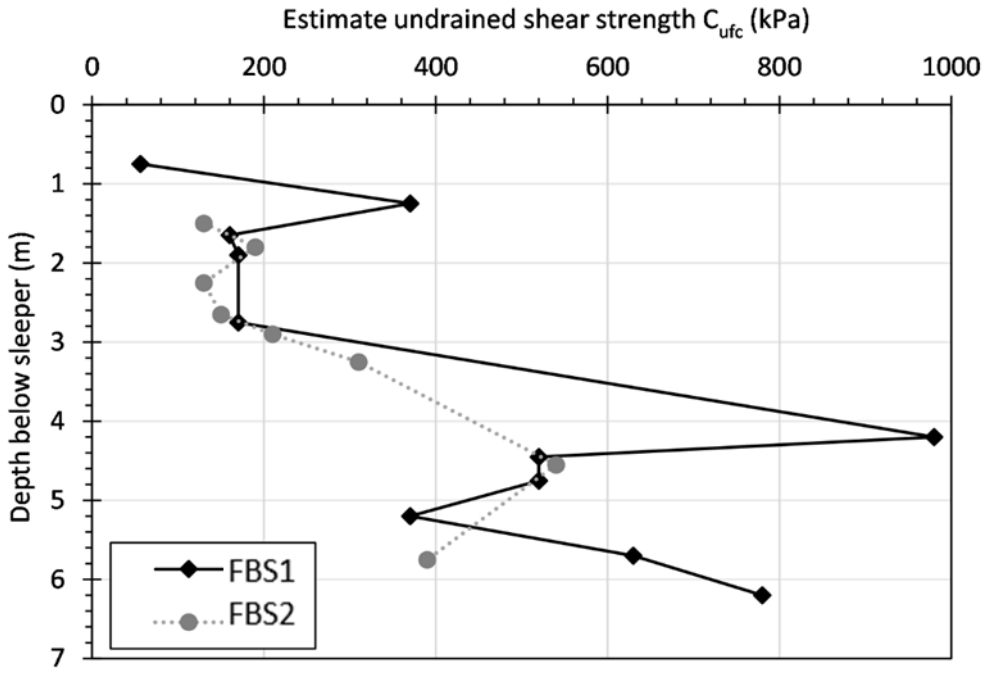

Figure 6.7: Estimate undrained shear strengths from drop cone test for Fishbourne borehole samples.

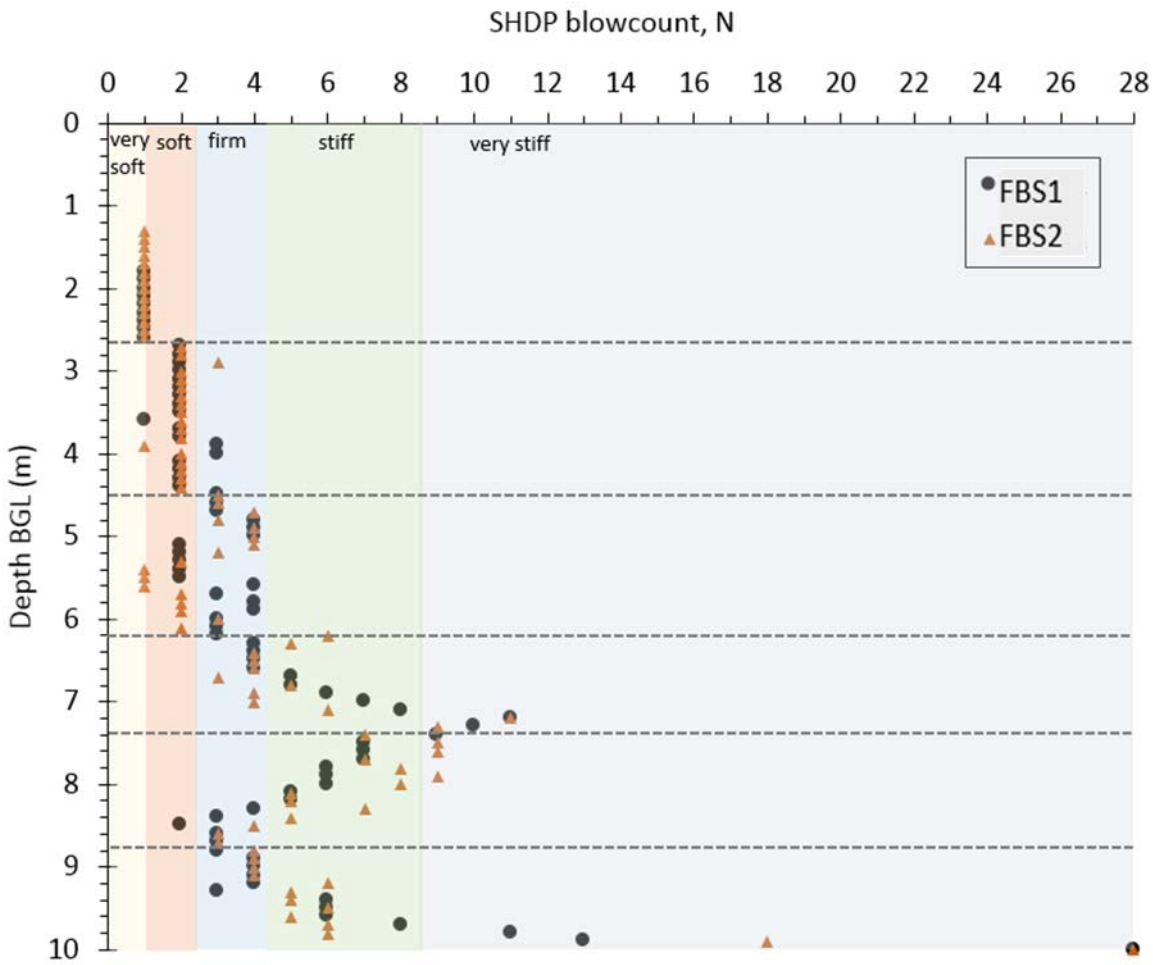

Figure 6.8: SHDP results for Fishbourne, with overlaid estimated relationship between SHDP and clay strength classification, taken from Huntley (1990).

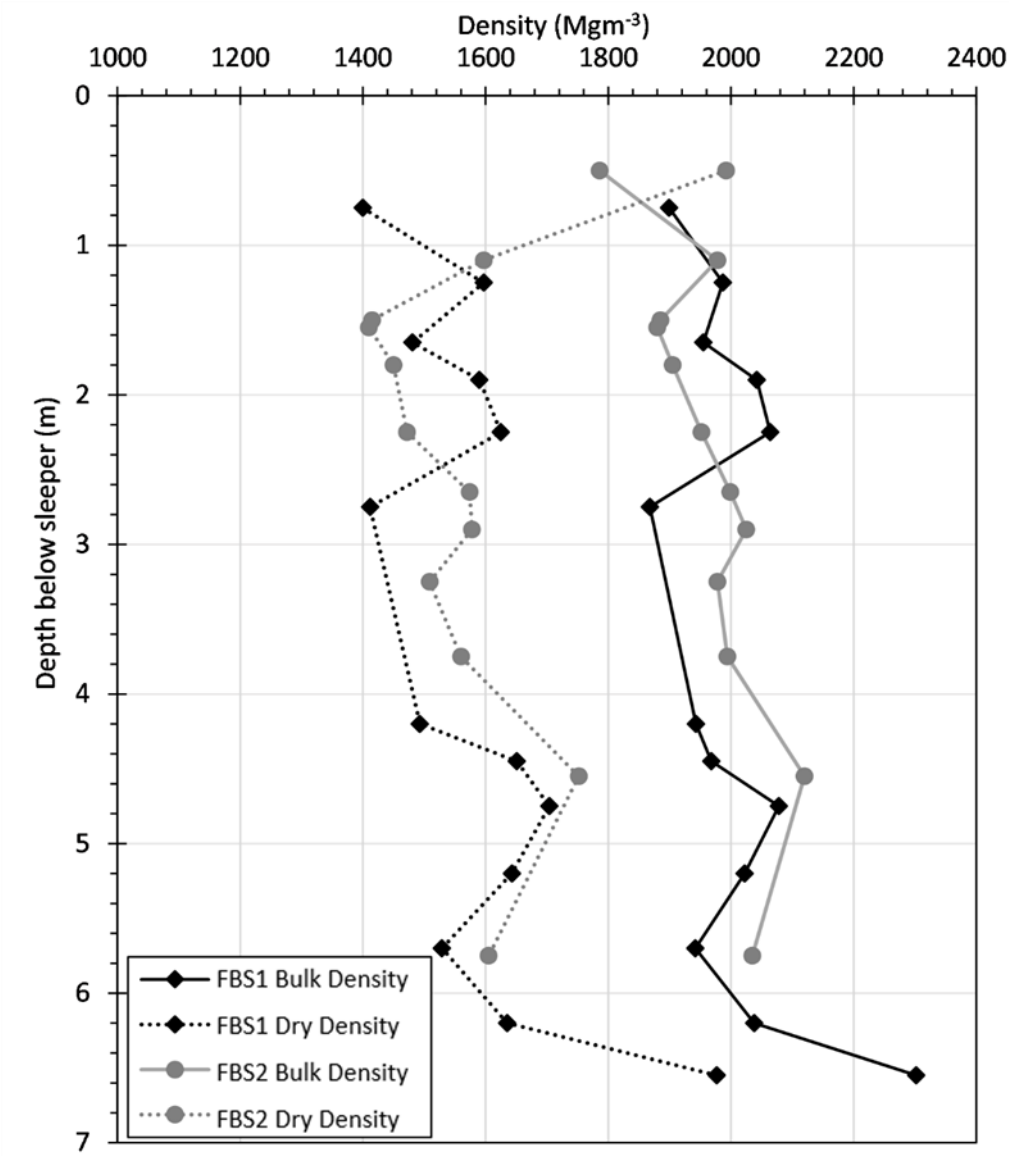

Figure 6.9: Fishbourne borehole density variation with depth

6.3 Initial modelling

6.3.1 Modelling with basic site investigation parameters

Initially a model was created based upon non-invasive site investigation parameters, similar to those available in a typical desk study. To select the model geometry and typical soil types, a combination of the local boreholes was used, and simplified, resulting in the geometry set out in Figure 6.10.

Density, damping and compressional wave speeds were all selected from typical ranges for saturated clays. The shear wave speed for layer 2 was selected from the dispersion curve measurements, whilst the shear wave speeds for the other two layers were selected from typical

values for soils of that type (Bowles, 1992). From these parameters the remaining parameters (Poisson's ratio, shear modulus, Young's modulus) were derived (Table 6.3).

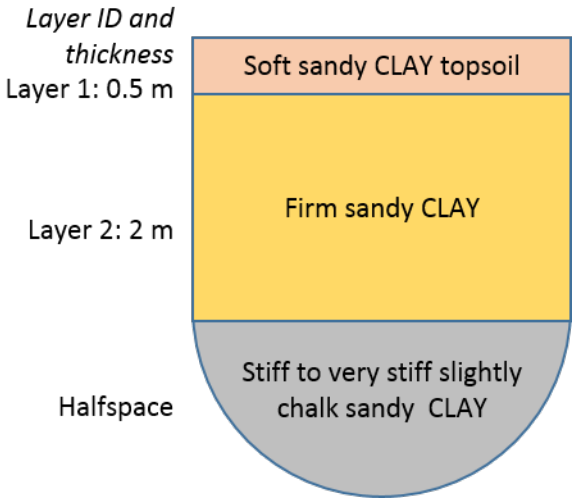

Figure 6.10: Fishbourne model FB1 (desk-study) geometry

Table 6.3: Fishbourne (FB1) initial modelling parameters

Model Id	*Parameter Source*	*Layer*	*Layer Thickness (m)*	*Density (kgm^{-3})*	*DLF (%)*	*G (MPa)*	*E (MPa)*	*V*	*V_S (ms^{-1})*	*V_P (ms^{-1})*
FB1	Desk Study	1	0.5	2000	0.05	12.8	37	0.4984	80	1400
		2	2	2000	0.05	28.8	86	0.4963	120	1400
		Halfspace	-	2000	0.05	33.8	100	0.4957	130	1400

Figure 6.11 presents the result of running model FB1 in MOTIV using a 4-vehicle loading, presuming the trains are at 50% loading capacity. Vehicle loading properties remained as Class 390's as used in the previous Gravel Hole monitoring. Overall the displacements are low, with a peak predicted of 2.1 mm at 111 ms^{-1} (400 kmh^{-1}), above the maximum speed of planned high speed trains in the UK. Due to limiting the output of MOTIV to a resolution of 0.1 mm, to reduce computational time, the resulting curve is not as smooth as for previous models, due to the smaller changes in displacement. An accuracy of greater than 0.1 mm is unnecessary for this modelling, due to the many uncertainties in ground parameter selection.

Figure 6.12 is the resulting dispersion curve, from MOTIV, for the FB1 ground model. The results are clear without the need for normalisation. Several surface wavespeeds are prominent. The first, between 10 Hz and 40 Hz, has a wavespeed of 106 ms^{-1} and is focused in the lower layers. This matches the site dispersion measurements well. A second slower wavespeed cuts on at approximately 40 Hz and has a wavespeed of between 100 ms^{-1} and 84 ms^{-1}, focused in the upper layers, which is not present in the site measurements. A second faster wavespeed in the lower layers is also prominent, between 10 Hz and 30 Hz with a wavespeed of 192 ms^{-1}, with another

wave cutting on in the low-mid layers with a speed of around 120 ms^{-1}, this shows some similarity with the second wavespeed measured on the site dispersion plot. Overall the model dispersion plot does not show some of the response at highest frequencies shown on the site model.

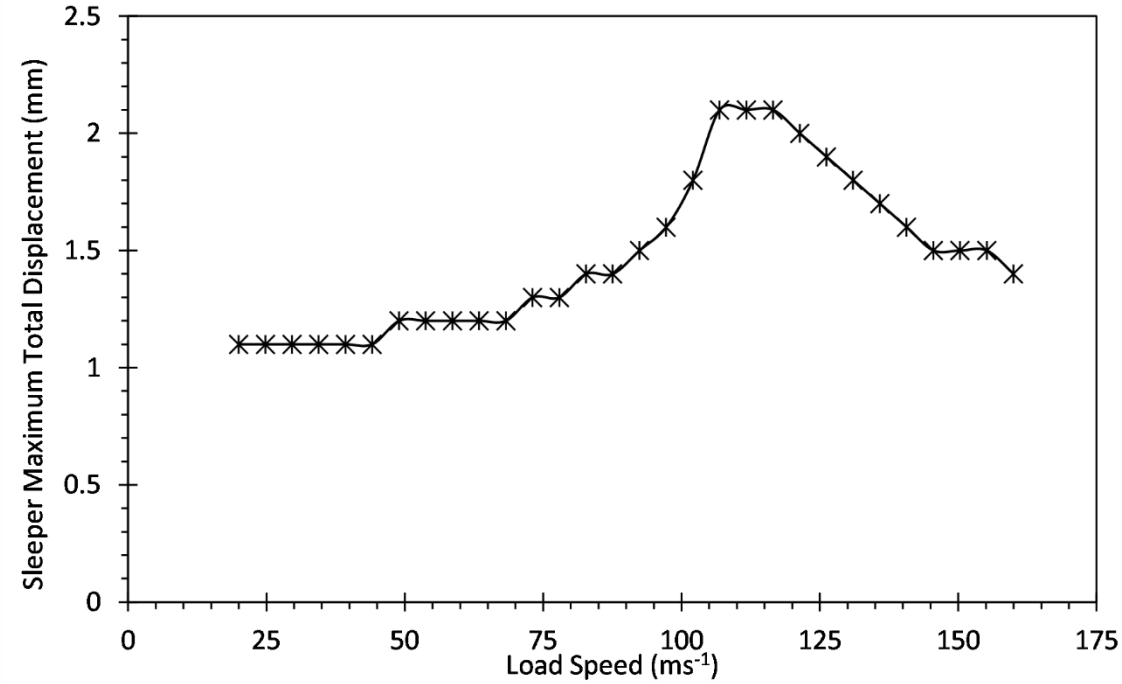

Figure 6.11: MOTIV displacement results for Fishbourne model FB1 - desk study parameters.

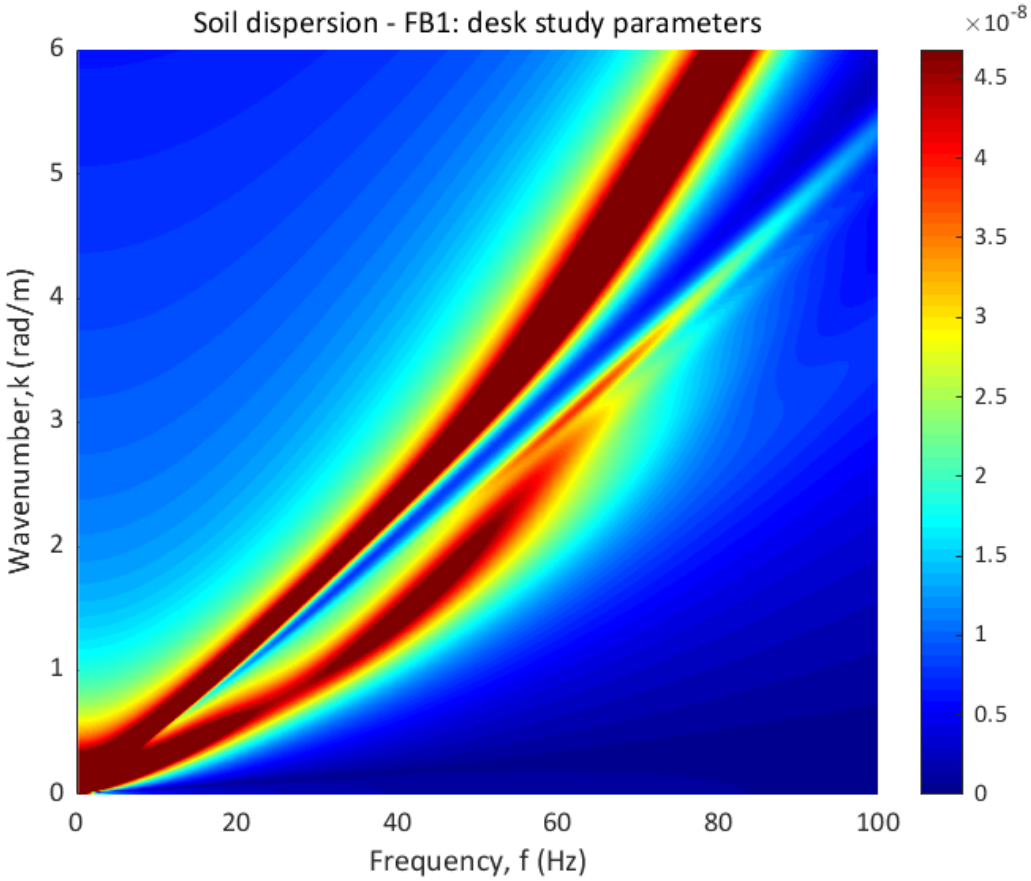

Figure 6.12: Dispersion plot for Fishbourne model FB1 - desk study parameters.

6.4 Laboratory testing regime for site samples

6.4.1 Sample selection

Figure 6.13 presents a visual example of the range of soils present across the bores, both in type and colouring. There are two predominant forms of clay present in the bores (Figure 6.14), the soft to firm grey mottled orange clay between 1 and 3 m, and the stiff dark brown clay from 3-4.2 m.

Figure 6.13: Fishbourne boreholes - selection of dried density samples, displaying variation in soil colouring and type.

Figure 6.14: Fishbourne bore 2, sections 1-2 m (left) and 3-4 m (right)

To be deemed suitable for lab testing samples must be of at least 100 mm diameter (to allow trimming to 70 mm), have a minimum height of 150 mm and be undamaged. Although 16 samples suitable for lab testing were recovered, time restraints only allowed testing of one Fishbourne sample in each of the pieces of equipment. Therefore samples from the softest clay section were selected, from bore 2. Samples FB2G and FB2H were selected as adjacent samples, coming from 1.4 to 1.65 m and 1.65 to 1.85 m depth in bore 2 respectively. Both samples appeared externally similar in soil type and density (Table 6.4).

Each sample was trimmed from its original diameter of 100 mm down to the testing diameter of 70 mm, and to a height of 140 mm, to remove any disturbed material on all faces. Figure 6.15

shows the disturbance caused by the sampling tube during the window sampling process, with the outer layer looking very different to the inner undisturbed clay after trimming. The mottling and small sand pockets within the samples are much clearer with the outer disturbed layer removed.

Table 6.4: Fishbourne lab sample details.

Sample Id	*Bore 2 depth BGL (m)*	*Soil Description*	*Initial bulk density (kgm^{-3})*	*Initial moisture content (%)*	*Initial dry density (kgm^{-3})*
FB2G	1.45-1.65	soft light grey mottled orange slightly silty CLAY with small pockets of white and orange fine sand	1920	32	1455
FB2H	1.65-1.85		1940	34	1470

Figure 6.15: Fishbourne samples 2G (left) and 2H (right) before trimming (top) and after trimming (bottom).

6.4.2 Testing stresses

Following the method set out in section 5.3.2, stresses for testing were calculated (Table 6.5). As the water table level is unknown a range of levels was selected. A higher stress level of 146 kPa was also selected, to represent the possibility of a future surcharge being applied to the area.

Table 6.5: Calculated in situ stresses and target testing stresses for samples FB2G and FB2H.

Assumed water table depth below surface (m)	*Target vertical effective stress σ'_v (kPa)*	*Target mean effective stress p' (kPa)*	*Target axial stress q (kPa)*
0.5	31	21	15.5
2	46	31	23
5	76	51	38
12	146	97.3	71.4

6.5 Laboratory test results

6.5.1 General index testing

In addition to density, moisture content and drop cone strength measurements (section 6.2.3), liquid and plastic limit tests were also carried out on the selected samples. FB2G/H (the soft to firm grey mottled orange clay from 1 to 3 m depth) was found to have a liquid limit of 72 %, a plastic limit of 20 % and a plasticity index of 52 %. When plotted on a plasticity chart (Figure 6.16) this soil is classified as a very high plasticity clay, close to the high plasticity clay border. The in-situ moisture content range of 25 % to 30 % therefore sits above the plastic limit but below the liquid limit.

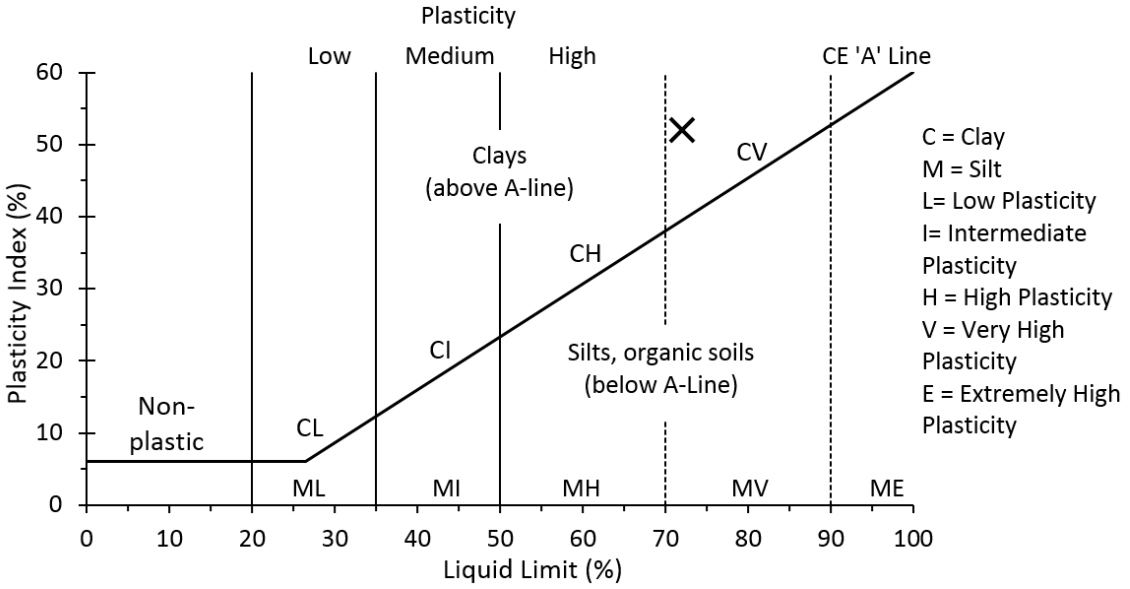

Figure 6.16: Fishbourne sample 2G/2H plasticity classification chart. Chart modified from BS5930 (British Standards Institute, 2015).

6.5.2 Resonant column results

Resonant column testing, including incorporated bender elements, was successfully carried out on sample FB2H. The sample was found to swell during consolidation, resulting in the drivehead coming into contact with the top plate and so affecting the results at the lowest target pressure (31 kPa). Difficulties were found with the clay particles partially blocking the back pressure line, despite the use of filter papers. A better adaptation would be the addition of a ceramic disc and paper into the base platen itself. No net height change occurred for this sample, as it swelled during consolidation by approximately 1 mm, and consolidated by a similar amount at higher pressures. It is not known how much the reduced flow in the back pressure line affected this. The average diameter of the sample increased by 0.5 mm between pre-saturation and the final 146 kPa test pressure.

Shear modulus

The shear modulus curves for sample FB2H are presented in Figure 6.17. The resulting values sit within typical strength ranges for soft clay (Bowles, 1992; Vardanega and Bolton, 2013) . The strain limit of Zone 1, where degradation begins, appears to be approximately 0.0015%, whilst the limit for Zone 2, beyond which strain is irrecoverable, was not met. This Zone 1 boundary is slightly smaller than that of slightly silty clay sample GH1O (0.025%) and far smaller than that of the silts GH2K and GH2C (0.06 % to 0.08%), implying that silt content increases the value of the Zone 1 boundary.

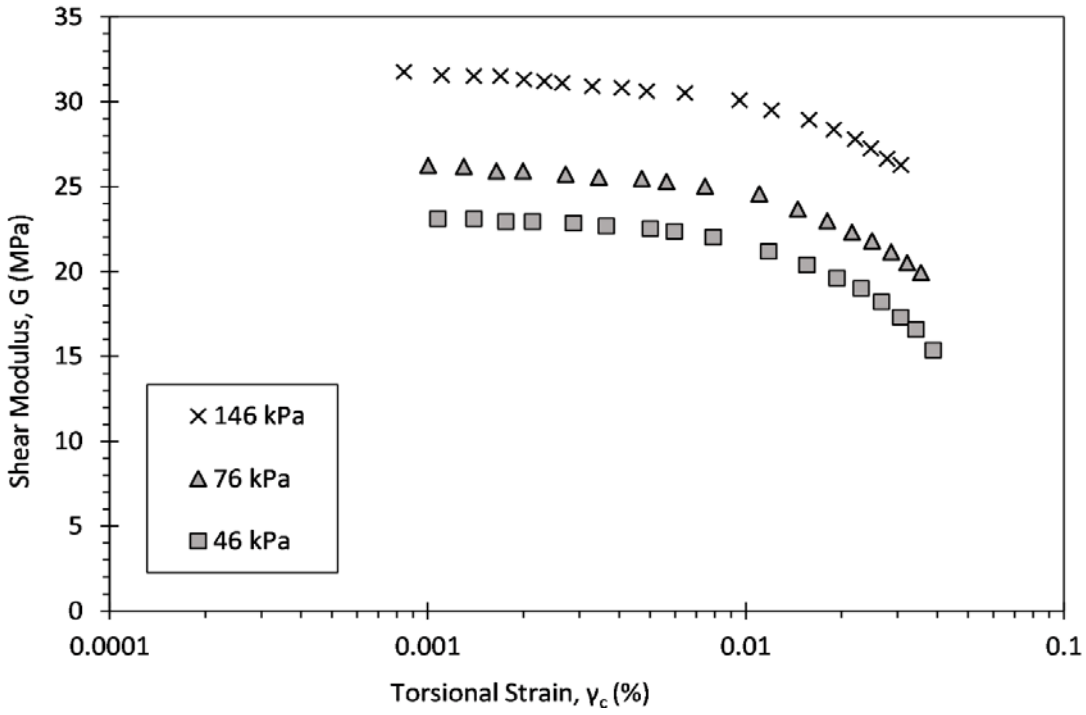

Figure 6.17: Shear modulus degradation with strain for sample FB2H during torsional excitation in the RC, at a range of mean effective stresses. Strain limits not met.

Damping

Damping was also successfully measured for sample FB2H, presented in Figure 6.18. An indication of increasing confining stress resulting in decreased damping is found, although the highest pressure does not correlate with this. Larger confining stresses would be needed, to produce a wider range of damping ratios, to better test this relationship. These measured damping ratios compare well to typical damping ratios for clay (Figure 6.19), which presents damping ratios for a range of clays collated by Sun *et al.* (1988). The measured torsional strains have been converted to distortional strain to enable comparison.

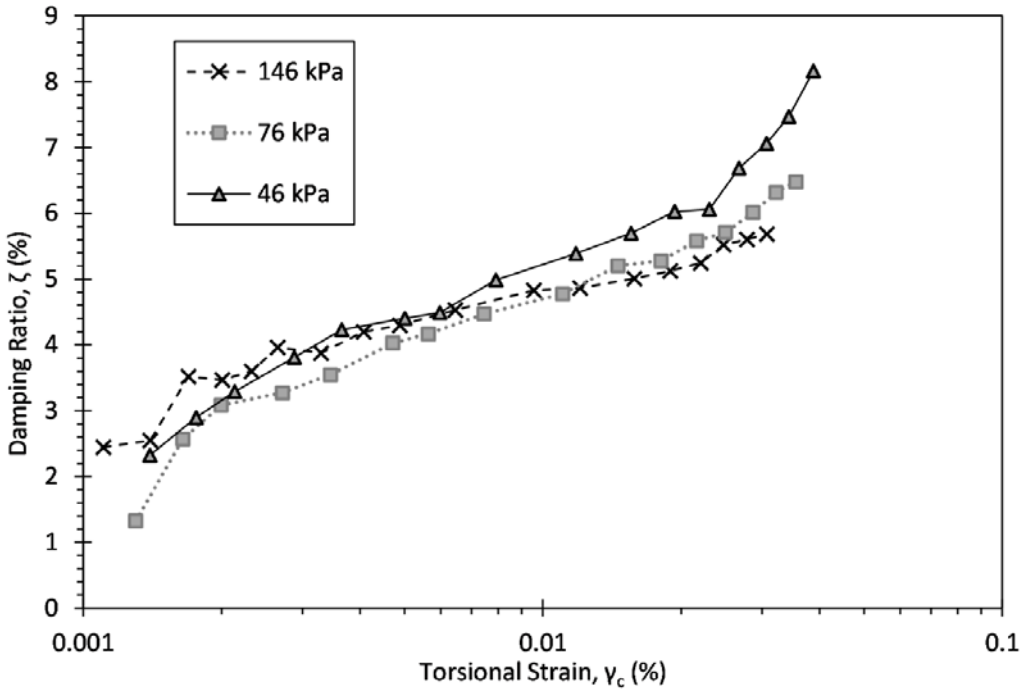

Figure 6.18: Relationship between damping and strain for sample FB2H, during torsional excitation in the RC, for a range of mean effective stresses.

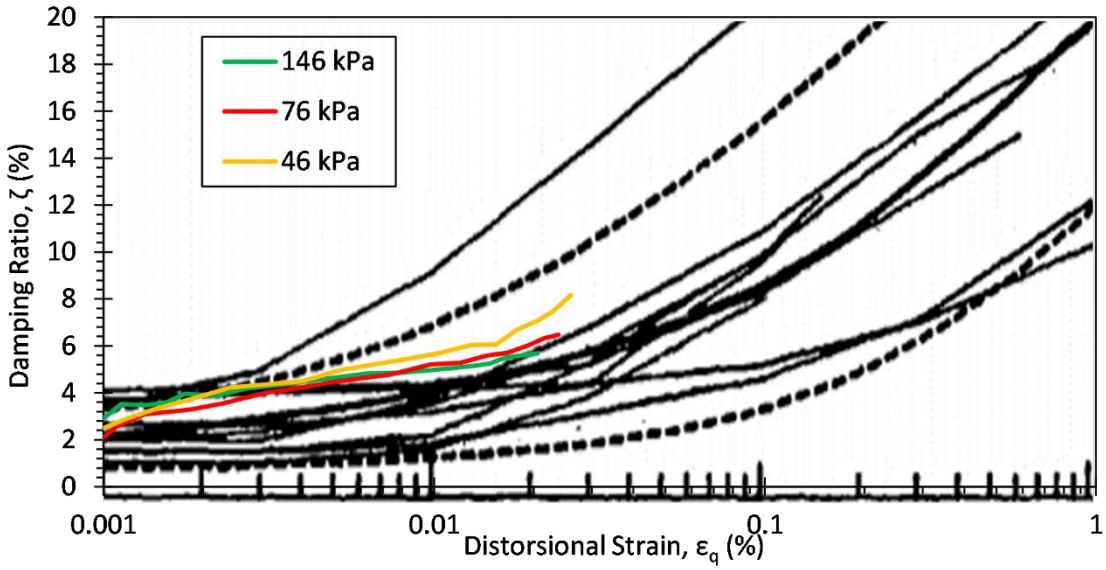

Figure 6.19: Measured damping for FB2H compared to typical clay damping ratios modified from Sun *et al.* (1988).

RC bender elements

Bender element measurements of shear modulus compare well to the resonant column measurements, with a mean difference of 1.5 % and a maximum difference of 2.7 %. Whilst the resonance method excites the entire sample and so gives a modulus of the bulk material, the bender element method is exciting waves through mainly the centre of the sample. Therefore the similarity in the shear moduli derived from these methods implies the sample is very homogeneous.

Compressional wave speeds were also measured using the bender elements, as discussed in section 5.4.2. The compressional wave speeds measured in the Fishbourne sample (Table 6.6) agree well with the expected clay values of 1100 ms^{-1} to 2500 ms^{-1} (Mavko, 2005), ranging from 1290 ms^{-1} to 1450 ms^{-1}

Table 6.6: Compressional and shear wave speeds measured in the RC using bender elements.

Sample ID	*Vertical Effective Stress, σ'_v (kPa)*	*V_S (ms^{-1})*	*V_P (ms^{-1})*
FB2H	46	109	1290
	76	114	1340
	146	128	1450

6.5.3 Triaxial / bender element results

After saturation sample FB2G was consolidated along the K_O line to each target stress, with drained and undrained constant q and constant p' probes being carried out at each target stress. The ratio of q to p' required to meet K_O conditions averaged 0.72. The size of each probe was adjusted as the stiffness of the sample increased (Table 6.7). The accuracy of control within these probe tests was similar to that found in the Gravel Hole testing, with a maximum drift in p' of 1.1 kPa during the constant p' probes (a total drift of 3.5 % to 0.75 %), and excellent q control with a drift of ± 0.025 kPa (± 0.32 % to ± 0.07 %). Estimations of error range in data measurements, and the analysis method followed, are as detailed in section 5.4.3. The sample decreased in height by 6 mm overall, with a diameter change of 0.1 mm.

Table 6.7: Details of probe tests for FB2G

Target vertical effective stress σ'_v (kPa)	*Drained constant q probe size (kPa)*	*Drained constant p' probe size (kPa)*	*Undrained constant q probe size (kPa)*	*Undrained constant p probe size (kPa)*
31	5	5	5	5
46	5	5	8	8
76	10	10	10	10
146	10	10	10	10

Figure 6.20 shows the shear modulus degradation curves for sample FB2G. The variation in curve shape implies that the probe at 76 kPa was impacted by residual sample movements, perhaps a result of insufficient time being left between probes to allow sample strains to slow to the creep rate. The transition strain between Zone 1 and 2 is not particularly clear, but appears lower than the 0.0015% measured in the resonant column for sample FB2H, with only the highest pressure for sample FB2G matching this.

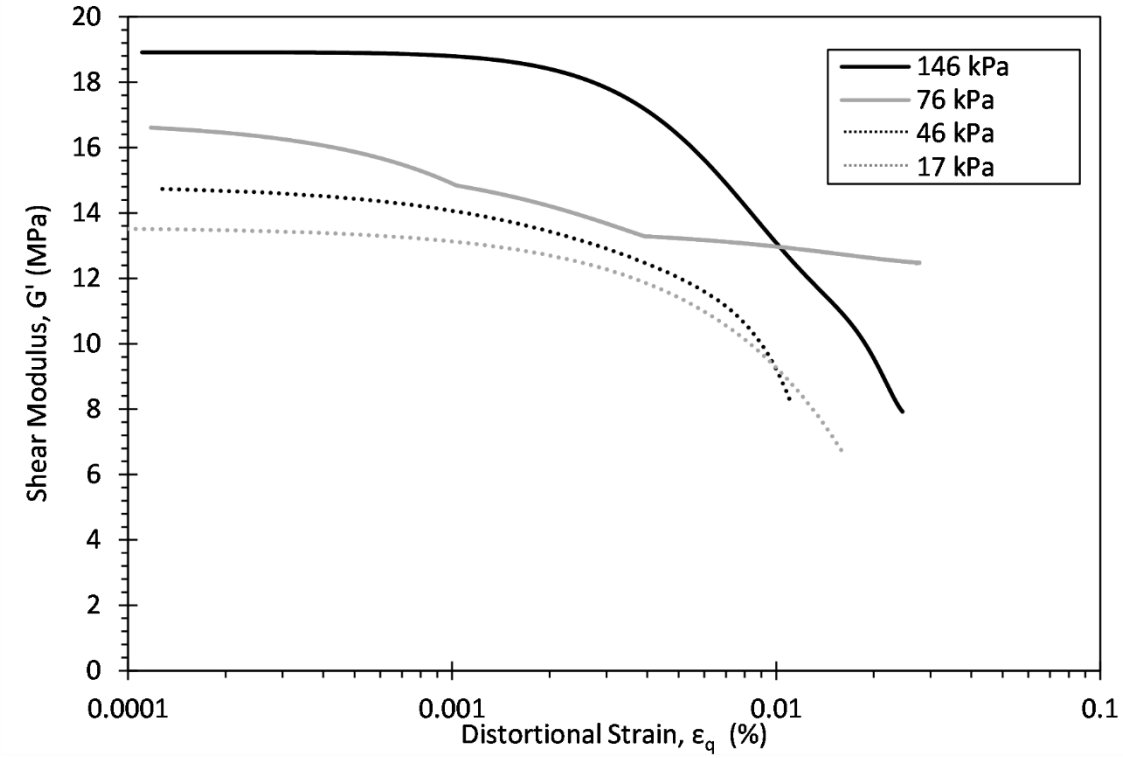

Figure 6.20: Shear modulus degradation with strain for sample FB2G from constant p', increasing q triaxial probes, at a range of mean effective stresses.

Poisson's ratio

Poisson's ratios (Figure 6.21) for sample FB2G are derived from the method set out in section 4.4.2. The results show some variation with stress level, with no clear correlation between confining stress and Poisson ratio. There appears to be a general trend of Poisson's ratio decreasing with strain, with a range of approximately 0.5 to 0.4. Overall these values sit within expected ranges for saturated clays (Bowles, 1992). The lack of correlation between confining stress and Poisson's ratio is possibly a combination of the data fitting method and insufficient resolution in the radial strain measurement.

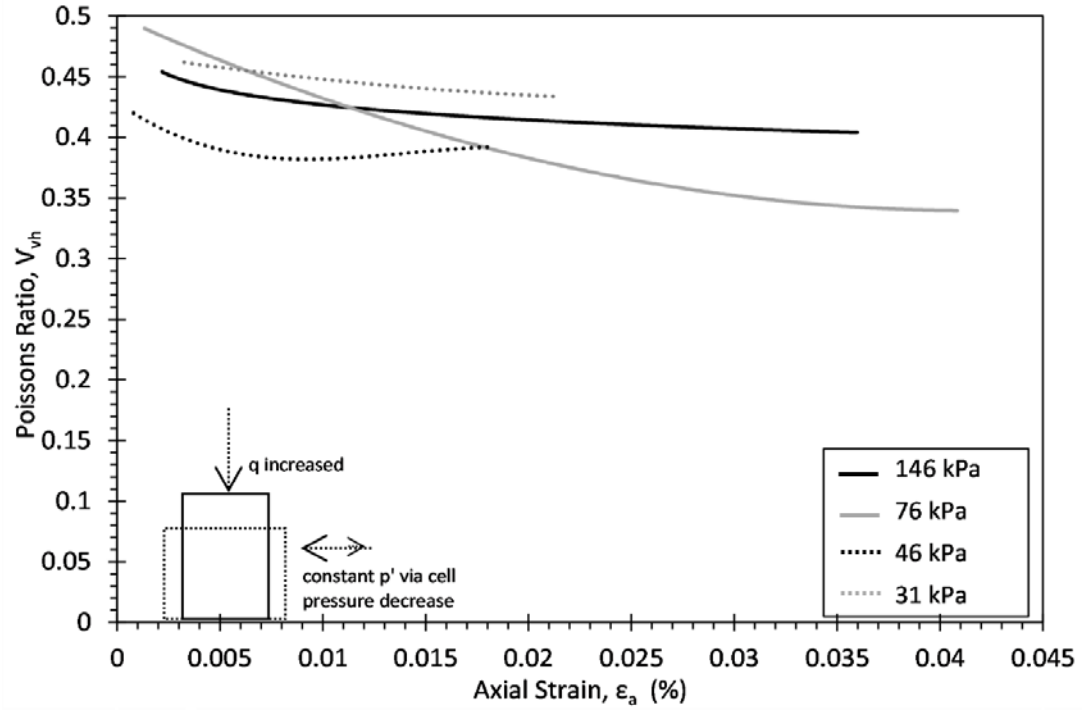

Figure 6.21: Relationship between Poisson's ratio and axial strain, for sample FB2G tested with constant p', increasing q triaxial probes.

Peak undrained strength

After probes at the largest consolidation pressures were complete, a large strain shear test was carried out. A global axial strain of 15 % was targeted, at a rate of 0.5 % per hour. Unfortunately, the load cell became erratic above a strain of 2.5 %. Figure 6.22 shows the resulting measurements up until this point. It appears a peak at approximately q = 100 kPa is reached, although without data from higher strains this is uncertain. This would equate to an undrained shear strength at a confining pressure of 146 kPa of 50 kPa.

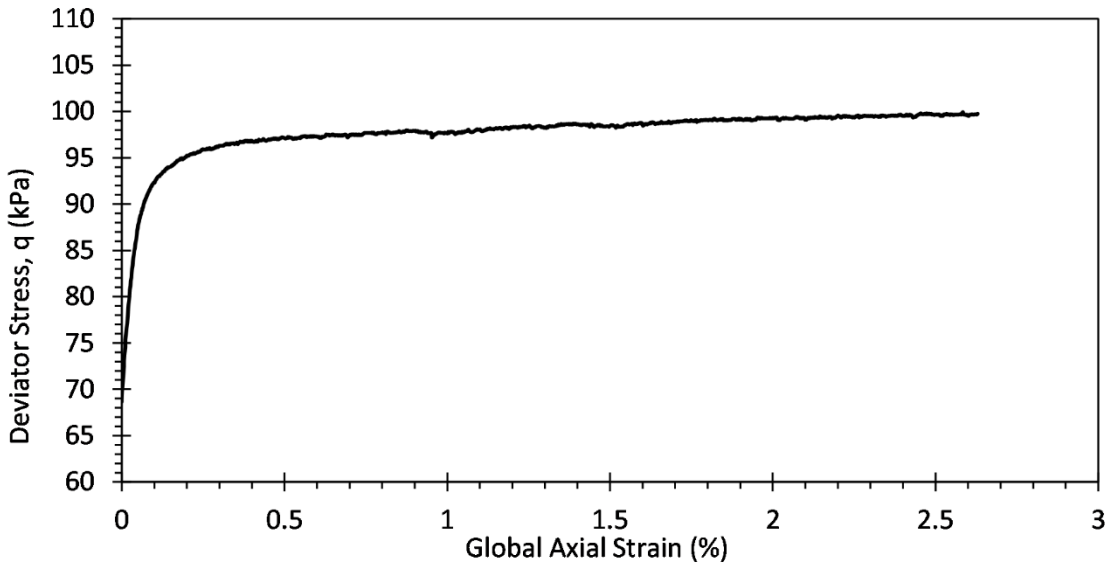

Figure 6.22: Large undrained triaxial shear result for FB2G, at a confining pressure of 146 kPa.

G* and G_{hv}

In samples FB2G successful horizontal bender element measurements were taken, allowing derivation of the vertical shear modulus (G_{hv}), as well as undrained probes, allowing derivation of G*, a shear modulus parameter proposed by Graham and Houlsby (1983). A comparison of the small strain stiffness results is presented in Figure 6.23. A strong relationship is found between the two sets of results, with G_{hv} consistently lower than G*. The difference between the moduli decreases from 27 % at 31 kPa to 14% at 146 KPa. The improved match at higher pressures may be partially attributable to the connection between the bender elements and the soil becoming more stable with increased pressure.

It should be noted that a relationship would only be expected for an isotropic soil, as in an anisotropic soil these two parameters are independent. Also, G* is a property of the bulk material, as the entire sample is tested, whereas G_{hv} passes shear waves through a relatively small section of the sample. As for the Gravel Hole samples G_{hv} appears consistently lower than G*, although a far stronger relationship is found for the Fishbourne sample. This is to be expected as the Fishbourne sample is a far more homogeneous soil.

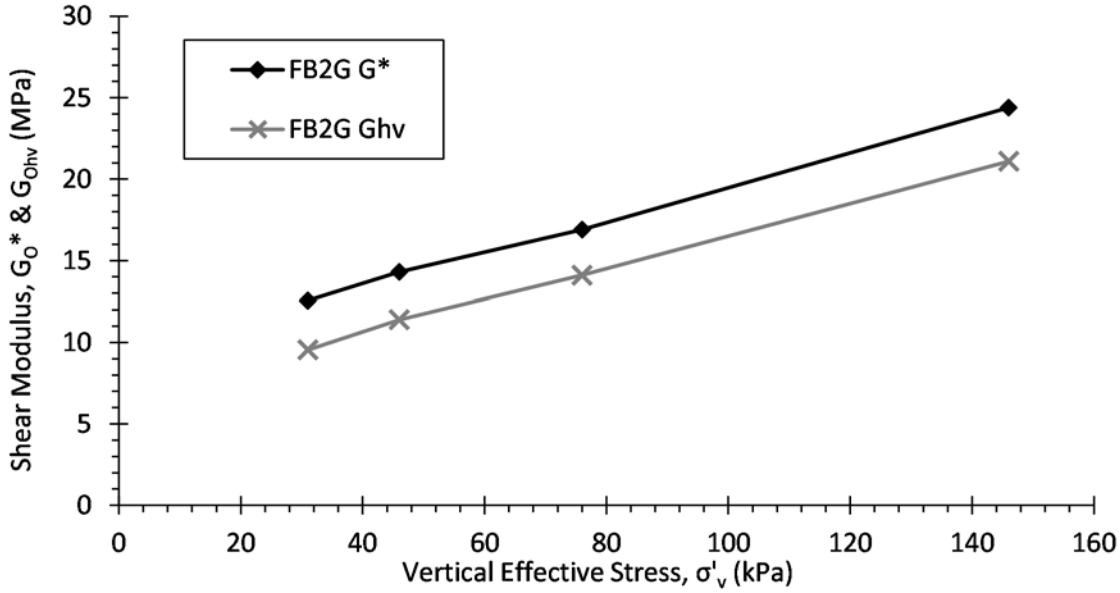

Figure 6.23: Comparison of the small strain shear moduli parameters G*, derived from undrained triaxial tests, and G_{hv}, derived from bender element tests, for a range of test pressures.

6.5.4 Comparison of results from both methods

Figure 6.24 shows the comparison between all methods of small strain shear modulus measurement – resonant column, bender elements and triaxial. The resonant column and bender element results agree extremely well, implying the sample is homogeneous. As in the Gravel Hole case study, the triaxial moduli are far lower than the moduli from other methods, in this case approximately 60 % of the higher values. Although not identical, the two samples were of very similar initial densities, dimensions and moisture content. As discussed previously, the difference in consolidation methods had a large impact on this difference in moduli, with the triaxial K_O consolidation resulting in a 6 mm (4.2 %) decrease in height and a 0.1 % change in diameter, compared to no net change in height and a 0.7 % change in diameter for the resonant column.

The shear wavespeeds from the resonant column (109 ms^{-1} at very small strains for an effective confining pressure of 46 kPa) agree well with the shear wavespeed estimates for that depth from the seismic measurements, which were approximately 100 ms^{-1} from the dispersion plot and 80 ms^{-1} to 140 ms^{-1} from the seismic based modelling.

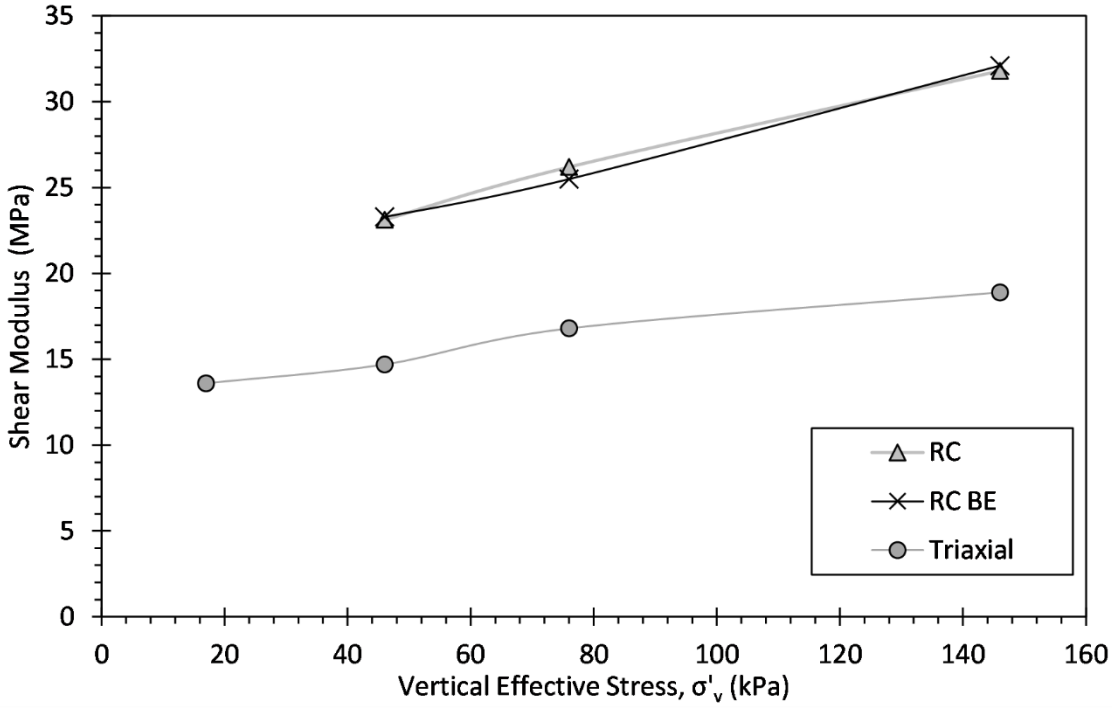

Figure 6.24: Comparison of relationship between very small strain shear modulus and vertical effective stress, for similar samples FB2G and FB2H tested in the RC, RC BE and triaxial machines.

Normalisation of the derived shear moduli by the small strain modulus enables comparison of the degradation rates between the resonant column and the triaxial samples (Figure 6.25). In general, the gradients of the degradation curves are similar across the methods, with the threshold strains being lower for the triaxial than the resonant column, as found in the Gravel Hole study.

Figure 6.25 also presents typical shear modulus degradation curves for clays of a range of plasticity indexes. Although lab testing estimated the plasticity index of FB2G and FB2H at 52 % neither the triaxial or the resonant column results follow the typical degradation curve for this level of index, instead showing a faster rate of degradation with strain.

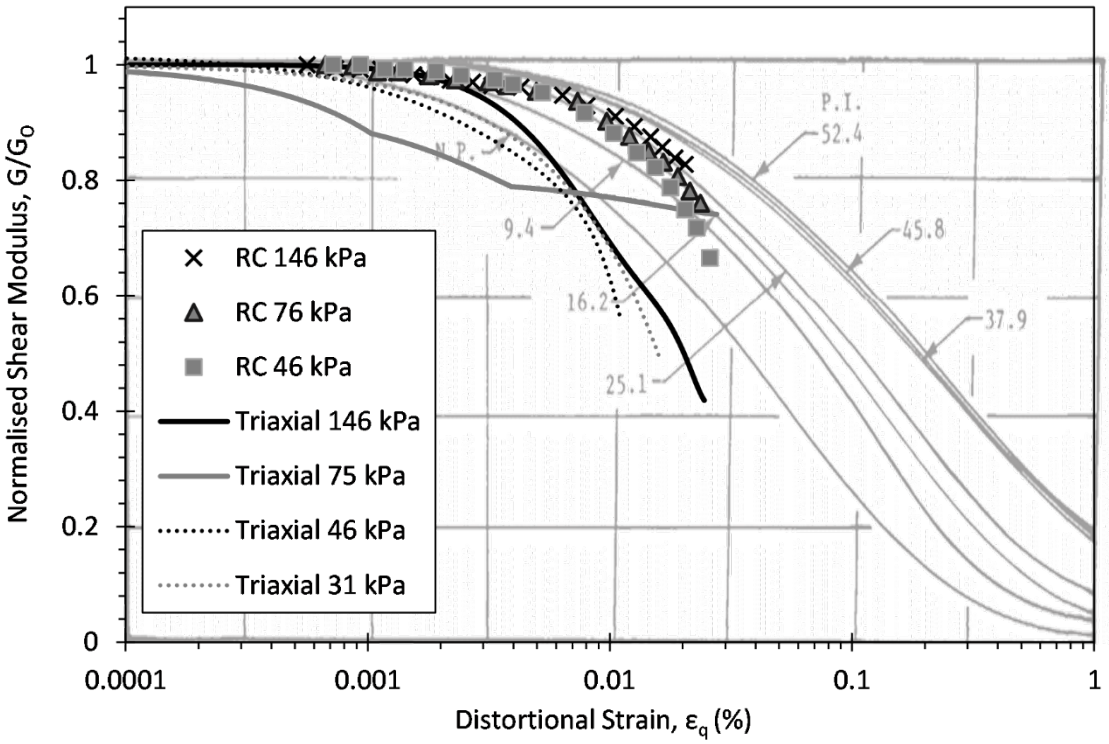

Figure 6.25: Normalised shear modulus degradation with strain for similar Fishbourne samples FB2H and FB2G in the RC and triaxial machines. Results shown are for a range of vertical effective stresses. Also shown are typical normalised shear modulus with distortional strain relationship for various clay plasticity indexes, after Zen *et al.* (1978).

6.6 Modelling with laboratory parameters

6.6.1 Parameter selection and incorporation of strain

As the water level on the site is unknown the laboratory values relating to a depth of 2 m (σ'_V = 46 kPa) were selected. A simplification of soil geometry was taken from the two site boreholes, accounting for the depths at which density and soil type changes are most prominent. Figure 6.26 shows the selected model geometry and the soil type which each layer represents.

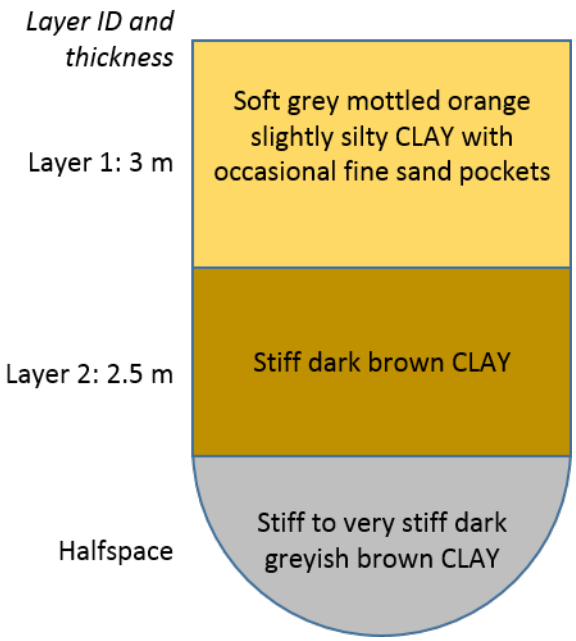

Figure 6.26: Model geometry for Fishbourne models FB2,FB3 and FB4.

Samples FB2G and FB2H are representative of layer 1, with parameters for this layer being selected from lab results. As there was insufficient time to allow testing on the other soil layer, estimates were made based upon the measured density and relative stiffness from the various in-situ measurements, in combination with typical clay strengths.

Layer 1 is based upon shear modulus, density, damping, shear wave speed and compressional wave speed measurements made in the laboratory. From these values, under the assumption of an isotropic material, Young's modulus and Poisson's ratio were evaluated. The Poisson's ratio evaluated from the measured wavespeeds in layer 1 was also assigned to layers 2 and 3, at 0.4965 it is a reasonable value for a saturated clay. Also, as the compressional wave speed does not have a significant influence on the model results any error in this estimation will not have a large impact.

The initial shear wave speed for layer 2 was taken from the seismic measurements, with damping taken as a mid-range of typical clay damping measurements at small strain (Figure 6.19). Note that damping loss factor is twice the value of damping ratio. Moduli and compressional wave speeds were derived from these values.

The initial shear modulus for the halfspace was estimated from published data for stiff clays of similar density and in-situ moisture content at similar low confining stresses (Lo Presti *et al.*, 1998; Vardanega and Bolton, 2013). Estimates were taken to err on the side of caution (weaker values). Damping was taken as for layer 2, with other parameters derived from these selected values.

Following the theory and process set out in the Gravel Hole modelling (section 5.5.1), parameter values were selected at increasing distortional strains. For layer 1, where these strain values fell within the measured values the laboratory measurements were used. When input strains higher than the measured strains were required estimates were made based upon a typical continuation of the measured curves (Figure 6.19, Figure 6.25). For layers 2 and 3, again these typical degradation rates of damping and shear modulus for clays were used. Other parameters were derived from these, with density and Poisson's ratio assumed constant. The model input parameters are set out in Table 6.8. Note that ND denotes non-degraded (small-strain) parameters.

Table 6.8: Fishbourne post-laboratory test modelling parameters.

Model ID	ε_q*(%)*	*Layer*	*Layer Size (m)*	*Density (kgm^{-3})*	*DLF*	*G (MPa)*	*E (MPa)*	*V*	V_S *(ms^{-1})*	V_P *(ms^{-1})*
	ND	1	3	1930	0.084	22.5	67.4	0.4965	108	1290
FB2	ND	2	2.5	2000	0.06	31.1	93	0.4965	125	1499
	ND	H/S	H/S	2100	0.06	36.8	110	0.4965	132	1586
	0.023	1	3	1930	0.15	16.4	49	0.4965	92	1104
FB3	0.023	2	2.5	2000	0.14	20	60	0.4965	100	1199
	ND	H/S	H/S	2100	0.06	36.8	110	0.4965	132	1586
	0.066	1	3	1930	0.22	8	24	0.4965	65	775
FB4	0.066	2	2.5	2000	0.26	13.4	40	0.4965	82	985
	ND	H/S	H/S	2100	0.06	36.8	110	0.4965	132	1586
	0.15	1	3	1930	0.28	4.1	12	0.4965	46	555
FB5	0.066	2	2.5	2000	0.26	13.4	40	0.4965	82	985
	ND	H/S	H/S	2100	0.06	36.8	110	0.4965	132	1586
	0.066	1	3	1930	0.22	4.1	24	0.4965	65	775
FB6	0.023	2	2.5	2000	0.14	20	60	0.4965	100	1199
	ND	H/S	H/S	2100	0.06	36.8	110	0.4965	132	1586
	0.06	1	3	1930	0.21	8.8	26	0.4965	67	807
FB7	0.02	2	2.5	2000	0.13	20.9	63	0.4965	102	1226
	ND	H/S	H/S	2100	0.06	36.8	110	0.4965	132	1586
	0.05	1	3	1930	0.2	10.4	31	0.4965	73	880
FB8	0.02	2	2.5	2000	0.13	20.9	63	0.4965	102	1226
	ND	H/S	H/S	2100	0.06	36.8	110	0.4965	132	1586

Model ID	ε_q(%)	Layer	Layer Size (m)	Density (kgm^{-3})	DLF	G (MPa)	E (MPa)	V	V_S (ms^{-1})	V_P (ms^{-1})
	0.01	1	3	1930	0.114	20.1	60	0.4965	102	1223
FB9	0.01	2	2.5	2000	0.12	25.4	76	0.4965	113	1352
	ND	H/S	H/S	2100	0.06	36.8	110	0.4965	132	1586
	0.04	1	3	1930	0.19	11.5	34	0.4965	77	926
FB10	0.02	2	2.5	2000	0.13	20.9	63	0.4965	102	1226
	ND	H/S	H/S	2100	0.06	36.8	110	0.4965	132	1586
	0.01	1	3	1930	0.114	20.1	60	0.4965	102	1223
FB11	0.005	2	2.5	2000	0.1	27	81	0.4965	116	1393
	ND	H/S	H/S	2100	0.06	36.8	110	0.4965	132	1586
	0.04	1	3	1930	0.19	11.5	34	0.4965	77	926
FB12	0.01	2	2.5	2000	0.12	25.4	76	0.4965	113	1352
	ND	H/S	H/S	2100	0.06	36.8	110	0.4965	132	1586
	0.08	1	3	1930	0.24	6.9	21	0.4965	60	717
FB13	0.015	2	2.5	2000	0.12	23.3	70	0.4965	108	1293
	ND	H/S	H/S	2100	0.06	36.8	110	0.4965	132	1586

6.6.2 Results – non-degraded parameters

Initial modelling was carried out using small–strain, non-degraded parameters, FB2 (Table 6.8). Figure 6.27 shows the resulting displacement–speed curve, with relatively small predicted displacements peaking at 2.3 mm, and a critical velocity of 113 ms^{-1} (407 km/h). These results are fairly similar to the non-degraded model FB1 based on desk-based parameters, showing that a reasonable estimation for well established materials can be possible for desk-based parameters assessments of simpler sites. The resulting dispersion plot for this model is shown in Figure 6.28. The first surface wave occurs between 0 Hz and 60 Hz with a speed of 103 ms^{-1}, extending towards the upper layers. This matches the first surface wave speed and location in the Fishbourne site measurements very well (Figure 6.3).

A faster wave speed is also shown in the lower layers, focused between 0 and 20 Hz, with a speed of between 140 ms^{-1} and 230 ms^{-1}. This shows some agreement to the site measurements, although the FB2 dispersion plot does not replicate the mid-wavenumber, mid-frequency surface waves shown on the site measurements. It may be that the site ground has layers of uneven depth or confined length, which the model is unable to replicate.

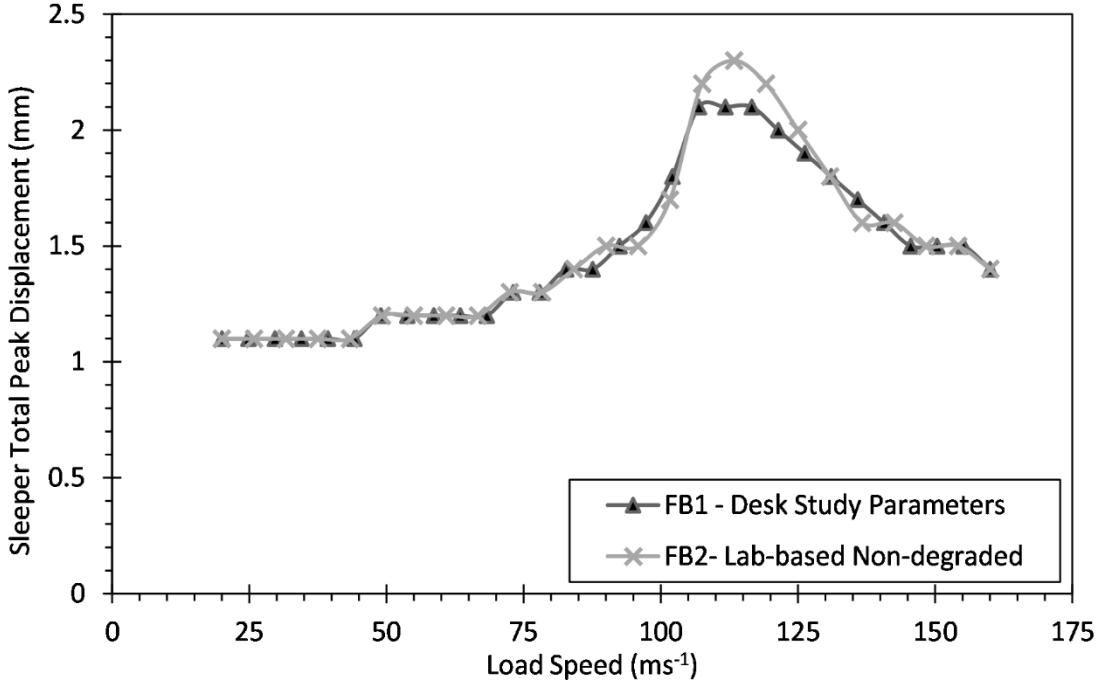

Figure 6.27: Relationship between load speed and sleeper displacement, 4 vehicle model–Fishbourne model FB2 (Lab-based parameters, non-degraded).

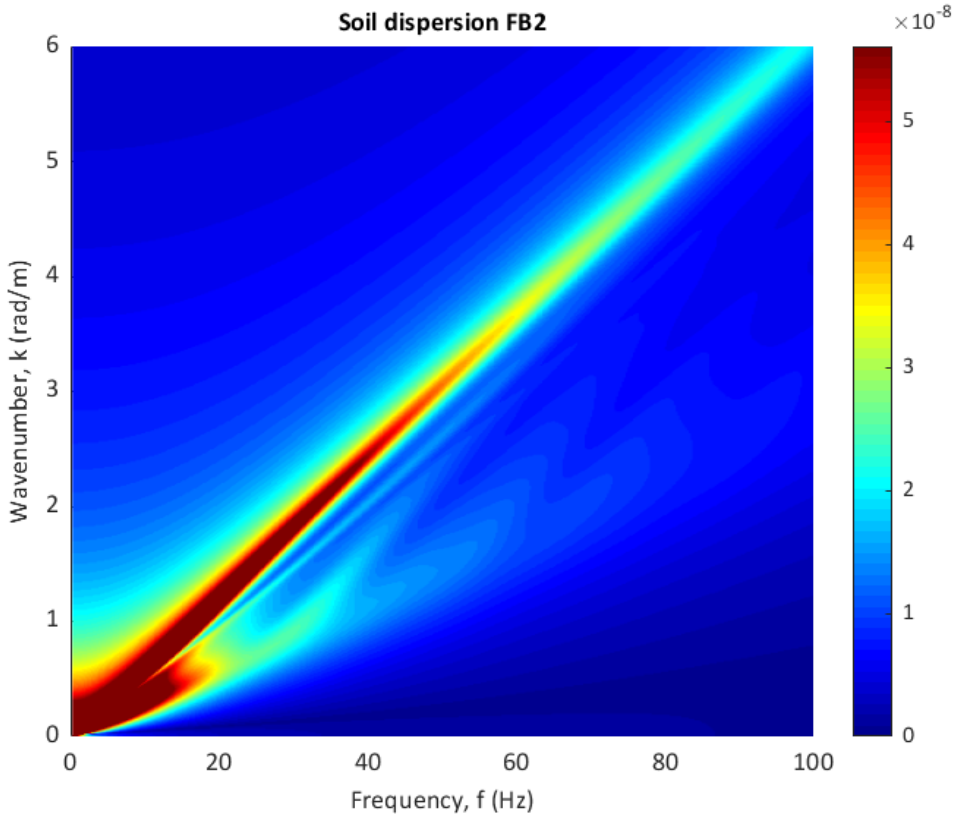

Figure 6.28: Dispersion plot for Fishbourne model FB2- Non-degraded lab based parameters.

6.6.3 Results - degraded parameters

A range of models were run, with their parameters set out in Table 6.8. No degradation was applied to the halfspace, as the strains below 4 m depth are very small, and previous modelling

has shown that degradation in the halfspace is unnecessary if there are surface layers of reasonable depth. A similar process was followed as for the Gravel Hole modelling, section 5.5.2, where a variety of input parameters were trialled, and the resulting output peak strains recorded, with the aim of finding the parameters sets where effective strain factors Rr of 0.65 and 0.2 were matched.

The resulting displacement–speed curves for all models are presented in Figure 6.29, with input, peak output and effective output strains for all models detailed in Table 6.9. A plot of peak output versus input (assumed) strains (Figure 6.30) was used to aid in selecting input strains for targeted output strains. Lines for the effective peak strain factor (Rr) of 0.2 and 0.65 are also presented on this plot.

A clear trend of decreasing critical velocity as displacements increase is seen. Model FB11 matches a value of Rr of 0.2, with input strains of 0.01% for layer one and 0.005% for layer 2, producing a peak displacement of 2.3 mm at 108 ms^{-1} (389 km/h). If this ground model is correct it suggests that the site would cope well with trains of up to around 90 ms^{-1} (324 km/h), with peak displacements staying below 1.5 mm in this case.

As Figure 6.30 shows, matching a value of Rr of 0.65 proved difficult in the softer clay (layer 1), with many models (FB6, FB7, FB8, FB13) matching Rr of 0.65 in layer 2, but consistently producing output strains equivalent to a value of Rr of 0.56 in layer one. This value sits within the range of Rr reported by Lysmer *et al.* (1975). Taking FB7 as the average of these models, a peak displacement of 4 mm at a velocity of 90 ms^{-1} (324 km/h) is predicted. This level of displacement is likely to be well above acceptable limits for the line. In the case of this model, displacements increase rapidly from approximately 50 ms^{-1} (180 km/h). Whilst this is well above the current line speed of 113 km/h, it implies potential problems should the site be upgraded to a higher speed line in the future.

The site dispersion measurements cannot be compared to the resultant dispersion curves, as the site was not under loading strain during their measurement. Therefore it is not possible to determine which factor of Rr is most applicable.

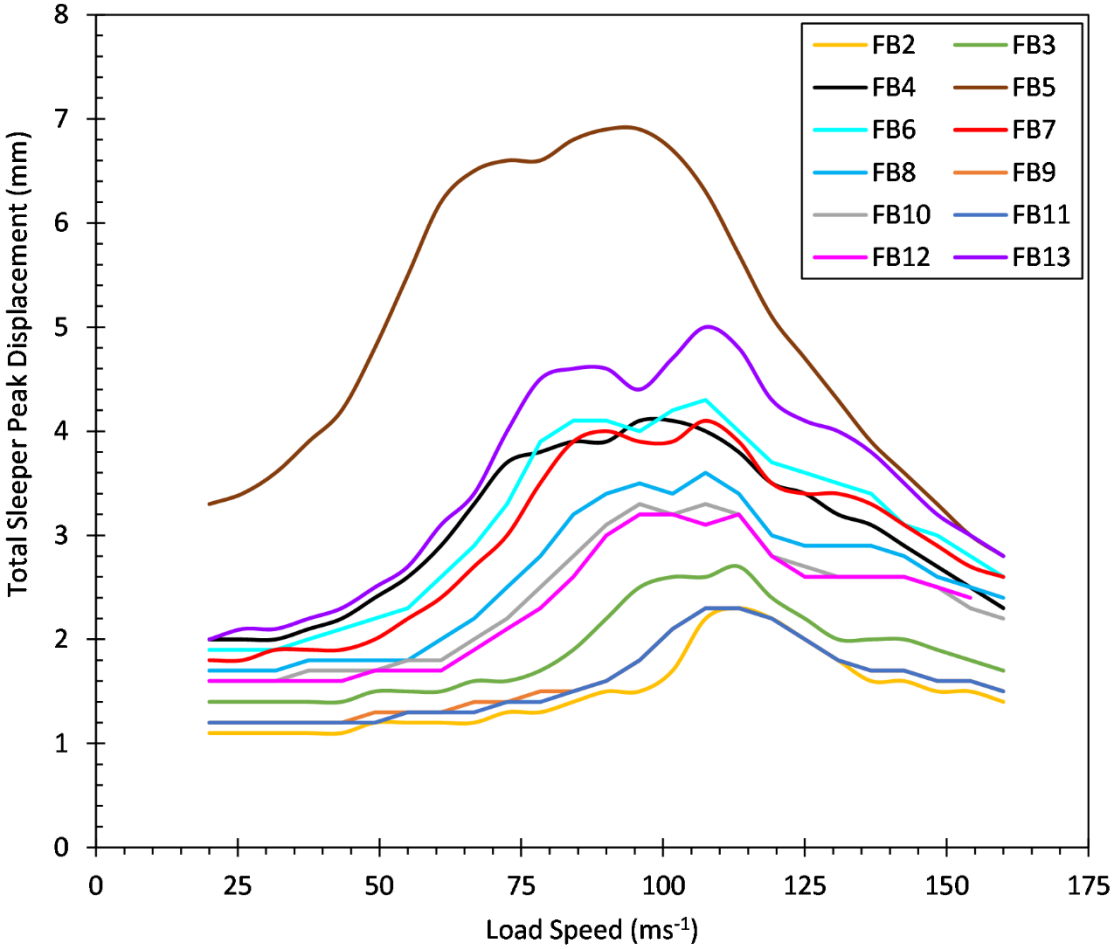

Figure 6.29: Total peak sleeper displacements with load speed for all Fishbourne lab-based models.

Table 6.9: Input and output strains for Fishbourne models.

Model ID	*Input* ε_q*(%)*	*Peak Output* ε_q*(%)*	*Effective Output* ε_q *for Rr 0.2 (%)*	*Effective Output* ε_q *for Rr 0.65 (%)*	*Model ID*	*Input* ε_q*(%)*	*Peak Output* ε_q*(%)*	*Effective Output* ε_q *for Rr 0.2 (%)*	*Effective Output* ε_q *for Rr 0.65 (%)*
FB2	ND	.042	0.01	0.03	FB8	0.05	0.09	0.02	0.06
	ND	.024	0	0.02		0.02	0.03	0.01	0.02
FB3	0.023	0.06	0.01	0.04	FB9	0.01	0.05	0.02	0.03
	0.023	0.03	0.01	0.02		0.01	0.02	0.00	0.01
FB4	0.066	0.10	0.02	0.06	FB10	0.04	0.08	0.02	0.05
	0.066	0.03	0.01	0.02		0.02	0.02	0.00	0.01
FB5	0.15	0.20	0.04	0.13	FB11	0.01	0.05	0.01	0.03
	0.066	0.05	0.01	0.03		0.005	0.02	0.00	0.01
FB6	0.066	0.12	0.02	0.08	FB12	0.04	0.08	0.02	0.05
	0.023	0.03	0.01	0.02		0.01	0.03	0.01	0.02
FB7	0.06	0.11	0.02	0.07	FB13	0.08	0.14	0.03	0.09
	0.02	0.03	0.01	0.02		0.015	0.03	0.01	0.02

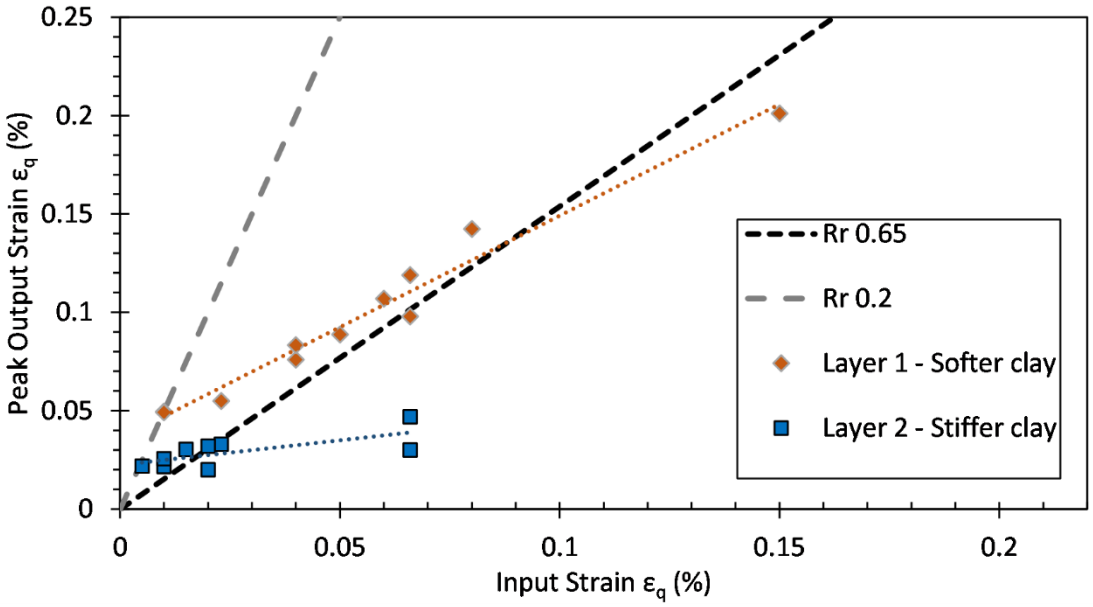

Figure 6.30: Input versus peak output strains for Fishbourne models.

6.7 Discussion of site testing and modelling

The site sampling programme for this case study was very successful, providing a large range of samples and other measurements from a variety of sources. However, it also show the difficulties in selecting which sources to use and the limitations from which some suffer.

As the ground beneath this site generally consists of clays, the assumption in the seismic testing of a density of 2000 kgm^{-3} is not a source of significant error, as the site was found to have a measured density of 1930 kgm^{-3} to 2100 kgm^{-3}. Whilst the compressional wave speeds from the seismic measurements were fairly close to the laboratory measurements, the shear wave speeds were not. These seismic estimations of wave speed are dependent on the quality of the tests, the complexity of the ground layering and the experience of the analyst.

The borehole results suggest a stratigraphy formed of fairly horizontal layers beneath the site, with both boreholes producing similar results, both in layer thickness and density tests. This uniformity means the selection of a model geometry was a more simple process than for Gravel Hole, and is also assumed to produce a more accurate result.

As for Gravel Hole, the SHDP proved a reasonable method of defining soil layering, although relating the blowcounts to general strength parameters proved inaccurate.

The RC again proved a relatively fast and effective method for defining the shear modulus and damping of the samples at a range of strains. Successful compressional and shear wave measurements were also taken using the bender elements within the RC. The comparison of these shear wave measurements to those from the RC itself showed a very close match, implying

the sample is very homogeneous, as expected. As for Gravel Hole, the consolidation method seems to have had an impact on the measured shear moduli, with the triaxial measurements being approximately 60% of the values from the RC.

The values of the vertical shear modulus G_{hv}, derived from triaxial horizontal bender elements, and G*, derived from triaxial undrained probes, differ by 14% to 27%, showing greater similarity than for the Gravel Hole samples. This implies the Fishbourne samples are relatively isotropic, considering the theoretical equivalence of G_{hv} and G* is based upon an assumption of isotropic homogeneity, with the Fishbourne samples being more homogeneous than those from Gravel Hole.

Modelling was successfully carried out based upon the parameters measured in the laboratory, for a range of strains. As before a strong variance in displacements with input strain is found. The strains from which input parameters were selected were varied for each of the model layers, aside from the halfspace where strength degradation has been shown to have little effect on the predicted displacements, due to the low strains. Strains were found to be largely focused in the softest layer, increasing rapidly as the load speed approaches critical velocity.

Both the desk study based model (FB1) and the small-strain lab based model (FB2) produce relatively similar results, in terms of both dispersion curves and sleeper displacement curves. For this site an unusually large amount of information was available for the desk study model, and without the seismic measurements any form of reliable model would have been hard to produce without lab testing.

As good agreement is found between model FB2 and the site measurements, the degraded parameter models may be assumed to give a reasonable prediction of potential higher strain displacement scenarios. The importance of using degraded parameters is clear, as even for a relatively 'standard' clay site such as Fishbourne, the predicted peak sleeper displacements almost double when strains are increased to 0.066%. Perhaps more importantly the velocity at which displacements significantly increase decreases from 270 km/h to 135 km/h, well within the speed range of higher-speed rail in the UK.

As discussed previously, the selection of a model representative of a degraded soil state is reliant upon which Rr factor is chosen. For this site a factor of 0.2 indicates that vehicles of up to 90 ms^{-1} (324 km/h) would be acceptable, with peak displacements staying below 1.5 mm for these speeds. In contrast a factor close to 0.65 predicts peak displacements of 4 mm at 90 ms^{-1}, with displacements increasing rapidly from approximately 50 ms^{-1} (180 km/h). Whilst this is well above the current line speed of 113 km/h, it implies potential problems should the site be upgraded to a

higher speed line in the future. Therefore further investigation into the correct selection of Rr for site modelling is essential.

Chapter 7 Discussion – Case Study Results

7.1 Key parameters and modelling factors

A parametric study has shown the most important parameters to focus on, and factors to include, when modelling critical velocity effects, are:

- Shear modulus / shear wave speed and their variation with strain
- Damping, including variation with strain
- Density
- Multiple vehicles, allowing for superposition of load displacements
- Track geometry – ballast depth and width
- Train loading levels (fully loaded vs. unloaded)

Less important parameters are:

- Compressional wave speed
- Ballast stiffness

7.2 The impact of parameter source

7.2.1 Density

The importance of directly measuring density, through in-situ probes, or preferably extracting samples, varies dependent on the underlying stratigraphy of the site. For a site such as Fishbourne, where historical boreholes of the surrounding area are in relative agreement with each other, and show commonly tested engineering materials (well known clay types, granular material etc.) further measurement of density is not necessary. Values based upon these soil descriptions appear to give reasonable estimates that will not greatly affect the modelling.

Conversely, for a site such as Gravel Hole where historic boreholes show large variance and indicate the site to be underlain by unusual ground materials, direct measurement of density is essential. In this case the actual density of the softest layers is only 59 % of the typical assumed density of 2000 kgm^{-3}. This should also be considered when analysing seismic measurements, as they are reliant on assumptions of density.

7.2.2 Stratigraphy

Whilst seismic measurements are non-invasive, their ability to estimate the depths of soil layers, especially in the most important upper surface layers, appears too limited to be of use, especially for particularly variable or soft ground. The use of SHDP or similar probe tests could prove a useful tool in the modelling of future sites. Whilst the estimation of soil strength from these measurements is difficult for unusual soils, as it is entirely reliant on correlations to previously measured data, they do provide a reasonable estimation of the thickness of soil layers of varying density on the site. As these methods are faster, cheaper and less invasive than drilling boreholes they may provide a useful method for defining a suitable model geometry.

For even greater model accuracy, especially on sites where significant variability is expected, several boreholes should be taken, to a minimum of 4 m depth, preferably with SHDP tests going deeper than this. Additional SHDP tests can be used effectively to further define the stratigraphy of the site. If the boreholes are not to be removed from site for analysis, then the appointment of an experienced engineering geologist is recommended to oversee the drilling. Sites particularly susceptible to critical velocity effects are more likely to have unusual ground materials beneath them, which an inexperienced drill logger may not correctly describe. For greatest model accuracy, borehole samples should be transported to a laboratory for full analysis of soil types, density and layering.

7.2.3 Strength parameters

For sites where the underlying materials are of a well-known material then correlations between SHDP blow count and density can be made with some accuracy. However, this does not offer a measurement of strength degradation, and accurate correlations may not be available for many ground types. If it is not possible to use advanced laboratory testing to define a material's parameters, then a combination of measurements of the small strain shear modulus and the plasticity index may be used to select a normalised degradation curve, should the material be similar to those tested in published data.

The RC proved a relatively fast and effective method for defining the shear modulus and damping of the samples at a range of strains. Additional care must be taken when testing on very soft compressible soils, to ensure the RC system remains aligned. The addition of bender elements to the RC proved a useful method of defining the compressional wave speed, and hence the Poisson's ratio, whilst also providing additional shear wave measurements.

The method of consolidation appears to have a great impact on the samples. Sample pair GH1O (RC) and GH1P (triaxial), were both consolidated isotropically, and show a good match in shear modulus between the two pieces of equipment. The remaining samples pairs were consolidated isotropically in the RC and along the K_O line in the triaxial. This appears to have had a large impact on the measured shear moduli, with the triaxial measurements being consistently considerably lower than for the RC.

The triaxial small-strain shear modulus for the Fishbourne sample was 60% of the value from the RC. Conversely, the Gravel Hole small strain moduli, for samples GH2C/D and GH2J/K, were approximately 22% of the RC shear moduli. It is assumed that the higher density and strength and reduced compressibility of the Fishbourne sample has resulted in the differing consolidation methods having a smaller impact. Further investigation is required into the impact of these consolidation methods, and whether a RC adjusted to provide K_O consolidation is necessary, before recommendations of which methods should be used for critical velocity modelling can be made.

Damping

As damping cannot be measured in a standard triaxial machine, the RC provides a relatively quick and easy method of measurement. Damping levels appear to not vary greatly with confining pressure, especially for the low pressures considered for soils in the upper ground layers. This suggests that regardless of consolidation method, the RC is a useful method of measurement.

7.3 The importance of model geometry

The first one or two metres of ground beneath the track appear to have a disproportionately large impact on the predicted displacements. A parametric study loosely based upon the Gravel Hole site investigated the impact of a range of parameters. In this case introducing just 0.7 m of sand and gravel over the soft 2 m layer reduced peak displacements by over 40 %. Another set of models assessed the impact of the thickness of a generic stiffer layer over the softer layer, and found thicknesses of 1.5 m reduced peak displacements by 50 %. This means additional care should be taken to note the depth of ballast on the site, as this can often be deeper than the standard of 0.3 m, due to historical track remediation. In addition, care should be taken to be taken to separate out thin layers of soil of differing parameters in the first few metres of ground depth, rather than homogenising them into one representative layer.

An additional model was to investigate the importance of the stiffness ratio between the soft layer and the stiffer ground around it. In this case it is suggested that once the ratio reaches a

value of 4 it is no longer necessary to further define the parameters for the stiffer layer, as additional stiffness increases beyond this will only have small impacts on the displacement.

Overall it is clear that the most effort should be focused in accurately defining the layer thicknesses of the top layers of a site's geometry, with the ground below around 5 m deep having a far smaller impact on displacements, assuming the soft layer sits above this depth. The large impact that relatively thin layers of stiffer material may have on a site implies easy displacement improvements may be found through the addition of this material beneath the track.

There is no simple answer as to how to select model geometry for sites with uneven layering, such as Gravel Hole, beyond averaging the available measurements. Further investigation is needed to assess the impact of incorporating a finite horizon of soft material, or one of varying depth, into a critical velocity model. However, the requirement to have layers which extend infinitely across 2.5D models make them more likely to safely over-predict rather than under-predict displacements, as long as a suitable layer thickness is selected.

7.4 The importance of strain degradation

The modelling results for both case study sites show consideration of strain degradation to be essential for critical velocity modelling, with peak strains of up to 0.2 % predicted in the soft layer at critical velocity. It is recommended that strains are varied for each layer of the model, as each will experience differing strains due to the varying density, damping and strength parameters. In general, it appears that the application of strength degradation to the underlying halfspace is unnecessary as it has little effect on the predicted displacements, due to the low strains induced. This assumes that there are several layers of considerable depth above the halfspace.

Strains were found to be largely focused in the softest layer, increasing rapidly as the load speed approaches critical velocity. It is necessary to apply a factor, Rr, to the peak output strains from the model, to assess the required input strains and select the most accurate model. For the Gravel Hole site a value of Rr value of 0.65 (Kramer, 1996) resulted in displacements which were a reasonable match to the site measurements. However, further investigation is needed into which value of Rr is actually most appropriate for the assumptions made in these types of models.

For the Gravel Hole site, with a value of Rr of 0.65, parameters for the softest layer are selected from a degraded distortional strain of 0.15 %, resulting in a shear modulus degradation of over 50 %, from 6.8 MPa to 3.3 MPa, and damping loss factor increasing by a factor of 6, from 4.1 % to 25.5 %. These degraded parameters predict a displacement of 6.6 mm at 57 ms^{-1}, compared to 1.9 mm for the same speed for the non-degraded parameters, a significant difference. For the

Fishbourne site, using a factor of 0.65, for a speed of 75 ms^{-1} (250 km/h) the predicted displacements increase from 1.4 mm, for the non-degraded model, to 3 mm for the degraded model. If correct this implies difficulties if the site line speed were raised in the future, however this estimate is greatly dependent on the selection of Rr.

When modelling using strain-degraded parameters is carried out using an equivalent linear model it must be remembered that at low speeds displacements will be overestimated, as strains in the soil will not have sufficiently developed for the input parameters to be valid at that train speed. If predictions at low speeds are required then the results from a set of models, using differing input strains for the differing speed sections, should be considered. However, as it is generally the speed and amplitude of the displacement peak that is of most interest the equivalent linear models are still a very useful modelling method.

Chapter 8 Conclusions and recommendations

8.1 Conclusions

The aim of this research was to assess methods of determining appropriate soil parameters for use in simple elasticity-based models for prediction of critical velocity effects. Specific objectives were set in Chapter 1, which are detailed in italic below, and addressed in turn:

- *To investigate the strain-dependent soil stiffness and damping of typical soil samples from example sites at which critical velocity effects may be expected, in particular organic, silt and clay soils.*

Site investigations, including the drilling of boreholes, the extraction and logging of samples and measurements using Super Heavy Dynamic Probes (SHDP) have taken place at two case study sites. These sites were adjacent to the railway track (Fishbourne) and from directly underneath the track bed (Gravel Hole), necessitating a night possession of the line. Critical velocity effects have been recorded at the Gravel Hole site. In total 24 m of borehole drilling took place, with 20 m of windowless sampling carried out. After general index testing of the windowless samples, including full soil descriptions, density and moisture content measurements throughout, 31 undamaged samples suitable for advanced laboratory testing remained.

10 of these samples were selected for further testing, with similar pairs being selected from the most interesting ground sections, totalling 5 pairs. 4 pairs were selected from Gravel Hole, consisting of a firm clay, a soft to firm slightly organic sandy silt, a highly organic soft silt and a highly organic very soft silt. Due to time limitations, just one pair was selected from the Fishbourne site, consisting of soft clay. Further indexing tests such as for liquid and plastic limits and organic content were also carried out, where applicable.

One sample from each pair was tested in the resonant column, with the shear modulus and its variance with strain measured for a range of confining pressures, including those representative of in-situ stresses. The increase of damping with strain was also measured, as were shear and compressional wave speeds from vertical bender elements installed in the resonant column end caps.

The remaining sample from each pair was tested in the triaxial machine, with the majority being consolidated along the K_O line prior to drained and undrained probe tests. These probes allowed evaluation of the shear modulus degradation with strain, and the Poisson's ratio. The peak

undrained shear strength of each sample was also measured, as well as the vertical shear modulus G_{hv}, derived from measurements taken using the installed horizontal bender elements.

The strain-dependant soil stiffness and damping of all soil sample types has been successfully investigated, producing a set of results which are not only extremely useful for modelling the case study sites, but also for general categorisation of some fairly untested soil types, such as the highly organic silts.

- *To compare different methods of obtaining these parameters for the various soil samples. This will include laboratory measurements using resonant column, bender elements, and triaxial tests and existing field measurements using SASW.*

Comparisons have been drawn between parameters measured in the laboratory in the triaxial machine, the resonant column and with bender elements, as well as with in-situ measurements including SHDP and seismic techniques such as SASW. The resonant column provides the only method for measuring the key modelling parameter of damping, and its variation with strain. The SASW tests are dependent on the assumed density of the soil layers, which can result in very inaccurate results for sites with unusual ground, such as Gravel Hole.

Whilst the SASW tests cannot be used to define unambiguously the boundaries of soil layers, especially those close to the surface, the SHDP provides a useful resource for defining the soil layer boundaries through a method that is cheaper, faster and less invasive than drilling boreholes. Although the SHDP could be used to estimate soil density and strength, through correlations to previously measured materials, this is not to be generally recommended for the upper soil layers, as it can be very inaccurate unless the site is of a well-known soil.

Vertical bender elements fitted within either the triaxial or resonant column provide a useful measurement of both shear and compressional wave speeds, allowing estimation of the Poisson's ratio. This measurement of shear wave speed is also a useful comparison to the shear wave speed measured during resonant column testing. For the samples tested in this research it was found that these values agreed very well, being extremely close for the more homogeneous samples, and varying by up to 7.5 % for the less homogeneous samples.

The shear moduli measured in the resonant column are consistently larger than those measured in the triaxial machine for matching sample pairs, although it should be noted that the sample pairs are natural soil samples so despite being similar will not be fully identical. On average, the modulus of the Gravel Hole samples measured in the triaxial are 25 % of those measured in the resonant column, whilst for Fishbourne the value is 60 %. It is believed the consolidation method caused the majority of difference in the moduli values between the pieces of equipment. The

resonant column is unable to apply an additional axial load, so consolidates the sample isotropically, whereas the triaxial machine follows the K_O line, which theoretically more accurately replicates the in-situ stresses. The difference between the shear moduli measured in each piece of equipment was greater for the Gravel Hole samples than for the Fishbourne sample, most likely due to the lower density and greater compressibility of the Gravel Hole samples making them more susceptible to the differences between the consolidation methods. For this research modelling was based upon the resonant column measurements, as values for damping were required. Future research is needed to further assess the impact of the consolidation methods.

- *To use suitable modelling to determine the impact of assumed soil stiffness on critical velocity assessment of example sites, and whether it is important to allow for the non-linear behaviour of soils. This will be based on linear elastic models, if necessary using equivalent parameters to allow for stiffness degradation.*

A wide variety of modelling has been carried out, utilising a range of degraded and non-degraded parameters for both case study sites. It is clear from the modelling in this research that the incorporation of the impact of strain degradation on soil stiffness is essential for the accuracy of modelling critical velocity sites. For the Gravel Hole site, modelling using non-degraded soil parameters from the linear section of the laboratory strength results predicts a displacement of 1.8 mm at the current maximum train speed of 57 ms^{-1}. In contrast, accounting for soil non-linearity at higher strains results in a reduction in shear modulus for the softest layer of 50%, increasing predicted displacements at 57 ms^{-1} by 328 % to 5.9 mm.

The use of non-degraded parameters to model critical velocity events is clearly unsuitable. However, incorporating non-linearity of soils, through an equivalent linear elastic model, necessitates the use of an effective strain factor Rr. This factor is used to convert the model peak output strains to a value to which the input strains can be compared. For the case study sites in this research an Rr value of 0.65 provides a reasonable match to site measurements. However, some authors have recommended different values to this and so further investigation is required.

Peak strains were focused within the softest soil layers, spreading further into the surrounding layers near critical velocity. The degradation of the halfspace is deemed generally unnecessary, as for both case study sites the strains in the halfspace were so small as to cause negligible effect on the predicted displacements if the degraded parameters were used. It should be noted that the model geometry for both of these sites consisted of at least 4 m of soil layering above the halfspace.

- *To determine the key soil and model parameters required when using 2.5D linear elastic models to predict track deflections on difficult sites.*

A parametric study has been carried out to define the most important soil parameters to focus on when modelling critical velocity effects. These are shear modulus / shear wave speed including variation with strain, damping including variation with strain, and density. Key track and vehicle parameters include the train loading levels, whether it is likely to be fully loaded or unloaded, and the track geometry such as ballast depth and width. Multiple vehicles should also be included, allowing for superposition of load displacements.

The selection of model geometry is one of the most important factors in critical velocity modelling, particularly for the upper soil layers in the first few metres below the surface. For example, the addition of as little as 0.7 m of sands and gravels above a soft material reduced predicted displacements by over 40 %. The thickness of the layer of softest (lowest strength, usually lowest density) soil on a site is an extremely important parameter for model accuracy. Additional focus in any site investigation should be placed upon defining the thickness and strength parameters of this layer.

- *To compare model predictions with field measurements of track deflections where available.*

For the Gravel Hole site, model predictions were compared to the site displacements measured across a range of train speeds. The non-degraded parameters gave poor agreement to the site measurements. A good match was achieved between the strain-degraded parameters and the site measurements, with ground parameters being selected at a strain of 0.06% for the 0.7 m upper ballast / gravel layer, 0.15 % for the 2.5 m soft organic silt layer, 0.05 % for the 0.7 m silty clay layer. No strain degradation was applied to the clayey sand and gravel halfspace.

For the Fishbourne site no track displacements have been measured, however some seismic measurements have been taken, providing dispersion curves of the surface waves for comparison. The seismic measurements correlate to a small-strain, non-degraded scenario, as no train loading was applied to the site during their measurement. A reasonable match is found between the lab-based non-degraded parameter model and the site dispersion measurements, with the first surface wave speed in the model results matching the speed and location of the first wave in the Fishbourne site measurements very well. The model results also show a faster wave speed in the lower ground layers, which shows some correlation to the site measurements, although the model results do not replicate the mid-wavenumber, mid-frequency surface waves shown on the

site measurements. It may be that the site ground has layers of uneven depth or confined width, which the model is unable to replicate.

- *To produce recommendations for the information required to obtain reliable critical velocity predictions using linear soil models and the best methods for obtaining this information.*

Chapter 7 in this thesis sets out a range of recommendations as to the key information required to obtain critical velocity predictions, and discusses the best methods for obtaining this information. In summary key soil parameters are shear modulus, density and damping. Density may be reasonably estimated from Super Heavy Dynamic Probes for well researched soil types, however directly measuring density through the drilling of boreholes and the extraction of samples is highly recommended for any unusual soil types.

It is important to directly measure the stratigraphy of the site, preferably through a range of SHDP and boreholes, to allow an accurate model geometry to be selected. Particular care should be taken to carefully assess the upper few metres of the ground below the track. In general, in-situ estimations of stiffness parameters are fairly inaccurate, especially so for unusual soil types. Therefore, the extraction of samples and testing in advanced laboratory equipment is necessary for accurate modelling of unusual sites.

It is essential to model using strain-degraded parameters. Both resonant column and triaxial machines can provide measurements of strength degradation with strain, although the impact of consolidation method must be further investigated. The resonant column provides an excellent method of measuring the variation of damping with strain, an important model parameter. The addition of vertical bender elements into both types of equipment is also recommended, to allow an additional method for measuring shear moduli, as well as providing measurements of compressional wave speed and Poisson's ratio.

8.2 Recommendations for future work

It is necessary for the impact of consolidation methods on measured shear moduli to be investigated. In this research shear moduli measured from a resonant column, which applies isotropic consolidation, are markedly different from shear moduli measured in the triaxial machine, which consolidates along the K_O line. It is recommended that several identical soft kaolin samples should be formed, to be tested after both isotropic and K_O consolidation in both a triaxial machine and a resonant column capable of applying both cell pressure and deviatoric load. The addition of vertical bender elements in both pieces of equipment would also aid the comparison.

Once the effect of the different consolidation methods is further understood, recommendations can be made as to whether resonant columns capable of K_O consolidation are required for measuring parameters for critical velocity modelling.

A significant number of samples from both the Gravel Hole and Fishbourne sites remain that are suitable for advanced laboratory testing. Tests on further Fishbourne samples could be carried out to improve the accuracy of the Fishbourne model. The Gravel Hole samples tested in this research could be formed into reconstituted samples, to further investigate the critical state framework or other key soil parameters for these unusual soil types.

Both drained and undrained constant mean stress and constant axial stress probes were carried out on all the samples tested in this research. Further analysis of this data should enable the anisotropic stiffness parameters as set out in the five parameter framework of Lings *et al.* (2000) to be evaluated, which would be extremely interesting for the highly organic silts. Further testing on the remaining untested Gravel Hole samples could be carried out to assist with this.

The impact on predicted displacements of modelling using a ground geometry including a finite horizon of soft material should be investigated. This could be carried out in a linear-elastic 2.5D model, such as WANDS, or a more computationally demanding 3D model such as in Abaqus. The Gravel Hole case study site would provide a useful framework for investigating the importance of the finite horizon, to enable recommendations for modelling for future sites.

Due to the large amount of information available on stratigraphy and soil parameters, the Gravel Hole site will also provide a useful framework for the investigation of the impact of uneven ground layers on model displacements, again through the use of 2.5D or 3D models. Once the impact of the inclusion of a finite horizon, or of uneven layers is known, judgements can be made as to whether the increased accuracy warrants the increase in computational time and the additional site knowledge required.

The selection of an effective strain parameter, Rr, to apply to the peak model output strain in order to select input strain and so to find a converging model is essential for future critical velocity modelling. A value of Rr of 0.65 is common among seismic engineering, and has been found to give results which match those of site measurements for both the Gravel Hole site in this research, and the Ledsgård site. However, the applicability of this value to critical velocity sites, and the corresponding models, is not known, with another author (Shih *et al.*, 2017) finding a match using an Rr of 0.2. It is therefore a key area of research, as without a more definitive value it is very difficult to predict displacements for sites where no existing critical velocity

displacements exist to match the model results too. The alternative is to use non-linear models where selection of an effective strain parameter is not necessary.

Further modelling to assess the impact of using effective stress versus total stress models for representing degraded site materials could provide an additional viewpoint from which to assess critical velocity modelling.

Appendix A Gravel Hole Borehole Results

Table 8.1: Full Gravel Hole borehole results – GHS1

Depth Below Sleeper (m)	*Main Soil Type*	*Soil Description*	*Sample IDs*	*M.C (%)*	*Bulk Density (kgm^{-3})*	*C_{ufc} (kPa)*	*Dry Density (kgm^{-3})*
0-0.26	MADE GROUND - ballast	grey mottled dark grey angular to subangular fine to coarse GRAVEL of igneous rock		-----	-----	-----	
0.26-0.67	MADE GROUND - ballast	dark grey mottled black very sandy angular to subangular fine to coarse GRAVEL of igneous rock. Sand is fine to coarse		-----	-----	-----	
0.67-0.9	MADE GROUND - sand	orangish brown fine to coarse SAND		-----	-----	-----	
0.9-1.25	SILT	soft dark blackish brown soft slightly clayey fine sandy SILT with dark black organic particles of up to 4mm	GH1B, GH1C	43	1719	-----	1199
1.25-1.73	SILT	soft to firm dark blackish brown fine sandy SILT with dark black organic particles of up to 4mm	GH1A, GH1D	44	1652	74	1150
=	=	=	=	73	1482	83	858
=	=	=	=	45	1672	-----	1156
1.73-2	SAND	very soft brownish grey fine	GH1E,	22	1900	25	1564

Depth Below Sleeper (m)	*Main Soil Type*	*Soil Description*	*Sample IDs*	*M.C (%)*	*Bulk Density (kgm^{-3})*	*C_{ufc} (kPa)*	*Dry Density (kgm^{-3})*
		to coarse SAND with some fine gravel	GH1F				
2-2.3	SAND	very soft brownish grey fine to coarse SAND with fine to coarse gravel and cobbles	GH1L, GH1M, GH1N, GH1H	14	-----	-----	-----
=	=	=	=	12	-----	-----	-----
2.3-3	SILT	soft to firm dark brown very sandy SILT. Sand is fine to coarse with numerous fine to coarse gravel. Gravel is angular to subangular.	GH1G, GH1I, GH1J, GH1K	13	2243	63	1977
3-3.17	CLAY	firm to stiff orangish brown slightly sandy CLAY with occasional organic particles. Sand is light brown fine to medium	-----	14	2218	-----	1953
3.17-3.55	CLAY	soft dark orangish brown sandy CLAY, sand is firm to medium light brown	-----	12	2223	76	1979
3.55-3.72	SILT	firm dark greyish brown very sandy SILT. Sand is fine to medium	-----	13	2153	120	1911
3.72-4	CLAY	firm greyish brown very sandy CLAY. Sand is fine to medium	-----	13	-----	110	-----
4-4.15	CLAY	very soft brown sandy silty	-----	22	-----	-----	-----

Depth Below Sleeper (m)	*Main Soil Type*	*Soil Description*	*Sample IDs*	*M.C (%)*	*Bulk Density (kgm^{-3})*	*C_{ufc} (kPa)*	*Dry Density (kgm^{-3})*
		CLAY. Sand is fine to medium					
4.15-4.3	SILT	firm to stiff brown slightly sandy clayey SILT	-----	11	2335	320	2095
4.3-4.5	SILT	firm to stiff brown very sandy clayey SILT		11	2081	-----	1871
4.5-4.73	SAND	firm to stiff brown silty SAND. Sand is fine to medium	-----	-----	-----	-----	-----
4.73-5	SAND	stiff brown slightly silty SAND with dark organic black particles and occasional coarse gravel. Sand is fine to medium	-----	15	-----	-----	-----
5-5.5	SAND	dark brown slightly silty fine to coarse SAND with occasional fine to medium gravel	GH1X	18	-----	-----	-----
5.5-5.6	SAND	brownish red fine to coarse SAND with frequent coarse gravel	GH1Y	12	-----	-----	-----
5.6-5.8	SAND	dark greyish brown silty fine to medium SAND with frequent medium to coarse gravel and cobbles	GH1V	15	-----	-----	-----
5.8-6	SAND	dark brown very silty fine to coarse SAND with occasional fine gravel	GH1W	15	2042	-----	1783

Table 8.2: Full Gravel Hole borehole results – GHS2

Depth Below Sleeper (m)	*Main Soil Type*	*Soil Description*	*Sample IDs*	*M.C (%)*	*Bulk Density (kgm^{-3})*	*C_{ufc} (kPa)*	*Dry Density (kgm^{-3})*
0-0.26	MADE GROUND - ballast	grey mottled dark grey angular to subangular fine to coarse GRAVEL of igneous rock	-----	-----	-----	-----	-----
0.26-0.67	MADE GROUND - ballast	dark grey mottled black very sandy angular to subangular fine to coarse GRAVEL of igneous rock. Sand is fine to coarse	-----	-----	-----	-----	-----
0.67-0.9	MADE GROUND - sand	orangish brown fine to coarse SAND	-----	-----	-----	-----	-----
0.9-1.3	SAND	soft orangish brown silty SAND with frequent pockets of dark brownish black very soft organic silty material and occasional medium to coarse gravel. Sand is fine to medium. Frequent black organic particles, small rootlets and fossilised leaves	GH2A, GH2B	330	1047	150	244
1.3-1.78	SILT	very soft dark brownish black SILT with occasional pockets of light brownish orange sand and frequent organic black particles and rootles.	GH2C, GH2D	52	1613	31	1062
1.78-2	SILT	soft to very soft dark brownish black SILT with	GH2E, GH2F	51	1620	-----	1070

Depth Below Sleeper (m)	*Main Soil Type*	*Soil Description*	*Sample IDs*	*M.C (%)*	*Bulk Density (kgm^{-3})*	*C_{ufc} (kPa)*	*Dry Density (kgm^{-3})*
		occasional pockets of light brownish orange sand and occasional organic black particles					
2-2.16	SAND	light brownish cream fine to medium SAND (assumed)		-----	----	-----	-----
2.16-2.4	SILT	soft light grey mottled dark greyish brown slightly fine sandy SILT with dark organic particles and occasional small pockets of fine to medium orangish cream sand. Strong organic smell. Oxidised to light brown around outside	GH2G, GH2H	48	1642	63	1110
2.4-2.84	SILT	soft blackish brown mottled light grey SILT with frequent dark organic particles. Oxidised very dark brown around outside	GH2I, GH2J	206	1195	76	390
2.84-3	SILT	soft to firm dark blackish brown clayey SILT with fark organic particles. Occasional tiny small white particles-crushable - chalk or shell? Rare coarse sand sized blue particles also crushable	GH2K	63	-----	-----	-----
3-3.48	SILT	very soft organic dark brownish black SILT	GH2L	221	1185	-----	369
=	=	=	=	138	1341	6.3	563

Depth Below Sleeper (m)	*Main Soil Type*	*Soil Description*	*Sample IDs*	*M.C (%)*	*Bulk Density (kgm^{-3})*	*C_{ufc} (kPa)*	*Dry Density (kgm^{-3})*
3.48-3.82	SILT	soft to very soft dark brown soft to very soft very gravelly sandy SILT. Sand is fine to medium. Gravel is evenly graded medium to coarse.	GH2M	19	2047	52	1725
3.48-3.82	SILT	soft to very soft dark brown soft to very soft very gravelly sandy SILT. Sand is fine to medium. Gravel is evenly graded medium to coarse.	GH2M	18	2120	-----	1791
3.82-3.96	SILT	soft to very soft dark brown sandy gravelly SILT with abundant cobbles	GH2N	-----	-----	-----	-----
3.96-4	COBBLES		GH2O	-----	-----	-----	-----
4-5	----	NO SAMPLE- BLOCKED		-----	-----	-----	-----
5-5.5		sample missing		-----	-----	-----	-----
5.5-5.7	SAND	soft dark brown very silty very gravelly coarse SAND. Sand is orange white. Gravel is fine to medium sub rounded to subangular	GH2P	13	-----	-----	-----
5.7-6	GRAVEL	soft dark brown sandy silty GRAVEL. Gravel is fine to coarse subangular to sub rounded. Sand is fine to coarse, occasional pockets of very soft organic material and occasional cobbles	GH2Q	-----	-----	-----	-----

Table 8.3: Gravel Hole sample register

WS1			*WS2*		
ID	*Depth Below Sleeper (m)*	*Type*	*ID*	*Depth Below Sleeper (m)*	*Type*
GH1B	1.1-1.25	bag	GH2A	1.2-1.4	bag
GH1C	1.1-1.25	bag	GH2B	1.25-1.41	bag
GH1A	1.25-1.42	undisturbed	GH2C	1.41-1.58	undisturbed
GH1D	1.52-1.7	undisturbed	GH2D	1.58-1.75	undisturbed
GH1E	1.7-1.8	bag	GH2E	1.78-1.95	undisturbed
GH1F	1.8-2	bag	GH2F	1.95-2	bag
GH1H	2-2.25	bag	GH2G	2.2-2.35	bag
GH1K	2.3-2.55	undisturbed	GH2H	2.35-2.45	bag
GH1I	2.55-2.7	bag	GH2I	2.45-2.68	undisturbed
GH1J	2.7-2.95	undisturbed	GH2J	2.68-2.84	undisturbed
GH1G	2.5-3	bag	GH2K	2.84-2.99	undisturbed
GH1L	2-3	bag	GH2L	3.28-3.48	bag
GH1M	2-3	bag	GH2M	3.6-3.8	bag
GH1N	2-3	bag	GH2N	3.8-3.96	bag
GH1O	3.17-3.34	undisturbed	GH2O	3.96-4	bag
GH1P	3.38-3.56	undisturbed	GH2P	5.5-5.7	bag
GH1Q	3.56-3.78	undisturbed	GH2Q	5.7-6	bag
GH1R	4.25-4.46	undisturbed			
GH1S	4.46-4.63	undisturbed			
GH1V	type 3	bag			
GH1W	typ3 4	bag			
GH1X	type 1	bag			
GH1Y	type 2	bag			
GH1Z	5-6	bag			

Appendix B Fishbourne Borehole Results

Table 8.4: Full Fishbourne borehole results - FBS1

Depth Below Sleeper (m)	*Main Soil Type*	*Soil Description*	*Sample IDs*	*M.C. (%)*	*Bulk Density (kgm^{-3})*	*C_{ufc} (kPa)*	*Dry Density (kgm^{-3})*
0-0.6	CLAY	soft dark brown CLAY (topsoil) with numerous rootlets	-----	-----	-----	-----	-----
0.6-1.0	CLAY	soft to firm light orangish brown fine silty CLAY with frequent angular flints, broken brick, gravel and roots	FO1B	36	1899	56	1400
1-1.5	CLAY	stiff light grey mottled orange CLAY with flint fragments	FO1C, FO1D	24	1987	370	1596
1.5-1.75	CLAY	stiff light grey mottled orange CLAY	FO1E, FO1X	32	1955	160	1481
1.75-2	=	=	FO1F	28	2042	170	1591
2-2.5	CLAY	stiff grey mottled orange CLAY	FO1G, FO1H	27	2064	980	1625
2.5-3	CLAY	stiff grey mottled orange CLAY with small pockets of fine orange sand	FO1I, FO1Z	32	1868	170	1412
3-3.3	CLAY	stiff dark brown CLAY	FO1J	-----	-----	-----	-----
3.3-4	CLAY	stiff dark brown CLAY	FO1K	26	-----	-----	-----
4-4.35	CLAY	stiff to very stiff dark brownish grey CLAY	FO1L	30	1943	980	1493
4.35-4.53	SILT	stiff dark greyish brown SILT	FO1M, FO1N	19	1968	520	1651
4.53-5	CLAY	very stiff dark greyish brown	FO1P,	22	2078	520	1704

Depth Below Sleeper (m)	*Main Soil Type*	*Soil Description*	*Sample IDs*	*M.C. (%)*	*Bulk Density (kgm^{-3})*	*C_{ufc} (kPa)*	*Dry Density (kgm^{-3})*
		CLAY with pockets of light brown fine sand and silt	FO1Q				
5.05-5.9	CLAY	very stiff dark brown CLAY	FO1R	23	2022	370	1643
5.3-5.9	CLAY	very stiff dark brown CLAY	FO1S, FO1T, FO1V	27	1942	630	1529
5.9-6	CLAY	very stiff dark brown CLAY with light brown silt pockets	-----	-----	-----	-----	-----
6-6.4	SILT	very stiff dark brown clayey SILT	-----	25	2038	780	1635
6.4-7	SILT	very stiff dark greyish brown SILT	FO1U, FO1W	16	2302	-----	1976

Table 8.5: Full Fishbourne borehole results – FBS2

Depth Below Sleeper (m)	*Main Soil Type*	*Soil Description*	*Sample IDs*	*M.C (%)*	*Bulk Density (kgm^{-3})*	*C_{ufc} (kPa)*	*Dry Density (kgm^{-3})*
0-1	CLAY	soft light brown sandy CLAY with frequent rootlets and fine to coarse gravel TOPSOIL	FB2A	28	1786	-----	1392
=	=	=	=	28	-----	-----	-----
1-1.2	CLAY	soft light orangish brown CLAY with occasional coarse sand, gravel and cobbles and frequent rootlets	FB2B	24	1978	-----	1597
1.4-1.6	CLAY	soft light grey mottled orange slightly silty CLAY with rare small	FB2G	31	1932	130	1478

Depth Below Sleeper (m)	*Main Soil Type*	*Soil Description*	*Sample IDs*	*M.C (%)*	*Bulk Density (kgm^{-3})*	*C_{ufc} (kPa)*	*Dry Density (kgm^{-3})*
		pockets of white and orange fine sand					
1.6-2	CLAY	soft light grey mottled orange slightly silty CLAY with rare small pockets of white and orange fine sand	FB2H, FB2I	30	1968	190	1510
2-2.5	CLAY	soft light grey mottled orange slightly silty CLAY with numerous small pockets of white and orange medium sand	FB2C, FB2E	33	1952	130	1472
2.5-2.8	CLAY	soft grey mottled orange CLAY with frequent dark orange fine sand and silt	FB2D	27	1999	150	1574
2.8-3	CLAY	soft grey mottled orange CLAY with abundant pockets and thin layers of dark orange fine sand and silt	FB2F	28	2025	210	1578
3-3.5	CLAY	stiff dark brown CLAY	FB2J, FB2K	31	1978	310	1509
3.5-4	CLAY	stiff dark brown CLAY	FB2L	28	1994	-----	1559
4.1-5	SILT	stiff dark brown clayey SILT with occasional pockets of light brown fine sand	FB2M	21	2120	540	1751
5-6.5	CLAY	very stiff dark brown CLAY with occasional pockets of light brown fine sand and silt	FB2N	27	2035	390	1605

Appendix B

Table 8.6: Fishbourne sample register

WS1			*WS2*		
ID	*Depth Below Sleeper (m)*	*Type*	*ID*	*Depth Below Sleeper (m)*	*Type*
FO1B	0.9-1.1	bag	FB2A	0-1	bag
FO1C	1.1-1.3	whole	FB2B	1-1.2	bag
FO1D	1-1.1	bag	FB2G	1.45-1.65	whole
FO1E	1.4-1.6	whole	FB2H	1.65-1.85	whole
FO1X	1.6-1.7	bag	FB2I	1.9-2	bag
FO1F	1.73-2	whole	FB2C	2.3-2.5	whole
FO1G	2.1-2.3	whole	DB2E	2.2-2.58	bag
FO1H	2.3-2.5	bag	FB2D	2.58-2.8	whole
FO1I	2.5-2.7	whole	FB2F	2.8-3	bag
FO1Z	2.8-3	bag	FB2J	3.05-3.23	whole
FO1J	3.1-3.4	bag	FB2F	2.8-3	bag
FO1K	3.5-3.9	bag	FB2J	3.05-3.23	whole
FO1L	4.2-4.35	whole	FB2K	3.3-3.5	whole
FO1M	4-4.2	bag	FB2L	3.5-4	bag
FO1N	4.4-4.55	whole	FB2M	4-5	bag
FO1O	4.35-4.4	bag	FB2N	5-5.5	bag
FO1P	4.55-4.75	whole			
FO1Q	4.8-5	bag			
FO1R	5.11-5.25	whole			
FO1S	5.3-5.55	bag			
FO1T	5.75-5.9	whole			
FO1V	5.55-5.7	bag			
FO1U	6.4-6.5	bag			
FO1W	6.8-7	bag			

Bibliography

Abadi, T. (2015) *Effect of sleeper and ballast interventions on rail track performance*. PhD Thesis. University of Southampton.

AECOM Ltd. (2016) Email -Site sampling options.

Aingaran, S. (2014) *Experimental investigation of static and cyclic behaivour of scaled railway ballast and the effect of stress reversal*. PhD Thesis. University of Southampton.

Alves Costa, P., Calçada, R., Silva Cardoso, A. and Bodare, A. (2010) 'Influence of soil non-linearity on the dynamic response of high-speed railway tracks', *Soil Dynamics and Earthquake Engineering*, 30(4), pp. 221-235.

Anderson, D.G. (1980) 'Uncertainty in determining dynamic nonlinear stress-strain relationships',*International Symposium on Soils under Cyclic and Transient Loading*. Swansea.

Anderson, G.B. and Stokoe, K.H. (1982) *Development of resonant column apparatus with anisotropic loading*. Austin: University of Texas Civil Engineering Dept.

AREMA (2003) *Economics of railway engineering and operations: Manual for railway engineering: Systems management: chapter 16*. American Railway Engineering and Maintenance-of-Way Association.

Arulnathan, R., Boulanger, R.W. and Riemer, M.F. (1998) 'Analysis of bender element test', *Geotechnical Testing Journal*, 21(2), pp. 120-131.

Aspin Foundations Ltd (2013) *Factual Ground Investigation Report CGJ6 14m 0342y to 14m 0287y Gravel Holes (Up)* (P2572-00). Preston.

ASTM (2007) *D4220-95: Standard practises for Preserving and Transporting Soil Samples*. West Conshohocken, PA: ASTM International.

ASTM. (2007) *D4015-07: Standard Test Methods for Modulus and Damping of Soils by Resonant-Column Method*. West Conshohocken, PA: ASTM International. Available at: www.astm.org.

Atkinson, J.H., Richardson, D. and Stallebrass, S.E. (1990) 'Effect of recent stress history on the stiffness of overconsolidated soil', *Gèotechnique*, 40(4), pp. 531-540.

Auersch, L. (2005) 'The excitation of ground vibration by rail traffic: theory of vehicle–track–soil interaction and measurements on high-speed lines', *Journal of Sound and Vibration*, 284(1–2), pp. 103-132.

Auersch, L. (2008) 'The effect of critically moving loads on the vibrations of soft soils and isolated railway tracks', *Journal of Sound and Vibration*, 310(3), pp. 587-607.

Avramidis, A.S. and Saxena, S.K. (1990) 'The modified "stiffened" drnevich resonant column apparatus', *Japanese Society of Soil Mechanics and Foundation Engineering,*, 30(3), pp. 53-68.

Baligh, M.M. (1985) 'Strain path method', *Journal of the Geotechnical Division of the American Society of Civil Engineers*, 111 (GT9), pp. 1108-1136.

Boulanger, R.W., Arulnathan, R., Harder, L., Torres, R. and Driller, M. (1998) 'Dynamic properties of Sherman Island Peat', *Journal of Geotechnical & Geoenvironmental Engineering*, 124(1), pp. 12-20.

Bibliography

Bowles, J.E. (1992) *Engineering Propeties of Soils and their Measurement*. 4th edn.: Mc Graw-Hill Companies.

Bowles, J.E. (1997) *Foundation Analysis and Design*. 5th edn. Singapore: The McGraw-Hill Companies, Inc.

Bowness, D., Lock, A.C., Powrie, W., Priest, J.A. and Richards, D.J. (2006) 'Monitoring the dynamic displacements of railway track', *Proceedings of the Institution of Mechanical Engineers,Part F: Journal of Rail and Rapid Transit*, 221, pp. 13-22.

Briaud, J.-L. (2013) *Geotechnical Engineering: Unsaturated and Saturated Soils*. Wiley.

British Geological Society (2016) *Geology of Britain viewer*. Available at: http://mapapps.bgs.ac.uk/geologyofbritain/home.html?

British Standards Institute (1990a) *BS 1377-2:1990 Methods of test for soils for civil engineering purposes. Classification tests*. BSI.

British Standards Institute (1990b) *BS 1377-8:1990 Methods of test for soils for civil engineering purposes - shear strength tests (effective stress)*. BSI.

British Standards Institute (2000a) *BE EN 13039:2000 Soil improvers and growing media. Determination of organic matter content and ash*. BSI.

British Standards Institute (2000b) *BS EN 12879:2000 Characterization of sludges. Determination of the loss of ignition of dry mass*. BSI.

British Standards Institute (2015) *BS 5930:2015 Code of practise for ground investigations*. BSI Standards Limited

British Standards Institute (2018a) *BS EN ISO 14688-1:2018 Geotechnical Investigation and Testing. Identification and classification of soil*. BSI Standards Limited.

British Standards Institute (2018b) *BS EN ISO 14688-2:2018 Geotechnical Investigation and Testing. Identification and classification of soil*. BSI Standards Limited.

Brough, M., Sharpe, P. and Hoffman, A. (2013) 'Investigation, design and remediation of critical velocity sites - a desk study',*Railway Engineering 2013 - 12th International Conference & Exhibition*. London, 2013.

Bui, M.T. (2009) *Influence of some particle characteristics on the small strain response of granular materials*. pHD thesis. University of Southampton.

Butler, F.G. (1974) 'Review Paper: Heavily Overconsolidated Clays: A State of the Art Review',*Conference on Settlement of Structures*. Cambridge. Pentech Press, London.

Camacho-Tauta, J.F., Álvarez, J.D.J. and Reyes-Ortiz, O.J. (2012) 'A procedure to calibrate and perform the bender element test', *DYNA (Colombia)*, 79(176), pp. 10-18.

Casagrande, A. (1936) 'The determination of preconsolidation load and its practical significance',*Proceedings of the 1st Int. Conf. Soil Mechanics and Foundation Engineering*. Cambridge. Harvard.

Cascante, G., Santamarina, C. and Yassir, N. (1998) 'Flexural excitation in a standard torsional-resonant column device', *Canadian Geotechnical Journal*, 35(3), pp. 478-490.

Cascante, G., Vanderkooy, J. and Chung, W. (2003) 'Difference between current and voltage measurements in resonant-column testing', *Canadian Geotechnical Journal*, 40, pp. 1-15.

Chandler, R.J., Harwood, A.H. and Skinner, P.J. (1992) 'Sample disturbance in London clay', *Geotechnique*, 46(4), pp. 577-585.

Chang, C.S., Adegoke, C.W. and Selig, E.T. (1980) 'GEOTRACK Model for Railroad Track Performance', *Journal of the Geotechnical Division of the American Society of Civil Engineers*, 106, pp. 1201-1218.

Chung, R.M., Yokel, F.Y. and Drnevich, V.P. (1984) ' Evaluation of dynamic properties of sands by resonant column testing', *Geotechnical Testing Journal*, 7(2), pp. 60-69.

Clayton, C.R.I. (2011) 'Stiffness at small strain: research and practice', *Géotechnique*, 61(1), pp. 5-37.

Clayton, C.R.I., Matthews, M.C. and Simons, N.E. (1995) *Site Investigation*. 2nd edn. Oxford: Blackwell Science.

Clayton, C.R.I., Priest, J.A., Bui, M., Zervos, A. and Kim, S.G. (2007) 'The Stokoe resonant column apparatus: Effects of stiffness, mass and specimen fixity', *Geotechnique*, 59(5), pp. 429-437.

Clayton, C.R.I., Siddique, A. and Hopper, R.J. (1998) 'Effects of sampler design on tube sampling disturbance - numerical and analytical investigations', *Geotechnique*.

Cole, J. and Huth, J. (1958) 'Stresses produced in a half plane by moving loads', *Journal of Applied Mechanics*, 24, pp. 433-436.

Connolly, D.P., Kouroussis, G., Giannopoulos, A., Verlinden, O., Woodward, P.K. and Forde, M.C. (2014a) 'Assessment of railway vibrations using an efficient scoping model', *Soil Dynamics and Earthquake Engineering*, 58(0), pp. 37-47.

Connolly, D.P., Kouroussis, G., Woodward, P.K., Giannopoulos, A., Verlinden, O. and Forde, M.C. (2014b) 'Scoping prediction of re-radiated ground-borne noise and vibration near high speed rail lines with variable soils', *Soil Dynamics and Earthquake Engineering*, 66(0), pp. 78-88.

Coop, M.R., Jovicic, V. and Atkinson, J.H. (1997) 'Comparisons between soil stiffnesses in laboratory tests using dynamic and continuous loading',*Proceedings of the 14th International Conference on Soil Mechanics and Foundation Engineering*. Hamburg.

de Nie, F.C. (1948) 'Undulation of railway embankments on soft sub-soil during passing of trains.', *the international conference on soil mechanics and foundation engineering*. Rotterdam, Netherlands.

Degrande, G. and Schillemans, L. (2001) 'Free field vibrations during the passage of a Thalys high-speed train at variable speed', *Journal of Sound and Vibration*, 247(1), pp. 131-144.

Desai, C.S. and Siriwardane, A.M. (1982) 'Numerical models for track support structures', *Journal of the Geotechnical Division of the American Society of Civil Engineers*, 108, pp. 461-480.

Dobry, R. and Ng, T.-T. (1992) 'Discrete modelling of granular media at small and large strains', *Engineering Computations*, 9(2), pp. 129-143.

Drnevich, V.P. (1978) 'Resonant column testing - problems and solutions', in *Dynamic Geotechnical Testing, ASTM STP 654*. ASTM, pp. 384-398.

Dyson, S.W. and Kirk, M.J.D. (2006) 'A high-speed railway through marshlands (CTRL)', *Proceedings of the Institute of Civil Engineers - Transport*, 159(TR2), pp. 75--82.

Dyvik, R. and Madshus, C. (1985) 'Lab measurements of Gmax using Bender Elements',*ASCE Conf. On Advances in the Art of Testing Soils under Cyclic Conditions*. Detroit, Michigan, October 1995.

Esveld, C. (2001) *Modern Railway Track*. MRT Productions.

Ferro, E. (2016) Email -Bulk density values from beneath sleeper in full scale rig tests.

Fryba, L. (1972) *Vibrations of soilds and structures under moving loads*. 3rd edn. London: Thomas Telford.

Gasparre, A. (2005) *Advanced laboratory characterisation of London clay*. PhD Thesis. Imperial College London.

Ghiassian, H. and Grozic, J.L.H. (2013) 'Strength behaviour of methane hydrate bearing sand in undrained triaxial testing', *Marine and Petroleum Geology*, 43, pp. 310-319.

Graham, J. and Houlsby, G.T. (1983) 'Anisotropic elasticity of a natural clay', *Gèotechnique*, 33(2), pp. 165-180.

Hardin, B.O. (1965) 'The nature of damping in sands', *Journal of Soil Mechanics and Foundations*, 91(SM1), pp. 63-97.

Hardin, B.O. and Drnevich, V.P. (1972) 'Shear modulus and damping in soils: Design equations and curves', *Journal of Soil Mechanics and Foundations*, 98(7), pp. 667-691.

Hardin, K., O., Drnevich, V.P., Wang, J. and Sams, C.E. (1994) 'Resonant column testing at pressures up to 3.5 MPa (500 psi)', in Ebelhar, R.J., Drnevich, V.P. and Kutter, B.L. (eds.) *Dynamic Geotechnical Testing II ASTM STP213*. Philadelphia: America: American Society of Engineers (ASCE), pp. 222-233.

Heisey, J.S., Stokoe, K.H. and Meyer, A.H. (1982) 'Moduli of pavement systems from spectral analysis of surface waves', *Transportation Research Record 852*, pp. 22-31.

Hight, D.W. and Burland, J.B. (1990) *Review of soil sampling and laboratory testing for the Science and Engineering Research Council , Summary Report, SERC*. Swindon, England.

Hird, C.C. and Pierpoint, N.D. (1994) 'A non-linear anisotropic elastic model for overconsolidated clay based on strain energy',*Proceedings of the third european conference on numerical methods in geotechnical engineering*. Manchester, UK.

Holm, G., Andreasson, B., Bengtsson, P.E., Bodare, A. and Eriksson, H. (2002) *Mitigation of Track and Ground Vibrations by High Speed Trains at Lesdgard, Sweden* (10).

Hopper, R.J. (1992) *The effects and implications of sampling clay soils*. PhD Thesis. University of Surrey.

Houbrechts, J., Schevenels, M., Lombaert, G., Degrande, G., Rucker, W., Cuellar, V. and Smekal, A. (2011) *RIVAS Deliverable D1.1: Test procedures for the determination of the dynamic soil characteristics*. RIVAS (Railway Induced Vibration Abatement Solutions collaborative project).

HS2 Ltd. (2012) *Review of the Technical Specification for High Speed Rail in the UK*. London: Department for Transport. Available at: https://www.gov.uk/government/uploads/system/uploads/attachment_data/file/8083/hs2-review-of_technical-specification.pdf (Accessed: 02/03/2014).

Huang, X., Restuccia, F., Gramola, M. and Rein, G. (2016) 'Experimental study of the formation and collapse of an overhang in the lateral spread of smouldering peat fires', *Combustion and Flame*, pp. 1-10.

Hunt, G.A. (1994) *Analysis of requirements for railway contruction on soft ground. Technical Report LR TM 031*. London, UK: British Rail Research.

Huntley, S.L. (1990) 'Use of a dynamic penetrometer as a ground investigation and design tool in Hertfordshire', in *Field Testing in Engineering Geology*. . Geological Society Engineering Geology.

Hvorslev, M.J. (1949) *Subsurface Exploration and Sampling of Soils for Civil Engineering Purposes*. Vicksburg, USA.

Idriss, I.M., Dobry, R., Doyle, E.H. and Singh, R.D. (1976) 'Behaviour of soft clays under earthquake loading conditions. OTC 2671',*Eighth Annual Offshore Technology Conference*. Houston, Texas, May 1976.

Indraratna, B., Ionescu, D., Christie, D. and Chowdhury, D. (1997) 'Compression and Degradation of Railway Ballast Under One-Dimensional Loading', *Australian Geomechanics Journal*, pp. 48-61.

Ishihara, K. (1996) '*Soil behaivour in earthquake geotechnics*', in *Volume 46 of Oxford Engineering Science Series*. Oxford, UK: Clarendon Press.

ISO. (2017) *ISO 17892-6: Geotechnical investigation and testing - Laboratory testing of soil - Part 6: Fall cone test*. Brussels: European Committee for Standardisation.

Iwasaki, T., Tatsuoka, F. and Takagi, Y. (1978) 'Shear moduli of sands under cyclic torsional shear loading', *Soils and Foundations*, 18(1), pp. 39-56.

Jardine, R.J. (1992) 'Some observations on the kinematic nature of soil stiffness', *Soils and Foundations*, 32(2), pp. 111-124.

Jones, C.J.C. (2009) 'Low Frequency Ground Vibration', in Thompson, D.J. (ed.) *Railway Noise and Vibration: Mechanisms,Modelling and Means of Control*. Oxford: Elsevier.

Kalantari, B., Prasad, A. and Huat, B.B.K. (2010) 'Peat stabilization using cement, polypropyleneand steel fibres', *Geomechanics and Engineering*, 2(4).

Kalliainen, A., Kolisoja, P. and Nurmikolu, A. (2016) 'A 3D finite element model as a tool for analysing the structural behaivour of a railway track',*Proceedings of the 3rd International Conference on Transportation Geotechnics*. Portugal.

Kallioglou, P., Koninis, G., Tika, T. and Pitilakis, K. (2008) 'Shear Modulus and Damping Ratio of Organic Soils', *Geotechnical and Geological Engineering*.

Karlström, A. and Boström, A. (2006) 'An analytical model for train-induced ground vibrations from railways', *Journal of Sound and Vibration*, 292(1–2), pp. 221-241.

Katayama, I., Ozeki, K., Yamaya, A., Seshimo, Y., Jeong, Y.W. and Suzuki, H. (1992) 'Non-linear free-field response analysis of a vertical array data. Technical Report NCEER-92-0019',*Fourth Japan-US workshop on earthquake resistant design of lifeline facilities and countermeasure for soil liquefaction*. New York, US, 12th August 1992. NCEER.

Kaynia, A.M., Madshus, C. and Zackrisson, P. (2000) 'Ground vibration from high-speed trains: Prediction and countermeasure', *Journal of Geotechnical & Geoenvironmental Engineering*, 126(6), p. 531.

Kenney, J.T. (1954) 'Steady state vibration of a beam on an elastic foundation for moving load', *Journal of Applied Mechanics*, (76), pp. 359-64.

Kim, D.S. (1991) *Deformational characteristics of soils at small to intermediate strains from cyclic tests*. PhD Thesis. University of Texas.

Kim, T.C. and Novak, M. (1981) 'Resonant column technique for dynamic testing of cohesive soils', *Canadian Geotechnical Journal*, 18(3).

Kirby, A. (2011) *Stiffness and damping of sand at small strains using a resonant column*. Unpublished undergraduate dissertation. University of Southampton.

Kolsky, H. (1953) *Stress waves in solids*. Oxford: Clarendon Press.

Kramer, S.L. (1993) *Seismic response - Foundation in soft soils*. Washington: Washington State Transport Center.

Kramer, S.L. (1996) *Geotechnical Earthquake Engineering*. New Jersey, US.: Prentice-Hall Inc.

Krylov, V.V. (1994) 'On the theory of railway-induced ground vibrations', *Le Journal de Physique IV*, 04(C5), pp. C5-769-C5-772.

Krylov, V.V. (1995) 'Generation of Ground Vibrations by Superfast Trains', *Applied Acoustics*, 44, pp. 149-164.

Krylov, V.V. (1998) 'Effects of track properties on ground vibrations generated by high-speed trains', *Acustica- Acta Acustica*, 84, pp. 78-90.

Kumar, J. and Madhusudhan, B.N. (2010) 'A note on the measurement of travel times using bender and extender elements', *Soil Dynamics and Earthquake Engineering*, 30(7), pp. 630-634.

Lai, C.G., Callerio, E. and Faccioli, A. (2000) 'Mathematical modelling of railway-induced ground vibrations', *Proceedings of the International Workshop Wave 2000*. Bochum,Germany. Germany, pp. 99-110.

Laird, J.P. (1994) *Linear and Nonlinear Dynamic Properties of Soils at High Confining Pressures*. MSc Thesis. University of Texas at Austin.

Le Pen, L. (2008) *Track behaivour: The importance of the sleeper to ballast interface*. PhD Thesis. University of Southampton.

Le Pen, L., Watson, G., Powrie, W., Yeo, G., Weston, P. and Roberts, C. (2014) 'The behaviour of railway level crossings: Insights through field monitoring', *Transportation Geotechnics*, 1(4), pp. 201-213.

Lee, J.S. and Santamarina, J.C. (2005) 'Bender elements: Performance and Signal Interpretation', *Journal of Geotechnical & Geoenvironmental Engineering, ASCE*, 131(9), pp. 1063-1070.

Leong, E.C., Yeo, S.H. and Rahardjo, H. (2005) 'Measuring shear wave velocity using bender elements', *Geotechnical Testing Journal*, 28(5), pp. 488-498.

Lings, M.L., Pennington, D.S. and Nash, D.F.T. (2000) 'Anisotropic stiffness parameters and their measurement in a stiff natural clay', *Geotechnique*, 50(2), pp. 109-125.

Lo Presti, D.C., Pallara, O., Maugeri, N. and Cavallaro, A. (1998) 'Shear modulus and damping of a stiff marine clay from in situ and laboratory tests in: Geotechnical Site Characterisation', *First International Conference On Site Characterization*. Atlanta Georgia, USA, 19-22 April 1998. Balkema, Rotterdam.

Lysmer, J., Udaka, T., Tsai, C. and Seed, H.B. (1975) *FLUSH- a computer program for approximate 3D analysis of soil-structure interaction problems*. University of California.

Madshus, C. and Kaynia, A.M. (2000) 'High-speed railway lines on soft ground: dynamic behaviour at critical train speed', *Journal of Sound and Vibration*, 231(3), pp. 689-701.

Madshus, C. and Kaynia, A.M. (2001) '*High-speed trains on soft ground: track-embankment-soil response and vibration generation*', in Krylov, V.V. (ed.) *Noise and vibration form high-speed trains*. London: Thomas Telford, pp. 315-344.

Mak, P. (2014) Email -Pendolino Parameters, 27/03/2014.

Mavko, G. (2005) 'Conceptual Overview of Rock and Fluid Factors that Impact Seismic Velocity and Impedance', in *Parameters That Influence Seismic Velocity*. Standford Rock Physics Laboratory, pp. 73-90.

Meng, J. and Rix, G.J. (2003) 'Reduction of equipment-generated damping in resonant column measurements', *Geotechnique*, 53(5), pp. 503-512.

Mondolfo, L.F. (1976) *Aluminum alloys: structure and properties*. London: Butterworths.

Nazarian, S. and Desai, M.R. (1993) 'Automated surface wave method: field testing', *Journal of Geotechnical Engineering*, 119(7), pp. 1094-1111.

Network Rail Ltd. (2010) *East Coast Main Line 2016 Capacity Review*. Available at: http://www.networkrail.co.uk/browse%20documents/rus%20documents/route%20utilisation%20strategies/east%20coast%20main%20line/east%20coast%20main%20line%202016%20capacity%20review/east%20coast%20main%20line%202016%20capacity%20review.pdf.

Ordnance Survey (2016) *OS Maps Online*. Available at: https://www.ordnancesurvey.co.uk/osmaps.

Otter, L. (2011) *The influence of suction changes on the stiffness of railway formation*. PhD Thesis. University of Southampton.

Paderno, C. (2009) 'Simulation of ballast behaivour under traffic and tamping process', *9th Swiss Transport Research Conference*. Ascona.

Paolucci, R., Maffeis, A., Scandella, L., Stupazzini, M. and Vanini, M. (2003) 'Numerical prediction of low-frequency ground vibrations induced by high-speed trains at Ledsgaard, Sweden', *Soil Dynamics and Earthquake Engineering*, 23(6), pp. 425-433.

Park, C.B., Miller, R.D. and Xia, J. (1999) 'Multichannel analysis of surface waves (MASW)', *Geophysics*, 64, pp. 800-808.

Powrie, W., Priest, J.A. and Clayton, C.R.I. (2008) 'Recent research on railway track sub-base behaviour.', in Ellis *et al.* (eds.) *Advances in Transportation Geotechnics*. London: Taylor & Francis Group.

Powrie, W., Yang, L.A. and Clayton, C.R.I. (2007) 'Stress changes in the ground below ballasted railway track during train passage', *J. Rail and Rapid Transit*, 221(2), pp. 247-261.

Priest, J.A. (2004) *The effects of methane gas hydrate on the dynamic properties of a sand*. PhD Thesis. University of Southampton.

Priest, J.A., Best, A.I. and Clayton, C.R.I. (2005) 'A laboratory investigation into the seismic velocities of methane gas hydrate-bearing sand', *Journal of Geophysical Research*, 110(B04102).

Priest, J.A., Powrie, W., Le Pen, L., Mak, P. and Burstow, M.C. (2012) 'The effect of enhanced curving forces on the behaviour of canted ballasted track', *Proceedings of the Institution of Mechanical Engineers, Part F: Journal of Rail and Rapid Transit*, 227(3), pp. 229-244.

Rees, E.V.L. (2009) *Methane gas hydrate morphology and its effect on the stiffness and damping of some sediments*. PhD Thesis. University of Southampton.

Rees, S. (2016) *Introduction to Triaxial Testing - GDS Instruments Ltd.* Available at: www.gdsinstruments.com.

Richart, F.E. (1962) 'Foundation Vibrations', *Transactions of the ASCE*, 127(1), pp. 863-898.

Richart, F.E., Hall, J.R. and Woods, R.D. (1970) *Vibrations of soils and foundations*. New Jersey: Prentice Hall.

Rollins, K.M., Evans, M.D., Diehl, N.B. and Daily III, W.D. (1998) 'Shear Modulus and Damping Relationships for Gravels', *Journal of Geotechnical & Geoenvironmental Engineering*, 124(5), pp. 396-405.

Rowe, R.K., MacLean, M.D. and Soderman, K.L. (1984) 'Analysis of a geotextile-reinforced embankment constructed on peat', *Canadian Geotechnical Journal*, 21, pp. 563-576.

Rushworth, S. (2014) Email - Gravel Hole Wavespeeds.

Sadeghi, J. (2012) 'New Advances in Analysis and Design of Railway Track System', in Perpinya, X. (ed.) *Reliability and Safety in Railways*. InTechOpen.

Schevenels, M., Degrande, G. and Lombaert, G. (2004) 'The influence of the depth of ground water table on free field road traffic-induced vibrations', *International Journal for Numerical and Analytical Methods in Geomechanics*, 28, pp. 395-419.

Schneider, J.A., Hoyos Jr, L., Mayne, P.W., Macari, E.J. and Rix, G.J. (1999) 'Field and laboratory measurements of dynamic shear modulus of piedmont residual soils',*Behavioral Characteristics of Residual Soils*. Charlotte, North Carolina, October 17-20. ASCE Geotechnical Special Publication No.92.

Seed, H.B. and Idriss, I.M. (1970) *Soil Moduli and Damping Factors for Dynamic Response Analysis* (Report No. UCB/EERC-70/10). University of California. Berkeley Structural Engineers and Mechanics.

Seed, H.B., Wong, R.T., Idriss, I.M. and Tokimatsu, K. (1986) 'Moduli and damping factors for dynamic analyses of cohesionless soils', *Journal of Geotechnical Engineering*, 112(11), pp. 1016-1032.

Sheng, X. (2001) *Ground Vibrations Generated from Trains*. PhD Thesis. University of Southampton.

Sheng, X., Jones, C.J.C. and Petyt, M. (1999) 'Ground vibration generated by a load moving along a railway track', *Journal of Sound and Vibration*, 228(1), pp. 129-156.

Sheng, X., Jones, C.J.C. and Thompson, D.J. (2003) 'A comparison of a theoretical model for quasi-statically and dynamically induced environmental vibration from trains with measurements', *Journal of Sound and Vibration*, 267(3), pp. 621-635.

Sheng, X., Jones, C.J.C. and Thompson, D.J. (2004a) 'A theoretical model for ground vibration from trains generated by vertical track irregularities', *Journal of Sound and Vibration*, 272(3–5), pp. 937-965.

Sheng, X., Jones, C.J.C. and Thompson, D.J. (2004b) 'A theoretical study on the influence of the track on train-induced ground vibration', *Journal of Sound and Vibration*, 272(3–5), pp. 909-936.

Sheng, X., Jones, C.J.C. and Thompson, D.J. (2006) 'Prediction of ground vibration from trains using the wavenumber finite and boundary element methods', *Journal of Sound and Vibration*, 293(3–5), pp. 575-586.

Shih, J.Y., Thompson, D.J. and Zervos, A. (2016) 'Modelling of ground-borne vibration when the train speed approaches the critical velocity', *The 12th International Workshop on Railway Noise*. Terrigal, Australia, September 2016.

Shih, J.Y., Thompson, D.J. and Zervos, A. (2017) 'The influence of soil nonlinear properties on the track/ground vibration induced by trains running on soft ground', *Transportation Geotechnics*, 11, pp. 1-16.

Shirley, D.J. and Hampton, L.D. (1978) 'Shear wave measurements in laboratory sediments', *Journal of Acoustical Society of America*, 63(2), pp. 607-613.

Siddique, A. (1990) *A numerical and experimental study of sampling disturbance*. PhD Thesis. Univeristy of Surrey.

Skempton, A.W. (1954) 'The pore pressure coefficients A and B', *Geotechnique*, 4(4), pp. 153-173.

Southern Testing Ltd. (2016) *Dynamic Probing*. Available at: http://www.southerntesting.co.uk/services/ground-investigation/dynamic-probing (Accessed: September 2016).

Stokoe, K.H., Darendeli, M.B., Andrus, R.D. and Brown, L.T. (1999) 'Dynamic soil properties: Laboratory, field and correlation studies', *2nd Int. Conf. on Earthquake and Geotechnical Engineering*. Lisbon, Portugal.

Stokoe, K.H., Isenhower, W.M. and Hsu, J.R. (1980) 'Dynamic properties of offshore silty samples. OTC 3771',*12th Annual Offshore Technology Conference*. Houston, Texas, May.

Sun, J.I., Golesorkhi, R. and Bolton Seed, H. (1988) *Dynamic moduli and damping ratios for cohesive soils* (Report No. UCB/EERC-88/15).

Takemiya, H. (2003) 'Simulation of track–ground vibrations due to a high-speed train: the case of X-2000 at Ledsgard', *Journal of Sound and Vibration*, 261(3), pp. 503-526.

Terzaghi, K. and Peck, R.B. (1948) *Soil Mechanics in Engineering Practice*. Hoboken: John Wiley & Sons.

Thompson, D.J. (2009) *Railway Noise and Vibration: Mechanisms, Modelling and Means of Control*. Elsevier.

Thompson, D.J., Jin, Q., Dijckmans, A., Lombaert, G. and Jiang, J. (2013) *Benchmark comparisons of models for track and ground vibration due to passing trains (cases with no mitigation measures)* (RIVAS_ISVR_WP4_D4_7_V04).

Triepaischajonsak, N., Thompson, D.J., Jones, C.J.C., Ryue, J. and Priest, J.A. (2011) 'Ground vibration from trains: experimental parameter characterization and validation of a numerical model', *Proceedings of the Institution of Mechanical Engineers, Part F: Journal of Rail and Rapid Transit*, 225(2), pp. 140-153.

USACE. (1994) *Engineering Manual EM 110-2-2504*.

Vardanega, P.J. and Bolton, M.D. (2013) 'Stiffness of Clays and Silts: Normalizing Shear Modulus and Shear Strain', *Journal of Geotechnical and Geoenvironmental Engineering*, 139(9), pp. 1575-1589.

Viggiani, G. and Atkinson, J.H. (1995) 'Interpretation of bender element tests', *Gèotechnique*, 45(1), pp. 149-154.

Viktorov, I. (1967) *Rayleigh and Lamb Waves Pysical Theory and Applications*. New York: Plenum Press.

Vucetic, M. and Dobry, R. (1991) 'Effect of soil plasticity on cyclic response', *Journal of the Geotechnical Engineering Division*, 117, pp. 89-117.

Walczak, R., Rovdan, E. and Witkowska- Walczak, B. (2002) 'Water retention characteristics of peat and sand mixtures', *International Agrophysics*, 16, pp. 161-165.

Wehling, T.M., Boulanger, R.W., Arulnathan, R., Harder, L. and Driller, M. (2003) 'Nonlinear dynamic properties of a fibrous organic soil', *Journal of Geotechnical & Geoenvironmental Engineering*, 129(10), pp. 929-939.

Wilson, S.D. and Dietrich, R.J. (1960) 'Effect of consolidation pressure on elastic and strength properties of clay',*ASCE Research Conference on Shear Strength Properties of Clay*. Boulder, Colorado.

Wiseman, M. (2015) *Investigation of ground vibration from trains and validation prediction models with measurements from two sites*. MEng Report. University of Southampton.

Woldringh, R. and New, B. (1999) 'Embankment design for high speed trains on soft soils',*Twelfth European Conference on Soil Mechanics and Geotechnical Engineering, 'Geotechnical Engineering for Transport Infrastructure'.* Amsterdam. Rotterdam: Balkema.

Woodward, P.K., Connolly, D. and Laghrouche, O. (2016) 'Exploring the role of peak particle velocity and critical speed when considering ballasted or fixed form high speed tracks',*Proceedings of the Permanent Way Institution & The Union of European Railway Engineer Associations 2016 Technical Conference - Fixed Track Forms for High Speed Lines*. Manchester, UK.

Woodward, P.K., Kennedy, J., Laghrouche, O., Connolly, D.P. and Medero, G. (2014) 'Study of railway track stiffness modification by polyurethane reinforcement of the ballast', *Transportation Geotechnics*, 1(4), pp. 214-224.

Woodward, P.K., Laghrouche, O., Mezher, S.B. and Connolly, D.P. (2015) 'Application of Coupled Train-Track Modelling of Critical Speeds for High-Speed Trains using Three-Dimensional Non-Linear Finite Elements', *International Journal of Railway Technology*, 4(3), pp. 1-35.

Yamashita, S., Kawaguchi, T., Nakata, Y., Mikami, T., Fujiwara, T. and Shibuya, S. (2009) 'Interpretation of international parallel test on measurement of Gmax using bender elements', *Soils and Foundations*, 49(4), pp. 631-650.

Yang, L.A., Powrie, W. and Priest, J.A. (2009) 'Dynamic Stress Analysis of a Ballasted Railway Track Bed during Train Passage', *Journal of Geotechnical & Geoenvironmental Engineering*, 135(5), pp. 680-689.

Yoshida, N., Kobayashi, S., Suetomi, I. and Miura, K. (2002) 'Equivalent linear method considering frequency dependent characteristics of stiffness and damping', *Soil Dynamics and Earthquake Engineering*, 22, pp. 205-222.

Youn, J.U., Choo, Y.W. and Kim, D.S. (2008) 'Measurement of small-strain shear modulus Gmax of dry and saturated sands by bender element, resonant column, and torsional shear tests', *Canadian Geotechnical Journal*, 45(10), pp. 1426-1438.

Yu, P. and Richart, F.E. (1984) 'Stress ratio effects on shear modulus of dry sands', *Journal of Geotechnical Engineering*, 110(3), pp. 331-345.

Yuan, D. and Nazarian, S. (1993) 'Automated surface wave method: inversion technique', *Journal of Geotechnical Engineering*, 119(7), pp. 1112-1126.

Zainorabidin, A. and Wijeyesekera, D.C. (2009) 'Shear modulus and damping properties of peat soils',*Advances in Computing and Technology Conference*. University of East London, Canary Wharf, London.

Zen, K., Umehara, Y. and Hamada, K. (1978) 'Laboratory tests and in-situ seismic survey on vibratory shear modulus of clayey soils with various plasticities',*Fifth Japan Earthquake Engineering Symposium*. Tokyo, Japan.